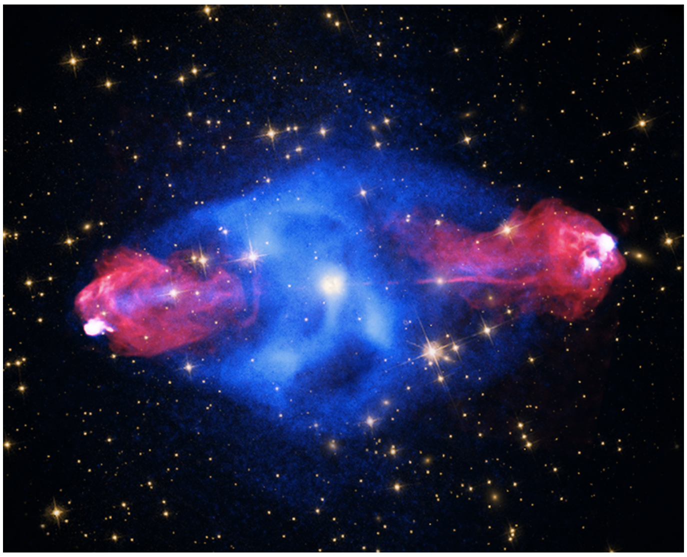

Probing Galaxy Evolution and Feedback using Giant Gaseous Structures associated with High Redshift Active Galaxies

Marckelson Santana da Silva
Programa Doutoral em Astronomia
Departamento de Física e Astronomia
2019

Orientador
Andrew Humphrey, Doctor, Instituto de Astrofísica e Ciências do Espaço (IA-CAUP)
Coorientador
Patricio A. Lagos Lizana, Doctor, Instituto de Astrofísica e Ciências do Espaço (IA-CAUP)

Probing Galaxy Evolution and Feedback using Giant Gaseous Structures associated with High Redshift Active Galaxies

by

Marckelson S. da Silva

A thesis submitted in conformity with the requirements
for the degree of Doctor of Philosophy
Graduate Department of Physics and Astronomy
University of Porto

Dedication

This thesis is dedicated to my mother and wife who have always been a constant source of support and encouragement during the challenges of the last four years. Also to my brother who often needed my help and I was not present, and my uncle whose good examples have taught me to work hard for the things that I aspire to achieve. This work is also dedicated to my friends Rodney, Adhemar, Tiago, Aécio, Alexandra, João, Paola, Jhon and Leandro who have always been a constant source of joy and encouragement in many, many moments.

Acknowledgements

As with so many things, this thesis is more than the sum of its parts. It represents the many people I have known and the many experiences I have had, all leaving their mark on me and contributing in large and small ways to this document. I am tremendously grateful to all who have in some way helped or supported me and my work that has lead to this thesis. I would like to thank Conselho Nacional de Desenvolvimento Científico e Tecnológico (CNPq) for funding my PhD studentship. I warmly thank my two supervisors Andrew Humphrey and Patricio Lagos for supervising my research project, and especially for their patient and meticulous proof-reading of all my manuscripts, and for their substantial contribution to so many of the ideas in this thesis, for happily assisting me with difficult observations and data analysis, whilst making sure I deeply understood every step along the way. I have learned incredibly much from both of you.

I am fortunate to have many, many wonderful people in my life. My family is possibly the most loving and enthusiastic group of people ever assembled. Their unwavering love and encouragement have buoyed me while pursuing this degree and living abroad. I am very grateful for the positive support during my numerous phases of confusion.

I also wish to acknowledge my collaborators/co-authors, Montse Villar-Martín, Sperello di Serego Alighieri, Andrea Cimatti, Robert Fosbury, Roderick Overzier, Joel Vernet, Luc Binette, Rodney Guimarães, Tom Scott and Polychronis Papaderos. These people have all helped me substantially throughout the last four years with valuable discussions and suggestions which have improved my work. A special thank you goes to Rodney Guimarães an extraordinary educator and friend who has been a great help and support from the beginning of the PhD, with the first observations and always with encouraging words.

Finally, a thanks to all my friends who made the work-days more pleasant and which provided moments of great joy during these four years.

Abstract

This thesis deals with a study of extended Lyα emitting nebulae and giant H I absorbers associated with active galaxies at high-redshift ($z > 2$). This work is split into three main parts.

In the first, the kinematic properties of the giant Lyα emitting gas associated with the radio galaxy MRC 0943–242 shows evidence for both outflows and inflows being induced by radio-mode feedback. The extended ionized gas appears consistent with super-solar metallicity.The explored degeneracy between the column density and Doppler width suggests a possible range in column density, with the two best-fitting being log N(H I/cm^{-2}) = 15.20 and 19.63. The extended H I absorber is blueshifted relative to the emission line gas, but shows a systematic decrease in blueshift towards larger radii, consistent with a large scale expanding shell.

The second part of the thesis provides a study of regions of five high-redshift radio galaxies that are unlikely to be illuminated by the active nucleus. Spatially extended Lyα emission is detected with large line widths, which although impacted by resonant scattering, is suggestive of turbulent motion. The gas dynamics indicates that radial motion dominates in the direction perpendicular to the radio axis, although it is not possible to distinguish between outflow and infall scenarios due to the resonant nature of the Lyα line. Extended, blueshifted Lyα absorption is detected in the direction perpendicular to the radio axis, supporting the idea that the absorbing structure covers the entire Lyα halo, consistent with being part of a giant, expanding shell of gas enveloping the galaxy and its gaseous halo.

Finally, focusing on the study of the UV emission line ratios of a sample of 145 type II quasars, and comparing against a grid of AGN photoionization models, the results presented in the third part of the thesis indicate that some objects show very high C IV/He II consistent with BLR densities. Solar or super-solar nitrogen abundances are required for most of the objects. A subset of the objects suggests that Si/C and Si/O abundances are an order of magnitude above their Solar values. A new UV-line based criteria to select genuine type II quasars with low-density narrow line regions is proposed, to identify intermediate-density objects.

Resumo

Esta tese trata do estudo de extensas nebulosas de Lyα e extensos absorvedores de H I associados com galáxias de núcleo ativo em alto *redshift* (z > 2). Este trabalho é dividido em três partes.

No primeiro, as propriedades cinemáticas da extensa nebulosa de Lyα associada com a galáxia de rádio MRC 0943–242 mostra evidências de ambos *outflows* e *inflows* sendo induzidos por *radio-mode feedback*. O extenso e ionizado gás aparece consistente com super solar metalicidade. A degenerescência entre a coluna de densidade e o parâmetro de alargamento Doppler sugere um possível intervalo em colunas de densidade, com os melhores resultados sendo log N(H I/cm^{-2}) = 15.20 and 19.63. O extenso absorvedor de H I mostra uma sistemática redução em *blueshift* à medida que se afasta do centro da galáxia, consistente com uma extensa camada de gás em expansão.

A segunda parte apresenta um estudo das regiões de 5 galáxias de rádio que provavelmente não são iluminadas pelo núcleo ativo. Emissão de Lyα espacialmente estendida é detectada com linhas de emissão muito largas sugerindo movimento turbulento do gás, embora o espalhamento de fótons de Lyα deva afetar a largura das linhas. As dinâmicas do gás indicam que o movimento radial é dominante na direção perpendicular ao eixo de rádio, embora não seja possível distinguir entre *outflow* e *infall* devido a natureza resonante de Lyα. Extensa e *blueshifted* absorção em Lyα é detectada na direção perpendicular ao eixo de rádio, consistente com a ideia de ser parte de uma extensa camada de gás em expansão, envolvendo a galáxia e o seu halo gasoso.

Focando no estudo de linhas de emissão no ultravioleta de uma amostra de 145 quasares do tipo 2, e comparando com modelos de fotoionização, os resultados apresentados na terceira parte da tese indicam que alguns objetos mostram valores muito altos de C IV/He II consistente com densidades da BLR. Para a maioria dos objetos, a abundância de nitrogênio parece ser solar ou super solar. Um subconjunto dos objetos sugerem que as abundâncias de Si/C e Si/O são uma ordem de magnitude acima do seus valores solares. Um novo critério, baseado nas linhas de emissão no ultravioleta, é proposto para selecionar genuínos quasares do tipo 2 com baixa densidade e identificar objetos com densidade intermediária.

Contents

List of Tables

List of Figures

Chapter 1

Introduction

The centers of many galaxies contain small, dense and luminous components known as active galactic nuclei (also known as AGN). AGNs can be so bright that they outshine their entire host galaxies, changing their emission properties. While normal galaxies predominantly emit thermal-radiation in a relatively narrow wavelength range between the near-infrared and the near-ultraviolet, AGNs are powerful emitters of non-thermal radiation covering the entire electromagnetic spectrum from the radio to the gamma-ray regime.

Understanding the properties and formation of AGNs is an important component of galaxy evolution studies. AGNs form a important population of galaxies, and for that reason any theory of galaxy formation must also address the formation of AGN. It is believed that AGNs are powered by matter accreting onto a supermassive black hole (hereafter SMBH), and the observed correlation between the masses of SMBHs and various properties of their host galaxies (e.g., bulge luminosity; Kormendy and Richstone 1995, mass; Häring and Rix 2004, velocity dispersion; Ferrarese and Merritt 2000 and light profile concentration; Gebhardt et al. 2000; Böker et al. 2001; Graham et al. 2001) strongly suggests that the formation of SMBHs is closely connected to galaxy formation. In addition, given that virtually all spheroids are found to harbor a SMBH, it is likely that a large number of (if not all) normal galaxies must have experienced an AGN phase in their past (Kormendy and Richstone, 1995; Kauffmann et al., 2003). Moreover, AGNs are powerful energy sources, and the energy involved in the feedback process must have important impact on the intergalactic medium (hereafter IGM) as well as on the formation and evolution of galaxies.

In this chapter, the background information relevant to this Thesis project is described.

1.1 Active Galactic Nuclei

Active galactic nuclei have been the subject of much attention among astronomers since the first example was identified in the 1940s (e.g. Seyfert, 1943). AGNs have powerful non-thermal emission that originates from a compact core, which is believed to be powered by the central, spinning, supermassive black-hole (hereafter SMBH) surrounded by the accretion disk.

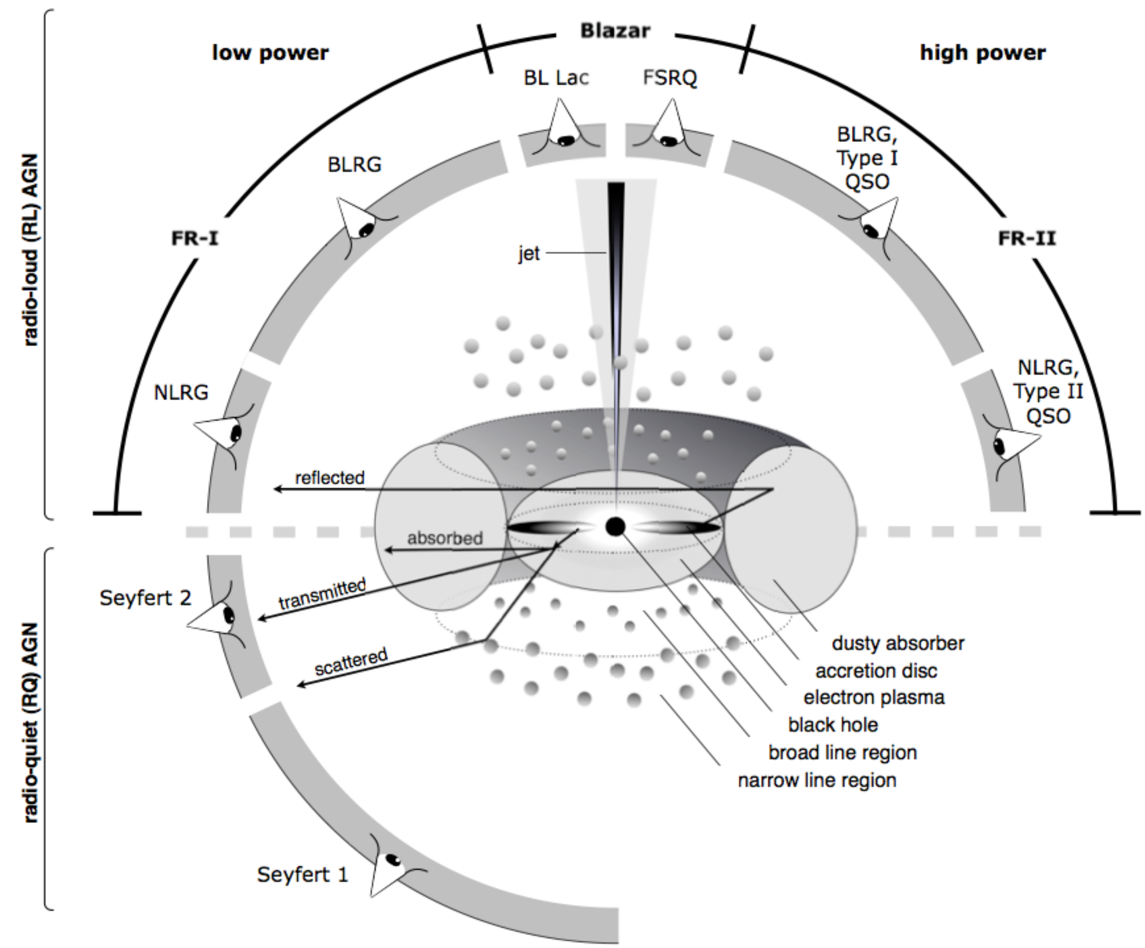

Figure 1.1: Schematic diagram of the unified model for AGNs, showing the most varied classifications according to the line of sight of the observer (Beckmann and Shrader, 2012).

AGNs have been classified based on the idea that the large diversity of observed properties can be explained by a small number of physical parameters. The unification model, developed by various authors (Barthel 1989; Antonucci 1993 and references therein), introduced the explanation that many of the observed characteristics in AGNs are based on the luminosity and inclination of the central source (see also Urry and Padovani, 1995; Urry, 2003; Netzer, 2015). In addition to the luminosity and inclination of the central source, current AGN classification has also been extended through higher-quality observations of a much larger number of sources, on better understanding of the physics of accretion and the line emitting processes, where the main classes of today are Type-I radio-quiet AGNs (Seyfert 1 galaxies and radio-quiet quasars (QSOs)), Type-I radio-loud AGNs (Broad Line Radio Galaxies (or BLRGs) and radio-loud QSOs), Type-II radio-quiet AGNs (Seyfert 2 and Type II radio-quiet quasars), Type-II radio-loud AGNs (Narrow Line Radio Galaxies or NLRGs), Low-ionization nuclear emission-line (LINER) and Blazars (BL-Lac and Flat-Spectrum Radio Quasars or FSRQ) (see Figure 1.1).

The first notably distinct observational characteristic of AGN is the presence of emission lines with widths upwards of 1000 km s^{-1} and far in excess of any known class of objects. These broad lines are thought to arise in a gas of fairly high density (e.g. $n_e > 10^6$ cm^{-3}; Zhang et al. 2018; Baskin and Laor 2018) situated around the accreting black hole, which is known as Broad Line Region or BLR. From this region, the strongest lines are usually Hα, Lyα, C IV λ1549 Å, and O VI λ1035 Å. The density is high enough to suppress all optical forbidden lines but not all the semi-forbidden lines such as C III] λ1909 Å and O III] λ1663 Å. In Figure 1.1, is shown that the observation of broad lines typically from the BLR belongs to the class of Type-I AGNs, which include the subclasses Seyfert 1, BLRG and Type I QSO. On the other hand, when the BLR is obscured by the geometrically and optically thick dusty and molecular torus (often referred to as the "dusty torus") the observer is able to see narrow lines that arise in a low density gas (e.g. $10^2 \leqslant n_e \leqslant 10^6$ cm^{-3}; Nagao et al. 2006a; Matsuoka et al. 2009) region several parsecs or more from the AGN called the Narrow Line Region or NLR. This region dominates the line spectrum of the class of Type-II AGNs that includes the subclasses Seyfert 2, NLRG and Type II QSO. Unlike the BLR, the spectrum from the low density gas include intense forbidden lines in addition to semi forbidden and permitted lines. Although obscured, from direct view, Type II active galaxies still harbour a BLR, as shown by the detections of scattered broad lines via spectropolarimetric observations (e.g. Miller and Goodrich, 1990; Young et al., 1998; Tran et al., 2000; Nagao et al., 2004).

1.1.1 Seyfert Galaxies

Seyfert galaxies were the first active galaxies to have been discovered (see Fath, 1909; Slipher, 1917; Hubble, 1926; Seyfert, 1943). They are characterized by spiral-like morphologies with bright star-like nuclei. Their luminosity is considerably lower than that of QSOs, and spectroscopic observations show that the spectra of Seyfert nuclei have non-thermal continua (i.e., not produced by O or B stars) and contain strong emission lines from a variety of species, often including high excitation lines.

Seyfert galaxies were initially subdivided into two categories, type 1 and type 2, according

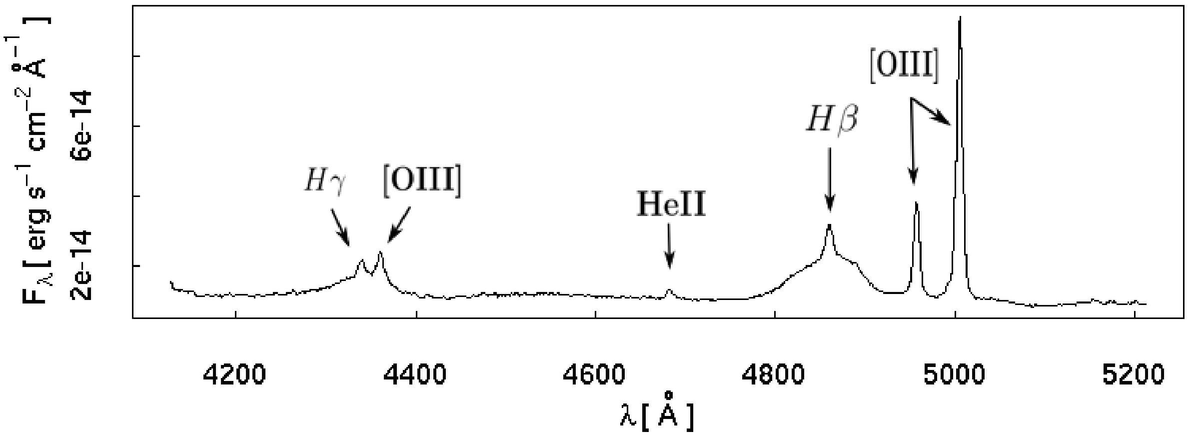

Figure 1.2: Optical spectrum of the nuclear region of the Seyfert 1 galaxy NGC 5548 showing broad hydrogen lines (up to about 10^4 km s^{-1}) but narrower forbidden lines (Weedman, 1977; Ho et al., 1995).

to the widths of their emission lines. In Seyfert 1 galaxies (Sy 1), the permitted lines such as H i, He i and He ii, are very broad with full widths at half maximum (FWHM) corresponding to velocities in the range 10^3 – 10^4 km s^{-1} (Osterbrock, 1976, 1989), which is significantly larger than characteristic velocities (like rotational velocities) found in normal galaxies (see Figure 1.2). The forbidden lines , such as [O iii] λ 5007 Å, [S ii] λ 6731 Å and [N ii] λ 5755 Å, are much narrower, with FWHM corresponding to velocities in the range 10^2 – 10^3 km s^{-1} (e.g. Osterbrock, 1976; Nelson and Whittle, 1995; Arribas et al., 1997). In Seyfert 2 galaxies (Sy 2) both permitted and forbidden lines have narrow velocity widths, typically of a few hundred km s^{-1} (see Figure 1.2; Lena et al. 2015). In Sy 2 galaxies, the intrinsic X-ray emission is attenuated by the obscuring torus and the observed flux, as well as the X-ray spectral shape, depend on the optical depth of the obscuring torus (Awaki et al., 1991; Smith and Done, 1996; Turner et al., 1997; Bassani et al., 1999; Cappi et al., 2006). Sy 2 and Sy 1 galaxies are expected to show systematically less difference for the observed hard X-ray luminosities and more difference for the soft X-ray luminosities (Smith and Done, 1996; Schurch et al., 2004).

The linewidths reflect the velocities of the emitting gas clouds, and the large difference in the FWHM between the permitted and forbidden lines in Sy 1 indicate that these two types of emission lines are produced in different regions. On the other hand, in the case of Sy 2 both permitted and forbidden lines are likely to emanate from the same region (Weedman, 1977). Usually, very broad lines with FWHM > 1000 km s^{-1}, are expected to come from a BLR, while lines with FWHM < 1000 km s^{-1} are expected to arise from a NLR (see Figure 1.1). The lack of broad emission lines in Sy 2 does not necessarily imply the absence of a BLR, it may merely reflect that this region is blocked due to its orientation relative to the line of sight.

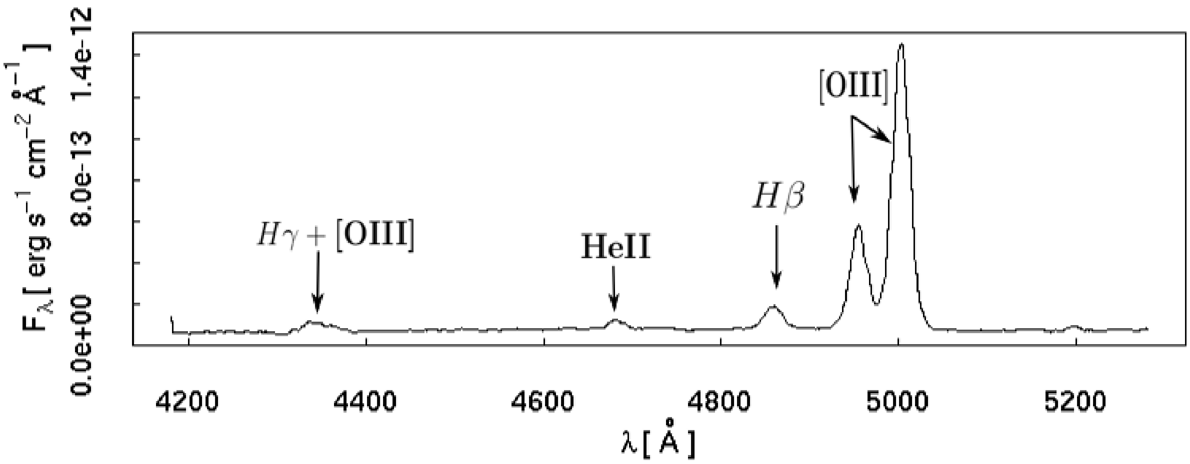

Figure 1.3: Optical spectrum of the nuclear region of the Seyfert 2 galaxy NGC 1068 showing hydrogen and forbidden lines with the same width (Weedman, 1977; Ho et al., 1995).

The optical spectrum of Sy 1 is very similar to that of radio-quiet quasars. The separation of Sy 1 and quasars is historical since these two categories were introduced only because of the different methods of discovering them. However, except for the different nuclear luminosity, no fundamental physical difference seems to exist. Based on the unified model for AGNs, both Sy 1 and quasars are combined under the name Type I AGNs, while Sy 2 is classified under the name Type II AGNs (see Figure 1.1).

Other subdivisions for Seyfert galaxies have been presented based on optical spectra, including Seyfert 1.2, 1.5, 1.8 and 1.9 (e.g. Osterbrock, 1977, 1981). Those galaxies in which the narrow and wide components of the Hβ emission line have the same intensity are classified as Seyfert 1.5. In Seyfert 1.2 galaxies, the intensity of the narrow component of the Hβ emission line is intermediate compared to the same emission line emitted by Seyfert 1 and 1.5. In Seyfert 1.8 galaxies it is observed that Hβ and Hα show strong narrow component with a weak but still visible component. When a Seyfert galaxy shows a strong narrow component in Hβ and Hα, but a weak broad Hα component is seen only in Hα, then it is classified as a Seyfert 1.9.

Although it is not highlighted in the schematic diagram of the unified model for AGNs, observations have also reported that there is a peculiar class of AGNs that are classified based on their optical emission line properties. Commonly known as Narrow Line Seyfert 1 galaxies (or NLSy 1), this class of objects usually have FWHM of the Hβ broad emission line < 2000 km s^{-1}, weak [O III] lines with a flux ratio of [O III]/Hβ < 3 and strong permitted optical/UV Fe II emission emission lines (Osterbrock and Pogge, 1985; Goodrich, 1989; Pogge, 2000; Véron-Cetty et al., 2001). The NLSy 1 galaxies are believed to be hosted by spiral galaxies (Crenshaw et al., 2003; Deo et al., 2006), although early-type galaxies have been considered as the host for the radio/γ-ray loud subset of NLSy 1 (Antón et al., 2008; León-Tavares et al., 2013). They usually show a rapid soft X-ray variability (Pounds et al., 1995; Leighly, 1999a), steep soft X-ray spectra (Boller et al., 1996; Wang et al., 1996; Leighly, 1999b) and low amplitude optical variability (Grupe, 2004; Rakshit and Stalin, 2017). From the analysis of optical spectroscopic data, it has been inferred that the NLSy 1 galaxies are powered by low mass black holes ($\sim 10^{6-8}$ $M_{\odot}$) having higher accretion rate (Xu et al., 2012; Foschini et al., 2015; Cracco et al., 2016; Rakshit et al., 2017). They are typically 1-2 orders of magnitude less massive than the black holes embedded in the cores of broad line Seyfert galaxies and more powerful radio sources, like blazars and radio-loud quasars, which are nearly always hosted by early-type galaxies (Scarpa et al., 2000; Boroson, 2002; Olguín-Iglesias et al., 2016), and have black hole masses $> 10^{8}$ $M_{\odot}$ (Dunlop et al., 2003; McLure and Jarvis, 2004; Chiaberge et al., 2005; Gopal-Krishna et al., 2008; Chiaberge and Marconi, 2011; Tadhunter, 2016; Coziol et al., 2017). Their detection at radio and γ-ray bands have suggested the unambiguous presence of relativistic jets emitting strong nonthermal radiation, which is characteristic of blazars (Yuan et al., 2008; Foschini et al., 2015). Multi-band broad band SED modeling of the γ-ray detected NLSy 1 galaxies indicate that these objects have many properties similar to the blazars (Paliya et al., 2013) and specifically resembling the flat spectrum radio quasar category (Paliya et al., 2018). In the radio band, the γ-ray emitting NLSy 1 galaxies show a compact core jet morphology, high brightness temperature, superluminal motion and significant radio variability (Komossa et al., 2006; Doi et al., 2006).

1.1.2 Quasars

When first recognized, by Schmidt (1963), quasars appeared at radio and optical wavelengths as faint, point-like objects with a very blue optical continumm ($f_{\nu} \propto \nu^{0.28}$; Oke 1963). The name comes from their alternative designations of 'Quasi-Stellar Radio Source' or 'Quasi-Stellar Object' (QSO), which was originally used for the optical identifications of compact radio sources with Seyfert-like spectra (prominent broad lines but rather weaker narrow lines). The radio characteristics of these objects were often similar to those of powerful radio sources, but their optical images showed unresolved, luminous nuclei that are unusually blue and often variable (see Figure 1.4).

Subsequent radio observations of high spatial resolution have shown that flat-spectrum quasars are generally core-dominated in the radio, indicating that the emission from the core is much stronger than emission from the extended regions (Padovani, 1999). Some of these show an elongated structure, generally classified as double lobed, due to the jets delivering energy to lobes hundreds of kpc from the core, whose relative motion to each other can be detected on time scales of a few years (Marshall et al., 2018). In some cases, the apparent velocity of

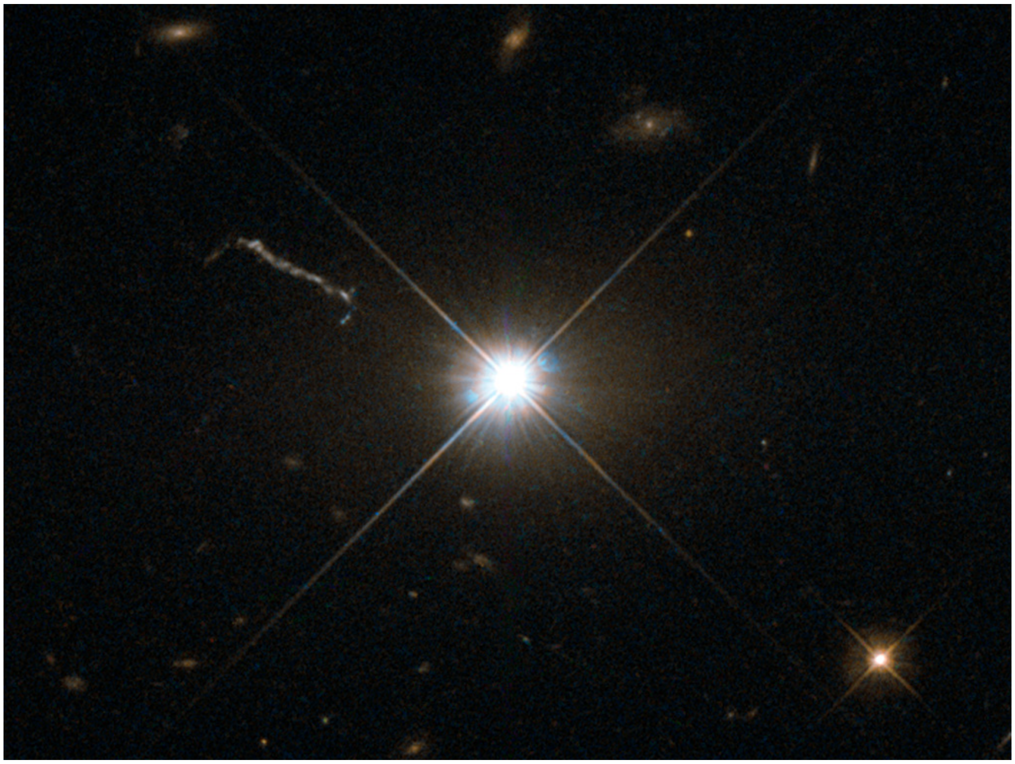

Figure 1.4: Image of the brighter quasar 3C 273 from Hubble's Wide Field and Planetary Camera 2 (HST and WFPC2; Optical B and V band), which resides in a giant elliptical galaxy in the constellation of Virgo. In addition, the optical jet can be seen SW of the quasar as a cloudy streak. *Credit: ESA/Hubble & NASA*

separation in the transverse direction is inferred to exceed the speed of light. Such superluminal motion is likely due to relativistic jets lying almost along the line of sight (Vermeulen and Cohen, 1994).

The extremely blue colors of quasars allows them to be efficiently detected using optical photometry, without the need to first detect them in the radio. This color-selection technique has proved very successful, and resulted in the detection of many intrinsically bright, high-redshift sources with broad emission lines. Most of these sources are faint in the radio domain of the spectrum, being classified as radio-quiet quasars. Originally, the term quasi-stellar object (or QSO) was used to refer to these radio-quiet quasars, however this terminology is no longer common today because the clear dichotomy between radio-loud and radio-quiet sources is not considered valid any more. In addition, radio emission can be detected in radio-quiet quasars if they are observed at sufficiently high sensitivity. Nowadays, the expression QSO is used for both radio-loud quasars and radio-quiet quasars, although the large majority of QSOs belong to the radio-quiet category (Barvainis et al., 2005).

With luminosities in the range $10^{45} < L_{bol} < 10^{48}$ erg s^{-1}, QSOs are the most luminous

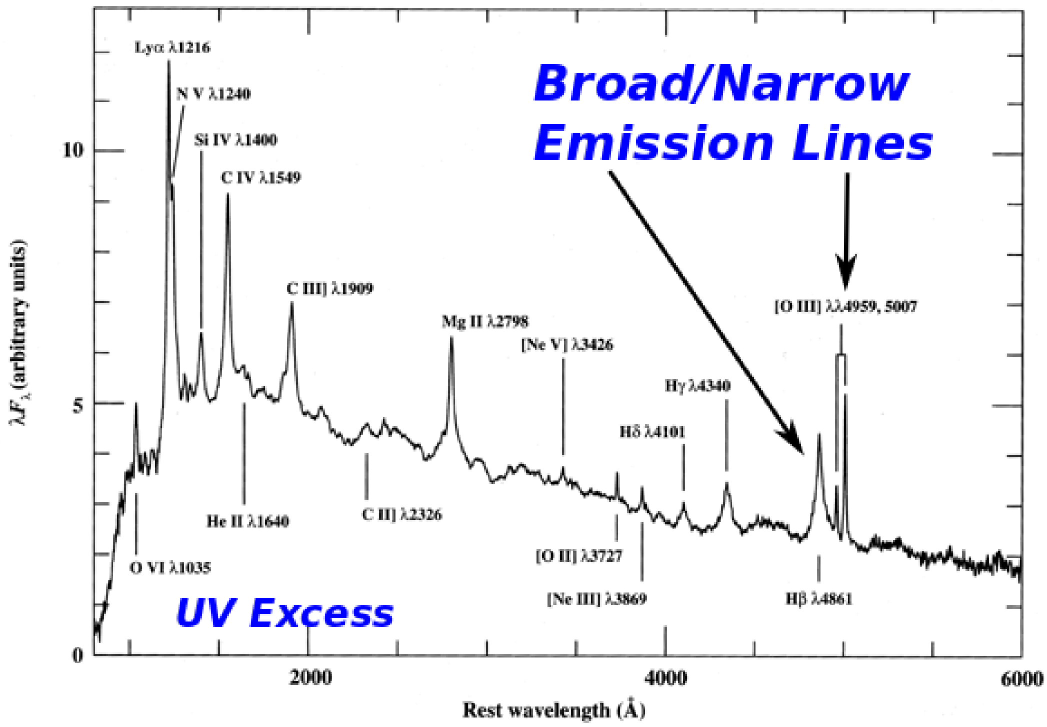

Figure 1.5: Composite spectrum plotted as λF(λ) *versus* rest-frame wavelength with the principal emission lines identified (Francis et al., 1991).

AGNs (e.g. Runnoe et al., 2012). Consequently, being outshined by the QSO, their host galaxies can be extremely difficult to detect. Nevertheless, largely due to the unprecedented spatial resolution achievable with the HST, host galaxies of several low-redshift QSOs have now been observed (Lehnert et al., 1999; Dunlop et al., 2003; Wylezalek et al., 2016). Although in many cases the images are not sufficiently clear to reveal the details about their morphologies, they suggest that the host galaxies of low-redshift QSOs have diverse properties; while some appear to be normal spirals and ellipticals, others are strongly disturbed or interacting systems (Bahcall et al., 1997; Dunlop et al., 2003; Bennert et al., 2008).

QSOs show strong permitted and semiforbidden emission lines, featuring the elements of Hydrogen (the Balmer and Lyman series are prominent), Helium (He), Carbon (C) and Magnesium (Mg), amongst others. The emission lines are also very broad and it was realized early on that this implied velocity widths of several thousand km s^{-1} for the line emitting gas (Greenstein and Schmidt, 1964). In addition to the broad emission lines are the narrow forbidden emission lines, with [O II] λ3727, [O III] λ5007 and [N II] λ6584 typically being the strongest (see Figure 1.5). A strong UV continuum and broad permitted and semi-forbidden emission lines (10^3 – $2{\times}10^4$ km s^{-1}) that originate very close to the central engine are typical of sight lines without significant obscuration. QSOs with such characteristics are classified as

Type I QSOs (see Figure 1.1). Similar to the Sy 1 and Sy 2 dichotomy, QSOs that do not show broad emission lines are classified as Type II QSOs (Zakamska et al., 2005; Alexandroff et al., 2013; Netzer, 2015; Greene et al., 2014).

Type II QSOs (QSO2s), also known as obscured quasars, are systems where the emission from the accretion disk is not directly detected due to the presence of material between the accretion disk and the observer. This material, which causes obscuration, is typically composed of dust and gas which can absorb the emission and scatter a large fraction away from the line of sight of the observer (Antonucci, 1993; Lacy et al., 2015). A number of studies have treated the physical nature of obscuration as dominated by a single regime (most often on the scale of a torus; Davies et al. 2015; Mateos et al. 2016, 2017), but evidence has grown that obscuration can occur on a range of scales and physical conditions. In general, previous works have focused on three main regimes of obscuration: (i) the nuclear torus posited by AGN unification models, which comprises of small-scale, broadly axisymmetric structure of dust and gas that surrounds the SMBH, accretion disk, and BLR clouds, and obscures them along some lines of sight (Antonucci, 1993; Urry and Padovani, 1995; Netzer, 2015), (ii) circumnuclear gas associated with central starbursts disks that can produce obscuring column density distributions (Ballantyne, 2008; Hopkins et al., 2016; Gohil and Ballantyne, 2017), and (iii) large-scale (> kpc) obscuration driven by galaxy mergers (Di Matteo et al., 2005; Hopkins et al., 2008; Alexander and Hickox, 2012).

Circumnuclear gas and dust make QSO2s faint at optical, ultraviolet and soft X-ray wavelengths. However, luminous QSO2s ($L_{bol} \gtrsim 10^{45}$ erg s^{-1}) may be identified using surveys at hard X-ray (Norman et al., 2002; Brandt and Hasinger, 2005; Gilli et al., 2007; Hasinger, 2008; Brusa et al., 2010), infrared (Lacy et al., 2004; Stern et al., 2005; Martin, 2005; Lacy et al., 2007; Donley et al., 2012; Stern et al., 2012; Eisenhardt et al., 2012; Glikman et al., 2012; Lacy et al., 2013, 2015), and radio (McCarthy, 1993; Martínez-Sansigre et al., 2006; Miley and De Breuck, 2008) wavelengths. Very large area surveys have shown to be of great relevance in the discovery of such rare sources, and thus despite the suppression of the apparent optical flux by obscuration, about 1000 QSO2s have been selected using their characteristic strong narrow emission lines from the Sloan Digital Sky Survey (SDSS), both at low-redshift ($z < 1$, Kauffmann et al. 2003; Zakamska et al. 2003; Hao et al. 2005; Reyes et al. 2008; Humphrey et al. 2010; Mullaney et al. 2013) and high-redshift ($z \gtrsim 2$, Alexandroff et al. 2013; Greene et al. 2014; Ross et al. 2015).

The search for high-redshift QSO2s has been carried out mainly in the X-rays (Norman et al., 2002; Stern et al., 2002; Brandt and Hasinger, 2005) and in the mid-infrared (hereafter MIR; Lacy et al. 2004; Martínez-Sansigre et al. 2005; Alonso-Herrero et al. 2006; Padovani et al. 2017). Although X-ray and pure spectroscopic observations are able to find this kind of sources at high-redshift, it is with Sptizer Space Telescope (hereafter SST) that this field has been revolutionized, with many groups using the fact that the dusty torus, heated by the central AGN, reradiates at MIR wavelengths (Stern et al., 2005; Alonso-Herrero et al., 2006; Mateos et al., 2012; Assef et al., 2013). Advances in MIR spectroscopy resulted in attempts to identify type-II AGNs (Lacy et al., 2004; Alonso-Herrero et al., 2006). The combination of radio and MIR data has been used to reduce the fraction of star-burst dominated sources from colour selected samples (Donley et al., 2005; Martínez-Sansigre et al., 2005, 2006) and deep radio surveys have been shown to harbor a considerable number of QSO2s (Simpson et al., 2006). All of these now seem to imply that a large population of QSO2s exist in the high-redshift Universe and that many may also be missed in the current deep X-ray surveys (Stern et al., 2014; Del Moro et al., 2016; Hickox and Alexander, 2018).

1.1.3 Radio Galaxies

Radio galaxies are a class of the overall AGN population characterized by relatively strong radio emission. Among the first AGNs to be discovered following the opening of the radio window in first half of the 20th century (Bolton et al., 1949; Edge et al., 1959), it was soon recognized that they are associated with giant elliptical host galaxies (Matthews et al., 1964). The extraordinary luminosity ($L_{1.4GHz} > 10^{24}$ W Hz^{-1}; Heckman et al. 1982; van Breugel et al. 1984; Ledlow et al. 2001; Emonts et al. 2008) at radio wavelengths means that they stand out at high redshifts. In this way, radio galaxies act as important signposts to the early Universe, in particular probing the evolution of the most massive galaxies in some of the highest density environments (McCarthy, 1993; Miley and De Breuck, 2008).

The emission in radio frequencies is mainly due to synchrotron radiation generated in the relativistic jet and in diametrically opposed hotspots and lobe structures that are the result of the interaction of the jets with the interstellar or intergalactic gas. The geometric scheme of radio galaxies was first developed by Blandford and Rees (1974) and Scheuer (1974) (see Figure 1.6). Due to a process related to the dynamics and energetics of a turbulent, magnetized accretion disk around a black hole, radio jets are launched from the core along the spin axis of the central accretion disk (Heinz and Begelman, 2000; Kuncic and Bicknell, 2004). The jets do not propagate in empty space but into or through an interstellar medium (ISM) that is generally much denser than the jet plasma, where they can remain highly collimated out to vast distances without significant disruption or dissipation. They can often propagate out to scales of hundreds of kpc (e.g. Pentericci et al., 1999, 2001) until they decelerate abruptly at a shock (Fabian et al., 2006) which involves the direct interaction of the jet with the relativistic plasma that fills the lobes in which the jets are typically embedded, giving rise to the hotspot

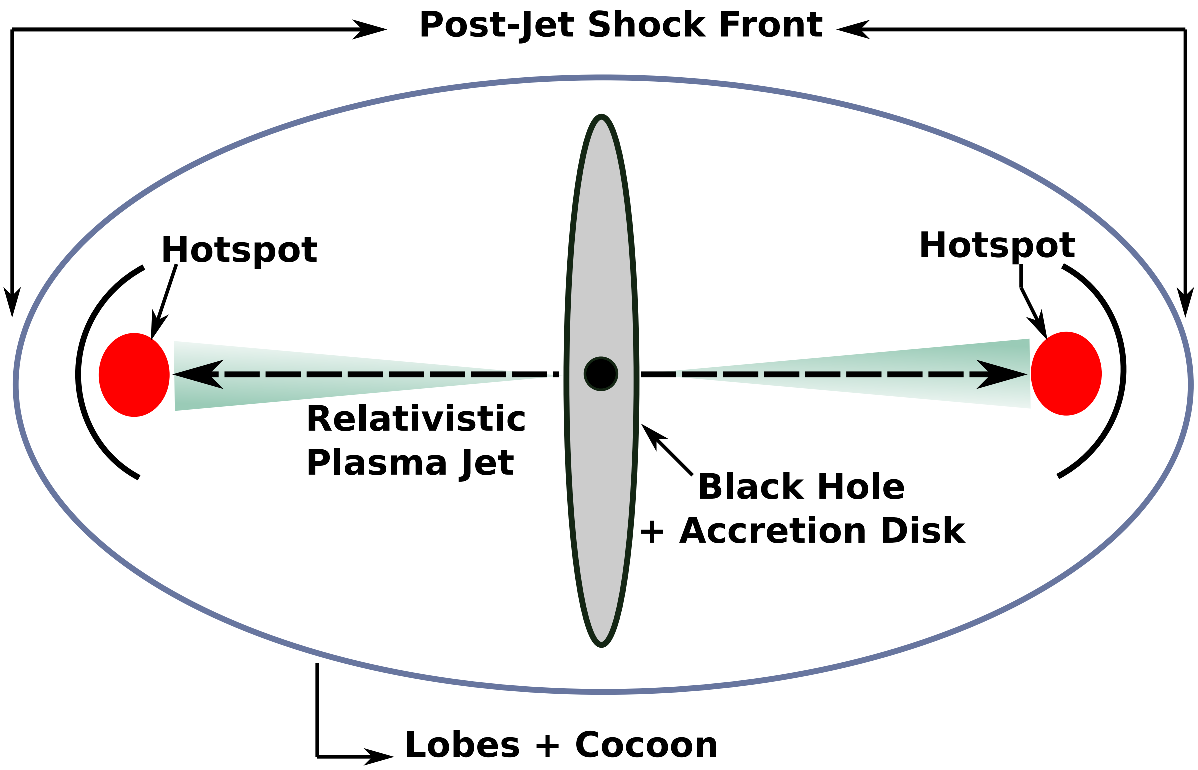

Figure 1.6: Representation of the global characteristics of radio galaxies first put forward by Blandford and Rees (1974) and Scheuer (1974).

and driving particle re-acceleration. Electrons in the hotspots leak out into lower density lobes, which expand adiabatically with time. The gradient between the higher pressure hotspots and the lower pressure intergalactic medium (IGM) behind the post-jet shock front induces plasma backflow toward the host galaxy until eventually, a cocoon of plasma builds up, enveloping the entire structure.

Although radio galaxies come in a variety of morphologies, a basic division in structural types was suggested by Fanaroff and Riley (1974). Their classification was based on the recognition that radio sources often came in two flavours, those having edge-darkened tails and plumes: high surface brightness radio emission occurring closest to the nucleus and fading with increasing distance (FR I, see Figure 1.7a), and those having edge-brightened sources with distinct jets and lobes (FR II, see Figure 1.7b). In addition, the two populations can also be distinguished as a function of their radio luminosity, where the break between low luminosity FR Is and higher luminosity FR IIs typically occurs at about 10^{26} W Hz^{-1} at 178 MHz (Fanaroff and Riley, 1974). Subsequent works have shown that the FR I/FR II break luminosity actually increases with host-galaxy optical luminosity (Owen and Ledlow, 1994; Ledlow and Owen, 1996).

The spectra of the optical sources associated with radio galaxies typically reveal strong

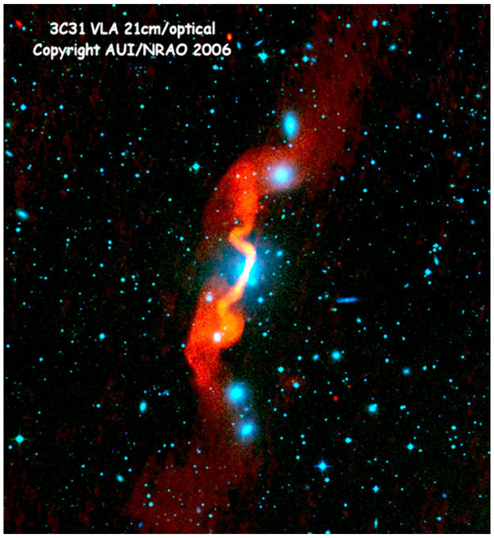

(a) FR I – 3C31

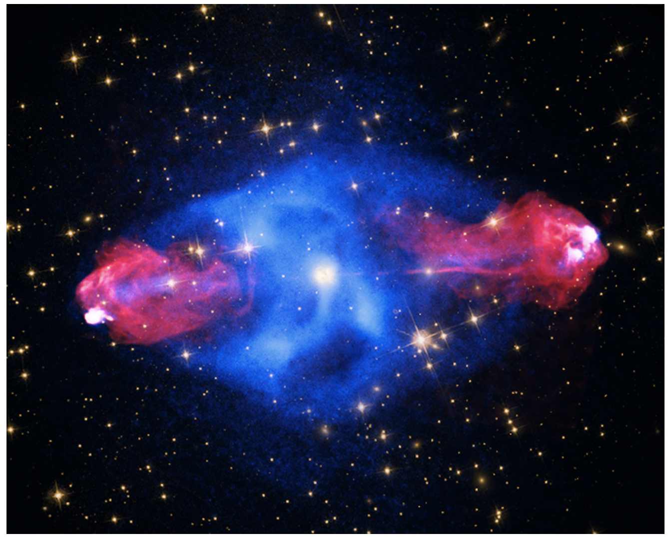

(b) FR II – Cygnus A

Figure 1.7: (a) VLA 21 cm radio (red) superposed on Palomar Sky Survey optical (blue) image of the Fanaroff-Riley type I radio galaxy 3C31 *Credit: NRAO/AUI*. (b) Image of the Fanaroff-Riley type II radio galaxy Cygnus A incorporating X-ray data (blue) from NASA/CXC/SAO, optical data (yellow) from NASA/STScI and radio emission from NSF/NRAO/AUI/VLA.

emission lines. Similar to Seyfert galaxies, one can make a distinction between Broad Line Radio Galaxies (BLRGs) and Narrow Line Radio Galaxies (NLRGs). Having optically visible host galaxies and optical spectra with broad recombination lines (a few thousand km s^{-1}; Netzer 2015; Padovani et al. 2017), the BLRGs exhibit characteristics of both the NLRGs and radio-loud QSOs. The BLRGs can be considered objects for which the line of sight is close to the torus edge. Thus the broad-line region is directly seen, but the central engine is still partially hidden from view (see Figure 1.1; van Bemmel and Barthel 2001; Grandi and Palumbo 2007). Unlike the BLRGs, the NLRGs are characterized by the presence of strong narrow emission lines (a few hundred km s^{-1}; Weedman 1977; Heckman et al. 1981; Netzer 2015; Padovani et al. 2017), and by the absence of broad components to permitted lines due to the position in which the object is observed (see Figure 1.1). The bulk of emission for the NLRGs generally originates within the central kpc (Humphrey et al., 2015; Villar-Martín et al., 2016), but for some systems emission from gas ionized by the AGN is observed on the scale of the entire galaxy, out to $\sim$ 10 kpc or more (Liu et al., 2013; Hainline et al., 2013, 2014). Due to its extension, this emission will generally not be obscured by the torus, although a large fraction of the emission could be obscured by dust in the galaxy. In principle BLRGs and NLRGs can be considered as radio-loud cousins of classical Sy 1 and Sy 2, respectivelly, albeit with a different morphology of the host galaxy and strong radio emission.

1.2 The radio-optical alignment effect

Powerful radio galaxies are often observed to be surrounded by extensive regions of UV/optical continuum, which is generally well aligned with the radio source axis at higher redshifts (McCarthy et al., 1987; Chambers et al., 1987; McCarthy, 1993; van Breugel et al., 1998). Known as the radio-optical alignment effect, it is a fundamental observational phenomenon concerning the environment of distant and powerful radio galaxies. Attempts to understand the radio-optical alignment effect have produced several ideas and results on AGN and their environment (McCarthy et al., 1987; Chambers et al., 1987; Dunlop and Peacock, 1993; McCarthy et al., 1995; Chambers et al., 1996; Cimatti and di Serego Alighieri, 1996; Best et al., 1997; Röttgering et al., 1997; Inskip et al., 2002; Humphrey et al., 2016) which would have been impossible to obtain for Type I quasars, due to their very strong nuclear luminosity.

Since the alignment effect has been confirmed for radio galaxies at high redshift, three physical interpretations for this phenomenon have been suggested (see McCarthy, 1993). First and arguably the most interesting interpretation is that the optical emission is dominated by light from young massive stars that formed via the collapse of dense gas clouds shocked by the passage of the plasma jet (e.g. Rees, 1989; De Young, 1989; Begelman and Cioffi, 1989; Daly, 1992; Bicknell et al., 2000; Mellema et al., 2003; Fragile et al., 2004). Secondly, optical/UV emission could be light from the obscured AGN that has been scattered by dust in the extended ISM of the host galaxy (e.g. di Serego Alighieri et al., 1989; Tadhunter et al., 1992; Fabian, 1989). Or thirdly, that there is a bias toward selecting radio galaxies which display this alignment effect (e.g. Eales, 1992). For the latter case, anisotropy in the optical/infrared emission reflects the anisotropy of the surrounding gas density distribution. Since radio sources will be most luminous when propagating into high density regions, those close to the lower flux limit in complete samples will be preferentially selected with their radio emission aligned along the major axis of the optical/infrared emission. Of course, a combination of the three mechanisms described above cannot be ruled out.

The alignment effect is seen in radio galaxies at $z \sim 1$, and becomes increasingly more common at $z \geqslant 2$. At lower redshifts, the rest-frame optical morphologies become smoother, smaller, more centrally concentrated, and less aligned with the radio source (van Breugel et al., 1998).

1.3 AGN feedback

Feedback has become a commonly invoked process in galaxy evolution. Within the current picture of galaxy formation, an AGN is associated with the energy and radiation release resulting from gas accretion onto SMBHs residing at the central few pc of most galaxies (Soltan, 1982; Kormendy and Richstone, 1995; Richstone et al., 1998; Kormendy and Gebhardt, 2001; Kormendy and Ho, 2013). The process by which this occurs is known as AGN feedback and this nuclear activity is thought to profoundly affect star formation through different physical processes such as the heating and compression of the IGM (Silk and Rees, 1998; Bîrzan et al., 2004; Springel, 2005; Di Matteo et al., 2005; Diamond-Stanic and Rieke, 2012; Mullaney et al., 2012a,b; Chamani et al., 2017; Eisenreich et al., 2017; Shabala et al., 2017).

In the overall picture of galaxy formation models, AGN feedback is required to heat the gas content of massive galaxies and their host dark matter halos, thereby quenching star formation and regulating the abundance of bright, massive galaxies (Benson et al., 2003; Granato et al., 2004; Bower et al., 2006; Croton et al., 2006b; Cattaneo et al., 2007). In this context, at least two major modes have been identified, differentiated by the nature of the energy outflow near the black hole: the radiative mode and the kinetic mode (Bower et al., 2006; Croton et al., 2006b; Somerville et al., 2008; Cattaneo et al., 2007; Lagos et al., 2008; Fanidakis et al., 2012, 2013; Henriques et al., 2015). The radiative-mode, also known as the quasar- or wind- mode, is considered to be driven by a wind created by the luminous accretion disk. In this case, the ignition of the nucleus in a star-forming galaxy heats up and removes the ISM gas from its host galaxy, reducing or even stopping star formation (Granato et al., 2001; Croton et al., 2006a; Hopkins and Elvis, 2010). During this process, the flow of matter to the central SMBH can be reduced, lowering the accretion flow and eventually extinguishing the AGN. Once the gas cools down and starts to collapse into the nucleus again, a new AGN phase may begin and the cycle resumes. The kinetic-mode, also known as the radio- or maintenance- mode, typically operates when the galaxy has a hot halo and the accreting black hole has powerful jets. Direct observations show that jets can influence gas many tens of kpc from the centre of the parent host galaxy (Nesvadba et al., 2010, 2011; Emonts et al., 2011a). Indeed, the brightest radio structures in radio-loud AGNs are often observed on kpc scales and are produced by the coupling of the AGN outflow to its environment (Dicken et al., 2012). Radio AGN energy output, in the form of heating, can prevent hot gas from cooling and falling into a galaxy to form stars (Croton et al., 2006a), especially in the more massive galaxies and at much smaller accretion rates than that of the quasar-mode feedback. The cooling of the hot gas onto the central region of the galaxy fuels intermittent AGN outbursts, which in turn heat the inflowing gas, stopping or slowing down the accretion inflow (Best et al., 2005). Although it can be expected that in real objects both types of feedback often will be operating simultaneously, it is still unclear how efficiently AGN feedback delivers energy (Silk and Rees, 1998) and momentum (King, 2003) to the gas of the galaxy and what mode of feedback dominates.

AGN can exert either negative or positive feedback on their surrounds (Antonuccio-Delogu and Silk, 2010; Gaibler, 2014). The negative feedback is the process by which AGN interacts with the cold star-forming gas in the galaxy, or the surrounding halo, and stop or slow down star-formation processes by ionizing and heating the gas, or by removing it from the galaxy. The positive feedback operates in the opposite way, where the AGN interacts with a low-density cold gas and increases its density until it starts to form stars. Both semi-analytical models (Croton et al., 2006a; Bower et al., 2006) and hydrodynamical cosmological simulations (Di Matteo et al., 2005; Sijacki et al., 2007; Di Matteo et al., 2008; Booth and Schaye, 2009; Dubois et al., 2010) argue that negative feedback from AGN is an important ingredient in the formation and evolution of massive galaxies and is, in particular, able to suppress star formation in order to reproduce the observed high-end tail of the galaxy luminosity function, and the low star formation rate (hereafter SFR) in massive galaxies. In addition, observations show that cooling flows in the hot circumgalactic and intracluster media can be suppressed by the energy transferred by AGN jets (Bîrzan et al., 2004; Dunn et al., 2005), negatively affecting star formation. This negative feedback is mitigated by evidence of the positive impact of AGN on star formation. In this case, jets propagating through an inhomogeneous ISM may also trigger or enhance star formation in a galaxy (i.e., positive feedback). Both process are not necessarily contradictory as AGN activity may both quench and induce star formation in different parts of the host galaxy, on different levels and timescales (Silk, 2013; Zubovas et al., 2013; Zinn et al., 2013; Cresci et al., 2015).

Recent studies have focused on high-redshift radio-loud AGNs (radio galaxies and quasars) to prove the existence of a coevolution between the AGN and their host galaxies (Holt et al., 2008; Nesvadba et al., 2006, 2007, 2008b, 2017a). Radio-loud AGNs are expected to be good candidates to trace AGN feedback for mainly three reasons. First, they sample some of the most massive galaxies at high-redshift (De Breuck et al., 2001; Seymour et al., 2007; Hatch et al., 2009; De Breuck et al., 2010; Hatch et al., 2013; Nesvadba et al., 2017b). Second, these objects lie in overdense regions (Hill and Lilly, 1991; Pascarelle et al., 1996; Best et al., 2000; Kurk et al., 2000, 2004a,b; Venemans et al., 2004; Hatch et al., 2011, 2014; Cooke et al., 2014; Orsi et al., 2016). Third, they are associated with energetic outflows of ionized gas powered by their central SMBHs (Nesvadba et al., 2008b; Swinbank et al., 2015; Nesvadba et al., 2017a; Carniani et al., 2017).

1.4 The Lyman-α line

Discovered in 1906 in a series of transitions in the extreme-ultraviolet region of the atomic hydrogen spectrum (e.g. Lyman, 1906, 1914), the Lyα line plays an important part in astronomy as one of the most fundamental atomic transitions in the Universe (e.g. Ahmadi et al., 2018).

Besides that, the detection of the Lyα line is an important method for studying the high-redshift Universe (Partridge and Peebles, 1967). Whether in emission or absorption, this strong spectral line is among the most direct probes of neutral hydrogen. Neutral hydrogen has a vital role in galaxy and star formation, since gas that has cooled to allow it to collapse into a halo will be predominantly neutral. Furthermore, stars are not formed out of warm ionized gas, they require cold neutral clouds as a precursor to molecular clouds.

The Lyα line is a resonant transition at a wavelength of 1215.67 Å (or 10.2 eV) and frequency of $2.47{\times}10^{15}$ Hz. A hydrogen atom emits Lyα once its electron is in the 2P state and decays to the ground state (1S),

$$H(2P) \leftrightarrow H(1S) + Ly\alpha. \tag{1.1}$$

There are a number of different physical processes that can produce Lyα photons. These physical process are typically divided into recombination, collisional excitation and Lyα scattering. Lyα photons are emitted as a result of the cascade of an electron in a recombined hydrogen atom. When an electron is captured by a free proton, it can either directly populate the ground state (1S) or an excited state from which it cascades by downward transitions to the ground state. Cascades that populate the 2P state decay to the ground state by emitting a Lyα photon, while cascades to the 2S state subsequently decay via two-photon emission (Gould and Weinberg 1996; see also Dijkstra 2017). Recombination is relatively efficient at producing Lyα photons. In particular, for a broad range of temperatures centered on $T = 10^4$ K, around 40% of the recombinations yield a Lyα photon (Osterbrock, 1989).

In the case of collisional excitation, free electrons colliding with H I in the ground state are expected to transfer a fraction of their energy to the H I atom. If this energy is high enough, the collision will excite the atomic levels with subsequent decay via line emission. Unlike recombination, the efficiency of the process is strongly temperature and density dependent (Gould and Weinberg 1996; see also Cantalupo 2017; Dijkstra 2017). Humphrey et al. (2019) have found that at low gas metallicities (i.e. 10% Solar or less), collisional excitation can become so significant that it competes with recombination emission; under some circumstances, collisional excitation produces more photons than recombination emission, and the number of Lyα photons emitted per ionizing photon absorbed can exceed 1.0.

Scattering of Lyα photons is the process by which an H I atom in the ground state absorbs a Lyα photon, and subsequently re-emits another Lyα photon. Given that there are no other states between the 2P and the ground state, the re-emission of a Lyα photon is the most likely way for the atom to return to the ground state (Gould and Weinberg, 1996). Hence, the absorption and emission together can be regarded as scattering. H I gas in the circumgalactic medium

(CGM) can scatter Lyα photons that were produced in the inner part of galaxies, and which subsequently escaped from the interstellar medium (e.g. Laursen and Sommer-Larsen, 2007; Zheng et al., 2010, 2011; Steidel et al., 2011; Laursen et al., 2011; Dijkstra and Kramer, 2012; Verhamme et al., 2012), making the emission line extended (Geach et al., 2005; Colbert et al., 2006; Beelen et al., 2008; Geach et al., 2009; Webb et al., 2009; Zheng et al., 2011; Cen and Zheng, 2013; Overzier et al., 2013). This scenario, for some nebulae and in particular for huge concentrations of gas emitting Lyα photons (also known as Lyα Blobs or LABs), has been proposed in the past as a possible origin of the level of polarization detected in some LABs (e.g. Hayes et al., 2011; Beck et al., 2016), and in the giant Lyα halo of a radio galaxy (e.g. Humphrey et al., 2013b). Cantalupo (2017) has argued that Lyα scattering is expected to be the dominant mechanism when the central source is not ionizing the gas but still producing copious amounts of Lyα and continuum photons at the wavelength of Lyα.

1.4.1 Extended Lyα Nebulae

Several decades of observations have shown that high-redshift AGNs and their massive galaxies are often surrounded by spatially extended Lyα nebulae. Soon after their discovery in the 1980s and until very recently, narrow-band (NB) imaging and spectroscopy of high-redshift AGNs have produced a large literature of detections and studies of giant Lyα nebulae (e.g. McCarthy et al., 1990b; Eales et al., 1993; van Ojik et al., 1996, 1997; Pentericci et al., 1998; Kurk et al., 2002; Francis et al., 2001; Reuland et al., 2003; Villar-Martín et al., 2003, 2007b; Humphrey et al., 2007; Sánchez and Humphrey, 2009; Humphrey et al., 2013a; Cantalupo et al., 2014; Swinbank et al., 2015; Borisova et al., 2016; Cai et al., 2017; Arrigoni Battaia et al., 2018).

Lyα nebulae provide to us an indispensable opportunity to study the intergalactic or circumgalactic medium (IGM or CGM). The IGM and CGM are tightly linked to the evolutionary phases of galaxies, both by hosting the gas reservoir necessary to fuel star formation and also being subject to galactic feedback and recycling (Prochaska et al., 2011; Tumlinson et al., 2011). As a primary coolant of gas with T ~ 10^4 K, extended Lyα emission can be used to directly probe the IGM/CGM, since at high redshifts ($z > 2$) the observation of other emission lines (e.g., Hβ) is challenging (Barnes et al., 2014; Dijkstra, 2014; Hayes, 2015).

The literature shows that the astrophysical source of extended Lyα nebulae can be divided into three main categories. The first, known as photoionization, is the process in which an incident photon ejects one or more electrons from an atomic or molecular system. The ionizing radiation that keeps the Lyα forest highly ionized is expected to come from inside a galaxy (Furlanetto et al., 2005; Weidinger et al., 2005; Nagamine et al., 2010) and also from distant sources such as quasars or other galaxies (Haiman and Rees, 2001; Alam and

Miralda-Escudé, 2002; Cantalupo et al., 2005; Adelberger et al., 2006; Cantalupo et al., 2007; Rauch et al., 2008a,b; Kollmeier et al., 2010; Hennawi and Prochaska, 2013; Cantalupo et al., 2014). Ionizing radiation can be produced by hot and young stars that condense out of dense nebulae in galaxies (e.g. Bromm et al., 2001). The ionizing radiation encounters H I in the surrounding interstellar medium (ISM) from which the star formed, producing interstellar H II regions. Recombining protons and electrons give rise to Lyα as well as other emission lines. If the surrounding medium is optically thick to ionizing radiation (also known as Case B recombination), any ionizing photon emitted as a result of a recombination will be captured again, giving another chance to produce Lyα photons (Osterbrock, 1962). The ionizing photons are reprocessed, while Lyα photons are scattered. Powerful AGNs are also the source of copious ionizing radiation. Ionizing photons from AGNs can ionize neutral hydrogen atoms and the subsequent recombination gives off Lyα emission.

Extended Lyα nebulae can also be a consequence of shock ionization. Shock ionization can take place when mechanical energy is deposited into the ISM/CGM by energetic processes such as the interaction with radio jets, fast outflows, or supernova explosions. Indeed, in some radio-loud AGNs there is a spatial coincidence between radio and line emission in radio sources (Baum and Heckman, 1989; McCarthy et al., 1995; Ridgway and Stockton, 1997; Lehnert et al., 1999). Such interactions may disturb the morphology, kinematics and physical conditions of the gas and potentially modify its ionization state (Villar-Martín et al., 1997, 1999a). With the help of theoretical models (Dopita and Sutherland, 1996), evidence of ionizing shocks has been found in an increasing number of AGNs from the analysis of their line ratios (Sutherland et al., 1993; Clark et al., 1998; Koekemoer and Bicknell, 1998; Villar-Martín et al., 1999c).

A numerous series of theoretical and numerical works have proposed that extended Lyα nebulae at high-z, apparently lacking a source of ionization, could be powered instead by Lyα cooling within dark matter halos (Haiman et al., 2000b; Fardal et al., 2001; Kereš et al., 2005; Furlanetto et al., 2005; Dijkstra and Loeb, 2009; Goerdt et al., 2010; Faucher-Giguère et al., 2010; Rosdahl and Blaizot, 2012). These studies suggested that a substantial fraction of the gravitational energy due to cosmological accretion of gas into massive dark matter halos may be radiated via collisionally excited Lyα emission. This scenario predicts very strong Lyα emission from low gas density, when both H I and free electrons are present and the electron temperature is around a few $\times$ 10^4 K (Cantalupo et al., 2008).

The first detection of an extended Lyα nebula was reported by McCarthy et al. (1990b) studying the z ~ 1.8 radio galaxy 3C 294 which showed highly elongated Lyα emission aligned with the radio source axis and extended over about 120 kpc. A few years later, the first detection of extended Lyα nebula around a radio galaxy with z > 2 was reported by Eales et al. (1993) studying the z = 3.2 radio galaxy 6C 1232+39, a system with a double lobed structure closely

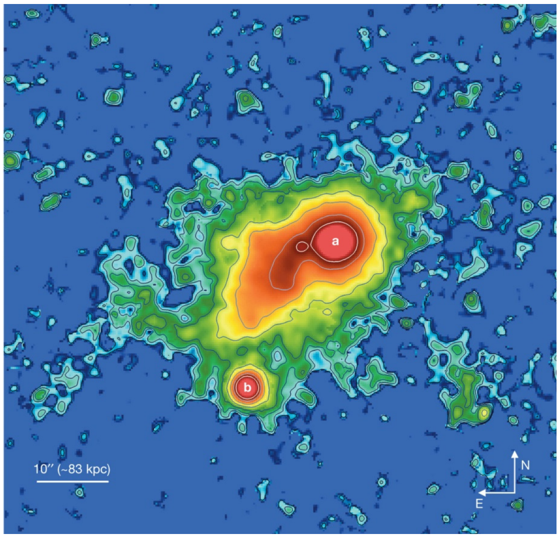

(a) UM 287

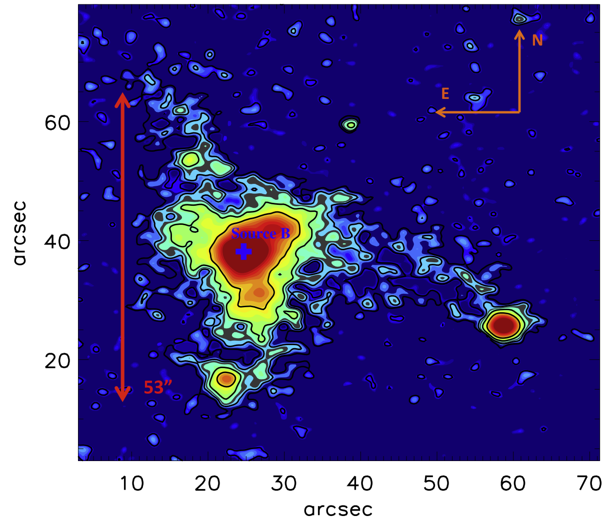

(b) BOSS1441

Figure 1.8: (a) Continuum subtracted NB image of the ELAN surrounding the radio-quiet quasar UM 287 (labeled "a") and the faint quasar (labeled "b"). The extended structure spans a projected linear size of 460 kpc (see Cantalupo et al., 2014, Figure 2 for more details). (b) Continuum subtracted, smoothed NB image of the ELAN surrounding the radio-quiet quasar (Source B) at z = 2.32 with projected extent of 442 kpc (see Cai et al., 2017, Figure 2 for more details)

aligned with the Lyα emission, but showing some differences in the morphology and symmetry of the optical emission with respect to the radio. In the second half of the 1990s, van Ojik et al. (1996) reported detection of spatially extended Lyα emission extending over 140 kpc around the z = 3.57 radio galaxy 1243+036, showing a complex kinematic structure spatially correlated with the radio jets. Recently, the most notably discoveries include an enormous Lyα nebulae (ELAN) surrounding the radio-quiet quasar UM 287 extending over 460 kpc (see Figure 1.8a), well beyond the virial radius of any plausible associated dark-matter halo (Cantalupo et al., 2014). In addition, Cai et al. (2017) identified an ELAN associated with relatively faint continuum surrounding the radio-quiet source associated with BOSS1441 (a field with a large-scale strucuture of Lyα emitters (or LAEs)) at z = 2.32 with spatial extent of 442 kpc (see Figure 1.8b). Moreover, Cai et al. (2017) also reported extended C IV and He II emission on a scale of $\gtrsim$ 30 kpc.

Detections of the extended Lyα emission around HzRGs have shown a wealth of morphological structures, including filaments, clumpy regions and cone-shaped structures (Reuland et al., 2003; Erb et al., 2011). The common features of all these detections include the apparent alignment between Lyα emission and the radio jet axis (Villar-Martín et al., 2007b), quiescent and perturbed kinematic components (van Ojik et al., 1997; Villar-Martín et al., 2002, 2003; Humphrey et al., 2006; Sánchez and Humphrey, 2009; Silva et al., 2018b,a), associated extended C IV and He II emission (Villar-Martín et al., 2002, 2003; Prescott et al., 2009; Cai et al., 2017; Morais et al., 2017; Silva et al., 2018b), invariable association with large overdensity as traced by companion Lyα galaxies (Venemans et al., 2007) or multi-wavelength observations from X-ray to the infrared (Pentericci et al., 1997). In terms of luminosities, the Lyα nebulae surrounding normal galaxies are relatively faint $L_{Ly\alpha} \sim 10^{42}$ erg s^{-1}, while the high-redshift radio galaxies (HzRGs; z > 2) and high-redshift quasars (HzQSOs; z > 2) have luminosities $L_{Ly\alpha} \sim 10^{44-45}$ erg s^{-1} (Reuland et al., 2003; Villar-Martín et al., 2007b; Trainor and Steidel, 2012; Cantalupo et al., 2014; Martin et al., 2015; Hennawi et al., 2015; Borisova et al., 2016).

The properties of the extended Lyα nebulae from a kinematic point of view are typically divided into two distinct kinematic components. The first one, commonly classified as a perturbed component, usually shows irregular gas kinematics with FWHM > 1000 km s^{-1} (van Ojik et al., 1997; Villar-Martín et al., 2003; Humphrey et al., 2006; Nesvadba et al., 2017b; Silva et al., 2018b,a). In very powerful HzRGs, these large FWHM are above the escape velocity from the gravitational potential of massive galaxies, suggesting this gas is outflowing (van Ojik et al., 1997; Humphrey et al., 2006; Nesvadba et al., 2006, 2008b, 2017b; Morais et al., 2017). Spectroscopic observations have also found that some HzRGs show evidence of a structure with lower surface brightness, and extending well beyond the brighter and perturbed regions that appear more kinematically quiet, being detected across the full spatial extent of the nebulae (Villar-Martín et al., 2002, 2003, 2007b). This quiescent component usually shows FWHM < 1000 km s^{-1} with no clear relationship with the radio jets (van Ojik et al., 1996; Villar-Martín et al., 2002, 2003; Sánchez and Humphrey, 2009). In addition, some of these quiescent components show velocity patterns that have been interpreted as a possible sign of a rotating structure (Villar-Martín et al., 2006) or gas infall towards the central regions of the host galaxy (Humphrey et al., 2007; Villar-Martín et al., 2007b; Humphrey et al., 2013a; Roche et al., 2014; Silva et al., 2018b).

Kinematic signatures of the Lyα nebula in HzRGs and HzQSOs are, however, difficult to interpret given the complexity of Lyα radiative transfer effects. Lyα photons can undergo many scatterings before escaping a nebula region, diffusing in both real and frequency space. The properties of the emergent radiation depend sensitively on the spatial distribution, kinematics, temperature and dust content of the gas. Thus, analytical models have helped isolate the signatures of various geometries (spheres, shells, filaments) and velocity structures (infall, outflow, rotation) in observations of Lyα (Cantalupo et al., 2005; Dijkstra et al., 2006a,b; Verhamme et al., 2006; Laursen et al., 2009). There is a need to develop a greater understanding of the degeneracies between these different scenarios, as well as the signatures of different sources of Lyα photons (star formation, cooling radiation, Lyα scattering).

1.4.2 Extended Lyα absorbers

Absorption lines provide a unique and powerful tool for probing tenuous gas clouds throughout the universe. The physical regimes probed in absorption differ from those which dominate the emission of galaxies and AGNs, and hence absorption provides a complementary view of the material composition of galaxies and AGNs. Consequently, absorption lines occurring very close to the HzRG emission line redshift are valuable probes of local environments, potentially tracing gas from a range of locations along the sightline.

Studies have shown that some HzRGs show spatially resolved H I absorption in their Lyα emission line profiles, usually blueshifted with respect to the Lyα emission (e.g. Röttgering et al., 1995a; van Ojik et al., 1997; Binette et al., 2000; Jarvis et al., 2003; Binette et al., 2006; Humphrey et al., 2008a, 2013b; Moyano et al., 2015; Swinbank et al., 2015; Gullberg et al., 2016; Silva et al., 2018b). Although poorly understood, the discrete nature of the absorption lines suggests that the H I is likely part of an expanding giant shell enveloping the Lyα emitting region (Binette et al., 2000; Jarvis et al., 2003; Wilman et al., 2004; Binette et al., 2007). In addition, the absorbing structures are believed to be outflowing due to feedback activity (see Binette et al., 2006; Humphrey et al., 2008a; Swinbank et al., 2015; Silva et al., 2018b).

Associated with roughly half of all radio galaxies at z > 2 (van Ojik et al., 1997; Jarvis et al., 2003; Wilman et al., 2004), the extended Lyα absorbers are at least as spatially extended as the Lyα emitting regions (~ 150 kpc; see Swinbank et al. 2015). The column densities can be divided into weaker systems with $N_{HI} \sim 10^{13-15}$ cm^{-2} and strong absorbers with $N_{HI} \sim 10^{18-20}$ cm^{-2} (Röttgering et al., 1995a; van Ojik et al., 1997; Binette et al., 2000; Jarvis et al., 2003; Wilman et al., 2004; Binette et al., 2007; Humphrey et al., 2008a; Swinbank et al., 2015; Silva et al., 2018b,a). At least a few of the H I absorbers also contain carbon, as shown by their detection in C IV absorption lines (Binette et al., 2000; Jarvis et al., 2003; Humphrey et al., 2008a; Gullberg et al., 2016; Silva et al., 2018b). The strong absorption in the Lyα emission indicates the presence of a large amount of neutral gas, which was first attributed to a reservoir of H I situated within the HzRG itself (Röttgering et al., 1995a). However, subsequent works have suggested that the reservoir of gas causing the absorption feature is not situated within the HzRG, but rather is low metallicity and low density gas that is situated in the outskirts or outside of the host galaxy (Binette et al., 2000; Jarvis et al., 2003). The current consensus continues to be that the absorber is outside the host galaxy (Humphrey et al., 2008a; Swinbank et al., 2015; Silva et al., 2018b), with low electron density (Humphrey et al., 2008a) and low metallicity (Silva et al., 2018b).

With the advent of sensitive integral field spectrographs (i.e., Visible Multi-Object Spectrograph (VIMOS) and Multi Unit Spectroscopic Explorer (MUSE) on the European Southern Observatory (ESO)/Very Large Telescope (VLT)), it has become possible to carry out the observations of these extended structures with improved spatial sampling, allowing the study of the morphologies and dynamics of the extended Lyα emitting or absorbing gas in order to understand the origin of both structures. Such instruments helped, for example, Humphrey et al. (2008a) to study the nature of the absorbing gas in front of MRC 2025–218 (z = 2.63) and Swinbank et al. (2015) to map the H I absorbers seen against the underlying emission of the z = 4.1 radio galaxy TN J1338–1942. In both cases, the strongest H I absorbing structures were found to have properties consistent with an outflowing shell driven by the AGN or the star-formation within the galaxy, covering the full two-dimensional spatial extent of the extended Lyα emission.

1.5 Thesis motivation and outline

Studying the formation and evolution of galaxies is currently one of the most active fields in astronomy, immensely assisted by the great technological advances over the past few decades. Advances like large telescopes, modern CCDs, integral field spectrographs (IFUs), and computing power now allow observations and predictions of galaxies in unprecedented detail. These novel capabilities open new and timely frontiers in our quest to understand galaxy formation and evolution using high-z galaxies – the progenitors of the 'normal' galaxies that surround us today in the local Universe.

Although our understanding of the evolution of galaxies across cosmic time is certainly growing, there are vast gaps in our knowledge of several key astrophysical processes (cold gas accretion, feedback, star formation, among others). Powerful radio galaxies and quasars at high-z ($z > 2$) , which are usually hosted by galaxies that are destined to become passive, massive elliptical galaxies as seen in the low-z Universe, represent excellent testbeds for probing these processes, due to (i) their high luminosity across most of the electromagnetic spectrum, (ii) the relative richness in gas of their host galaxy and nearby environment, (iii) the apparent/potential strength of feedback activity.

In this thesis I will examine the morphological, kinematic, chemical and excitation properties of the giant Ly-α emitting nebulae and giant H I absorbers associated with AGNs at $z > 2$. The main scientific goal is to elucidate the origins of both kinds of gaseous structures, to extract crucial new information about feedback processes that operate in massive galaxies and their high-z progenitors.

More specifically, for both the Ly-α emitting nebulae and the H I absorbers, I will examine the following issues:

- The two-dimensional and one-dimensional kinematic properties of the Ly-α emitting and absorbing structures will be used to distinguish between the gas infall and outflow scenarios. These scenarios will help to elucidate the origins of the gaseous structures and which feedback process may be affecting the star formation;
- The one-dimensional kinematic properties of the Ly-α emitting and absorbing structures will also be used to characterize these structures in the direction perpendicular to the radio axis. The results will add new information about the global properties of the extended ionized gas and extended absorbers;
- The gas chemical abundances will be estimated using emission and absorption lines from various species, to assess the chemical enrichment histories of the nebulae and absorbers. This information, together with the results from the kinematic analysis, will give additional key information about the origins of these giant gaseous structures;
- A combined analysis of radio-loud and radio-quiet AGNs at $z > 2$ will provide more representative information about the ionization and chemical enrichment history of the ISM in powerful AGN hosts at high-z.

Chapter 2

The MUSE 3D view of feedback in a high-metallicity radio galaxy at $z = 2.9$

2.1 Abstract

We present a detailed study of the kinematic, chemical and excitation properties of the giant Lyα emitting nebula and the giant H I absorber associated with the z = 2.92 radio galaxy MRC 0943–242, using spectroscopic observations from VLT/MUSE, VLT/X-SHOOTER and other instruments. Together, these data provide a wide range of rest-frame wavelength (765 Å – 6378 Å at z = 2.92) and 2D spatial information. We find clear evidence for jet gas interactions affecting the kinematic properties of the nebula, with evidence for both outflows and inflows being induced by radio-mode feedback. We suggest that the regions of relatively lower ionization level, spatially correlated with the radio hotspots, may be due to localised compression of photoionized gas by the expanding radio source, thereby lowering the ionization parameter, or due to a contribution from shock-heating. We find that photoionization of super-solar metallicity gas ($Z/Z_{\odot}$ = 2.1) by an AGN-like continuum (α=–1.0) at a moderate ionization parameter (U = 0.018) gives the best overall fit to the complete X-SHOOTER emission line spectrum. We identify a strong degeneracy between column density and Doppler parameter such that it is possible to obtain a reasonable fit to the H I absorption feature across the range log N(H I/cm^{-2}) = 15.20 and 19.63, with the two best-fitting occurring near the extreme ends of this range. The extended H I absorber is blueshifted relative to the emission line gas, but shows a systematic decrease in blueshift towards larger radii, consistent with a large scale expanding shell.

The work presented in this chapter was published in Monthly Notices of the Royal Astronomical Society in March 2018 (Silva et al. 2018b; MNRAS, 474:3649–3672)

2.2 Introduction

The study of high-redshift galaxies ($z \gtrsim 2$) allows us to look back to the young Universe, giving us the opportunity to witness and understand the processes by which galaxies form and evolve. In particular, powerful active galaxies such as high-z radio galaxies (HzRGs) or quasars offer the chance to examine a crucial phase in the evolution of massive galaxies, when the host galaxy is still relatively gas-rich and when radio and quasar mode feedback is also taking place. As such, HzRGs represent laboratories for studying the interplay between the "ingredients" of galaxy formation, such as active galactic nuclei (AGN), gas, stars, feedback and other processes.

Many powerful HzRGs (or quasars) lie within giant haloes[1] of gas which are prodigious sources of Lyα (and other emission lines), and which have sizes often exceeding 100 kpc (Fosbury et al., 1982; di Serego Alighieri, 1988; McCarthy et al., 1990b; van Ojik et al., 1997; Pentericci et al., 1998; Francis et al., 2001; Reuland et al., 2003; Humphrey et al., 2013a; Cantalupo et al., 2014; Swinbank et al., 2015; Borisova et al., 2016; Cai et al., 2017).

These haloes have typical masses in gas of $\sim 10^{9-10}$ $M_{\odot}$, Lyα luminosities up to $\sim 10^{45}$ erg s^{-1} and estimated electron densities of a few to several hundred cm^{-3} (McCarthy, 1993; Reuland et al., 2003; Villar-Martín et al., 2003; Sánchez and Humphrey, 2009; Humphrey et al., 2013a; Cantalupo et al., 2014; Cai et al., 2017). Typically the haloes can be divided into two kinematic and structural components: a high surface brightness region showing a clumpy, irregular morphology (Reuland et al., 2003) often aligned with the radio jets (McCarthy et al., 1995) and characterised by extreme kinematics (FWHM > 1000 km s^{-1}; van Ojik et al. 1997; Villar-Martín et al. 2003; Humphrey et al. 2006), and a low surface brightness region sometimes extending beyond the maximum extent of the radio structures, showing relatively quiescent kinematics (FWHM $\lesssim$ 1000 km s^{-1}) and no clear relationship with the radio source (van Ojik et al., 1996, 1997; Villar-Martín et al., 2002; Sánchez and Humphrey, 2009). In addition, Humphrey et al. (2007) proposed that the quiescent gas of some HzRGs are in infall towards the central regions of the host galaxy, though it is not clear whether the infalling gas has an external origin, or is instead a back-flow of material after the passage of a large scale outflow.

The ionization of the Lyα haloes of HzRGs is not fully understood, but several different mechanisms have been proposed, including photoionisation by the central AGN (see McCarthy et al., 1990b; Villar-Martín et al., 2003; Geach et al., 2009; Kollmeier et al., 2010; Cai et al., 2017), cooling radiation (see Haiman et al., 2000a; Steidel et al., 2000; Fardal et al., 2001; Yang et al., 2006; Dijkstra et al., 2006a; Faucher-Giguère et al., 2010; Rosdahl and Blaizot, 2012), shocks driven by radio jets (see Emonts et al., 2005; Villar-Martín et al., 2007b; Humphrey et al.,

[1]These haloes are sometimes also known as the 'extended emission line region' (EELR), the 'extended narrow line region' (ENLR), or 'Lyα blobs' (LAB)

2008a), or resonant scattering (for Lyα) (see Gould and Weinberg, 1996; Villar-Martín et al., 2007b; Dijkstra et al., 2006a; Dijkstra and Loeb, 2009; Humphrey et al., 2013b; Cantalupo et al., 2014; Yang et al., 2014). Other structures that are also not fully understood are the extended Lyα absorbers that are associated with roughly half of all radio galaxies at $z > 2$ (van Ojik et al., 1997; Jarvis et al., 2003; Wilman et al., 2004). They are at least as spatially extended as the Lyα haloes and appear to have column densities in the range $\sim 10^{14-20}$ cm^{-2} (Röttgering et al., 1995a; van Ojik et al., 1997; Binette et al., 2000; Jarvis et al., 2003; Wilman et al., 2004; Binette et al., 2007), with properties suggestive of an expanding shell with covering factor of, or approaching, unity (see Binette et al., 2000; Jarvis et al., 2003; Wilman et al., 2004; Binette et al., 2007). It has been suggested that these giant absorbing structures are the product of a past feedback event in the galaxy (e.g. Binette et al., 2006), and that their properties are somehow related to the size or passage of the radio jets (van Ojik et al., 1997). The presence of this type of shell around some HzRGs may have important implications for the escape of Lyα and ionizing photons.

In this paper, we present previously unpublished VLT X-SHOOTER[2] spectroscopy of the $z = 2.92$ HzRG MRC 0943–242, and pool this data with archival spectroscopic data from other VLT instruments (MUSE and UVES), spectra from the AAT and Keck II, in order to conduct a detailed study of the spatially-resolved kinematics and ionization of this galaxy's large-scale Lyα emitting halo and its large-scale H I absorber. Gullberg et al. (2016) presented a primarily morphological study of this object combining the MUSE dataset with multi-wavelength data (see Section 2 below); here we present a detailed study of the kinematic and ionization properties of the Lyα halo and the large-scale Lyα absorbing structure.

The paper is organised as follows. In § 2.3 we describe the key previous results from the literature concerning this well studied HzRG. In § 2.4, we introduce the selected observations and data reduction for MRC 0943–242. In § 2.5, we discuss our observational results. In § 2.6, we discuss the physical properties and several powering mechanisms that could be responsible for such extended Ly α emission and Ly α absorber. In § 2.7, we give a brief summary concluding our results. A $\Omega_\Lambda = 0.713$, $\Omega_m = 0.287$ and $H_\circ = 69.3$ km s^{-1} Mpc^{-1} (Hinshaw et al., 2013) cosmology is adopted in this paper so that 1$''$ corresponds to 7.94 kpc at the redshift of our target ($z = 2.92$).

2.3 MRC 0943-242: previous results

MRC 0943-242 was first catalogued in the Molonglo Reference Catalogue (Large et al., 1981), and selected as a possible HzRG on the basis of its ultra steep radio spectrum by Röttgering

[2]We abbreviate X-SHOOTER to 'XSH' in some tables and figures in the interest of brevity.

et al. (1994). Optical imaging and spectroscopy confirmed the high redshift of this galaxy ($z = 2.92$; Röttgering et al. 1995a).

The radio continuum of MRC 0943–242 has a simple double-morphology (Fanaroff-Riley Class II), consisting of two bright hotspots separated by 3.9″, with no core detected, at 1.4, 4.7 and 8.2 GHz (Röttgering et al., 1995a; Carilli et al., 1997). Its spectral index between 1.5 GHz and 30 GHz is $\alpha = -1.44$ (Emonts et al., 2011b). With a 1.4 GHz radio power of $10^{35.4}$ erg s^{-1} Hz^{-1} (De Breuck et al., 2000a), this is among the most radio-luminous galaxies known.

Rest frame ultraviolet and optical HST images of MRC 0943–242 show a bright, elongated and curved morphology, with a close alignment between the major axis of this emission and that of the radio source (Pentericci et al., 1999, 2001). Using Keck II spectropolarimetry, Vernet et al. (2001) found the extended UV continuum emission along the radio/optical axis to be significantly polarized ($P_{\%} = 6.6 \pm 0.9\%$ at ∼1250 – 1400 Å) with the electric field vector approximately perpendicular to this axis, indicating a substantial contribution from scattered AGN continuum (22 – 66 %), but still allowing a potentially significant contribution from young stars (14 – 53 %). Along the radio/optical axis, Vernet et al. (2001) also estimated that nebular continuum emission contributes around 20 % of the UV continuum. Ground-based K-band imaging shows a rounded and more centrally concentrated morphology than seen in the optical images (van Breugel et al., 1998). Moreover, studying the contribution of the host galaxy stellar emission at rest-frame H band, Seymour et al. (2007) estimated the stellar luminosity of the radio galaxy which implied stellar mass of $\log(M_\star/M_\odot) = 11.22^{+0.15}_{-0.07}$. This HzRG also appears to be located in a proto-cluster (Venemans et al., 2007).

Spectroscopic studies have revealed that MRC 0943–242 is embedded within a giant Lyα halo (Röttgering et al., 1995a, 1997; Binette et al., 2000; Villar-Martín et al., 2003; Jarvis et al., 2003; Venemans et al., 2007; Gullberg et al., 2016). Using Keck II spectroscopy, Villar-Martín et al. (2003) found that the Lyα halo is metal-enriched and has a high surface brightness, kinematically perturbed region (FWHM $\gtrsim$ 1000 km s^{-1}) within the spatial extent of the radio structure, and a giant low surface brightness region with quieter kinematics (FWHM $\lesssim$ 600 km s^{-1}) surrounding the entire object. Villar-Martín et al. (2003) and Humphrey et al. (2006) argued that the close spatial association between the kinematically perturbed gas and the radio structures suggests that jet-gas interactions are responsible for the kinematic perturbation in the high surface brightness regions. Furthermore, Humphrey et al. (2006) found that the kinematically more perturbed gas has a lower level of ionization than the quiescent gas, possibly due to the impact of shocks on the former.

Röttgering et al. (1995a) detected a strong and spatially extended absorption feature in the profile of the Lyα line. By fitting the Lyα velocity profile, Röttgering et al. (1995a), Binette et al. (2000), Jarvis et al. (2003) and Gullberg et al. (2016) have estimated the H I column density of the absorbing gas to be log N(H I/cm^{-2}) $\sim$ 19. It has been suggested that this absorbing structure is a large scale shell that might surround the radio galaxy and its Lyα halo (Binette et al., 2007; Gullberg et al., 2016). Gas mass estimates for this absorbing structure range from $\gtrsim 10^9$ M$_\odot$ to 10^{12} M$_\odot$ (see Binette et al., 2007; Gullberg et al., 2016).

In addition, Binette et al. (2000) detected the C IV doublet in absorption, with a column density log N(C IV/cm^{-2}) = 14.5 ± 0.1 and a redshift close to that of the main Lyα absorber. Based on the ratio of column densities derived from the Lyα and C IV absorption features, Binette et al. (2000) argued that the absorbing structure has a low metallicity ($Z = 0.01 Z_\odot$) and is not co-spatial with the ionized gas responsible for the detected emission lines; the authors suggest that the absorbing gas represents material expelled from the HzRG during an earlier phase of starburst activity (see Binette et al., 2006, 2007).

Gullberg et al. (2016) presented a study of MRC 0943–242, combining ALMA submillimetre observations and MUSE IFU spectroscopy to perform a multiwavelength morphological study of the AGN, starburst and molecular gas components of the galaxy. They report a highly complex morphology, with a reservoir of molecular gas offset by ~ 90 kpc from the AGN, and identify a linear feature that emits Lyα, CO lines and dust continuum which they suggest may be due to an accretion flow onto the radio galaxy. Assuming the main extended absorber surrounds the HzRG and has a roughly spherical shape, Gullberg et al. (2016) estimated a total gas mass of the main Lyα absorber of M(H I) $\gtrsim 3.8 \times 10^9$ M$_\odot$.

In summary, the observational properties of MRC 0943–242 make it an excellent target for a detailed case study into various processes that are expected to play an important role in the evolution of massive galaxies, particularly the interplay between the "ingredients" of galaxy formation, such as AGN, gas, stars, feedback, and gas accretion.

2.4 Observations

This study makes use of deep spectroscopic observations (proprietary and archival) from several different telescopes and instruments (see Table 2.1).

2.4.1 X-SHOOTER Long-Slit and IFU Spectra

Here we present previously unpublished X-SHOOTER (see Vernet et al., 2011) intermediate-resolution échelle spectroscopic observations of MRC 0943–242, obtained at the VLT UT3 on 2009 March 18 and May 3 – 5, during commissioning of the instrument under the program 60.A-9022(C). The wavelength range of X-SHOOTER (3000 Å – 25000 Å) provides a continuous rest-frame wavelength range of 765 Å – 6378 Å at $z = 2.92$, within which are expected to lie a multitude of diagnostically important emission or absorption lines. The pixel scale is ∼0.15″ for UVB and VIS arms, and ∼0.20″ for the NIR arm.

The X-SHOOTER observations were taken in two different modes: long-slit and IFU. In long-slit mode, the slit widths were 1.0″(UVB), 0.9″(VIS), and 0.9″(NIR). In IFU mode, the 4″× 1.8″field of view was reformatted into 12″× 0.6″pseudo slits.

The integration time using the slit mode was split into 6×1500s exposures for the UVB and VIS arms, and 6×500s exposures for the NIR arm, with the slit oriented at a position angle of 55°. The slit observations were made in nodding mode. In IFU mode, the integration time was split into 1×1700s for UVB arm, 1×1700s for VIS arm, and 3×600s for NIR arm, with the position angle identical to that used for the slit observations. The IFU observations were made in offset mode.

The data were processed using ESO's X-SHOOTER reduction pipeline, which performs bias/dark subtraction, background subtraction, flat-fielding, order tracing and merging, wavelength calibration, and finally flux calibration, for which the spectrophotometric standard star EG274 was used. The spectral resolution (FWHM) measured from the sky-lines was ∼ 39 km s^{-1} (UVB), ∼ 32 km s^{-1} (VIS), and ∼ 51 km s^{-1} (NIR) on slit mode, and ∼ 29 km s^{-1} (UVB), ∼ 22 km s^{-1} (VIS), and ∼ 39 km s^{-1} (NIR) on IFU mode.

The data were corrected for Galactic extinction using the NOAO IRAF task DEREDDEN, assuming $E(B-V) = 0.0512$ ($A_V = 0.1587$) and the empirical selective extinction function of Cardelli et al. (1989).

2.4.2 VLT MUSE IFU Spectrum

We also make use of IFU spectroscopy which was obtained using the Multi Unit Spectroscopic Explorer (MUSE, Bacon et al. 2010) at the VLT UT4 on 2014 February 21, during the first commissioning run of the instrument (see Bacon et al., 2014) under the program 60.A-9100(A). Wide Field Mode was used, resulting in a field of view of 1′ × 1′ at 0.2″ spatial sampling. The wavelength range is 4650 Å – 9300 Å and the mean spectral resolution is ∼ 100 km s^{-1} (FWHM). The target was observed for a total of 3600s, which was split into 3×1200s exposures oriented at the position angles 45°, 135° and 225°. Full details of the MUSE observations, their reduction and some analysis has been previously published by Gullberg et al. (2016).

2.4.3 KECK II LRIS Long Slit Spectrum

Additional spectral information comes from a Low Resolution Imaging Spectrometer (hereafter LRIS) spectrum taken at the Keck II 10 m telescope on 1997 December 27 (see Vernet et al., 2001) under the program C56L. The observation was done in polarisation mode with the

Table 2.1: Long slit and IFU spectroscopic observations. (1) Instruments used in the observation. (2) Period during which the observation was made. (3) Spectral Resolution of the instrument. (4) Aperture of the spectrum extraction. (5) Slit width. (6) Total observation time. (7) Spatial sampling. (8) Position Angle.

Instrument	Date	Resolution (km s^{-1})	Aperture ($''$)	Slit width ($''$)	Exp. Time (sec)	Scale/pixel ($''$)	P.A. (^{o})
(1)	(2)	(3)	(4)	(5)	(6)	(7)	(8)
XSH SLIT	March 2009	39, 32, 51	0.75,0.8	1.0,0.9	9000	0.16, 0.21	55
XSH IFU	March 2009	29, 22, 39	0.8	–	1700	0.16, 0.21	55
MUSE IFU	February 2014	100	0.8	–	3600	0.20	45, 135, 225
UVES	December 2001	7	1.0	1.2	10800	0.18	74
AAT	April 1993, March 1995	91	0.79	1.6	25000	0.79	74
LRIS	December 1997	493	0.856	1.0	13800	0.214	73

spectrum covering a wavelength range of ∼ 3900 – 9000 Å, and a spectral resolution of ∼ 493 km s^{-1} (FWHM). The 1$''$ slit was oriented at a position angle of 73°, i.e. along the radio axis. This spectrum has been presented and discussed in several previous publications (Vernet et al., 2001; Villar-Martín et al., 2002, 2003; Humphrey et al., 2006, 2007). See (Vernet et al., 2001) for full details of the observation and reduction of this data.

2.4.4 VLT UVES Archival Spectrum

To complement the above observations, we have also made use of VLT Ultraviolet and Visual Echelle Spectrograph (hereafter UVES) observations on the night of 2001 December 8 – 9 of the radio galaxy, previously published by Jarvis et al. (2003). The spectrum comprises only the red arm and is centred on 5200 Å so as to include Lyα and C IV, and the spectral resolution is ∼ 7 km s^{-1} (FWHM). The raw spectra taken under the program 68.B-0086(A), were obtained from the ESO VLT/UVES archive and were reduced using the UVES pipeline in which the data was automatically bias-subtracted, flat-fielded, wavelength calibrated using Th–Ar arc lamp spectra, and flux calibrated using the spectrophotometric standard star LTT3864. The spectrum was corrected for Galactic extinction with IRAF's DEREDDEN task, using $E(B-V) = 0.0512$ and the extinction function of Cardelli et al. (1989).

2.4.5 AAT RGO Archival Spectrum

In addition, a spectrum of MRC 0943–242 taken using the RGO spectrograph of the Anglo Australian Telescope (hereafter AAT) is used, which was previously published by Röttgering et al. (1995a) and Binette et al. (2000). The spectrum covers the spectral regions around Lyα, C IV and He II at a resolution of ∼ 91 km s^{-1} (FWHM) with a slit PA of 74°, i.e. aligned with the radio axis. The raw spectra were obtained from the AAT archive and were bias subtracted, flat-fielded, and then wavelength calibrated using Cu-Ar arc lamp spectra. In addition, flux calibration was done with the spectrophotometric standard stars FEIGE110 and LTT3864. Finally, the spectrum was corrected for Galactic extinction using IRAF's DEREDDEN, assuming $E(B-V) = 0.0512$ ($A_V = 0.1587$) and the extinction curve of Cardelli et al. (1989).

2.5 Data Analysis

2.5.1 Emission and Absorption Line Fitting

2.5.1.1 Fitting routine

We created a Python routine to fit the emission and absorption line parameters, with Gaussian and Voigt profiles being used to model the emission and absorption lines, respectively. The routine minimizes the sum of the squares of the difference between the model and data using the LMFIT algorithm (Newville et al., 2014). Parameters for the best fits are shown in Tables 2.2, 2.3, 2.4.

2.5.1.2 Lyα and the degeneracy in *N* and *b*

The Lyα profile was parametrized assuming that the underlying emission line is a single Gaussian, and adopting Voigt profiles for the superimposed H I absorption features. Figures 2.1 and 2.2 show the one-dimensional spectra of the Lyα emission-line from the X-SHOOTER observations of MRC 0943–242 as well as other instruments.

When fitting absorption lines there can be a strong degeneracy between column density (N) and the Doppler width (b), and we find this to be the case with the main H I absorption feature seen in the Lyα profile of MRC 0943–242. We find two widely separated 'best-fitting' to the column density of this absorber, one at log N(H I/cm^{-2}) = 15.20 with $b \sim 153$ km s^{-1} ($\tilde{\chi}^2_\nu$ = 0.08), and another at log N(H I/cm^{-2}) = 19.63 with $b \sim 52$ km s^{-1} ($\tilde{\chi}^2_\nu$ = 0.07).

We illustrate this degeneracy in Figure 2.3, where we show column density (N(H I)) *versus* reduced chi-square ($\tilde{\chi}^2_\nu$). With the exception of the two 'best-fitting', the data points in this Figure were obtained by running our fitting code with N(H I) fixed at specific values, but with all other parameters left free to vary. In addition to the presence of the two 'best-fitting', Figure 2.3 also illustrates the presence of a broad range of intermediate N(H I) values where the fits are still reasonably good.

Throughout this paper, we will ensure that the degeneracy described above is fully taken into account when we derive properties of the extended H I absorber. Where we make use of the flux of the Lyα emission line (e.g., Sect. 5.2), we adopt the absorption-corrected flux obtained from our log N(H I/cm^{-2}) = 19.63 fit to the line profile (20.27 ± 0.38 $\times 10^{-16}$ erg cm^{-2} s^{-1}). Using instead the flux obtained from our log N(H I/cm^{-2}) = 15.20 fit (17.64 ± 0.38 $\times 10^{-16}$ erg cm^{-2} s^{-1}) does not have any significant impact on our conclusions.

2.5.1.3 C IV

The methodology used to fit the C IV profile is similar to that used for Lyα. Because C IV is a doublet, two gaussians were used for the emission and two Voigt profiles for the absorption, with the doublet's (rest-frame) wavelength separation set to its theoretical value (see Fig. 2.4). In the case of the emission components, we set the flux ratio C IV λ1548.2 / C IV λ1550.8 to 2.0 and constrained both lines to have equal FWHM and redshift (z) . For the absorption lines, we constrained both lines to have the same values for z, b and N.

2.5.1.4 Other lines

Other emission lines were fitted with a single Gaussian component. Emission doublets were specified to have equal FWHM, fixed wavelength separation and a fixed flux ratio. For instance, we set the flux ratio N V $\lambda\lambda$1239,1243 to 2.0, C III] $\lambda\lambda$1907,1909 to 0.66, [Ne IV] $\lambda\lambda$2422,2424 to 1.5, [O II] $\lambda\lambda$3726,3729 to 1.4 and [O III] $\lambda\lambda$4959,5007 to 0.35. In order to obtain a fiducial systemic velocity we use the non-resonant He II λ1640 emission-line.

2.5.2 Kinematic maps

From the MUSE datacube, we have extracted the spatially resolved kinematic properties of the UV emission and absorption lines using the fitting procedure outlined in §2.5.1. Due to the relatively low spectral resolution of the MUSE data, we only included a single absorption line in our fit to Lyα, which represents the main absorber.

In Figure 2.5 we show the maps of the FWHM, and the velocity offset relative to the He II emission at the position of the UV continuum peak. Figures 2.17a and 2.17b show the velocity offset for the extended absorber in Lyα and C IV, respectively. To facilitate consistency checks, we also extracted the kinematic properties of the Lyα, He II and/or C IV from the X-SHOOTER and Keck II long slit spectra (see Figure 2.6).

2.5.3 Pseudo-Narrowband images and line ratio maps

In order to study the emission line morphology, we have produced pseudo-narrowband (hereafter, pseudo-NB) images from the MUSE datacube. These images were created by summing pixels along the dispersion axis within spectral windows that include all of the detected line flux: λ_{obs} = 4705.55 – 4718.05, 4722.68 – 4726.84, 4734.71 – 4740.72, 4742.64 – 4754.61 Å for Lyα aiming to exclude the absorption troughs of the emission-line, λ_{obs} = 5745.74 – 5812.24 for C IV, λ_{obs} = 6037.49 – 6094 for He II and λ_{obs} = 6875.09 – 6931.81 for C III]. An image of the adjacent continuum was then subtracted from each, giving a pure emission-line image. The resulting continuum-subtracted, pseudo-NB images are shown on the left of Fig. 2.5.

Our flux ratio maps use the flux maps produced by our line fitting procedure (§2.5.1 and §2.5.2), and we have simply divided one line flux map by another (see Fig. 2.9).

2.5.4 Ionization Models

To assist in understanding the physical conditions and nature of the extended line emitting gas of the radio galaxy, a grid of photoionization models (see Figure 2.11 to 2.15) were computed using the multipurpose code MAPPINGS Ie (Binette et al., 1985; Ferruit et al., 1997).

Our model grid contains two possible values for the ionizing spectral index, $\alpha = -1.5$ with a high-energy cut-off of 5×10^4 eV, and $\alpha = -1.0$ with a high energy cut-off of 1×10^3 eV. The gas chemical abundances were varied between $0.5Z_\odot$ and $3.0Z_\odot$ (with $Z_\odot$ being the solar metallicity), with all metals being scaled linearly with O/H except for nitrogen. The nitrogen abundance was varied such that N/H $\propto$ O/H at $Z/Z_\odot$<0.3 and N/O $\propto$ O/H at $Z/Z_\odot \geq 0.3$, to take into account its expected secondary behaviour at moderate to high metallicity (e.g. Villar-Martín et al., 1999b; Henry et al., 2000). We adopt the Solar chemical abundances of Asplund et al. (2006). The ionization parameter[3] varies from $U = 10^{-4}$ to 1.6. For all models, we use hydrogen density of 100 cm^{-3} and adopt a single-slab, ionization-bounded, isochoric geometry.

Because MRC 0943–242 is a powerful radio galaxy, it is plausible that the radio jets drive ionizing shocks into the interstellar medium. Thus, we also make use of shock and shock plus precursor models from the literature, computed by Allen et al. (2008) using MAPPINGS III. The models used consist of one sequence in which the emission comes solely from shock-heated gas, while the other sequence is a combination of shock heated gas and a photoionized precursor. In order to be as consistent as possible with our MAPPINGS 1e photoionization models, we have selected sequences with solar abundance, shock velocities covering the range v_s = 100 up to 1000 km s^{-1} in steps of 25 km s^{-1}, hydrogen density n_H = 100 cm^{-3} and magnetic field B = 100 μ G.

The large number of emission lines now detected from this radio galaxy makes it challenging to diagnose the physical conditions using only diagnostic diagrams. For this reason, we have

[3]The ionization parameter U is defined as the ratio of ionizing photons to hydrogen atoms and its expression is $Q/(4\pi r^2 n_H c)$, with Q as the ionizing photon luminosity of the source, r is the distance of the cloud from the ionizing source, n_H is the hydrogen density and c is the speed of light.

written a simple Python code that searches the assembled grid of ionization models to find the model that best reproduces an ensemble of emission line ratios. The routine includes extinction A_V as a free parameter, and we have assumed $R_V = 3.1$ and the dust extinction curve of Fitzpatrick (1999). For this we use all possible line ratios formed using lines detected in our X-SHOOTER long-slit spectrum, with the exception of ratios involving Lyα, where transfer effects are likely to be strong. All line ratios included in this analysis are given equal weighting, and the goodness of fit is evaluated using reduced chi-square (χ^2_ν).

HIGH N(H I) SOLUTION LOW N(H I) SOLUTION

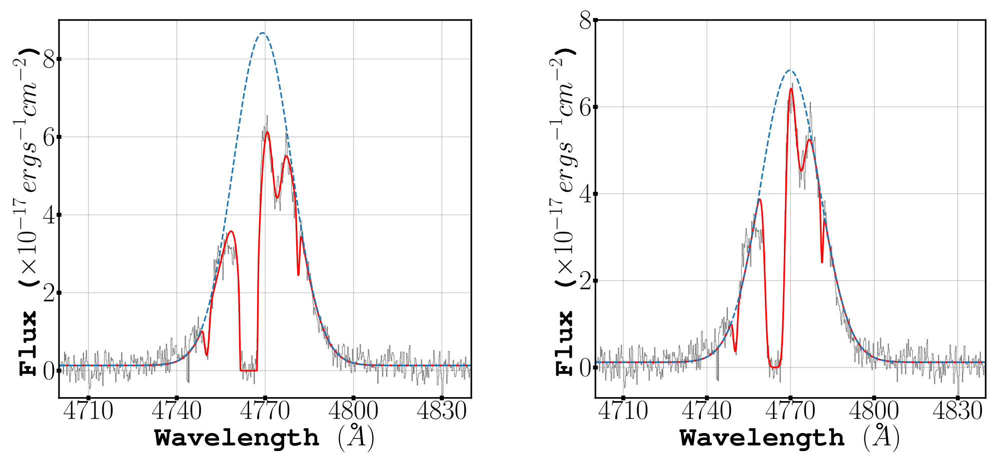

(a) XSHOOTER SLIT

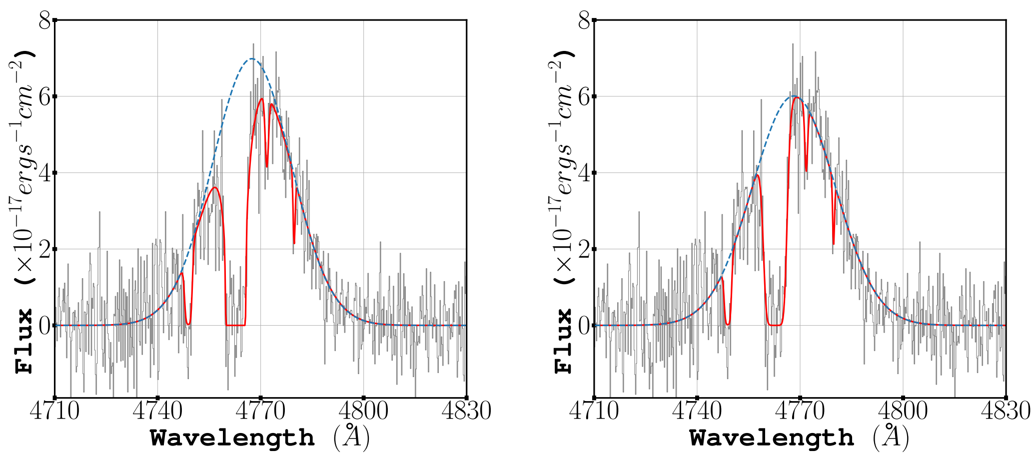

(b) X-SHOOTER IFU

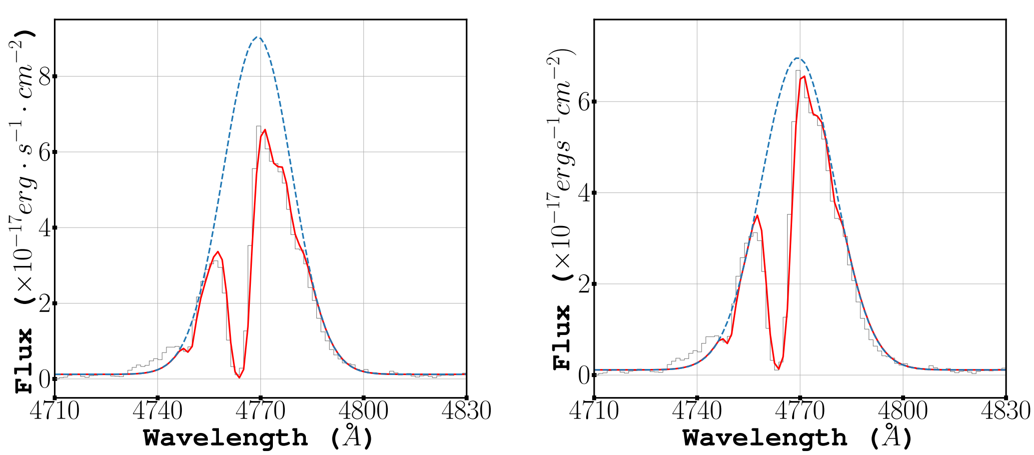

(c) VLT MUSE

Figure 2.1: Lyα profile of MRC 0943–242 extracted from the VLT/X-SHOOTER (long-slit and IFU) and VLT/MUSE, with the Gaussian emission component (dashed blue line) plus absorption model overlaid (red line). The left and right columns show the high and low column density best-fitting, respectively.

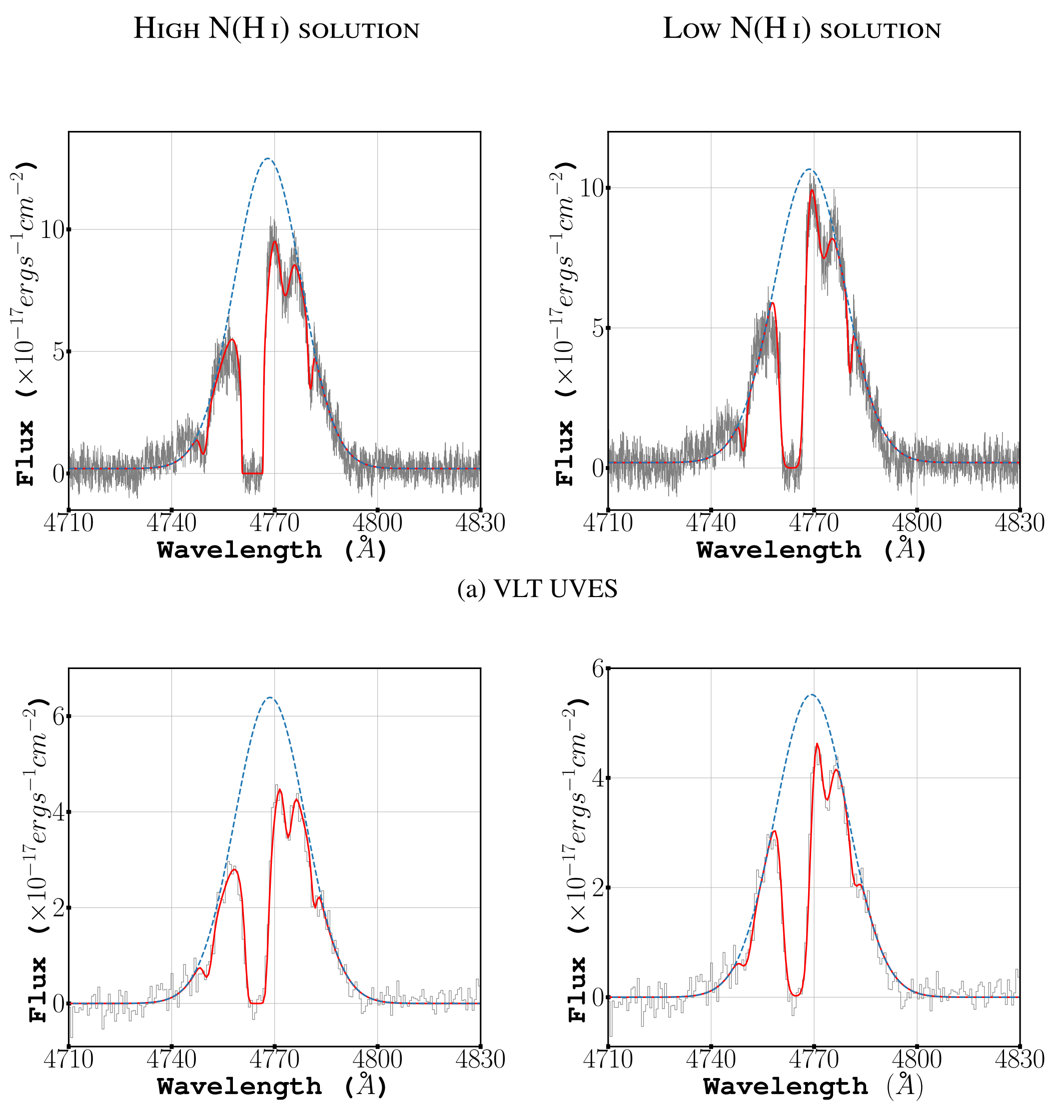

(a) VLT UVES

(b) AAT

Figure 2.2: Lyα profile of MRC 0943–242 extracted from the VLT/UVES and AAT, with the Gaussian emission component (dashed blue line) plus absorption model overlaid (red line). The left and right columns show the high and low column density best-fitting, respectively.

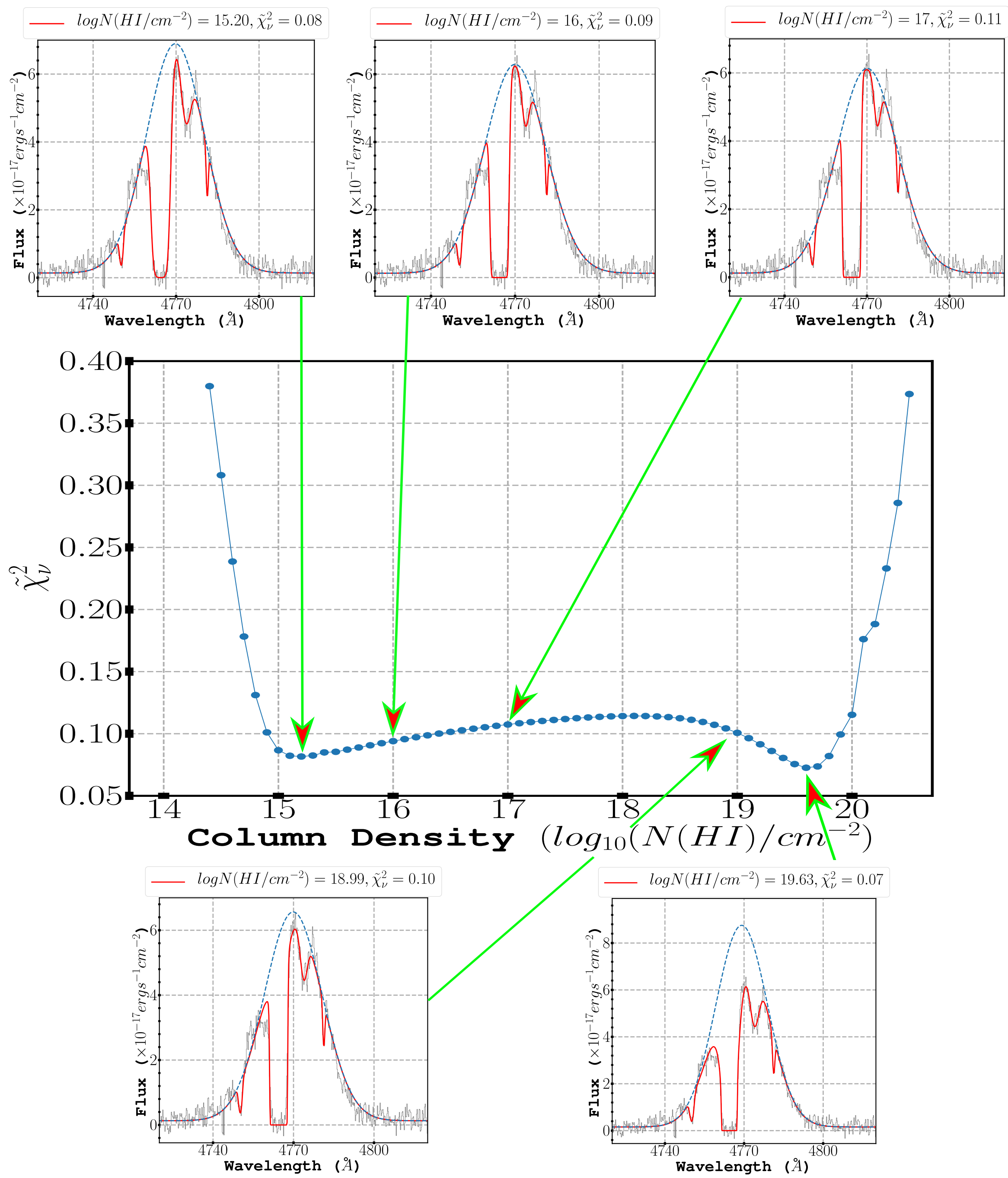

Figure 2.3: Plot of column density (N(H I)) *versus* reduced chi-square ($\tilde{\chi}^2_\nu$), showing the presence of two widely-spaced 'best-fitting', between which lie a broad range of inferior, but nonetheless reasonable fits. Data points other than the two 'best-fitting' were produced by running our fitting code with N(H I) fixed to specific values. Around the main plot we show selected fits to the X-SHOOTER long-slit Lyα profile, to further illustrate how the fits evolve as a function of N(H I).

Table 2.2: Measurements of the rest-frame UV and optical emission lines obtained with the fitting routine. Lyα_{15} and Lyα_{19} correspond to the lower (log N(H I/cm^{-2}) ~ 15.20) and higher (log N(H I/cm^{-2}) ~ 19.63) column density results, respectively.

Line	λ_{rest} Å	λ_{obs} Å	Line Flux ($\times10^{-16}$ erg cm^{-2} s^{-1})	FWHM (km s^{-1})	Δv (km s^{-1})
		XSHOOTER SLIT			
O VI+C II	1031.9,1037.6	4050.0 ± 0.7, 4072.4 ± 0.7	1.57 ± 0.24	869 ± 100	6 ± 48
Lyα_{15}	1215.7	4769.8 ± 0.1	17.64 ± 0.29	1557 ± 18	-84 ± 6
Lyα_{19}	1215.7	4769.1 ± 0.1	20.27 ± 0.38	1458 ± 16	-126 ± 5
N V	1238.8, 1242.8	4858.7 ± 1.0, 4874.3 ± 1.0	0.62 ± 0.11	883 ± 130	-204 ± 64
C IV	1548.2,1550.8	6076.2 ± 0.5, 6086.4 ± 0.3	3.02 ± 0.20	1045 ± 53	-1 ± 23
He II	1640.4	6436.5 ± 0.26	2.05 ± 0.08	1018 ± 32	0 ± 12
C III]	1906.7, 1908.7	7481.9 ± 0.6, 7489.9 ± 0.6	1.11 ± 0.07	1087 ± 59	-49 ± 22
C II]	2325.4, 2326.9	9123.2 ± 2.0, 9129.2 ± 2.0	0.55 ± 0.09	1298 ± 181	-105 ± 64
[Ne IV]	2421.8, 2424.4	9502.6 ± 0.9, 9512.9 ± 0.9	0.37 ± 0.10	386 ± 87	-69 ± 29
Mg II	2795.5, 2802.7	10974.0 ± 1.4, 11002.2 ± 1.4	0.97 ± 0.14	565 ± 66	67 ± 38
[Ne V]	3425.9	13437.0 ± 1.2	1.27 ± 0.11	951 ± 64	-188 ± 27
[O II]	3726.0, 3728.8	14617.9 ± 0.8, 14628.8 ± 0.8	4.83 ± 0.18	1238 ± 39	-113 ± 16
[Ne III]	3868.7	15180.2 ± 0.8	1.79 ± 0.10	992 ± 45	-67 ± 17
H γ	4340.4	17032.8 ± 2.1	0.84 ± 0.12	844 ± 91	-34 ± 37
[O III]	4363.2	17118.4 ± 0.4	0.47 ± 0.04	327 ± 18	-101 ± 8
[O III]	4958.9	19459.4 ± 0.4	5.18 ± 0.12	1002 ± 17	-42 ± 6
[O III]	5006.8	19647.5 ± 0.4	14.97 ± 0.33	1002 ± 17	-42 ± 6
		XSHOOTER IFU			
Lyα_{15}	1215.7	4768.2 ± 0.3	18.14 ± 0.67	1778 ± 45	-189 ± 18
Lyα_{19}	1215.7	4767.2 ± 0.3	20.81 ± 0.99	1674 ± 42	-250 ± 18
C IV	1548.2,1550.8	6076.4 ± 0.5, 6086.6 ± 5.8	5.78 ± 0.32	1372 ± 61	-64 ± 25
He II	1640.4	6438.0 ± 0.5	1.30 ± 0.11	773 ± 51	0 ± 21
C III]	1906.7, 1908.7	7478.6 ± 0.6, 7486.7 ± 0.6	1.14 ± 0.08	1050 ± 66	-252 ± 24
[O III]	4958.9	19461.2 ± 0.5	8.15 ± 0.16	1030 ± 19	-88 ± 8
[O III]	5006.8	19649.3 ± 0.5	23.56 ± 0.16	1030 ± 19	-88 ± 8
		MUSE IFU			
Lyα_{15}	1215.7	4769.4 ± 0.1	18.28 ± 0.50	1572 ± 19	−86 ± 6
Lyα_{19}	1215.7	4769.0 ± 0.1	20.67 ± 1.00	1532 ± 25	−92 ± 7
N V	1238.8, 1242.8	4860.4 ± 0.3, 4876.1 ± 0.3	0.70 ± 0.04	746 ± 34	−52 ± 18
Si IV	1402.8	5501.0 ± 1.2	0.46 ± 0.05	2244 ± 182	−207 ± 66
N IV]	1483.3, 1486.5	5825.0 ± 2.8, 5837.5 ± 2.8	0.29 ± 0.09	1785 ± 321	220 ± 142
C IV	1548.2,1550.8	6075.6 ± 0.2, 6085.8 ± 0.1	2.88 ± 0.06	1120 ± 16	12 ± 8
He II	1640.4	6435.6 ± 0.2	1.91 ± 0.05	1034 ± 19	0 ± 7
O III]	1660.8, 1666.1	6512.6 ± 0.9, 6535.7 ± 0.9	0.33 ± 0.04	921 ± 88	-211 ± 40
C III]	1906.7, 1908.7	7480.6 ± 0.3, 7488.6 ± 0.3	1.21 ± 0.04	1008 ± 32	-60 ± 12
C II]	2325.4, 2326.9	9119.3 ± 1.1, 9125.3 ± 1.1	0.49 ± 0.04	1445 ± 110	-193 ± 37
		VLT UVES			
Lyα_{15}	1215.7	4768.6 ± 0.1	26.95 ± 0.33	1516 ± 9	-161 ± 3
Lyα_{19}	1215.7	4768.0 ± 0.1	31.03 ± 0.43	1439 ± 8	-199 ± 3
C IV	1548.2,1550.8	6076.1 ± 0.2, 6086.3 ± 0.1	2.76 ± 0.08	1173 ± 29	-7 ± 11
		AAT			
Lyα_{15}	1215.7	4769.2 ± 0.2	14.36 ± 0.65	1529 ± 35	-11 ± 10
Lyα_{19}	1215.7	4768.7 ± 0.2	16.46 ± 0.80	1486 ± 31	-45 ± 10
C IV	1548.2,1550.8	6071.3 ± 0.4, 6081.5 ± 0.1	4.36 ± 0.34	1331 ± 66	-136 ± 18
He II	1640.4	6434.2 ± 0.6	1.41 ± 0.14	885 ± 69	0 ± 27
		KECK II			
Lyα	1215.7	4773.1 ± 0.2	19.76 ± 0.47	1695 ± 19	156 ± 9
N V	1238.8, 1242.8	4864.1 ± 0.5, 4879.7 ± 0.5	0.43 ± 0.05	1318 ± 125	162 ± 29
N IV]	1483.3, 1486.5	5820.1 ± 1.8, 5832.6 ± 1.8	0.11 ± 0.04	757 ± 193	-44 ± 93
C IV	1548.2,1550.8	6076.6 ± 0.2, 6086.8 ± 0.2	2.75 ± 0.07	1183 ± 18	51 ± 12
He II	1640.4	6435.8 ± 0.2	1.94 ± 0.05	1098 ± 20	0 ± 8
O III]	1660.8, 1666.1	6512.8 ± 1.3, 6533.7 ± 1.3	0.30 ± 0.05	1320 ± 203	-215 ± 62
C III]	1906.7, 1908.7	7480.9 ± 0.3, 7488.9 ± 0.3	1.16 ± 0.04	1008 ± 32	-58 ± 11

Table 2.3: Best fit parameters for the Lyα absorption features, for different instruments. Column (1) gives the redshift for the Lyα emission Gaussian. Column (2) gives the redshift for each Lyα absorption. Column (3) gives the column density ($N_{\rm H\,I}$). Column (4) gives the Doppler width b. Column (5) gives the velocity shift of the main absorber with respect to He II emission in the same spectrum. Note: The He II emission line was outside the spectral range covered by the red arm of VLT UVES and thus we do not give the velocity shift for this instrument.

Lyα emission redshift (z_{em})	Absorption redshift (z_{abs})	Column Density (cm^{-2})	Doppler b Parameter (km s^{-1})	Δv (km s^{-1})
		XSHOOTER SLIT		
	2.90746 ± 0.00009	(9.17 ± 1.57)×10^{13}	55 ± 8	
2.92303 ± 0.00007	2.91917 ± 0.00002	(4.27 ± 0.20)×10^{19}	52 ± 1	-421 ± 1
	2.92702 ± 0.00006	(8.06 ± 0.70)×10^{13}	142 ± 9	
	2.93301 ± 0.00004	(2.30 ± 0.30)×10^{13}	35 ± 5	
	2.90747 ± 0.00311	(8.09 ± 1.66)×10^{13}	48 ± 9	
2.92360 ± 0.00007	2.91915 ± 0.00001	(1.52 ± 0.12)×10^{15}	153 ± 4	-422 ± 2
	2.92672 ± 0.00002	(6.39 ± 0.73)×10^{13}	142 ± 12	
	2.93304 ± 0.00001	(1.95 ± 0.30)×10^{13}	31 ± 5	
		XSHOOTER IFU		
	2.90643 ± 0.00003	(3.15 ± 2.51)×10^{14}	54 ± 17	
2.92165 ± 0.00024	2.91777 ± 0.00006	(3.46 ± 0.50)×10^{19}	52 ± 2	-533 ± 4
	2.92525 ± 0.00012	(1.95 ± 0.63)×10^{13}	40 ± 13	
	2.93178 ± 0.00010	(1.84 ± 0.76)×10^{13}	23 ± 10	
	2.90643 ± 0.00015	(3.16 ± 0.14)×10^{14}	51 ± 19	
2.92226 ± 0.00024	2.91778 ± 0.00003	(1.86 ± 0.65)×10^{15}	136 ± 12	-600 ± 6
	2.92522 ± 0.00012	(1.58 ± 0.58)×10^{13}	34 ± 13	
	2.93178 ± 0.00010	(1.66 ± 0.75)×10^{13}	22 ± 10	
		MUSE IFU		
	2.90692 ± 0.00020	(1.13 ± 0.23)×10^{14}	67 ± 32	
2.92291 ± 0.00010	2.91843 ± 0.00008	(3.50 ± 0.39)×10^{19}	50 ± 3	-434 ± 6
	2.92714 ± 0.00018	(2.76 ± 1.04)×10^{13}	114 ± 40	
	2.93192 ± 0.00021	(2.69 ± 0.83)×10^{13}	92 ± 39	
	2.90686 ± 0.00032	(9.27 ± 3.44)×10^{13}	60 ± 21	
2.92324 ± 0.00008	2.91858 ± 0.00002	(1.06 ± 0.07)×10^{15}	175 ± 6	-442 ± 2
	2.92666 ± 0.00020	(1.77 ± 0.76)×10^{13}	88 ± 51	
	2.93207 ± 0.00033	(1.54 ± 0.67)×10^{13}	55 ± 41	
		VLT UVES		
	2.90674 ± 0.00006	(1.02 ± 0.09)×10^{14}	81 ± 6	
2.92213 ± 0.00004	2.91845 ± 0.00001	(4.29 ± 0.11)×10^{19}	54 ± 1	
	2.92618 ± 0.00004	(5.80 ± 0.32)×10^{13}	128 ± 5	
	2.93229 ± 0.00003	(3.33 ± 0.20)×10^{13}	50 ± 3	
	2.90682 ± 0.00005	(8.65 ± 0.89)×10^{13}	56 ± 5	
2.92263 ± 0.00004	2.91840 ± 0.00001	(1.58 ± 0.07)×10^{15}	158 ± 2	
	2.92581 ± 0.00005	(4.99 ± 0.38)×10^{13}	138 ± 8	
	2.93232 ± 0.00003	(2.94 ± 0.20)×10^{13}	45 ± 3	
		AAT		
	2.90776 ± 0.00683	(9.43 ± 2.83)×10^{13}	82 ± 30	
2.92268 ± 0.00014	2.91947 ± 0.00003	(5.11 ± 0.47)×10^{19}	52 ± 2	-290 ± 3
	2.92696 ± 0.00013	(4.79 ± 0.80)×10^{13}	100 ± 39	
	2.93321 ± 0.00018	(2.85 ± 0.81)×10^{13}	50 ± 26	
	2.90770 ± 0.00029	(6.72 ± 2.66)×10^{13}	65 ± 33	
2.92313 ± 0.00014	2.91944 ± 0.00005	(1.36 ± 0.15)×10^{15}	185 ± 8	-293 ± 4
	2.92660 ± 0.00014	(6.16 ± 1.30)×10^{13}	128 ± 22	
	2.93328 ± 0.00020	(2.81 ± 0.88)×10^{13}	56 ± 3	

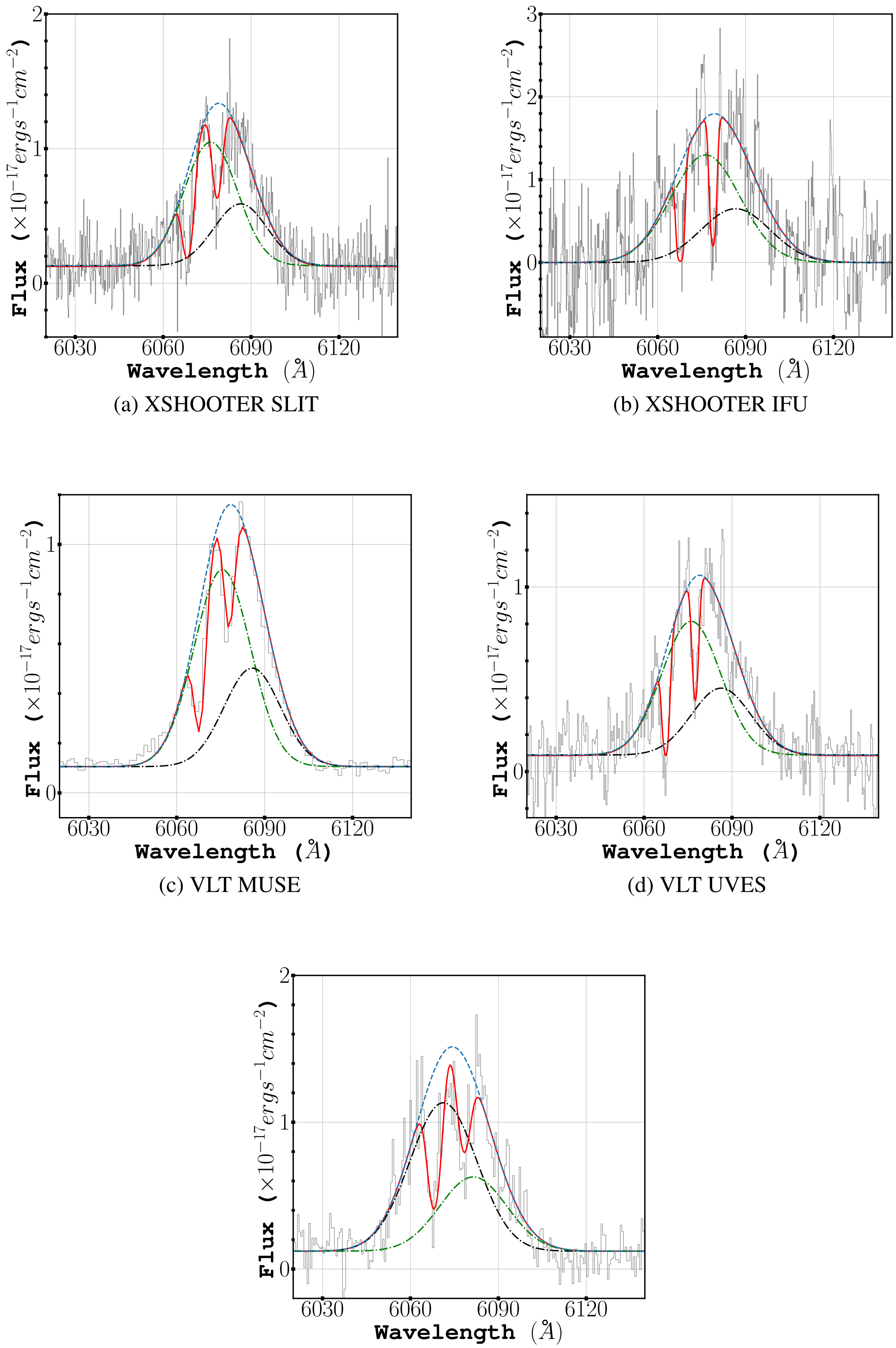

(a) XSHOOTER SLIT
(b) XSHOOTER IFU
(c) VLT MUSE
(d) VLT UVES
(e) AAT

Figure 2.4: The C IV profile of MRC 0943–242, with the Gaussian emission component (dashed blue line) and emission plus absorption model overlaid (red line). The two individual doublet components are also shown.

Table 2.4: Best fit parameters for the C IV absorption features, for different instruments. Column (1) gives the redshift for the C IV emission Gaussian. Column (2) gives the redshift for each C IV absorption. Column (3) gives the column density ($N_{C\,IV}$). Column (4) gives the Doppler width b. Column (5) gives the velocity shift of the main absorber with respect to He II emission in the same spectrum. Note: The He II emission line was outside the spectral range covered by the red arm of VLT UVES and thus we do not give the velocity shift for this instrument.

CIV emission redshift (z_{em})	Absorption redshift (z_{abs})	Column Density (cm^{-2})	Doppler Parameter (km s^{-1})	Δv (km s^{-1})
		XSHOOTER SLIT		
2.92466 ± 0.00030	2.91965 ± 0.00011	$(3.65 \pm 0.53)\times10^{14}$	114 ± 14	-384 ± 8
		XSHOOTER IFU		
2.92479 ± 0.00033	2.91921 ± 0.00031	$(6.19 \pm 1.27)\times10^{14}$	62 ± 7	-491 ± 9
		MUSE IFU		
2.92427 ± 0.00010	2.91927 ± 0.00004	$(3.14 \pm 0.18)\times10^{14}$	100 ± 7	-371 ± 3
		VLT UVES		
2.92459 ± 0.00015	2.91899 ± 0.00001	$(3.04 \pm 0.24)\times10^{14}$	67 ± 5	
		AAT		
2.92149 ± 0.00008	2.91950 ± 0.00003	$(3.89 \pm 0.54)\times10^{14}$	140 ± 15	-288 ± 8

2.6 Results and Discussion

2.6.1 Radio mode feedback

In Fig. 2.5, we show maps of the flux and kinematic properties of the lines Lyα, C IV, He II and C III] from our analysis of the MUSE datacube, with the position of the nucleus and the radio hotspots marked. To supplement the MUSE results, we also show kinematic results from our single-slit observations from X-SHOOTER and Keck II in Fig. 2.6. Taking into account differences in spatial resolution, spectral resolution and slit position between the different observations, we find good consistency between the kinematic results from the MUSE, X-SHOOTER and Keck II datasets.

The pseudo narrow band images show an extended emission line halo with a major axis that is well aligned with the PA of the radio source (see also Gullberg et al., 2016), similar to the close alignment found by Pentericci et al. (1999, 2001) using broad-band HST images of this object.

In agreement with previous kinematic studies of this galaxy (Villar-Martín et al., 2003; Humphrey et al., 2006), we find that the extended emission line halo shows a central, extended region of kinematically turbulent gas with relatively high FWHM ($>$ 800 km s^{-1}) which almost reaches the radio hotspots, with kinematically more quiescent gas ($<$ 800 km s^{-1}) located at larger radii. In addition, we find the most extreme gas kinematics within ~1″of the position of the West radio hotspot, with all of these lines showing their highest FWHM and greatest relative blueshift there. Along the Keck II PA, the FHWMs of both C IV and He II show a modest increase from the nucleus towards the radio hotpots, but peaking ~0.6″short and sharply falling to smaller FWHM values.

Our velocity maps (see Fig. 2.5) and velocity curves (see Fig. 2.6) show that the central, kinematically perturbed gas shows the most redshifted velocities, with a dramatic transition to blueshifted velocities taking place near the positions of the radio hotspots. At the position of the West radio hotspot, spatially coincident with the largest measured FWHM, we find the highest relative blueshift (> 300 km s^{-1}) in Lyα, C IV, He II and C III].

Thus, there is clear evidence for jet gas interactions strongly affecting the kinematic properties of the extended emission line gas (see Fig. 2.7). However, the precise nature of this interaction is not immediately clear. Whereas our data only give us the line of sight velocity, the radio jet motion is likely to be close to the plane of the sky.

Naively, one might have expected the perturbed gas at radii smaller than the hotspots to be in outflow from the galaxy, and thus blueshifted relative to the ambient quiescent gas. However, with the notable exception of a localised region of gas associated with the West hotspot, the vast majority of the perturbed gas shows a relative *redshift* with respect to the quiescent gas. In addition, we find that the quiescent gas that lies beyond the highly perturbed, inner regions shows a net blueshift, a feature that is seen on the east and west sides of the object, in both C IV and He II.

In Fig. 2.8 we illustrate two scenarios that may explain the remarkable kinematic properties observed in MRC 0943–242. In both cases, the relativistic jets of radio plasma are produced in the central active nucleus and propagate outward through the host galaxy, terminating in a hotspot that represents the working surface of the jet against the ambient ISM. Upon reaching the hotspot, the radio plasma cools and diffuses/flows laterally away from the hotspot, carrying with it condensations of warm ionized gas that are seen as localised blueshifted line emission with relatively large FWHM, closely associated with the hotspots. Beyond the radio cocoon, the ambient ISM remains untouched by the radio jets and thus shows relatively narrow emission lines. Within this general framework, the fact that much of the kinematically perturbed gas is *redshifted* suggests that we are witnessing the inflow of gas driven by radio-mode feedback, due to (1) gas being pulled in towards the radio jets as part of the entrainment process; or (2) a backflow of material from the radio hotspots which cycles material back into the host galaxy. An interesting implication of the second scenario is that, judging by the fact that this perturbed and blueshifted component dominates the overall line emission from within the radius of the radio source, a significant quantity of gas is funnelled back towards the host galaxy after being entrained/accelerated by the radio jets.

Although the long-term effect of the radio-loud activity may well be to quench star-formation (hereafter SF) and starve the AGN of fuel, we speculate that MRC 0943–242 may be in a phase of *positive* radio-mode feedback where fuel is cycled back into the central regions of the galaxy to form stars and fuel the AGN. Indeed, a number of studies have found a correlation between small radio-jets and a relatively higher star formation rate (e.g. Humphrey et al., 2006, 2011), and this HzRG appears to have a substantial rate of star-formation in the range 200 – 1400 $M_{\odot}$ yr^{-1} (Gullberg et al. 2016; see also Humphrey et al. 2006).

The two scenarios described above are not necessarily mutually exclusive; it seems plausible that both could operate simultaneously. In either case, we point out that the ISM would need to contain dust so as to dim the perturbed gas located on the far side of the galaxy from the observer, suggesting that significant quantity of dust is able to survive the shocks driven into the ISM during the passage/growth of the radio source through the host galaxy, consistent with the detection of significant UV continuum polarization (Vernet et al., 2001).

Maps of several important UV line ratios are shown in Fig. 2.9 (see also Fig. 2.10). The large variation of C IV/C III] in our map suggests there is a substantial range in ionization level across the object. In addition, we find a spatial correlation between the radio hostpots and several of the emission line ratios, with relatively low values of C IV/He II and C IV/C III], and high values of C III]/He II, spatially associated with both radio hotspots, and qualitatively consistent with lower U in the vicinity of the hostpots.

The Lyα/He II ratio shows no direct spatial correlation with the positions of the radio hotspots. However, we do find relatively low values for this ratio (< 6) to the immediate East of the Eastern radio hotspot and ~0.9″ South of the Western hotspot, in both cases spatially coincident with a region of kinematically quiescent gas as seen in the He II and C III] kinematic maps (see Fig. 2.5), suggesting that the Lyα escape fraction is much lower in regions that are unaffected by radio mode feedback. Scenarios that may explain this result include: (i) reduction of dust in the kinematically perturbed regions due to jet-driven shocks (e.g. Villar-Martín et al., 2001); (ii) greater velocity overlap between emitting and absorbing gas phases in the kinematically quiescent regions (e.g. Tenorio-Tagle et al., 1999); (iii) the presence of an optically thick shell of gas encasing the expanding radio cocoon (e.g. Binette et al., 2006). The ionization/excitation and metallicity of the extended gas will be examined in greater detail in §2.6.2.

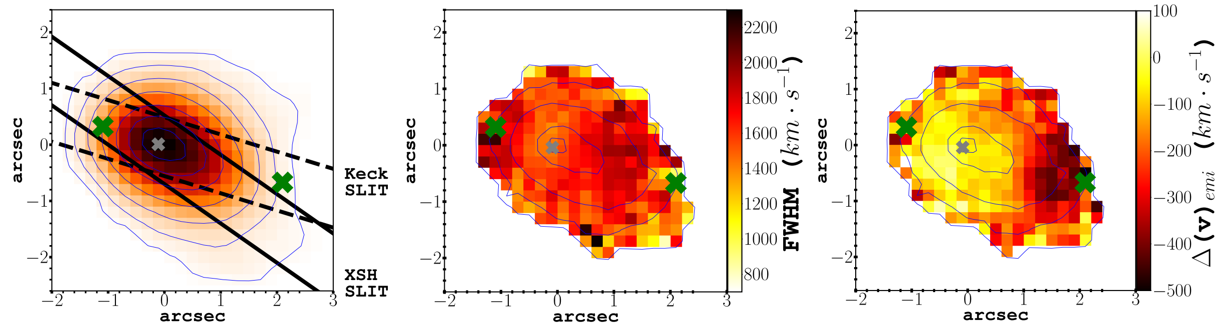

(a) Lyα λ1216

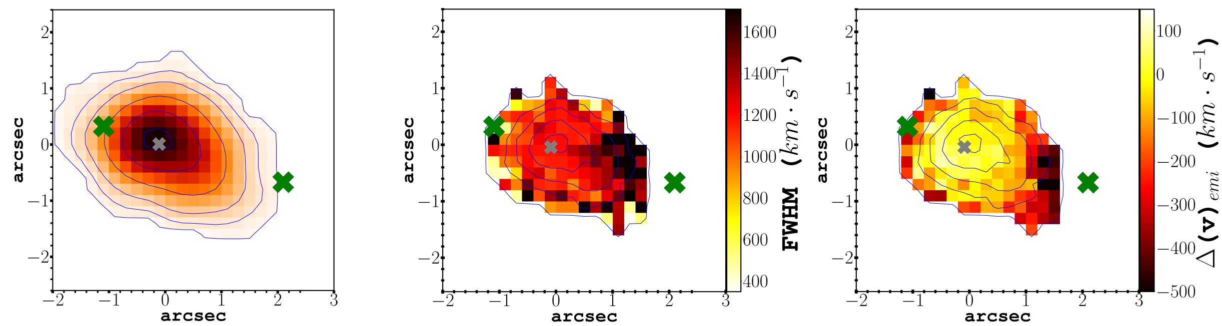

(b) C IV $\lambda\lambda$1548,1550

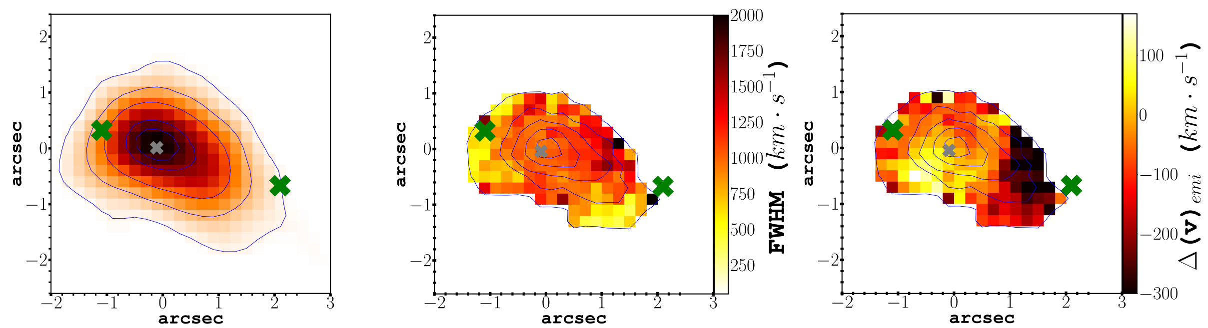

(c) He II λ1640

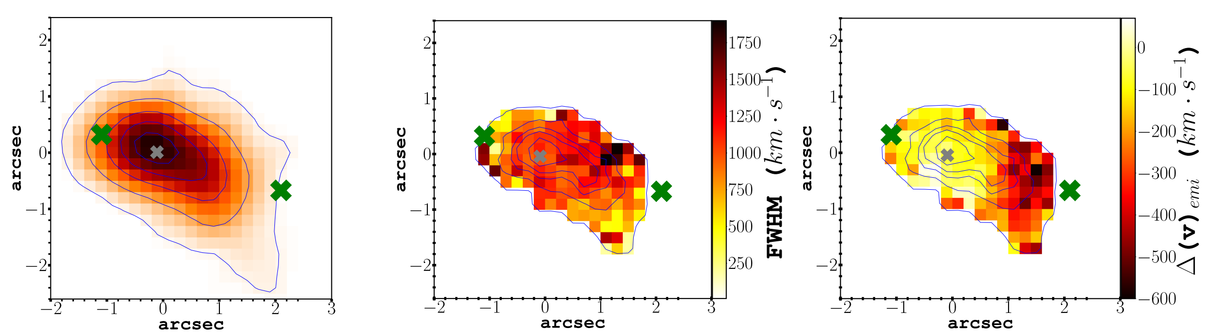

(d) C III] $\lambda\lambda$1907,1909

Figure 2.5: From left to right, we show the pseudo-narrowband images, the FWHM map and the velocity map. The pseudo-narrowband image of Lyα is overlaid with the position of the X-SHOOTER slit (solid lines) and KECK slit (dashed lines). Contour levels: Lyα - (0.3,1.3,3.8,12.5,16.8)$\times 10^{-16}$, C IV - (0.5,1.0,2.0,3.5,4.3)$\times 10^{-16}$, He II - (0.1,0.8,1.0,1.5,2.0)$\times 10^{-16}$ and C III] - (0.08,0.5,0.8,1.0,1.3)$\times 10^{-16}$ erg cm^{-2} s^{-1} arcsec^{-2}. The green "X" represents the positions of the radio hotspots. The coordinate (0,0) correponds to the assumed position of the AGN which is marked with a grey "x". The scale of $5'' \times 5''$on the axes corresponds to the physical scale of 40 kpc $\times$ 40 kpc.

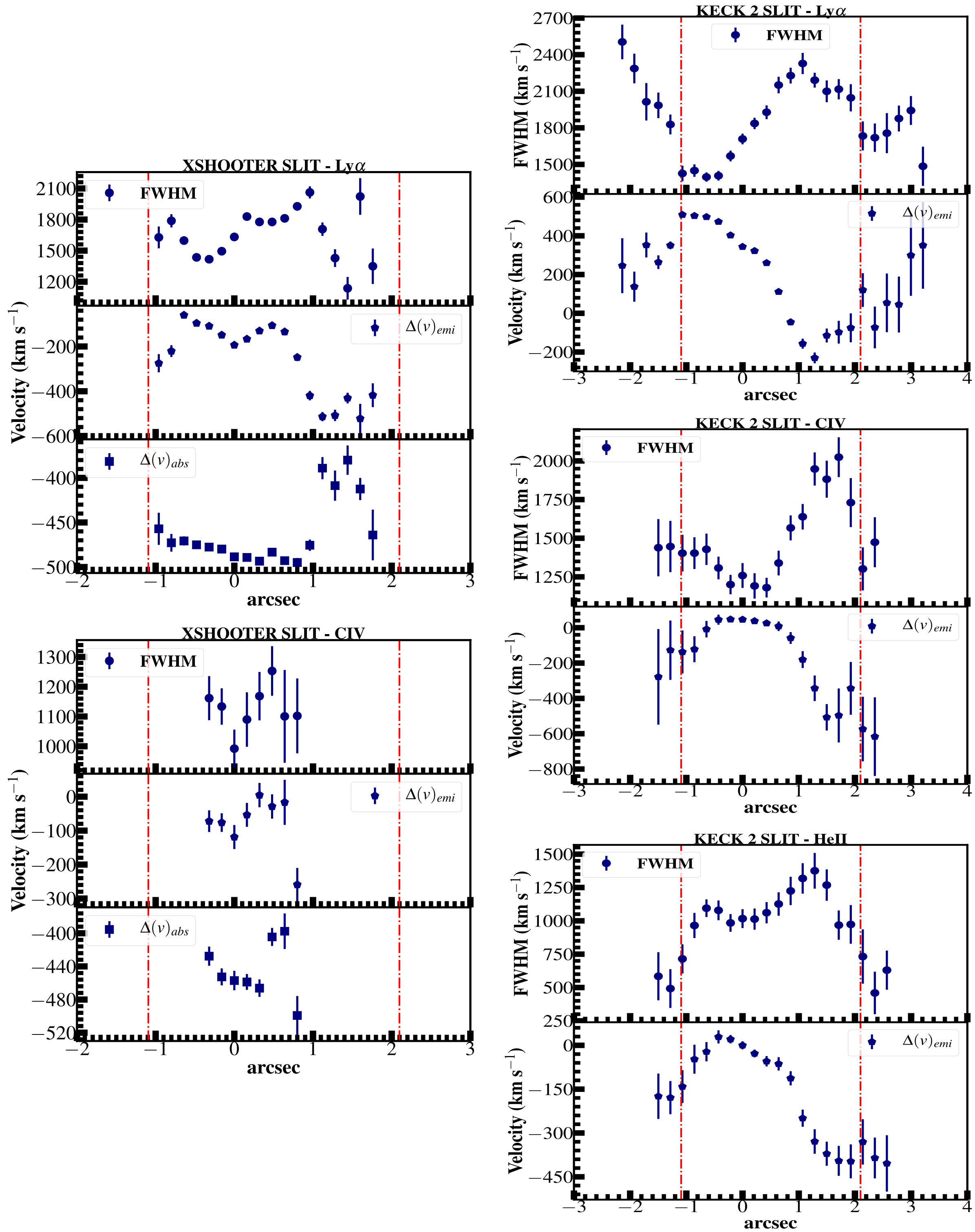

Figure 2.6: Kinematic properties of the MRC 0943–242 radio galaxy extracted from the XSHOOTER SLIT and KECK II long-slit data. We present the velocity dispersion for the emission-lines and velocity offset for the emission and absorption lines as a function of the position along the slit in arc seconds. The red dashed-dot lines represent the positions of the radio hotspots.

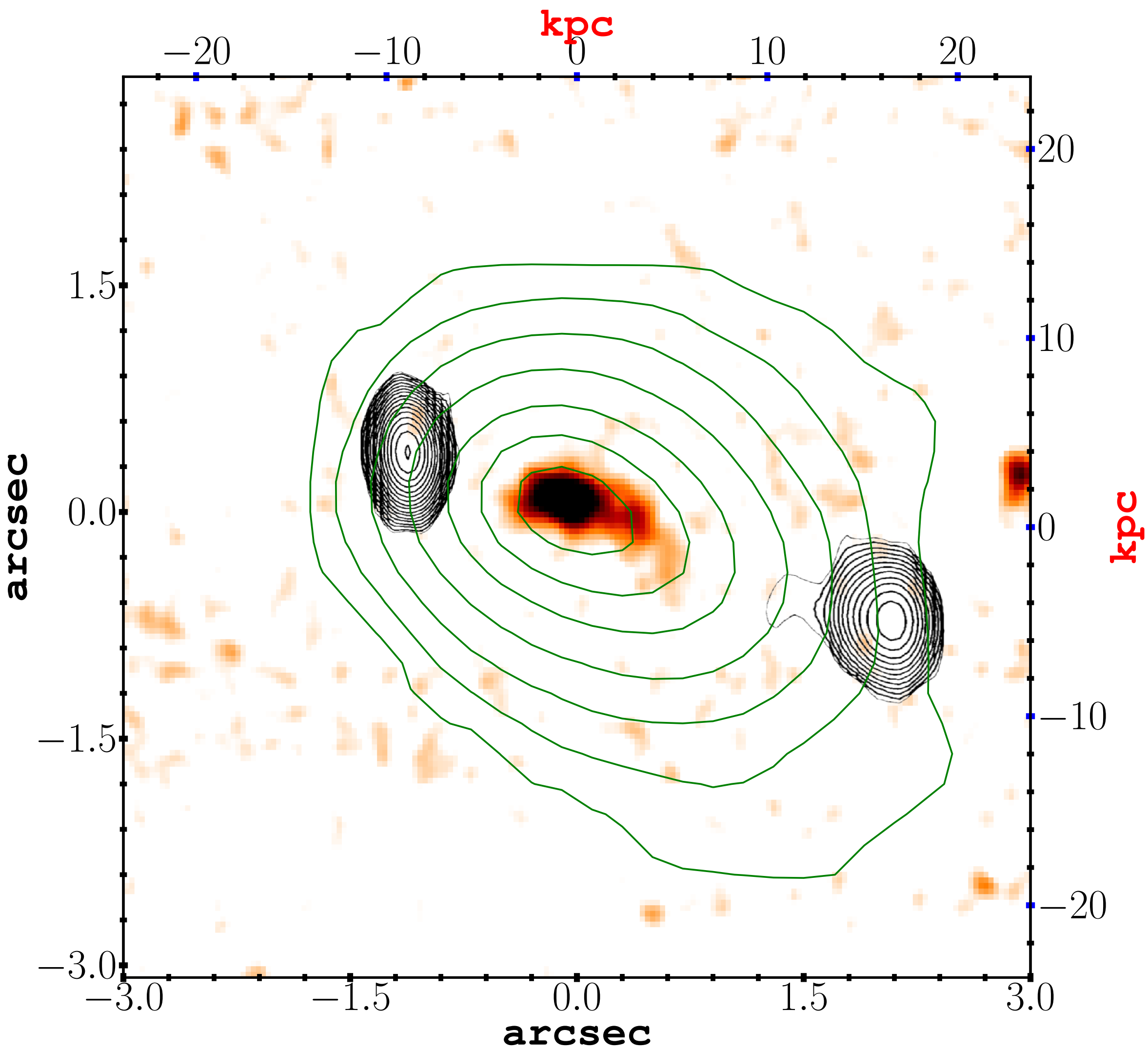

Figure 2.7: A HST NICMOS continuum image of MRC 0943–242 at z = 2.92 with VLA radio contours (black) and Lyα contours (green; see Fig. 2.5a) superimposed.

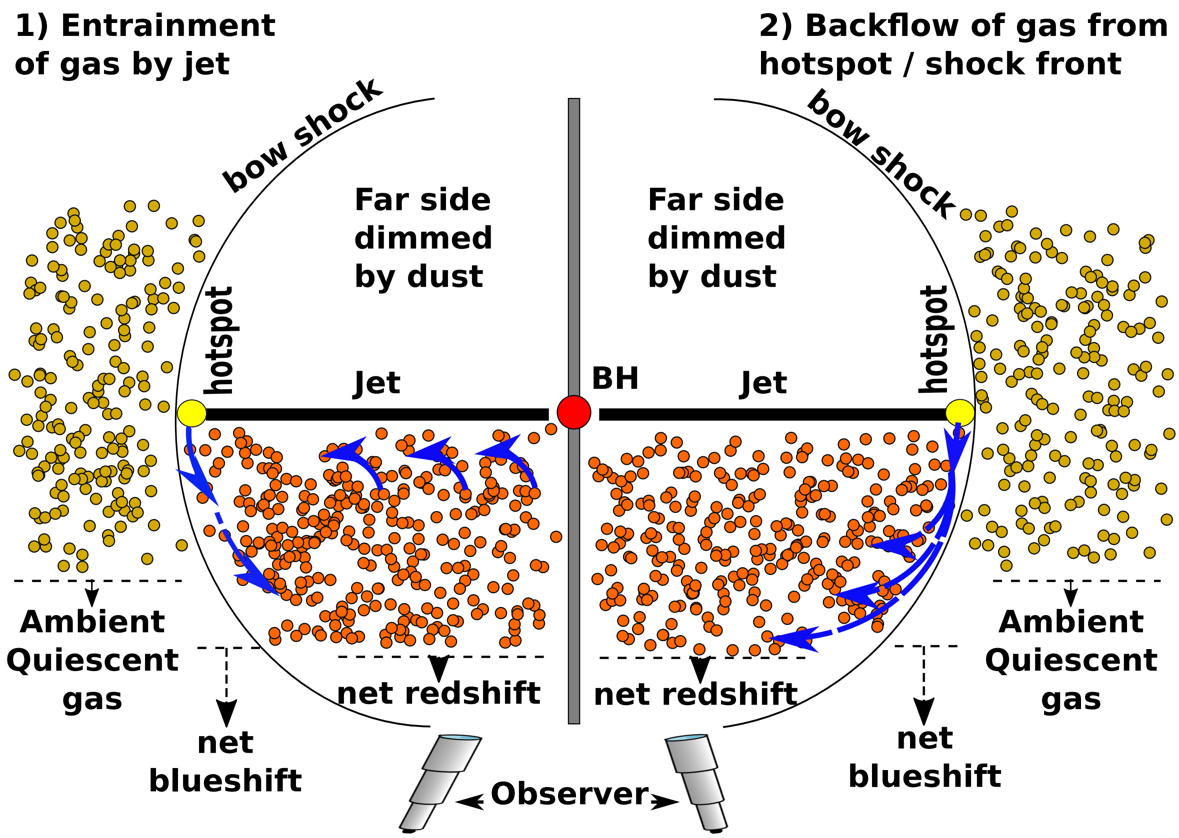

Figure 2.8: Here we show two simple scenarios to explain the emission line kinematics in MRC 0943–242. (1) The relativistic radio jets are produced in the central active nucleus and propagate outward through the host galaxy, terminating in a hotspot that represents the working surface of the jet against the ambient ISM. The radio plasma cools and diffuses/flows laterally away from the hotspot, carrying with it condensations of warm ionized gas which are then seen as localised blueshifted line emission with relatively large FWHM, closely associated with the hotspots. Beyond the radio cocoon, the ambient ISM remains untouched by the jets and thus shows relatively narrow emission lines. The jets entrain gas from the ISM of the galaxy, dragging gas in towards the jet as well as along the velocity vector of the jet. The inward motion of the entrained gas results in a net redshift when the radio jet axis is viewed side-on. (2) As above, but with a backflow of material away from the head of the radio jet, instead of entrainment, producing the observed redshifting of the kinematically perturbed gas. In both cases, the ISM would need to contain a significant quantity of dust, to dim the emission from gas on the far side of the galaxy.

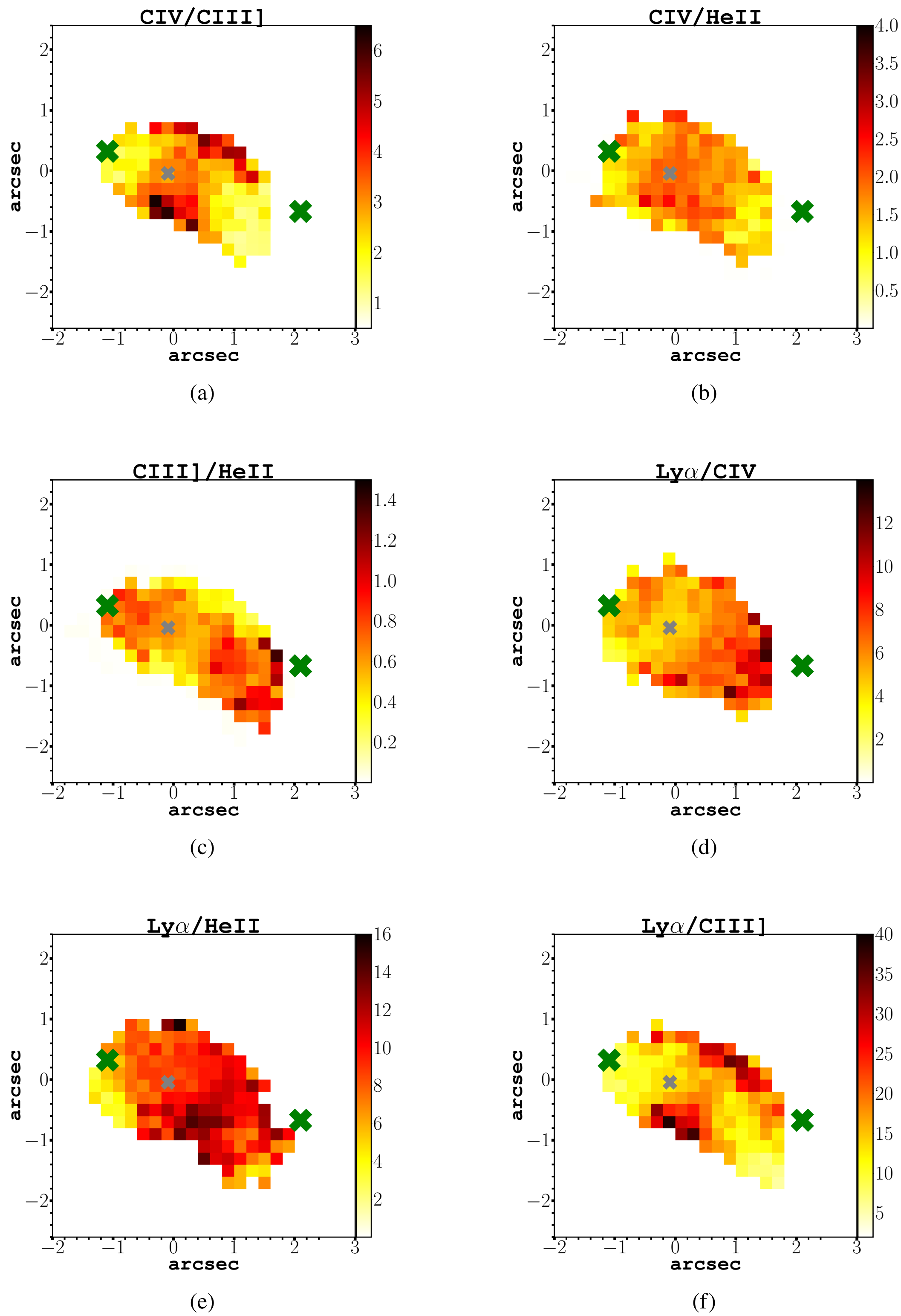

Figure 2.9: Flux ratio maps of the MRC 0943–242. See text for a detailed description of the flux ratio maps. The most remarkable feature in this maps is that the gas close to the locations of the hotspots appear clearly differentiated in several maps, such as C IV/C III], C IV/He II, C III]/He II and Lyα/C III]. The green "X" represent the positions of the radio hotspots and the grey "x" the position of the AGN.

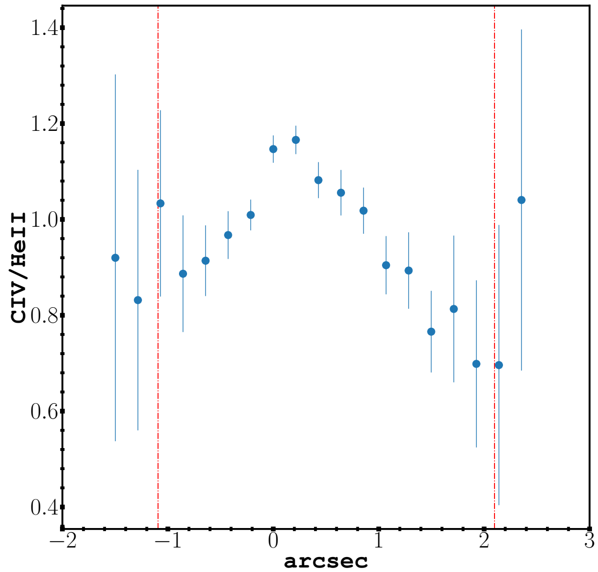

Figure 2.10: Flux ratio of the MRC 0943–242 radio galaxy extracted from the KECK II slit data. The red dashed-dot lines represent the positions of the radio hotspots.

2.6.2 Ionization and metallicity of the extended emission line gas

Our X-SHOOTER spectrum of MRC 0943–242 covers a wide range of wavelength and contains numerous emission lines from various species, making it particularly useful for studying the ionization and chemical abundances in the extended ionized gas. From our ionization model grid (see Sect. 2.5.4), the single model that provides the best overall fit to the X-SHOOTER emission line spectrum is a photoionization model with $U = 0.018$, $\alpha = -1.0$ and gas metallicity $Z/Z_{\odot} = 2.1$. In addition, our best fitting model has $A_V = 0$. Table 2.5 shows the X-SHOOTER emission lines normalised to the flux of HeII λ1640. Our best-fitting model parameters are generally consistent with conclusions obtained from smaller subsets of the UV lines by previous authors (Vernet et al., 2001; Humphrey et al., 2008b; Gullberg et al., 2016).

Although the reduced chi-square is reasonably small (χ^2_ν =2.75) and many line ratios are well reproduced by the model, a number of other line ratios are not well reproduced. In particular, the model produces too low a value of [O III] λ4363 / [O III] λ5007 (see Figure 2.11), indicating that T_e is too low in the model. This could be due to the presence of some shock-heating in the extended gas in addition to the dominant AGN-photoionized gas (see also Tadhunter et al., 1989), as also suggested by Gullberg et al. (2016) based on the strength of C II] relative to C IV, C III] and He II in the integrated MUSE spectrum.

Table 2.5: Comparison of model line ratios with observed line ratios. (1) Emission line ratios. (2) Observed X-SHOOTER line fluxes normalised by He II λ1640. (3) Parameters and relative line fluxes produced by our best-fitting MAPPINGS model. (4) Our best-fitting model using $\alpha = -1.5$ instead of $\alpha = -1.0$. Parameters and relative line fluxes produced by our best-fitting shock models (5) and shock + precursor models (6) extracted from Allen et al. (2008).

Line ratios (1)	Obs. flux (2)	Model 01 (3)	Model 02 (4)	Model 03 (5)	Model 04 (6)
		$U = 0.018$	$U = 0.032$	shocks	shock + prec.
		$\alpha = -1.0$	$\alpha = -1.5$	$v = 225$ km s^{-1}	$v = 725$ km s^{-1}
		$Z/Z_\odot = 2.1$	$Z/Z_\odot = 1.2$	$Z/Z_\odot = 1.0$	$Z/Z_\odot = 1.0$
		$\chi^2_\nu = 2.75$	$\chi^2_\nu = 4.66$	$\chi^2_\nu = 7.15$	$\chi^2_\nu = 6.53$
Lyα $^{(*)}$/HeII	9.90 ± 0.43	11.30	16.56	59.15	28.50
(OVI+CII)/HeII	0.77 ± 0.12	0.31	0.24	4.90	5.70
NV/HeII	0.30 ± 0.06	0.39	0.21	3.01	0.69
CIV/HeII	1.47 ± 0.11	2.14	2.05	6.99	1.48
CIII]/HeII	0.54 ± 0.04	1.24	1.01	1.68	2.21
CII]/HeII	0.27 ± 0.05	0.17	0.08	1.13	2.33
[NeIV]/HeII	0.18 ± 0.05	0.43	0.31	1.00	1.51
MgII/HeII	0.56 ± 0.08	0.50	0.45	2.81	3.58
[NeV]/HeII	0.64 ± 0.06	0.58	0.43	0.48	0.49
[OII]/HeII	2.79 ± 0.15	0.93	0.46	3.45	1.10
[NeIII]/HeII	1.06 ± 0.08	0.69	0.64	1.03	1.12
Hγ/HeII	0.50 ± 0.10	0.17	0.31	0.84	0.44
[OIII]4363/HeII	0.19 ± 0.02	0.11	0.09	0.20	0.68
[OIII]5007/HeII	8.49 ± 0.33	8.79	8.45	2.90	0.95

$^{(*)}$ Lyα was not used in the fitting.

In addition, we notice that O VI+C II, [O II] and C II] are underpredicted in the model relative to our measurements, suggesting the presence of clouds with a substantial range in U within the extended gas sampled by our X-SHOOTER spectrum (e.g. Humphrey et al., 2008b).

The best-fitting model also produces an Hγ/He II λ1640 ratio that is significantly below the observed value. This suggests that the ionizing SED (α=–1.0) may be too hard, or that reddening, for which we have no reliable diagnostic, may be important in this object.

To supplement our analysis and partially illustrate the above results, we also show selected diagnostic diagrams (Figs. 2.11, 2.12, 2.13 and 2.14).

In order to study the spatial variation of the UV emission line ratios, we show in Figs. 2.15 and 2.16 several diagnostics diagrams with UV line ratios measured from the individual spaxels in the MUSE datacube. In these diagrams we use line ratios involving Lyα, C IV, He II and C III] only, due to the narrower spectral range of MUSE and the lower chance of detecting the faint lines in the individual spaxels.

The MUSE spaxels show a substantial dispersion in each of the diagrams (Fig. 2.15 and

Table 2.6: Comparison of model line ratios with observed line ratios. (1) Emission line ratios. (2) Observed X-SHOOTER line fluxes normalised by He II λ1640 using a larger (2.1″) aperture. (3) Parameters and relative line fluxes produced by our best-fitting MAPPINGS model. (4) Our best-fitting model using $\alpha = -1.5$ instead of $\alpha = -1.0$. Parameters and relative line fluxes produced by our best-fitting shock models (5) and shock + precursor models (6) extracted from Allen et al. (2008).

Line ratios	Obs. flux	Model 01	Model 02	Model 03	Model 04
(1)	(2)	(3)	(4)	(5)	(6)
		$U = 0.019$	$U = 0.035$	shocks	shock + prec.
		$\alpha = -1.0$	$\alpha = -1.5$	$v = 200$ km s^{-1}	$v = 750$ km s^{-1}
		$Z/Z_{\odot} = 1.8$	$Z/Z_{\odot} = 1.1$	$Z/Z_{\odot} = 1.0$	$Z/Z_{\odot} = 1.0$
		$\chi^2_\nu = 3.11$	$\chi^2_\nu = 6.44$	$\chi^2_\nu = 7.41$	$\chi^2_\nu = 8.24$
Lyα $^{(*)}$/HeII	7.88 ± 0.26	10.53	16.47	58.65	29.06
(OVI+CII)/HeII	0.87 ± 0.10	0.48	0.31	3.70	4.51
NV/HeII	0.70 ± 0.03	0.47	0.23	3.78	0.33
CIV/HeII	1.21 ± 0.11	2.47	2.25	8.60	2.22
CIII]/HeII	0.55 ± 0.02	1.34	1.10	1.62	1.21
CII]/HeII	0.24 ± 0.01	0.16	0.08	1.14	0.64
[NeIV]/HeII	0.21 ± 0.02	0.45	0.31	1.22	0.28
MgII/HeII	0.42 ± 0.03	0.48	0.45	2.16	2.01
[NeV]/HeII	0.66 ± 0.04	0.63	0.45	0.53	0.34
[OII]/HeII	2.84 ± 0.08	0.84	0.44	3.25	3.02
[NeIII]/HeII	0.99 ± 0.04	0.71	0.85	0.81	1.20
Hγ/HeII	0.38 ± 0.04	0.17	0.31	0.83	0.22
[OIII]4363/HeII	0.27 ± 0.02	0.13	0.10	0.23	0.13
[OIII]5007/HeII	7.97 ± 0.21	8.94	8.65	2.75	8.02

$^{(*)}$ Lyα was not used in the fitting.

Fig. 2.16), with a 'centre of gravity' that corresponds approximately with the position of the X-SHOOTER data point (yellow pentagon).

The distribution of data points in diagrams involving only C IV, He II and C III] is qualitatively consistent with a range in U. Of these ratios, C IV/C III] is likely to be the most reliable indicator of U, and given its large variation (~0.6 dex) we conclude that there is likely to be a large variation in U (or ionization state) throughout the extended ionized halo, as suggested by our analysis of the 1D X-SHOOTER spectrum above. However, we note that exploring the spatial variation in metallicity and ionization parameter using the X-SHOOTER spectrum with a different aperture (2.1″) has only a minor effect on these parameters. From our ionization model grid, we find that the single model that provides the best overall fit to the new aperture shows metallicity and ionization parameter affected by changes <15% when compared with that obtained with a smaller aperture (0.8″)(see Tables 2.5 and 2.6).

We also note the presence of significant scatter perpendicular to the U-sequence loci (see

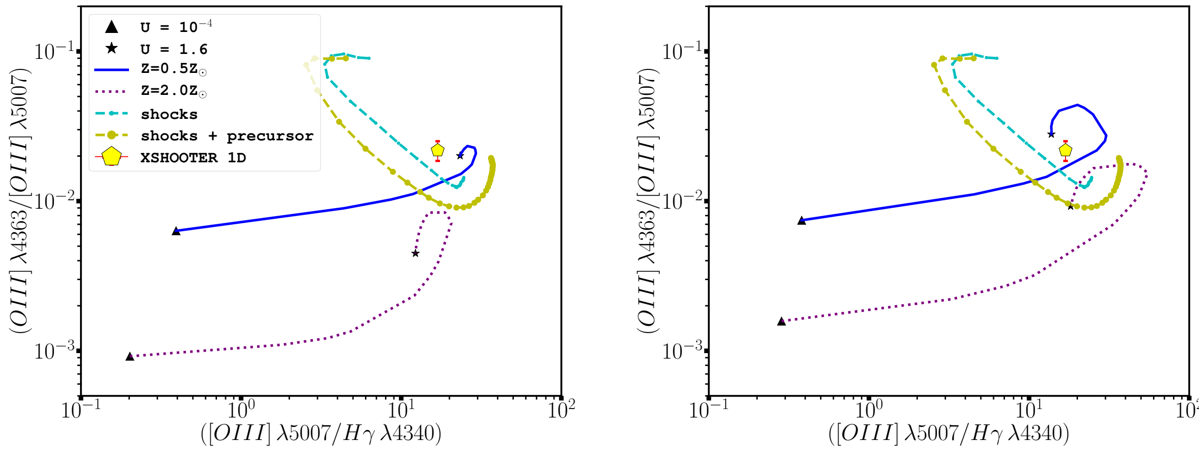

(a) $\alpha = -1.5$ (b) $\alpha = -1.0$

Figure 2.11: Comparison of the observed emission line ratios using integrated spectra from the X-SHOOTER long-slit (yellow pentagon) with photoionization ($0.5Z_\odot$ sequence is represented by the solid blue line and the $2.0Z_\odot$ sequence by the purple dotted line), pure shock models (blue solid circles connected by a dashed line) and the composite shock + precursor models (large yellow solid circles connected by a dashed line). In the case of the photoionization models, we use ionizing continuum power law index α=–1.5 (left side) or α=–1.0 (right side). At the end of each sequence, a solid black triangle corresponds to the initial value of the ionization parameter ($U = 10^{-4}$) and a solid black star that corresponds to the maximum value of the ionization parameter ($U = 1.6$). The pure shock and the composite shock + precursor models are from Allen et al. (2008). Both shock model sequences are characterized by hydrogen density 100 cm^{-3}, magnetic field 100 μ G and velocity covering the range v_s = 100 up to 1000 km s^{-1}.

the flux ratio maps (Fig. 2.9) plotted on the diagrams in Figs. 2.15 and 2.16). We suggest this may be due to metallicity inhomogeneities or local differences in the hardness or source of ionization.

The spaxels with relatively low values of C IV/C III] (black circles), which are also relatively close to the radio hotspots, clearly have different ionization conditions to the rest of the nebula, but degeneracies between models make it challenging to determine the origin of this difference. Although they are consistent with having among the lowest values of U, these spaxels are also close to the shock model loci. Thus, we suggest that the radio source induces a lower ionization parameter where it most strongly interacts with the ISM, perhaps due to compression of gas, or that shock ionization contributes significantly in these specific regions of the Lyα halo.

The Lyα/He II values show a dispersion within the nebula (~0.6 in dex), with most points having lower values than the minimum values produced by the plotted photoionization or shock models. This is likely due to a varying impact of transfer effects across the nebula, but it is not clear whether the observed Lyα flux is being suppressed by resonant scattering due to dust or due to redirection of photons into other lines of sight. Interestingly, the locus of photionization models using α=–1.0 and $Z/Z_{\odot}$=2.0 passes through the cloud of MUSE points in the C IV/C III] vs. Lyα/He II diagram, suggesting that the systematically low Lyα/He II ratios of MRC 0943–242 may be partly due to a relatively hard ionizing SED and relatively high gas metallicity. Unlike the other UV ratios, we find no correlation between Lyα/He II and proximity to the radio hotspots.

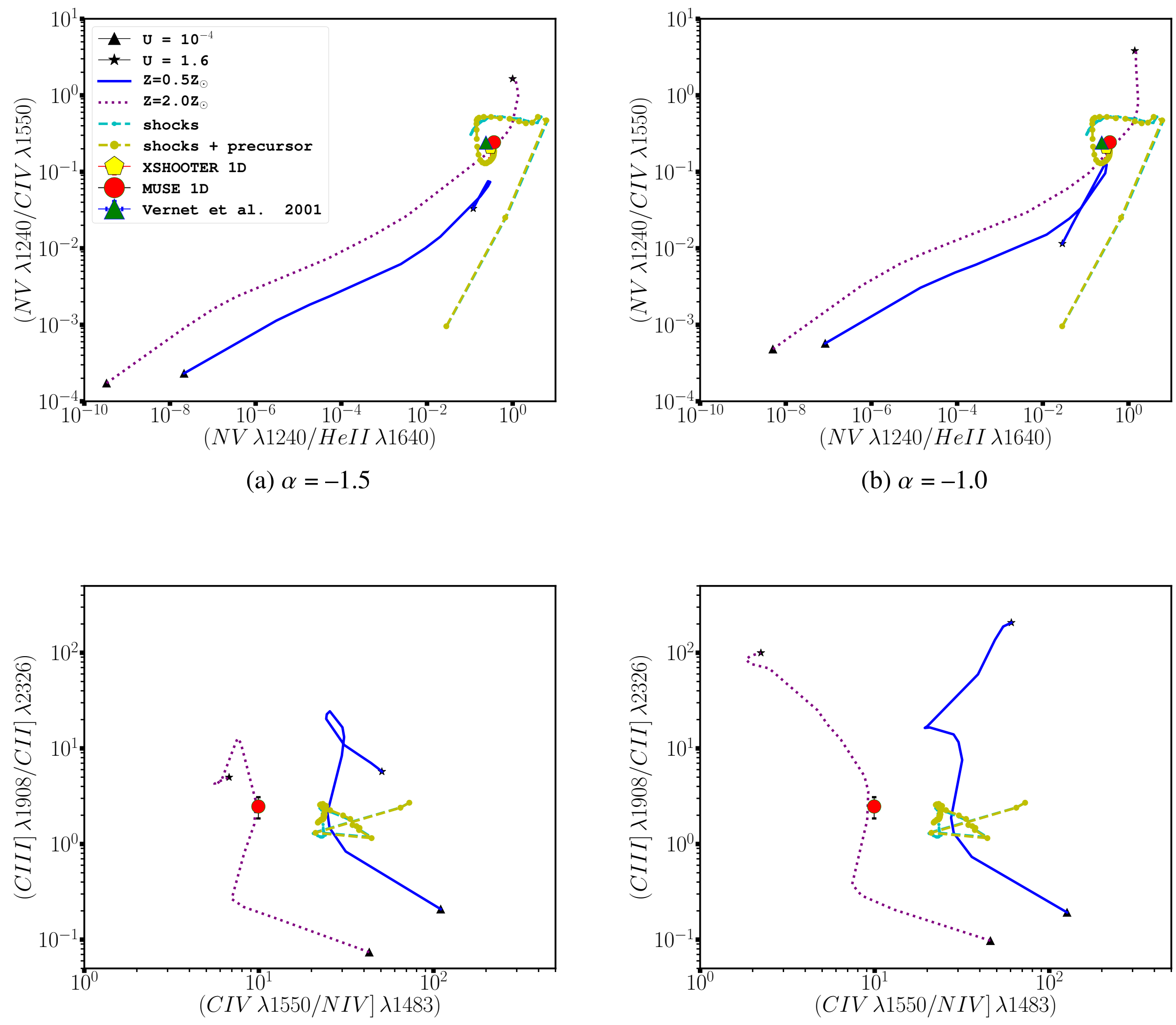

(a) $\alpha = -1.5$ (b) $\alpha = -1.0$

(c) $\alpha = -1.5$ (d) $\alpha = -1.0$

Figure 2.12: Comparison of the observed emission line ratios using integrated spectra from the MUSE IFU (red circle), X-SHOOTER long-slit (yellow pentagon) and KECK II LRIS spectra from Vernet et al. (2001) (green triangle) with photoionization, shocks and the composite shock + precursor models shown. See Fig. 2.11 for more details.

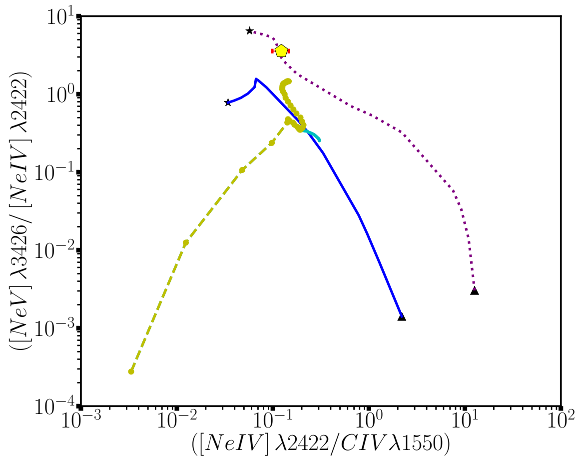

(a) $\alpha = -1.5$

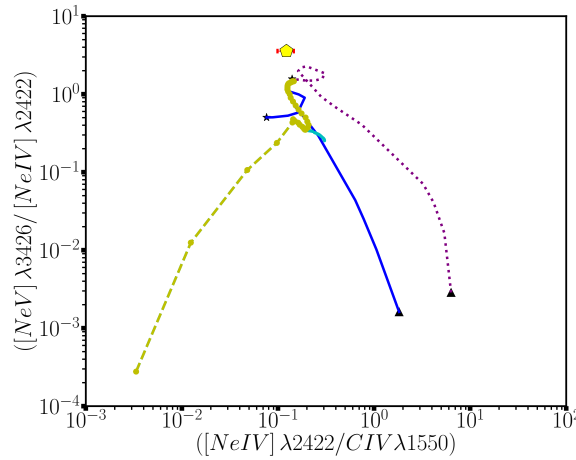

(b) $\alpha = -1.0$

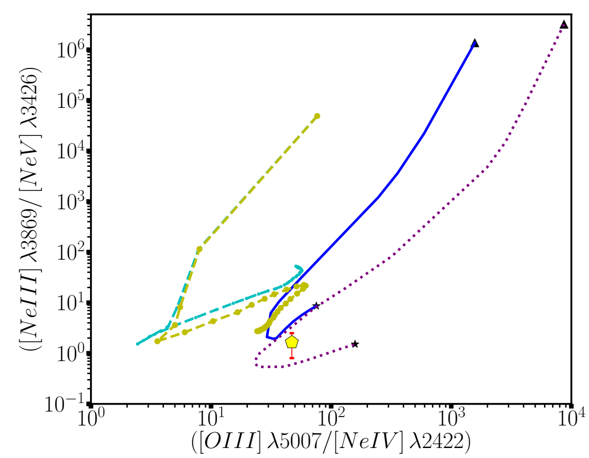

(c) $\alpha = -1.5$

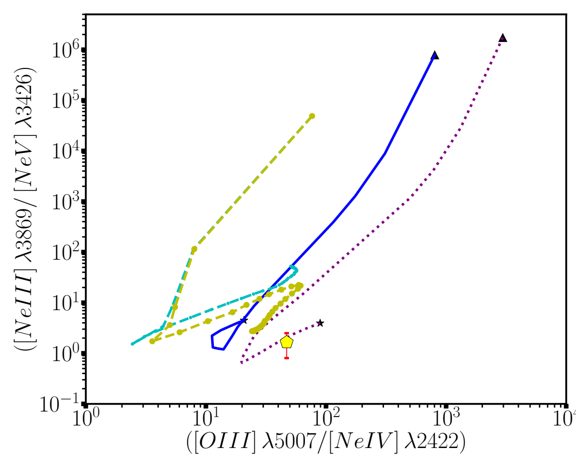

(d) $\alpha = -1.0$

Figure 2.13: Comparison of the observed emission line ratios using integrated spectra from the X-SHOOTER long-slit (yellow pentagon). See Fig. 2.11 for more details.

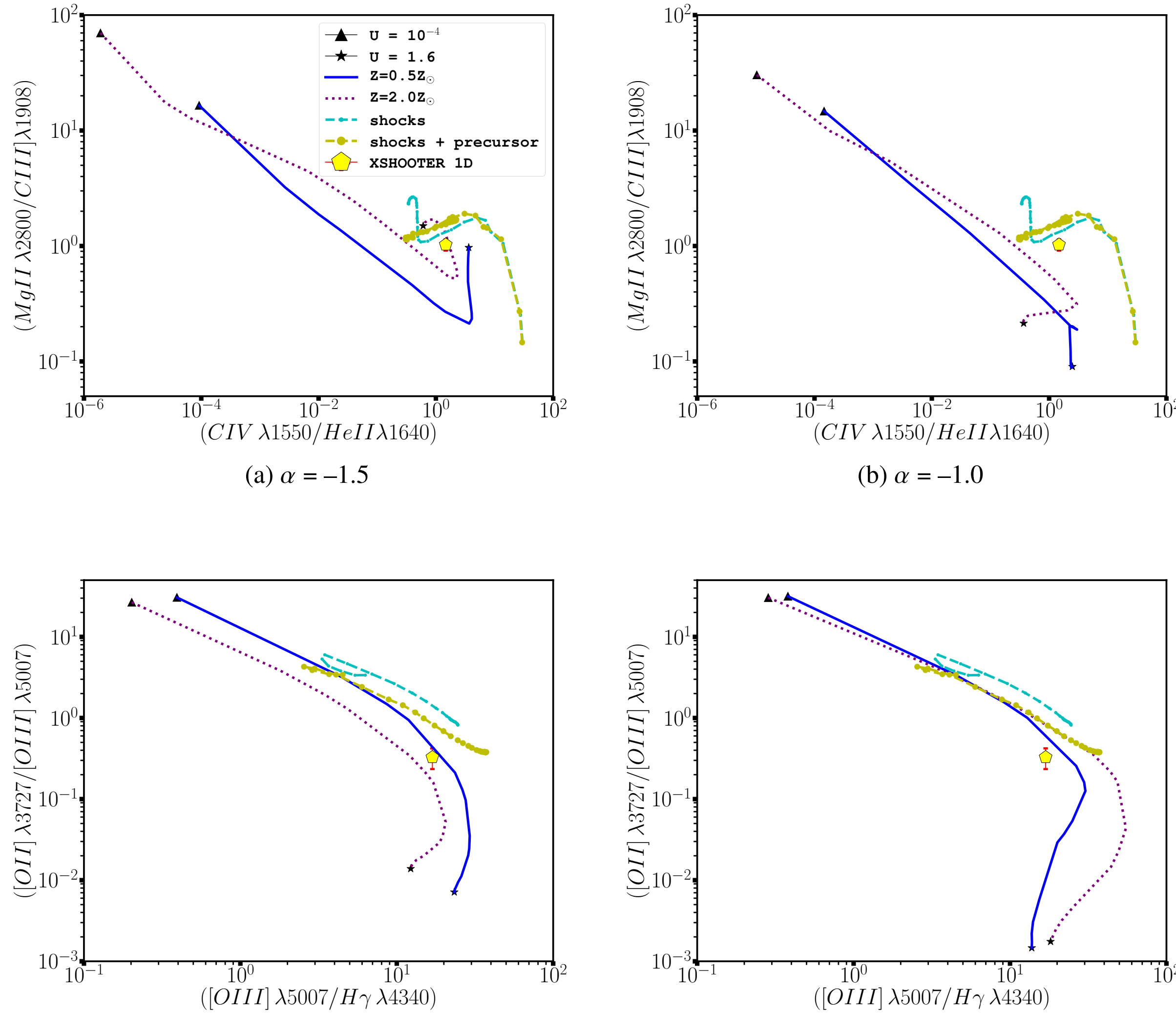

(a) $\alpha = -1.5$

(b) $\alpha = -1.0$

(c) $\alpha = -1.5$

(d) $\alpha = -1.0$

Figure 2.14: Comparison of the observed emission line ratios using integrated spectra from the X-SHOOTER long-slit (yellow pentagon) with photoionization, shocks and the composite shock + precursor models. See Fig. 2.11 for more details.

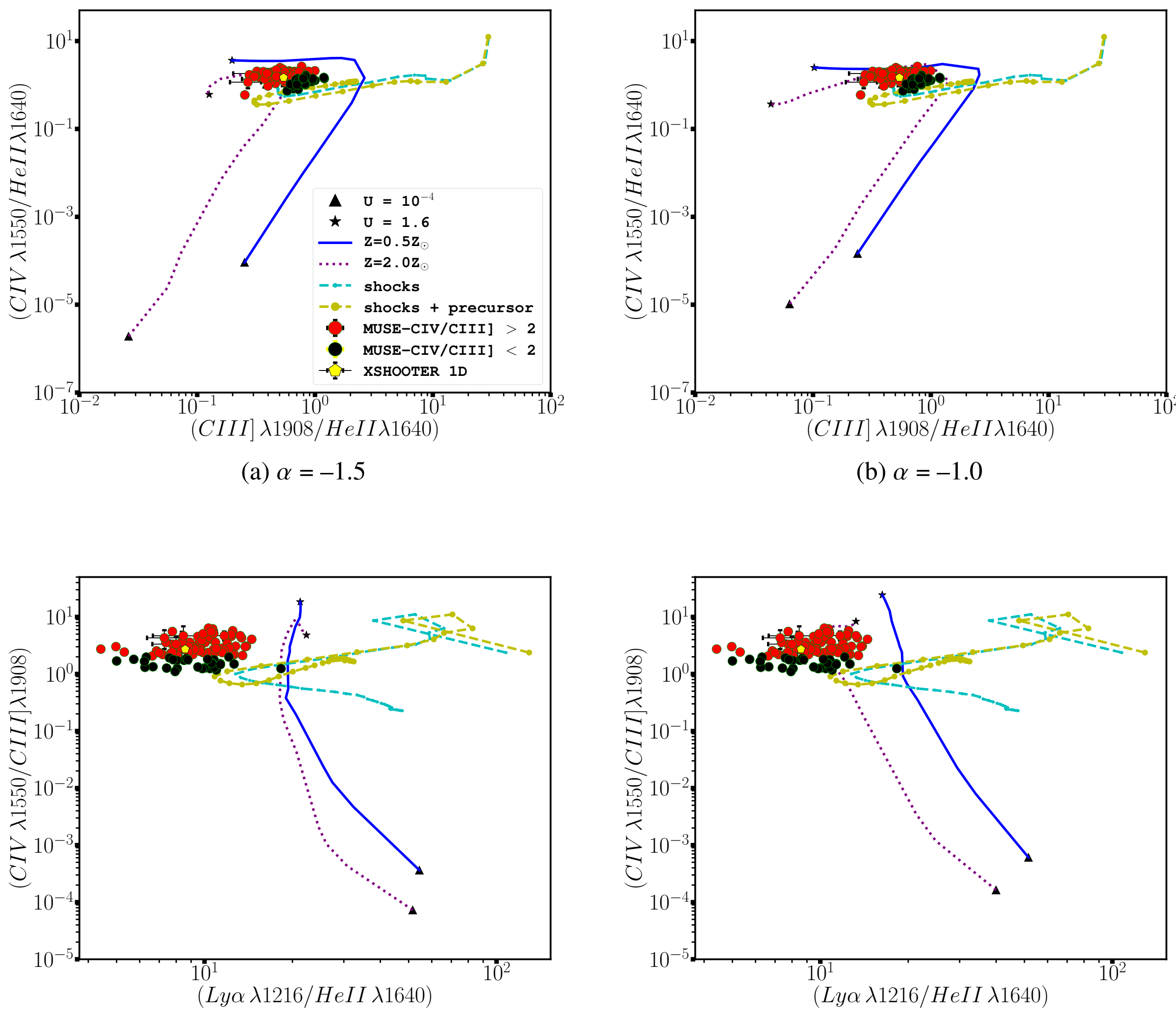

(a) $\alpha = -1.5$ (b) $\alpha = -1.0$

(c) $\alpha = -1.5$ (d) $\alpha = -1.0$

Figure 2.15: Comparison of the observed spatial variation of the MUSE UV emission line ratios with photoionization models ($0.5Z_\odot$ sequence is represented by the solid blue line and the $2.0Z_\odot$ sequence by the purple dotted line), pure shock models (blue solid circles connected by a dashed line) and the composite shock + precursor models (large yellow solid circles connected by a dashed line). In the case of the photoionization models, we use ionizing continuum power law index α=–1.5 (left side) or α=–1.0 (right side). The red circles represent the regions in which C IV/C III] > 2, while the black circles represent that regions with C IV/C III] < 2 which lie close to the positions of the radio hotspots. The yellow pentagon represent the integrated spectrum extracted from the X-SHOOTER data. At the end of each sequence, a solid black triangle corresponds to the initial value of the ionization parameter ($U = 10^{-4}$) and a solid black star that corresponds to the maximum value of the ionization parameter ($U = 1.6$). The pure shock and the composite shock + precursor models are from Allen et al. (2008). Both shock model sequences are characterized by hydrogen density 100 cm^{-3}, magnetic field 100 μ G and velocity covering the range v_s = 100 up to 1000 km s^{-1} .

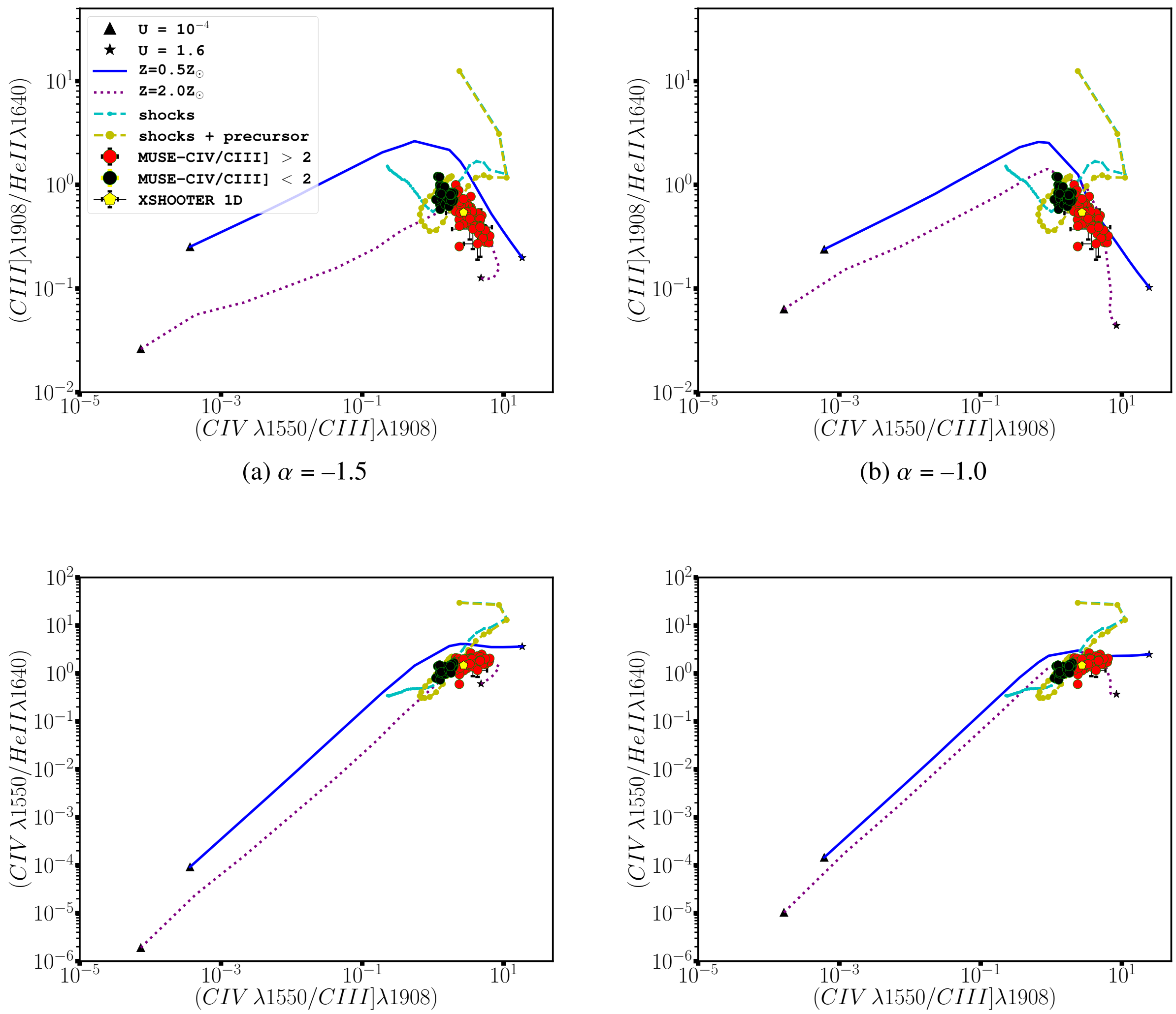

(a) $\alpha = -1.5$

(b) $\alpha = -1.0$

(c) $\alpha = -1.5$

(d) $\alpha = -1.0$

Figure 2.16: Comparison of the observed spatial variation of the MUSE UV emission line ratios with photoionization models ($0.5Z_\odot$ sequence is represented by the solid blue line and the $2.0Z_\odot$ sequence by the purple dotted line), pure shock models (blue solid circles connected by a dashed line) and the composite shock + precursor models (large yellow solid circles connected by a dashed line). In the case of the photoionization models, we use ionizing continuum power law index α=–1.5 (left side) or α=–1.0 (right side). See Fig. 2.15 for more details.

Table 2.7: Low-ionization absorption lines extracted from the Keck II spectrum at the redshift of the main absorber. (1) Absorption lines; (2) Rest-frame wavelength; (3) Oscillator strength; (4) Rest-frame equivalent width; (5) Column density.

Line	λ_{rest} (Å)	f	W_{rest} (Å)	N (cm^{-2})
(1)	(2)	(3)	(4)	(5)
O I	1302.2	0.05	< 5	$< 1.5 \times 10^{15}$
C I	1277.2	0.10	< 4	$< 8.0 \times 10^{14}$
C I	1328.8	0.06	< 3	$< 8.2 \times 10^{14}$
C I	1560.3	0.08	< 2	$< 3.0 \times 10^{14}$
C I	1656.9	0.14	< 2	$< 1.5 \times 10^{14}$
C II	1334.5	0.13	< 4	$< 5.0 \times 10^{14}$

2.6.3 Nature of the extended H I Absorber

2.6.3.1 H column density

One of the key findings from our analysis of the Lyα velocity profile of MRC 0943–242 is the strong degeneracy between the column density (N(H I)) and the Doppler width (b) of the main absorber, with a broad range in N(H I) yielding a reasonable fit to the data, and with the best-fitting located near each end of this range: log N(H I/cm^{-2}) = 15.20 and 19.63. The latter value is in agreement with the fits obtained in previous studies of MRC 0943–242 (e.g. Röttgering et al., 1995a; Binette et al., 2000; Jarvis et al., 2003; Gullberg et al., 2016). None of the previous studies identified the N-b degeneracy or the second, low column density fit. Clearly, this degeneracy has implications for our understanding of the properties of the absorbing gas where they are derived from N(H I).

As argued by previous authors, detection of C IV in the main absorber indicates that the gas is at least partially ionized and contains some metal enriched gas, but the column ratio between C IV with H I does not allow a straightforward determination of the ionization structure or metallicity of the gas (e.g. Binette et al., 2000; Jarvis et al., 2003). In addition, we can calculate a lower limit on the total H column density by assuming $N_C \geqslant N_{C\,IV}$ and appropriate limits for the column ratio N_C/N_H. Assuming $N_C \geqslant N_{C\,IV}$ and C/H $\leqslant$ 3 times Solar, we obtain $N_H \gtrsim 5{\times}10^{17}$ cm^{-2}. Note that this limit is not dependent on the value of N(H I).

2.6.3.2 Ionization structure and metallicity

To obtain additional constraints on its chemical and ionization properties, we have searched our deep Keck II spectrum for low-ionization absorption lines at the redshift of the main absorber. Our analysis has not revealed any detection of additional absorption lines, and we show the most relevant 3σ upper limits in table 2.7. To convert equivalent width W_λ to column density

N, we use

$$N = \frac{1.13 \times 10^{20} W_{\lambda,0}}{f \lambda_0{}^2}\, cm^{-2} \qquad (2.1)$$

where f is the oscillator strength, $W_{\lambda,0}$ is the rest-frame equivalent width (in Å) and λ_0 is the rest-frame wavelength of the line (in Å) (e.g. Humphrey et al., 2013a).

Interestingly, the fact that $N_{C\,IV}$ is at least twice $N_{C\,I}$ indicates that the gas is mostly ionized, while $N_{C\,II}$ / $N_{C\,IV}$ < 1.3 indicates that the ionized zone itself is highly ionized. By extension, hydrogen is also likely to be mostly ionized, with the total H column density likely to be more than three times that of H I, independently of which value of $N_{H\,I}$ we adopt.

Provided the H I absorption is dominated by gas in a neutral zone, it can then be assumed that $N_{C\,I}/N_{H\,I}$ ~ C/H and $N_{O\,I}/N_{H\,I}$ ~ O/H, which would allow constraints to be placed on the gas chemical abundances. In the extreme case where $N_{H\,I}$ = 4.3×10^{19} cm^{-2}, we would then obtain abundance ratios C/H < $0.013 Z_{\odot}$ and O/H < $0.076 Z_{\odot}$, meaning the absorber would be extremely metal poor. Conversely, if the H I absorption is due to gas in an ionized zone with low, but non-negligible H I fraction, i.e., if the absorber is 'matter bounded', then the assumption that $N_{C\,I}/N_{H\,I}$ ~ C/H and $N_{O\,I}/N_{H\,I}$ ~ O/H does not necessarily hold.

2.6.3.3 Size, shape and mass

The most likely geometry for the main absorber is a shell or bubble of gas surrounding the host galaxy and at least part of its Lyα emitting halo (Binette et al., 2000). The simplest way to obtain a lower limit to the radius of the absorbing structure is to determine the maximum observed offset between the projected position of the nucleus, and the most distant pixel or spaxel where the absorber is detected. Measuring from the MUSE data cube, Gullberg et al. (2016) obtained a maximum offset from the nucleus of $\gtrsim$ 60 kpc, and we adopt this value as a lower limit to the radius of the shell.

In Fig. 2.17a we show a map of the line of sight velocity of the main H I absorber, measured from the MUSE data. The absorption feature shows a gradient in velocity, with a significant decrease in blueshift outward from the (projected) central region of the galaxy (see also Fig. 2.6). The presence of this trend is independent of whether we adopt the log N(H I/cm^{-2}) = 15.20 or 19.63 fit to the H I absorber. Similarly, the C IV absorption doublet also appears to show a radial decrease in its blueshift (Fig. 2.17b). This result is consistent with what one would expect if the absorber is an expanding shell centred on the radio galaxy: At larger projected distances from the centre, the bulk velocity vector of the shell material is at a larger inclination to the line of sight, and thus appears to be less blueshifted. As a consistency check on the radius of the shell, we can also estimate its radius using the velocity gradient of the HI absorption feature.

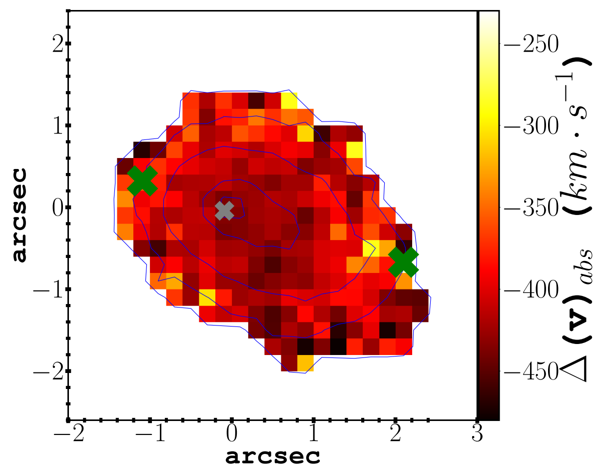

(a)

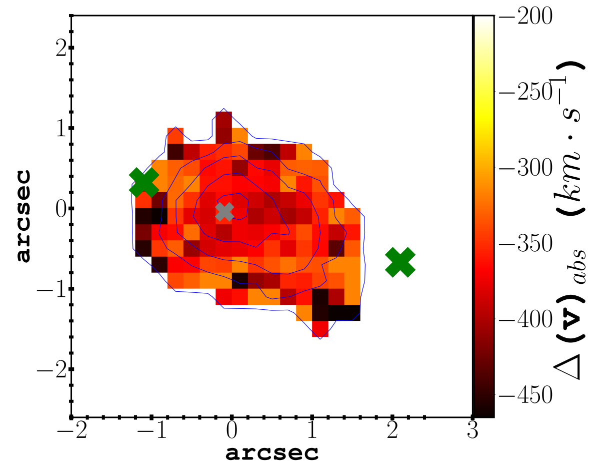

(b)

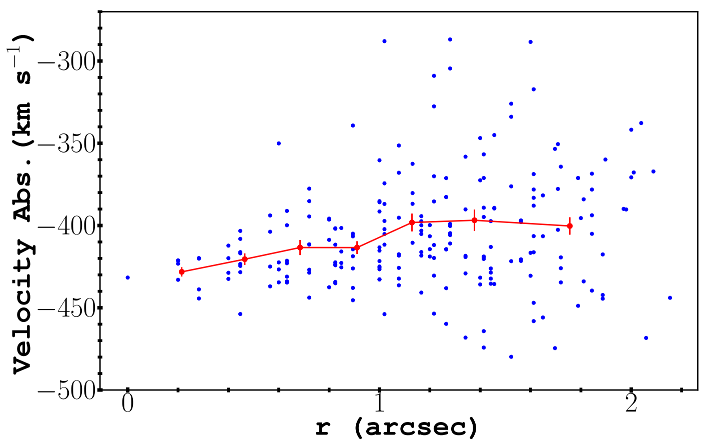

(c)

Figure 2.17: (a) Velocity offset map of the main absorber in the Lyα profile extracted from the MUSE IFU data. The velocity offset was measured relative to the He II emission line at the centre of the radio galaxy. The map also shows the contour levels of the emission line intensity recovered by the fitting procedure. Contour levels: (0.3,1.3,3.8,12.5,16.8)$\times 10^{-16}$ erg cm^{-2} s^{-1} arcsec^{-2}. (b) Velocity offset map for the absorption trough in C IV profile extracted from MUSE IFU. The velocity offset was measured relative to the He II emission line at the centre of the radio galaxy. The map also shows the contour levels of the emission line intensity recovered by the fitting procedure. Contour levels: (0.5,1.0,2.0,3.5,4.3)$\times 10^{-16}$ erg cm^{-2} s^{-1} arcsec^{-2}. The green "X" represent the positions of the radio hotspots and the grey "x" the position of the AGN. (c) The diagram shows the velocity offset of the main Lyα absorption as a function of the projected distance from the centre of the galaxy. The black points are the individual pixels, and the red points are bins in distance, with their 1σ error bars. Evaluating the strengths of correlation between the velocity offset of the main absorber and the projected distance using Spearman's rho and t-distribution, we find $\rho = 0.24$ with a p-value = 0.0003 (for unbinned data) and $\rho = 0.86$ with a p-value = 0.014 (for binned data).

Assuming the shell is spherical and using the velocity gradient of 30 km s^{-1} measured between $r = 0$ to $r = 14$ kpc (see Fig. 2.17a and Fig. 2.17c) we obtain $R \sim 38$ kpc, which is much smaller than the value derived by Gullberg et al. (2016) using the maximum observed spatial offset of the absorber (60 kpc), perhaps indicating that the shell is not spherically symmetric.

Assuming the absorber is a spherical shell with uniform column density, and assuming its covering factor is 1 based on the fact that the absorption feature is black at its centre, we calculate the mass of the absorber using the expression

$$M_H \gtrsim 3.6 \times 10^9 (R/60\,kpc)^2 (N_H/10^{19} cm^{-2}) M_\odot, \tag{2.2}$$

where R is the radius of the absorption system in kpc and N_H is the H column density in cm^{-2}. Assuming $R \gtrsim 60$ kpc and $N_H > 5\times10^{17}$ cm^{-2}, we obtain the hard lower limit log ($M_H/M_\odot$) $\gtrsim$ 8.3.

Clearly, because this is a lower limit, the mass of the shell could be even more massive than log ($M_H/M_\odot$) $\gtrsim$ 8.3. Indeed, if we were instead to use the value from our high column density fit (log N(H I/cm^{-2}) = 19.63) and assume that the absorber is entirely neutral, we would then obtain log (M_H/M) $\gtrsim$ 10.2. If one were to assume the gas is partially ionized would lead to an even higher limit.

2.6.4 On the evolutionary status of MRC 0943-242

With a stellar mass of $\sim 10^{11.2}$ $M_\odot$ (Seymour et al., 2007), MRC 0943–242 is remarkably massive for its redshift of 2.92. Significant star formation activity is present in the host galaxy ($\sim$200 $M_\odot$ yr^{-1}) and in companion galaxies ($\sim$1400 $M_\odot$ yr^{-1}; Gullberg et al. 2016), and the powerful active nucleus appears to be subjecting its associated extended gas reservoir to substantial radio- and quasar-mode feedback. In the long-run, this feedback activity may quench the modest star formation activity found in the host galaxy, but our kinematic results suggest that processes related to the radio-mode feedback are drawing gas deeper into the potential well of the galaxy, and we speculate this could give rise to a short-lived enhancement in star formation and the fueling of the AGN. Indeed, this would be consistent with the reported anti-correlation between the luminosity of young stellar populations in HzRGs and the age of their radio sources (Humphrey et al., 2006).

The very high metallicity of the ionized gas within the radio galaxy demonstrates the precence of an already highly enriched gas, compatible with the scenario that this system could evolve into a passive spheroidal system characterised by supersolar metallicity (e.g. Lonoce et al. 2015 and references therein; see also Vernet et al. 2001).

Interestingly, the high gas metallicity appears inconsistent with the scenario of smooth accretion of pristine gas, because in that scenario the gas metallicity should be low (e.g. Dekel et al., 2009). Although there is evidence for filamentary gas accretion into MRC 0943–242, the filamentary material appears to be dusty and metal-enriched (Gullberg et al., 2016) and thus is likely to have been stripped from companion galaxies, rather than being low metallicity gas from the cosmic web. In fact, there appears to be no convincing evidence for smooth accretion of pristine gas in MRC 0943–242, although we cannot rule out the presence of faint, filamentary accretion structures of the kind detected near the $z = 3.1$ radio galaxy MRC 0316–257 (Vernet et al., 2017).

In summary, we suggest that we are witnessing MRC 0943–242 after the bulk of gas accretion has taken place, and the galaxy is now moving towards transformation into a spheroidal galaxy where the AGN feedback will probably, ultimately quench the star-formation.

2.7 Conclusions

Making use of observations from MUSE, X-SHOOTER and other instruments we have studied the kinematic, chemical and excitation properties of the giant Lyα emitting halo and the giant H I absorber associated with the $z = 2.92$ radio galaxy MRC 0943–242. The main conclusions of this study are summarized as follows:

- We find clear evidence for jet gas interactions affecting the kinematic properties of the Lyα nebula of MRC 0943–242. The MUSE datacube reveals a region of kinematically turbulent gas with relatively high FWHM extending from the nucleus out to the positions of the radio hotspots, where we see the most extreme kinematic properties, beyond which the gas has rather more quiescent kinematics in agreement with the long-slit study of Villar-Martín et al. (2003). The gas most closely associated with the radio hotspots shows a blueshift relative to other regions, consistent with jet-induced outflows. However, at smaller radii the emission line gas shows a relative redshift, even compared to the kinematically quiscent gas, which we suggest might signal the presence of a feedback-driven *inflow* due to gas being pulled inwards as part of the entrainment process, and/or a backflow of material from the radio hotspots.

- We have computed a grid of photoionization models, to which we have added shock ionization models from the literature (Allen et al., 2008), and have searched for the model that best reproduces the complete ensemble of emission line relative fluxes measured from our X-SHOOTER spectrum. We find that a photoionization model with moderate ionization parameter ($U = 0.018$), a relatively hard ionizing SED ($\alpha = -1.0$) and high gas metallicity ($Z/Z_{\odot} = 2.1$) provide the best overall fit. However, we note that the [O III]

λ4363 / [O III] λ5007 flux ratio is not well reproduced by this model, suggesting the presence of some shock-heating in the extended gas. In addition, the apparent inability to simultaneously reproduce lines of all ionization states suggests the presence of clouds with a substantial range in U, a result that is validated by our analysis of the 2D ionization properties.

- We find a substantial range in ionization level across the object, with a clear spatial correlation between the radio hotspots and UV emission line ratios indicative of relatively low ionization which we suggest may be due to shock heating and/or the compression of gas by the radio source. We also find evidence for a lower Lyα escape fraction in regions unaffected by radio mode feedback, and speculate scenarios that may explain this result: (i) reduction of dust in the kinematically perturbed regions due to jet-driven shocks (e.g. Villar-Martín et al., 2001); (ii) greater velocity overlap between emitting and absorbing gas phases in the kinematically quiescent regions (e.g. Tenorio-Tagle et al., 1999); (iii) the presence of an optically thick shell of gas encasing the expanding radio cocoon (e.g. Binette et al., 2006).

- Our Lyα/He II flux ratio map reveals a large range of values across the nebula, with most spaxels having values lower than the ionization in our grid. We attribute this to an inhomogeneity in the impact of transfer effects such as quenching by dust and/or the scattering of Lyα photons into different sight-lines.

- We identify and explore a strong degeneracy between column density and Doppler width of the strong, blueshifted HI Lyα absorber. We have been able to obtain a reasonable fit to the absorption feature across the range log N(H I/cm^{-2}) = 15.20 and 19.63, with the best-fitting occurring near the extreme ends of this range. Independently of our fits to Lyα, we use $N_{\mathrm{C\,IV}}$ to obtain a lower limit to the total H column density of $N_H > 5\times10^{17}$ cm^{-2}. Given the lower limit of the spatial extent of the H I obtained with the absorber velocity map, we assume a spherical shell of gas with radius $\gtrsim$60 kpc obtained by Gullberg et al. (2016). Assuming $N_H > 5\times10^{17}$ cm^{-2}, the shell would have log $(M_H/M_\odot) \gtrsim 8.3$.

Chapter 3

Detection of large scale Lyα absorbers perpendicularly to the radio axis of high-redshift radio galaxies using SOAR

3.1 Abstract

We present an investigation of the properties of the extended Lyα halo and the large-scale H I absorbing structures associated with 5 high-redshift radio galaxies at z > 2, using the Goodman long-slit spectrograph on the SOAR telescope[1], with the slit placed at large angles (>45°) to the radio axis, to study regions that are unlikely to be illuminated by the active nucleus. Spatially extended Lyα emission is detected with large line widths (FWHM = 1000 – 2500 km s^{-1}), which although impacted by resonant scattering, is suggestive of turbulent motion. We find a correlation between higher blueshifts and higher FWHM, which is an indication that radial motion dominates the bulk gas dynamics perpendicular to the radio axis, although we are unable to distinguish between outflow and infall scenarios due to the resonant nature of the Lyα line. Extended, blueshifted Lyα absorption is detected in the direction perpendicular to the radio axis in three radio galaxies with minimum spatial extents ranging from $\gtrsim$ 27 kpc to $\gtrsim$ 35 kpc, supporting the idea that the absorbing structure covers the entire Lyα halo, consistent with being part of a giant, expanding shell of gas enveloping the galaxy and its (detected) gaseous halo.

[1]Based on observations obtained at the Southern Astrophysical Research (SOAR) telescope, which is a joint project of the Ministério da Ciência, Tecnologia, Inovação e Comunicações (MCTIC) da República Federativa do Brasil, the U.S. National Optical Astronomy Observatory (NOAO), the University of North Carolina at Chapel Hill (UNC), and Michigan State University (MSU).

The work presented in this chapter was published in Monthly Notices of the Royal Astronomical Society in November 2018 (Silva et al. 2018a; MNRAS, 481:1401–1415)

3.2 Introduction

High-redshift radio galaxies (hereafter HzRGs; z > 2) are among the most spectacular objects in the sky. Producing prodigious luminosities (e.g., $L_{500MHz} > 10^{27}$ W Hz^{-1}; De Breuck et al. 2010 and references therein) from tiny volumes, with radiation spread over a broad range of frequencies, HzRGs are noteworthy in providing us with a unique opportunity to investigate the formation and evolution of massive galaxies and active galactic nuclei (hereafter AGN).

These galaxies are among the most massive galaxies, with stellar masses up to $\sim 10^{12}$ $M_{\odot}$ (e.g. De Breuck et al., 2001; Seymour et al., 2007; Hatch et al., 2009; De Breuck et al., 2010; Hatch et al., 2013; Nesvadba et al., 2017b), often with evidence for significant star formation rates (up to ~ 1400 $M_{\odot}$ yr^{-1}; Ogle et al. 2012; Seymour et al. 2012; Rocca-Volmerange et al. 2013; Hatch et al. 2013; Drouart et al. 2014). HzRGs are also commonly associated with spatially extended Lyα halos, with luminosities up to $\sim 10^{45}$ erg s^{-1}, which are gas rich ($M_{HI} \sim 10^{9-11}$ $M_{\odot}$) and extend over tens or even a few hundred kpc (Fosbury et al., 1982; di Serego Alighieri, 1988; McCarthy et al., 1990b; McCarthy, 1993; van Ojik et al., 1997; Pentericci et al., 1998; Francis et al., 2001; Reuland et al., 2003; Villar-Martín et al., 2003; Sánchez and Humphrey, 2009; Humphrey et al., 2013a; Cantalupo et al., 2014; Swinbank et al., 2015; Borisova et al., 2016; Cai et al., 2017; Arrigoni Battaia et al., 2018). These large scale Lyα structures usually show a clumpy and irregular morphology (Reuland et al., 2003) often aligned with the radio jets (McCarthy et al., 1995) that exert significant feedback onto the surrounding intergalactic medium (hereafter IGM; Villar-Martín et al. 2003; Nesvadba et al. 2006; Humphrey et al. 2006; Ogle et al. 2012). Generally, the halos can be divided into two distinct kinematic components: quiescent and perturbed. The quiescent component shows kinematics with full width at half maximum (hereafter FWHM) < 1000 km s^{-1} and no clear relationship with the radio jets (van Ojik et al., 1996; Villar-Martín et al., 2002, 2003; Sánchez and Humphrey, 2009). This component has been reported to be a common feature of the Lyα halos being detected across the full spatial extent of the halos (e.g. Villar-Martín et al., 2003). In some HzRGs, the quiescent component seems to be infalling towards the central regions of the host galaxy (e.g. Humphrey et al., 2007; Villar-Martín et al., 2007b; Humphrey et al., 2013a; Roche et al., 2014; Silva et al., 2018b), which may be explained by a scenario whereby cold gas streams fall onto the dark matter halos along the cosmic web (e.g. Goerdt et al., 2010) or by an alternative scenario in which gaseous debris falls back into the host galaxy after a feedback 'blowout' (e.g Humphrey et al., 2013a). The perturbed component usually shows an irregular gas kinematics with FWHM > 1000 km s^{-1} (van Ojik et al., 1996; Villar-Martín et al., 2003; Humphrey et al., 2006; Silva et al., 2018b). With clear spatial association with the radio structure in some HzRGs, the perturbed component provides evidence of gas that has been disturbed by the passage of the radio jets, and which may be outflowing (see Nesvadba et al., 2006, 2008a; Morais et al., 2017). As such, the Lyα halos allow us to probe the evolution of massive galaxies during a phase of significant feedback, black hole growth and, in many cases, star formation. The study of the properties of these halos provides keys to understand how hosts of powerful radio galaxies form and evolve.

In addition, studies have shown that some HzRGs show spatially resolved H I absorption features in their Lyα emission line profiles (e.g. Röttgering et al., 1995a; van Ojik et al., 1997; Binette et al., 2000; Jarvis et al., 2003; Binette et al., 2006; Humphrey et al., 2008a, 2013b; Moyano et al., 2015; Swinbank et al., 2015; Gullberg et al., 2016; Silva et al., 2018b), which are thought to be produced by a giant shell of H I gas enveloping the Lyα emitting region, and which appears to be expanding or outflowing due to feedback activity (see Binette et al., 2006; Humphrey et al., 2008a; Swinbank et al., 2015; Silva et al., 2018b). For example, in the case of the main extended absorber associated with MRC 0943–242 (z = 2.92), Silva et al. (2018b) found a significant radial evolution in the H I absorber's line of sight velocity which they argued is consistent with it being an expanding shell with a radius of at least several tens of kpc. With H I column densities in the range $\sim 10^{14-20}$ cm^{-2}, observations with the slit placed along the radio axis have shown that strong absorbers (N(H I) > 10^{18} cm^{-2}) extend over the full spatial extent of the Lyα emission, although the properties of the absorption does not always remain constant over the full spatial extent (van Ojik et al., 1997; Binette et al., 2006). Although the precise nature and origins of these large scale absorbing structures are not well understood, they are clearly relevant for understanding issues such as feedback, the dispersion of metals through the interstellar medium (hereafter ISM) of massive galaxies and into the surrounding IGM, as well as the escape of Lyα and ionizing photons from HzRGs.

Previous studies of the Lyα halos and H I absorbers associated with HzRGs have focused mainly on the relatively high surface brightness emission regions aligned with the radio jet axis, where the jet-gas interactions and the ionizing radiation of the AGN are expected to have their greatest impact (e.g. Rush et al., 1997; De Breuck et al., 2000b; Taniguchi et al., 2001; De Breuck et al., 2001; Villar-Martín et al., 2003; Nesvadba et al., 2006; Humphrey et al., 2006, 2008b, 2009; Nesvadba et al., 2017a,b). By studying the extended Lyα emission regions that are located significantly away from the radio jet axis, it may be possible to obtain a more complete picture of the extended gaseous environment of HzRGs (e.g. Gullberg et al., 2016; Morais et al., 2017; Vernet et al., 2017; Silva et al., 2018b), allowing us to investigate questions such as what produces the Lyα emission when it is not illuminated by the AGN, and whether the impact of radio mode feedback is global or instead confined to the radio axis. Likewise, the 2-dimensional spatial distribution of the H I absorbers is also poorly known, with spatial information predominantly coming from long slit spectra where the slit was placed along the radio axis (e.g. van Ojik et al., 1997). A handful of H I absorbers have now been studied using IFU spectroscopy (e.g. Humphrey et al., 2008a; Swinbank et al., 2015; Silva et al., 2018b), in each case showing that the absorber is also extended perpendicularly to the radio axis, consistent with the idea that the absorbing gas is part of a giant shell enveloping the Lyα emitting region. However, similar observations of a larger number of HzRGs are needed to confirm that this is a general property of this class of absorbers.

This paper aims to characterize the properties of the extended Lyα halos and the large-scale H I absorbing structures in the direction perpendicular to the radio axis of HzRGs, adding new information about the global properties of the extended ionized gas and extended absorbers associated with HzRGs. The paper is organized as follows. In § 2.4, we describe the sample selection, observations and data reduction. In § 2.5, we discuss our data analysis methods. In § 2.3,we present the results of our study. In § 2.6, we discuss the gas dynamics of the extended Lyα halo and the nature of the extended H I absorbers. In § 2.7, we give a brief summary concluding our results. Throughout this paper we assume $\Omega_\Lambda = 0.713$, $\Omega_m = 0.287$ and $H_\circ$ = 69.3 km s^{-1} Mpc^{-1} (Hinshaw et al., 2013).

3.3 Sample selection and SOAR observations

We selected 5 Lyα-bright, steep spectrum HzRGs from the list of De Breuck et al. (2000a) within a redshift range of $2.16 < z < 2.76$. This redshift range ensured that Lyα, C IV λ1549 and He II λ1640 fell within the wavelength coverage of the spectrograph. Our sample (see Table 2.1) is characterized by galaxies with relatively bright Lyα emission (1.95×10^{43} to 2.91×10^{44} erg s^{-1}, measured through a long slit aligned along the radio axis) of powerful radio sources (log(P_{325}) ranging from 35.48 to 36.46 erg s^{-1} Hz^{-1}), and covers a large range in radio source diameter (< 2.5 to 196 kpc: De Breuck et al. 2000a and references therein.).

The observations were performed on 2014 September and on 2015 April, using the Goodman High Throughput Spectrograph (GTHS; Clemens et al. 2004) on the Southern Astrophysical Research (SOAR) 4.1 m telescope during the commissioning of the instrument under the program SO2014B-013 (PI: R. N. Guimarães) in classical mode, and SO2015A-024 (PI: R. N. Guimarães) in remote mode. The observations were set to use the blue camera combined with the 600l/mm grating which allowed us to obtain a wavelength range of $\sim$ 3500 – 6200 Å. This wavelength range allows, for some objects, the detection of important diagnostic lines such as N V $\lambda\lambda$1239,1243, C IV $\lambda\lambda$1548,1551 and He II λ1640 along with Lyα λ1216. For all observations, on-chip binning of 2 × 2 (spatial x spectral) was used, resulting in a pixel size of 0.3″. In addition, the slit widths were set to be 1.03″ and 1.68″ (see Table 3.1). The instrumental profile (FWHM) was estimated using the mean of the Gaussian FWHMs measured for a number of unblended arc-lamp and the night-sky lines over the whole spectral range of a wavelength-calibrated spectrum, which gave us an instrumental profile FWHM of 3.9 Å (or 266 km s^{-1}) and 8.0 Å (or 560 km s^{-1}), respectively. The seeing was obtained by reconstructing the spatial profile of the seeing disk along the slit using a non-saturated star in images taken before or after the observation of the science target.

The exposure time for each of the five radio galaxies was set in intervals of 1800s, totaling at the end of the program in 20 hours of observation. The slit alignment was chosen to be perpendicular to the radio jets (see Table 3.1) as determined from radio images in the literature (e.g. Carilli et al., 1997; Pentericci et al., 1997), for 3 out of 5 targets. The position angle of the radio axis was determined by simply measuring the angle made by the brightest radio hotspot on either side of the nucleus. This assumes that the hotspots are well aligned with the radio jets, which is generally the case in HzRGs where jets have been detected in HzRGs (e.g. Carilli et al., 1997; Pentericci et al., 1997).

In the case of MRC 0030–219, whose radio source is unresolved (<0.3″or <2.5 kpc), we have used the parallactic angle for the slit position. Although it is not clear whether the extended emission in our spectrum of this target is influenced by the ionizing radiation field of the AGN, we can be fairly confident that the extended gas is not affected by interaction with the radio source.

In the case of 4C–00.54 we have used an angle perpendicular to the UV-optical emission in Hubble Space Telescope image of the galaxy (e.g. Pentericci et al., 1997, 2001), rather than placing the slit perpendicular to the large scale radio axis. While most HzRGs show a close correlation between the position angles of the UV-optical emission and the radio source (e.g. Chambers et al., 1987; McCarthy et al., 1987), 4C–00.54 is somewhat unusual in showing a large misalignment between the UV-optical emission and the large-scale radio emission. This substantial ~45° misalignment has been suggested to be the result of precession of the radio jets, where the radio axis defined by positions of the radio hotspots would represent the axis of the AGN $\gtrsim$ 1 Myr earlier than the currently observed nuclear activity (Pentericci et al., 1997). Unfortunately, existing radio observations do not allow us to definitely test this scenario due to the lack of detection of extended nuclear radio jets. Nevertheless, we have adopted the position angle of the UV-optical emission as the most probable current orientation of the AGN and radio jets. We do not expect this decision to have a significant effect on our data analysis or interpretation, because even in the extreme case where the inner radio source has the same position angle as the outer radio hotpsots, our slit position angle would still be at a large angle

Table 3.1: Details of the sample and log of the observations. (1) Objects. (2) Redshift. (3) Maximum angular size of the radio source in arcseconds. (4) Maximum angular size of the radio source in kpc using the cosmology adopted in this paper. (5) Lyα luminosity. (6) Date of the observation. (7) On target integration time. (8) Projected linear scale per angular scale. (9) Position Angle (East of North). (10) Slit width. (11) Spectral resolution.

Object	Redshift	Size	Size	L(Lyα)	Date	T_{exp}	Scale/″	P.A.	Slit width	FWHM
		(″)	(kpc)	(erg s^{-1})		(sec)	(kpc/″)	(^{o})	(″)	(km s^{-1})
(1)	(2)	(3)	(4)	(5)	(6)	(7)	(8)	(9)	(10)	(11)
MRC 0030–219	2.17	< 0.3	< 2.5	1.95×10^{43}	2014-09-(25–27)	6×1800	8.46	175	1.03	266
MRC 0406–244	2.44	7.3	61	2.31×10^{44}	2014-09-(25–27)	6×1800	8.30	30	1.03	266
4C–00.54	2.37	23.5	196	1.28×10^{44}	2015-04-(20–21)	10×1800	8.34	90	1.68	560
PKS 1138–262	2.16	11.4	97	5.06×10^{43}	2015-04-20	9×1800	8.47	360	1.68	560
TN J0920–0712	2.76	1.4	11	2.91×10^{44}	2015-04-21	9×1800	8.06	210	1.68	560

(~45°) to the radio jets.

The data reduction was performed with IRAF. The raw spectra were bias subtracted, flat-fielded, wavelength calibrated using Hg-Ar arc lamp spectra, and then sky subtracted. In all cases, the 1σ uncertainty in the wavelength calibration is $\leq$ 2.1 A ($\leq$ 140 km s^{-1}). The uncertainty in the wavelength calibration was estimated by calculating the median of the difference between the theoretical and the observed wavelength of the emission lines of the arc lamp spectra and also of the night-sky emission lines. In addition, flux calibration was carried out with the spectrophotometric standard stars LTT 1020, LTT 377, LTT 1778, EG 274 and LTT 6248. Finally, the spectra were corrected for Galactic extinction using IRAF'S DEREDDEN task, assuming the extinction curve of Cardelli et al. (1989).

3.4 Data Analysis

3.4.1 Line profile fitting

We created a PYTHON routine to fit the emission and absorption line parameters, with Gaussian and Voigt profiles being used to model the emission and absorption lines, respectively. The routine minimizes the sum of the squares of the difference between the model and data using the LMFIT algorithm (Newville et al., 2014). The analysis was applied first to a 3″ aperture centred on the HzRG, and then applied to the 2D spectrum at each position (pixel) along the slit, where the signal to noise ratio (S/N) of the emission line profile (based on the total flux) is $\geqslant$ 7.

The Lyα profile was parametrized using a single emission (Gaussian) kinematic component for those HzRGs which show no H I absorption features (i.e. MRC 0030-219 and 4C-00.54), with a single absorption Voigt profile added for the three HzRGs which show clear H I absorption (i.e. MRC 0406–244, TN J0920–0712 and PKS 1138–262).

For the emission doublets, two Gaussians were used, with the two double components constrained to have equal FWHM, fixed wavelength separation and a fixed flux ratio (e.g., $R_{N\,V} = F_{\lambda 1239} / F_{\lambda 1243} = 2.0$ and $R_{C\,IV} = F_{\lambda 1548.2} / F_{\lambda 1550.8} = 2.0$)[2]. No significant C IV absorption features were detected in our data, but the S/N and spectral resolution are insufficient to place scientifically useful upper limits on the column density of C IV.

As a non-resonant recombination line, He II is expected to provide a more reliable determination of the systemic velocity of a HzRG than Lyα, N V or C IV, which can be susceptible to absorption and radiative transfer effects that can result in line broadening and velocity shifts. Following Villar-Martín et al. (2003), we use the nuclear He II to define the fiducial systemic velocity of each HzRG, with the exception of MRC 0030–219 where we instead use Lyα due to non-detection of He II.

The kinematic properties of the extended gas were determined using the fitting routine already mentioned, from where we obtained the FWHM and the velocity offset for the emission and absorption lines, at each spatial position along the slit.

In Table 3.2, we show the emission lines detected for each radio galaxy along with the parameters from the best fits. In addition, in Table 3.3 we show the best fit parameters for the Lyα absorption. In Figures 3.1 to 3.5, we show (i) the 2-D spectra of the Lyα spectral region, which were smoothed using a Gaussian with kernel = 3.0 pixels (or 0.9″); (ii) the spatial variation of the flux of the Lyα emission line; (iii) Lyα spatial profile compared with the seeing; (iv) the 1-D spectra of the Lyα profile; (v) the spatial variation of FWHM corrected for the instrumental broadening; (vi) the spatial variation of velocity offset relative to our fiducial systemic velocity; (vii) the FWHM as a function of the velocity offset of Lyα; (viii) the spatial variation of the flux of the He II emission line (the radio galaxy 4C–00.54 was the only one that provided a sufficient S/N at each spatial position along the slit); (ix) the Lyα/He II flux ratio for the radio galaxy 4C–00.54; (x) the spatial variation of the velocity offset for the extended H I absorber when detected and (xi) the spatial profile of the H I column density compared with the seeing.

3.4.2 Spatial extent constraints using the seeing

In order to investigate whether the Lyα halos detected in our sample are spatially extended along the slit, we have compared the Lyα spatial profile with the seeing profile reconstructed from stars in images taken immediately before or after the observation of the science target (see

[1]The doublet ratio for both emission lines ranges from 2:1 in the optically thin case to 1:1 in the optically thick case. We adopted the optically thin case, but using the optically thick case did not result in significant changes to the recovered kinematic properties.

Table 3.2: Rest-frame UV emission lines properties. (1) Object name. (2) Detected line species. (3) Rest wavelength. (4) Observed wavelength. (5) Line flux. (6) Line width. (7) Velocity shift with respect to fiducial systemic velocity.

Object	Line	λ_{rest} Å	λ_{obs} Å	Line Flux ($\times 10^{-16}$ erg cm^{-2} s^{-1})	FWHM (km s^{-1})	Δv (km s^{-1})
(1)	(2)	(3)	(4)	(5)	(6)	(7)
MRC 0030–219	Lyα	1215.7	3854.5 ± 0.3	7.06 ± 0.52	1102 ± 62	-43 ± 25*
MRC 0406–244	Lyα	1215.7	4161.1 ± 0.2	21.07 ± 0.85	1827 ± 44	-124 ± 13
	C IV	1548.2,1550.8	5278.1 ± 2.0, 5296.8 ± 2.0	1.54 ± 0.42	1445 ± 332	-763 ± 115
	He II	1640.4	5610.3 ± 1.1	1.93 ± 0.49	1359 ± 313	-311 ± 59
4C–00.54	Lyα	1215.7	4095.4 ± 0.1	19.84 ± 0.54	1037 ± 22	152 ± 9
	N V	1238.8,1242.8	4168.2 ± 2.4, 4181.6 ± 2.4	1.44 ± 0.38	2279 ± 545	-219 ± 173
	C IV	1548.2,1550.8	5210.7 ± 3.2, 5218.9 ± 0.9	3.22 ± 0.52	1059 ± 139	-132 ± 52
	He II	1640.4	5522.2 ± 0.4	2.80 ± 0.40	999 ± 131	7 ± 22
PKS 1138–262	Lyα	1215.7	3846.7 ± 0.4	14.07 ± 0.78	2289 ± 86	-95 ± 31
	C IV	1548.2,1550.8	4890.5 ± 2.9, 4907.8 ± 2.9	0.96 ± 0.28	2081 ± 520	-614 ± 178
	He II	1640.4	5187.4 ± 1.8	0.85 ± 0.20	1451 ± 257	-215 ± 103
TN J0920–0712	O VI	1031.9,1037.6	3874.3 ± 0.6,3894.8 ± 0.7	1.58 ± 0.24	738 ± 87	-179 ± 46
	Lyα	1215.7	4564.2 ± 0.1	46.78 ± 0.89	1775 ± 22	-180 ± 7
	N V	1238.8,1242.8	4650.3 ± 2.0, 4665 ± 2.0	1.02 ± 0.27	1934 ± 467	-237 ± 127
	C IV	1548.2,1550.8	5807.7 ± 1.6, 5820.7 ± 0.5	3.70 ± 0.40	958 ± 84	-438 ± 83
	He II	1640.4	6161.0 ± 0.7	2.16 ± 0.26	903 ± 80	-3 ± 32

(*) We used the nuclear Lyα to define the fiducial systemic velocity of the radio galaxy MRC 0030–219.

Humphrey et al. 2015 and Villar-Martín et al. 2016 for more details of this methodology). The flux of a non-saturated star was extracted by simulating the slit width used for the spectroscopic observation of the science targets (see Table 2.1). The sky background was then removed from the stellar spatial profile.

In Figures 3.1c to 3.5c, we show the spatial profile of the Lyα emission along with the spatial profile of the seeing. We measured the FWHM ($\mathrm{FWHM}_{source} \pm \Delta\mathrm{FWHM}_{source}$) of the spatial profile of the Ly-alpha line by fitting a single Gaussian. If the seeing has FWHM′ ± ΔFWHM′, we assume that the source is spatially unresolved when

$$FWHM_{source} \leq FWHM' + \Delta FWHM' + \Delta FWHM_{source}. \tag{3.1}$$

In this case, the right hand side of this inequality will be used as an upper limit for the intrinsic FWHM. For a resolved source, we estimate the intrinsic FWHM by subtracting the seeing FWHM from the observed FWHM in quadrature.

3.5 Results for individual objects

3.5.1 MRC 0030–219

3.5.1.1 Previous results

In the z = 2.17 radio galaxy MRC 0030–219 the radio source consists of a single compact component with maximum angular size < 0.3″(or < 2.5 kpc in the adopted cosmology) and has a steep radio spectrum ($\alpha \approx$ -1.0; Carilli et al. 1997), as revealed by VLA observations. Optical spectroscopy observations from the Cerro Tololo 4 m Telescope revealed strong UV emission lines such as Lyα, C IV and He II (McCarthy et al., 1990a). The Lyα emission line has a rest equivalent width W_{λ}^{rest} = 174 Å and luminosity L(Lyα) = $10^{43.66}$ erg s^{-1} (McCarthy et al., 1990a).

3.5.1.2 Results from SOAR

Figure 3.1a reveals the spatially compact Lyα emission of MRC 0030–219. Figure 3.1b shows the spatial variation of the Lyα flux, with this emission being detected further to the NW direction. In Figure 3.1d, we also show the integrated 1-D spectrum of the Lyα profile. Figures 3.1e and 3.1f show the spatial variation of the FWHM and velocity offset of the Lyα emission line. The line width varies in the range FWHM = 800 – 2500 km s^{-1}. Within a radius of ≤ 1″ of the nucleus, Lyα shows FWHM < 1400 km s^{-1}, increasing to 1600 – 2500 km s^{-1} at radii of ≥ 1″. The spatially integrated Lyα emission line appears blueshifted from the systemic velocity with velocity offset -43 ± 25 km s^{-1}. In order to investigate the possible correlations between the FWHM and the velocity offset (see Fig. 3.1g), we use the Spearman correlation (ρ) and the t-distribution (p-value), which indicates a positive relationship between the FWHM and velocity curve of the Lyα emission with ρ = 0.78 and p-value = 7.6×10^{-3}. The kinematic properties will be discussed in §3.6.1.

The Lyα spatial profile with FWHM = 1.62 ± 0.07″ is dominated by a central compact source (see Fig. 3.1c), which appears barely resolved in the central regions compared with the seeing (1.60 ± 0.02″). Correcting for seeing broadening in quadrature, we infer $FWHM_{obs}$ = 0.54 ± 0.09″ or 4.6 ± 0.7 kpc. In addition, the variation seen in the kinematic properties of the radio galaxy (Figures 3.1e and 3.1f), in the outer parts of the Lyα profile at ≥ 1″ from the centroid also suggests that it may be barely resolved. None of the other UV emission lines are found to be extended in this spectrum.

MRC 0030–219

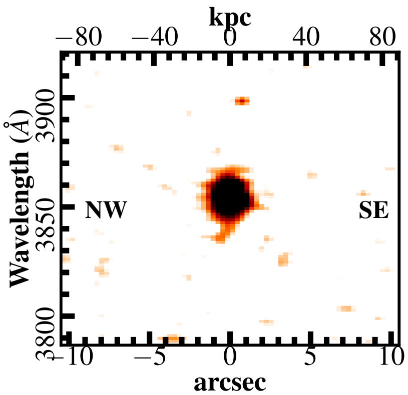

(a) Lyα 2-D spectrum

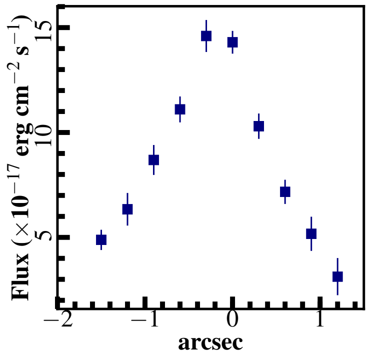

(b) Lyα Flux

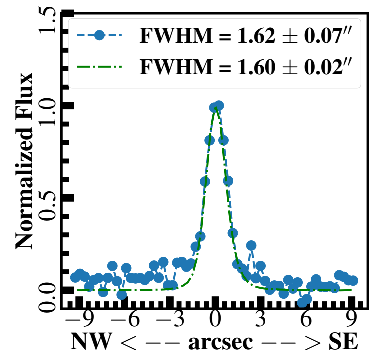

(c) Lyα Source *vs.* Seeing

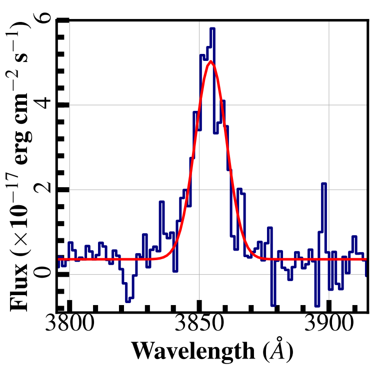

(d) Lyα 1-D spectrum

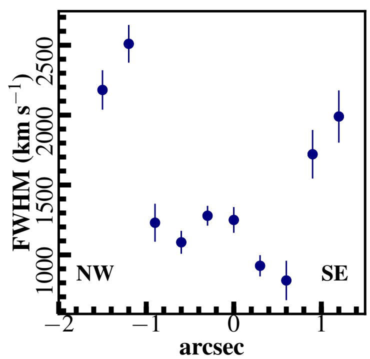

(e) Lyα FWHM

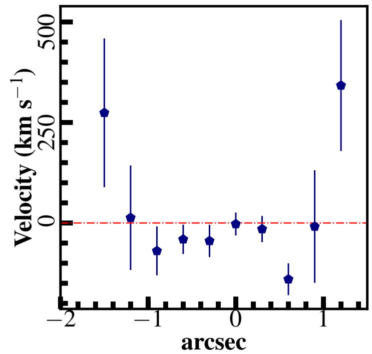

(f) Lyα Velocity

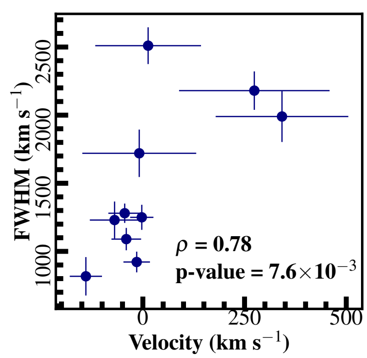

(g) Lyα FWHM *vs.* Velocity

Figure 3.1: Radio galaxy MRC 0030–219: (a) 2-D spectrum of the Lyα spectral region, (b) Flux of the Lyα emission line, (c) Lyα spatial profile (blue circle with dashed lines) compared with the seeing (green dot dashed lines) and (d) 1-D spectrum of the Lyα spectral region extracted from the SOAR long-slit. The Lyα emission-line was extracted by summing over a 3″ region of the slit length. Spatial variations of (e) FWHM, (f) Velocity and (g) Variation of FWHM as a function of the velocity offset of Lyα with ρ and p-value representing the Spearman's rank correlation coefficient and t-distribution, respectively.

3.5.2 MRC 0406–244

3.5.2.1 Previous results

This object consists of a massive host galaxy ($M_\star \sim 10^{11}$ $M_\odot$; Seymour et al. 2007; Hatch et al. 2013) with a high star-formation rate (790 ± 75 $M_\odot$ yr^{-1}; Hatch et al. 2013). Hubble Space Telescope (HST) images show spatially resolved continuum emission, with several connecting bright clumps in a figure of eight morphology elongated along the radio source of the radio galaxy (e.g. Rush et al., 1997; Pentericci et al., 2001; Hatch et al., 2013). Rush et al. (1997) concluded that the complex morphology of the spatially resolved continuum in MRC 0406–244 could be a consequence of a recent merger. On the other hand, Taniguchi et al. (2001) and Humphrey et al. (2009) argued that this morphology might be a consequence of AGN-driven winds (AGN feedback) or a superwind from a starburst event which swept up superbubbles from the ambient ISM. Hatch et al. (2013), however argued that the continuum emission is most likely to be due to young stars or dust-scattered light from the AGN. Using VLT/SINFONI imaging spectroscopy of the rest-frame optical emission lines, (Nesvadba et al., 2008b, 2017a,b) find extended emission line regions with large velocity offset in the range −600 to +600 km s^{-1} and line widths in the range 500 to 1500 km s^{-1} consistent with very turbulent outflowing gas. They conclude that the radio jets are the main driver of the gas kinematics. Taniguchi et al. (2001) and Humphrey et al. (2009) studied the emission line ratios of the extended gas and concluded that photoionization by the AGN is the most probable excitation mechanism of this gas. A Lyα image taken using the 2.5 m du Pont Telescope reveals line emission with an extent of 3″× 5″ (or 24.9 kpc × 41.5 kpc at the adopted cosmology) in which the long axis is about 130° east of north aligned with the radio source (Rush et al., 1997). In addition, using data from the 3.58 m ESO New Technology Telescope (NTT), Pentericci et al. (2001) identified a strong, extended H I absorption feature superimposed on the bright Lyα emission line.

3.5.2.2 Results from SOAR

In our SOAR data, three emission lines were detected in the spectrum of MRC 0406–244 (see Table 2.3). Strong Lyα emission is detected in the direction perpendicular to the radio axis of the galaxy (see Fig. 3.2a). The Lyα emission shows an asymmetric spatial distribution, which is detected further in the SW direction (see Fig. 3.2b). C IV and He II emission lines are also detected, however they are spatially compact and also detected more in the SW direction. In Figure 3.2d, we show the integrated 1-D spectrum of the Lyα profile. Figure 3.2e shows the spatial variations of the FWHM of the Lyα nebula (1000 – 2300 km s^{-1}). The line width is relatively high across the full extent of the emission line, decreasing to 1000 km s^{-1} in the outermost regions. The Lyα velocity shift relative to fiducial velocity shows the most blueshifted gas (~ 200 km s^{-1}) around the nuclear region of the nebula (within 1″). Towards to the outermost regions of the nebula we find velocity offset varying from -135 km s^{-1} to -8 km s^{-1} (see Fig. 3.2f). Investigating the possible correlations between the FWHM and the velocity offset (see Fig. 3.2g), we find a weak negative relationship with ρ = - 0.32 and p-value = 0.23.

The Lyα spatial profile with FWHM = 2.86 ± 0.08″ is clearly spatially resolved compared with the seeing FWHM = 1.21 ± 0.01 (see Fig. 3.2c), indicative of a extended emission line. Correcting for seeing broadening, the intrinsic FWHM is 2.59 ± 0.09″(or 22 ± 1 kpc). None of the other UV emission lines are found to be extended in this spectrum.

We detected a Lyα absorption feature in the spectrum of MRC 0406–244 (see Fig. 3.2a). The best fit to the Lyα profile is shown in Fig. 3.2d. Table 3.3 lists the parameters of the best fitting model together with the diameter of the absorber, and the maximum detected radius. The absorber has column density log N(H I/cm^{-2}) = 14.81 ± 0.03 with Doppler parameter b = 205 ± 11 km s^{-1}. This structure is detected across the full spatial extent of the Lyα emission where S/N in the line is sufficient to detect an absorber with that column density. In Figure 3.2h, we show the line of sight velocity of the H I absorber measured from the SOAR spectrum across its detected spatial extent. The absorbing gas appears blueshifted from the systemic velocity with line of sight velocity -184 ± 8 km s^{-1}. We find that the absorber is detected extending over across 4.2″ (or 35 kpc) in the direction perpendicular to the radio axis of the galaxy. In addition, the Lyα absorption feature detected in the spectrum of MRC 0406–244 shows a constant N(H I) along the slit, which suggests to be spatially extended when comparing the spatial profile of the H I column density with the seeing profile (see Fig. 3.2i). If the Lyα emission is extended and the absorber is not extended, we should expect a radial decline in the strength of the absorber (e.g. N(H I)).

Assuming that this structure is a spherically symmetric shell, its H I mass is given by

$$M_{HI} = 4\pi R^2 N(HI) m_H \tag{3.2}$$

which simplifies to

$$M_{HI} \gtrsim 5.3 \times 10^3 (R/23\,kpc)^2 (N(HI)/10^{14} cm^{-2}) M_{\odot}, \tag{3.3}$$

where R is the radius of the absorption system in kpc, and N(H I) is the H I column density in cm^{-2}, and m_H is the mass of a hydrogen atom. We estimate the mass of the absorbing shell of gas to be log $(M_{HI}/M_{\odot}) \gtrsim 4.5$. If the absorbing gas is partly ionized, then its total mass (i.e. M(H I) + M(H II)) could be substantially higher.

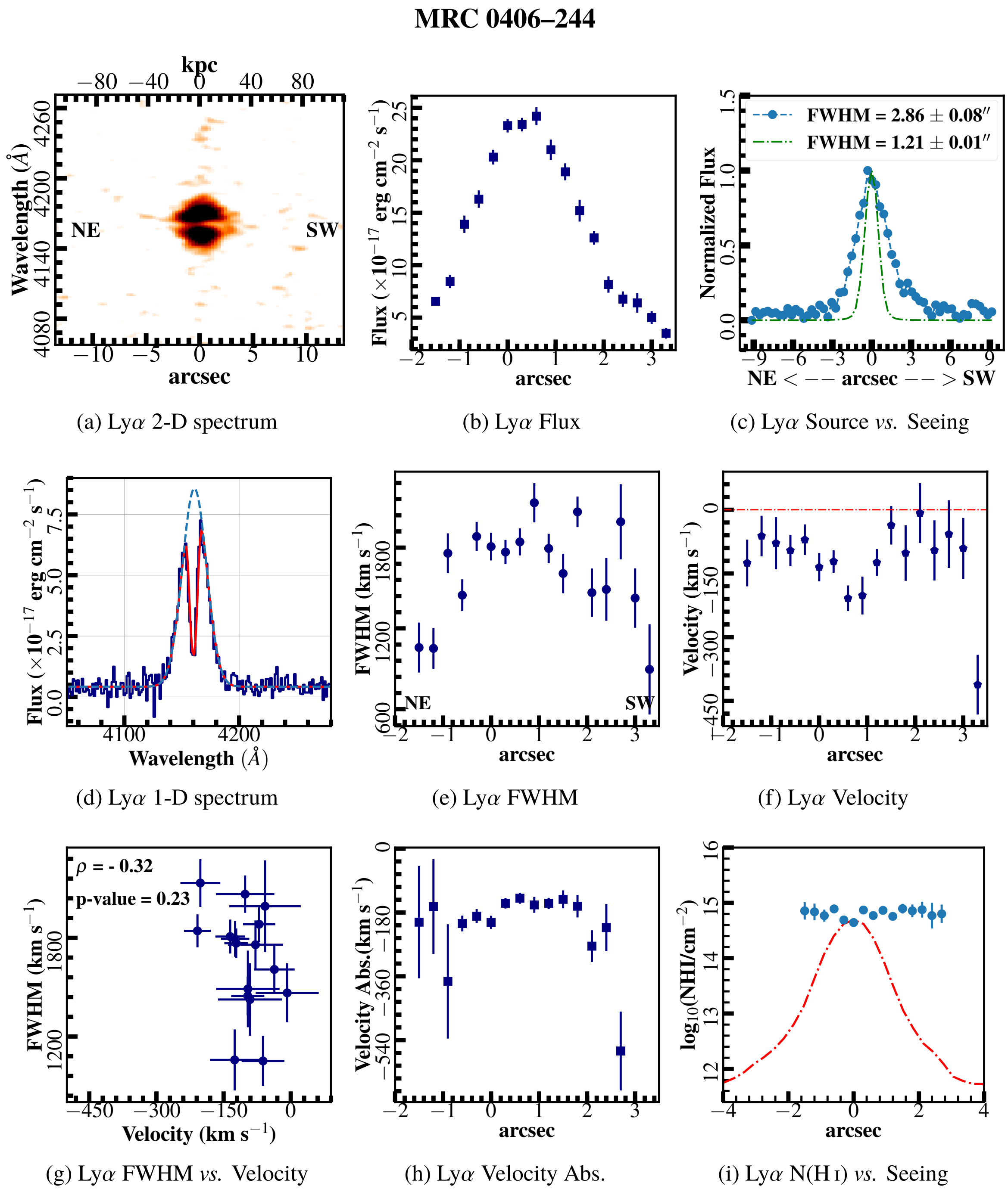

(a) Lyα 2-D spectrum (b) Lyα Flux (c) Lyα Source *vs.* Seeing

(d) Lyα 1-D spectrum (e) Lyα FWHM (f) Lyα Velocity

(g) Lyα FWHM *vs.* Velocity (h) Lyα Velocity Abs. (i) Lyα N(H I) *vs.* Seeing

Figure 3.2: Radio galaxy MRC 0406-244: (a) 2-D spectrum of the Lyα spectral region, (b) Spatial variation of the flux of Lyα line, (c) Lyα spatial profile (blue circle with dashed lines) compared with the seeing (green dot dashed lines) and (d) 1-D spectrum of the Lyα spectral region extracted from the SOAR long-slit. The Lyα emission-line was extracted by summing over a 3″ region of the slit length. Spatial variations of (e) FWHM, (f) Velocity, (g) Variation of FWHM as a function of the velocity offset of Lyα with ρ and p-value representing the Spearman's rank correlation coefficient and t-distribution, respectively, (h) Velocity of the H I absorber and (i) Spatial profile of the H I column density (blue circle points) compared with the seeing (red dot dashed lines), both on a logarithmic scale. In addition, the seeing profile has been normalised and shifted in order to allow the comparison.

3.5.3 4C–00.54

3.5.3.1 Previous results

The z = 2.36 radio galaxy 4C–00.54 (also known as USS 1410–001) consists of a very optically elongated host galaxy (e.g. Pentericci et al., 1999, 2001) for the UV/optical morphology. With $M_\star \sim 10^{11.4}$ $M_\odot$ (e.g. Seymour et al., 2007) and a star formation rate $\sim 460^{+480}_{-270}$ $M_\odot$ yr^{-1} inferred from 7.7 μm polycyclic aromatic hydrocarbon luminosity (e.g. Rawlings et al., 2013). The radio source has a double lobe morphology with total extent of 24″ (or 196 kpc at the adopted cosmology) and it has a misalignment of ~ 45° relative to the UV-optical continuum emission in the central few tens of kpc of the galaxy (e.g. Pentericci et al., 1999, 2001). Spectroscopic studies with the ESO-NTT have revealed extended Lyα emission (~ 80 kpc) without any sign of H I absorption (e.g. van Ojik et al., 1997). Long slit spectropolarimetry using Keck II has shown that the UV continuum emission along the radio axis is significantly polarized ($P_{\%}$ = 11.7 ± 2.7) with contribution from the scattered AGN continuum (47 – 88 %), young stellar population (41 – 0 %) and nebular continuum (12 %) (e.g. Vernet et al., 2001). Using the same data, Villar-Martín et al. (2003) and Humphrey et al. (2006) concluded that the extended gas along the radio axis is part of a giant quiescent halo (FWHM $\leqslant$ 472 – 800 km s^{-1}) without any evidence of jet-gas interactions. Using VLT/SINFONI imaging spectroscopy of the rest-frame optical emission lines of HzRGs, Nesvadba et al. (2017a,b) find line emission extending over an area of 2″×5.6″(or 14 kpc × 41 kpc) with the major axis going from south to north. They find line widths in the range FWHM = 400 – 1300 km s^{-1} in which a small region to the north-east of the nucleus shows the highest FWHM. In addition, with velocity offsets in the range -400 – +400 km s^{-1}, they conclude that the radio jets are the main driver of the turbulent outflowing gas. Also using rest-frame optical emission lines obtained with the VLT/ISAAC, Humphrey et al. (2008b) concluded that AGN photoionization is the dominant ionization mechanism operating in the extended emission line region possibly with a fractional contribution from shocks.

3.5.3.2 Results from SOAR

The Lyα emission detected in the direction perpendicular to the UV-optical emission of the galaxy (see Fig. 3.3a) shows an asymmetric spatial distribution, which is slightly more extended in the S direction (see also Fig. 3.3b). In addition to Lyα (see the 1-D spectrum in Fig. 3.3f), we could also detect N V, C IV and He II emission lines (see Table 3.2). In Figures 3.3g and 3.3h, we show the spatial variations of the FWHM and velocity of the Lyα emission line, respectively. We find that the extended emission line halo shows a central region of kinematically quiescent gas[3] with FWHM < 1000 km s^{-1}. From the nucleus towards the outermost regions we find a gradual increase in FWHM, with values reaching up to 1600 km s^{-1}. The velocity offset of the extended gas varies from -578 km s^{-1} to 216 km s^{-1}. In Figure 3.3i, we show the correlation between the FWHM and the velocity offset of Lyα. The diagram suggests a strong negative relationship between the parameters with ρ = -0.60 and p-value = 7.4 $\times$ 10^{-7}. We note that a similar anticorrelation between velocity shift and FWHM is also present in Fig. 4 of Villar-Martín et al. (2003), albeit along a different slit PA to ours.

With the slit position angle set to 90°, which is perpendicular to the UV-optical emission in the HST images, we note that the slit is at an angle of 45° to the radio axis as defined by the line running through the 2 hotspots and the radio core (see Pentericci et al., 1999, 2001). However, as Pentericci et al. (1999) suggest, the AGN axis (or the radio jet axis) might be precessing, in which case the radio axis near the nucleus might be different to what the radio axis was when the material in the hotspots was ejected from the nucleus. It does seem plausible that due to jet precession, the slit position angle used might intersect gas that has been disturbed by the radio jets. However, it seems odd since that at the nucleus and along the UV-optical axis the kinematics are more quiescent. We should expect the jets going through and perturbing gas in the nuclear region as well.

The Lyα spatial profile of the radio galaxy 4C–00.54 with FWHM = 2.22 ± 0.06″ shows that the emission line is spatially extended compared with the seeing FWHM = 1.08 ± 0.02″ (see Fig. 3.3c). In addition, the spatial profile shows an excess above the seeing disk especially obvious towards the South. Correcting for seeing broadening in quadrature, we infer the intrinsic FWHM as 1.94 ± 0.07″ or 16 ± 1 kpc. None of the other UV emission lines are found to be extended in this spectrum.

In Figure 3.3e, we show the spatial variation of the Lyα/He II flux ratio along the slit. We find a significant variation in Lyα/He II, with a radial increase from 5.0 ± 0.3 near the spatial zero position, up to 16.3 ± 1.9 (r = - 0.9″) and 17.2 ± 1.3 (r = + 1.5″). The spatial variation of the Lyα/He II shows flux ratios that are consistent with the standard photoionization models, which predict Lyα/He II in the range 15 – 20 for HzRGs (e.g. Villar-Martín et al., 2007a). The possible reasons for such variation will be discussed in §3.6.2.

[3]We define kinematically 'quiescent' to mean FWHM<1000 km s^{-1} and kinematically 'perturbed' to mean FWHM≥1000 km s^{-1}. This definition, although somewhat arbitrary, is motivated by some previous studies which found ionized gas with FWHM≥1000 km s^{-1} associated with the radio structures of HzRGs, and gas FWHM<1000 km s^{-1} present across the full spatial extent of the extended nebulae of the HzRGs (e.g. Villar-Martín et al., 2003), suggesting that the 'quiescent' gas is a common feature of the nebulae of HzRGs and represents gas that has not been disturbed by radio mode feedback.

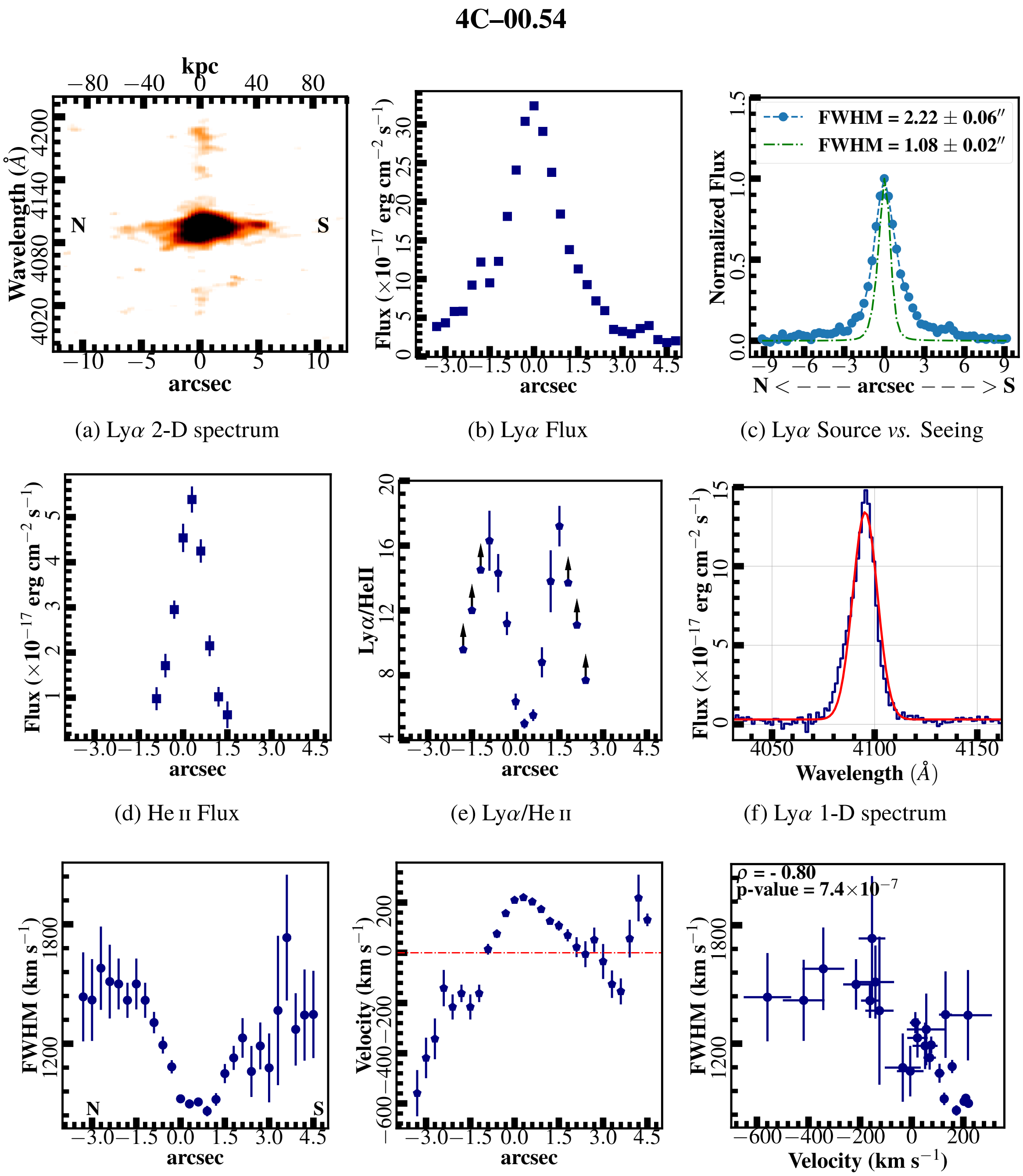

(a) Lyα 2-D spectrum (b) Lyα Flux (c) Lyα Source *vs.* Seeing

(d) He II Flux (e) Lyα/He II (f) Lyα 1-D spectrum

(g) Lyα FWHM (h) Lyα Velocity (i) Lyα FWHM *vs.* Velocity

Figure 3.3: Radio galaxy 4C–00.54: (a) 2-D spectrum of the Lyα spectral region, (b) Spatial variation of the flux of Lyα line, (c) Lyα spatial profile (blue circle with dashed lines) compared with the seeing (green dot dashed lines), (d) Spatial variation of the flux of He II line, (e) the Lyα/He II line ratio and (f) 1-D spectrum of the Lyα spectral region extracted from the SOAR long-slit. The Lyα emission-line was extracted by summing over a 3″ region of the slit length. Spatial variations of (g) FWHM, (h) Velocity, (i) Variation of FWHM as a function of the velocity offset of Lyα with ρ and p-value representing the Spearman's rank correlation coefficient and t-distribution, respectively. The black arrows seen in the Lyα/He II line ratio diagram represent the 3σ lower limit of the line ratios.

3.5.4 TN J0920–0712

3.5.4.1 Previous results

VLA observations of the HzRG TN J0920–0712 at z = 2.76 revealed a radio source consisting of a single component with a maximum angular size of 1.4″ (11 kpc in the adopted cosmology), and spectral index α = -1.51 (e.g. De Breuck et al., 2000b, 2001). Using the Faint Object Spectrograph and Camera 1 (EFOSC1) on the ESO 3.6 m telescope at La Silla, De Breuck et al. (2001) found extended Lyα emission with FWHM = 2050 ± 150 km s^{-1} and a large equivalent width (W$_{\lambda}^{rest}$ = 350 ± 60 Å). Additionally, they also detected Si IV + O IV, C IV and He II emission lines. They also reported the detection of an extended H I absorber on the blue side of the Lyα line althoulgh it has not been explored. De Breuck et al. (2000a) compared the UV line ratios of this HzRG, and found that photoionization by the central AGN offers a plausible explanation for the excitation of the line emitting gas, with potential for a significant additional contribution from shock ionization.

3.5.4.2 Results from SOAR

The Lyα nebula shows an elongated and symmetric spatial distribution (see the 2-D spectrum of the Lyα spectral region in Fig. 3.4a, and also Fig. 3.4b). In Figure 3.4d, we show the integrated 1-D spectrum of the Lyα extracted from the SOAR long-slit, with the Gaussian emission component plus absorption model overlaid. Together with Lyα, we also detected the emission lines such as O VI + C II, N V, C IV and He II (see Table 3.2). The spatial variation of the FWHM shows a smooth transition from SW to the NE during which the line width varies from 1220 km s^{-1} to 2400 km s^{-1} across the entire nebula (see Fig. 3.4e). The velocity shift varies from - 242 km s^{-1} to 208 km s^{-1} (see Fig. 3.4f). We find a correlation between the FWHM and the velocity offset of Lyα, such that regions with higher FWHM also tend to have a higher blueshift (see Fig. 3.4g). The result indicates that there is a relationship between the parameters with ρ = - 0.70 and p-value = 5.4 × 10^{-4}.

The Lyα spatial profile with FWHM = 1.78 ± 0.03″ shows that the emission line is spatially extended compared with the seeing FWHM = 1.08 ± 0.02″ (see Fig. 3.4c). In addition, the spatial profile shows excess of emission above the seeing wings at both sides of the central source showing that the Lyα halo is extended. We infer the intrinsic FWHM to be 1.42 ± 0.04″ (or 11.4 ± 0.3 kpc). None of the other UV emission lines are found to be extended in this spectrum.

Like De Breuck et al. (2001), we also detect a spatially extended Lyα absorption feature on the blue side of the Lyα emission in the spectrum of TN J0920–0712 (see Fig. 3.4a). The best fit to the Lyα is shown in Fig. 3.4d. Table 3.3 lists the parameters of the best fitting

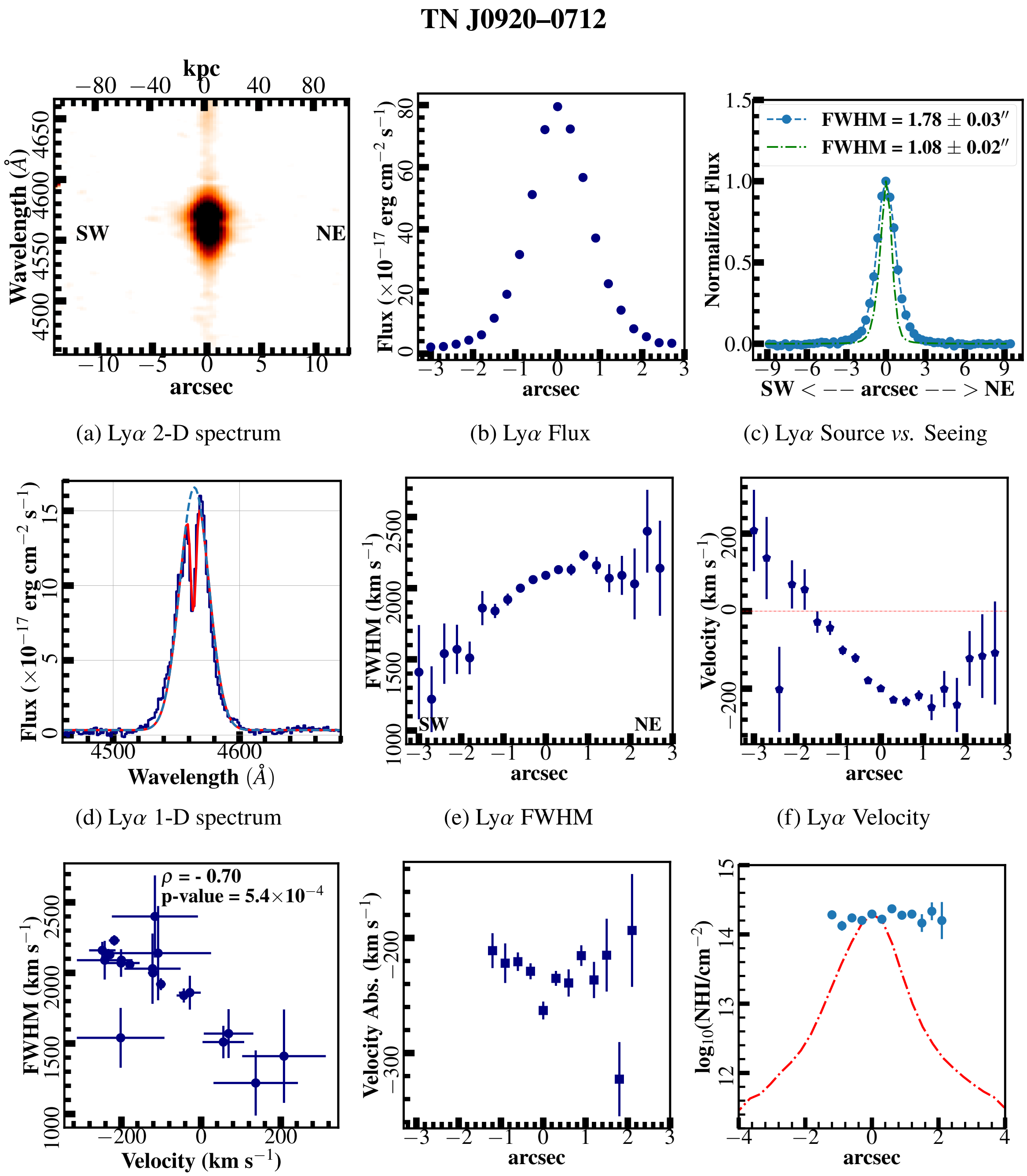

(a) Lyα 2-D spectrum (b) Lyα Flux (c) Lyα Source *vs.* Seeing

(d) Lyα 1-D spectrum (e) Lyα FWHM (f) Lyα Velocity

(g) Lyα FWHM *vs.* Velocity (h) Lyα Velocity Abs. (i) Lyα N(H I) *vs.* Seeing

Figure 3.4: Radio galaxy TN J0920–0712: (a) 2-D spectrum of the Lyα spectral region, (b) Spatial variation of the flux of the Lyα line, (c) Lyα spatial profile (blue circle with dashed lines) compared with the seeing (green dot dashed lines) and (d) 1-D spectrum of the Lyα spectral region extracted from the SOAR long-slit. The Lyα emission-line was extracted by summing over a 3″ region of the slit length. Spatial variations of (e) FWHM, (f) Velocity, (g) Variation of FWHM as a function of the velocity offset of Lyα with ρ and p-value representing the Spearman's rank correlation coefficient and t-distribution, respectively, (h) Velocity of the H I absorber and (i) Spatial profile of the H I column density (blue circle points) compared the seeing (red dot dashed lines), both on a logarithmic scale. In addition, the seeing profile has been normalised and shifted in order to allow the comparison.

model together with the diameter of the absorber, and the maximum detected radius. We obtain a column density log N(H I/cm^{-2}) = 14.23 ± 0.03 with Doppler parameter b = 185 ± 10 km s^{-1}, and velocity offset of the absorber -232 ± 6 km s^{-1}. In Figure 3.4h, we show the line of sight velocity of the H I absorber measured from the SOAR spectrum across its detected spatial extent, which shows that the absorbing gas appears blueshifted from the systemic velocity. This absorber is detected across the full spatial extent of the Lyα emission where the S/N of the line is sufficient to detect an absorber with that column density, i.e., 3.3″ or 27 kpc. This absorption is clearly spatially extended compared to the the seeing profile (see Fig. 3.4i). Assuming that the absorbing gas is a spherically symmetric shell, using the expression 3.3 we estimate log $(M_{\rm H\,I}/M_{\odot}) \gtrsim 3.7$.

3.5.5 PKS 1138–262

3.5.5.1 Previous results

VLA observations of the z = 2.16 radio galaxy PKS 1138–262 (Spiderweb galaxy) shows that the radio source consists of multiple hotspots in the eastern lobe, which shows a double bend towards south (e.g. Carilli et al., 1997; Pentericci et al., 1997). The radio source has a maximum angular size of 11.4″ (97 kpc in the adopted cosmology) and spectral index α = -1.3 (e.g. Carilli et al., 1997; Pentericci et al., 1997). The rest-frame near-infrared (near-IR) light and the K-band luminosity indicate that the host galaxy is very massive (e.g. $M_{\star} \sim 10^{12}$ $M_{\odot}$; Seymour et al. 2007; Hatch et al. 2009) and infrared luminosity implies a star formation rate of 1390 ± 150 $M_{\odot}$ yr^{-1} (see Seymour et al., 2012). The radio galaxy presents a diffuse halo of young stars (Hatch et al., 2008) and observations with the Australia Telescope Compact Array (ATCA) have allowed the detection of CO(1-0) emission from cold molecular gas (Emonts et al., 2013). Chandra X-ray imaging of the galaxy shows extended X-ray emission aligned with the radio structure (e.g. Carilli et al., 2002), and observations with the HST indicate that the optical emission is clumpy and disturbed (e.g. Pentericci et al., 1998; Kuiper et al., 2011) suggestive of a merging structure (Miley et al., 2006; Kuiper et al., 2011). With the major axis oriented along the radio axis, the enormous Lyα halo extends by at least 25″ (214 kpc in the adopted cosmology) surrounding the host galaxy, which indicates a large reservoir of atomic gas (Pentericci et al., 1997; Miley et al., 2006). Using VLT/SPIFFI IFU (SPectrometer for Infrared FaintField Imaging) of the rest-frame optical emission line, Nesvadba et al. (2006) conclude that the kinematic properties and energy arguments favor the AGN as the plausible mechanism that efficiently power the outflowing gas. Furthermore, using VLT/SINFONI imaging spectroscopy of the rest-frame optical emission line of the warm ionized gas, Nesvadba et al. (2017a) find that the kinetic energy and momentum injection rates from the radio jets seem to be the most efficient mechanism powering the outflowing gas.

Investigating the Lyα emission line using medium resolution spectroscopy (instrumental FWHM = 2.8 Å) with the slit approximately along the radio axis, Pentericci et al. (1997) report the detection of several H I absorbers at a similar redshift to the HzRG. They find column densities of the order log N(H I/cm^{-2}) $\simeq$ 15 – 16 and Doppler parameters between 40 and 100 km s^{-1}. In addition, studying optical images of the extended Lyα halo obtained with FORS1 at the 8.2m VLT Antu, Kurk (2003) identified the presence of H I absorption associated with the Lyα emission line. Simulating 3 slits placed in different regions of the Lyα halo, Kurk could identify up to two absorption troughs in the Lyα line with column density in the range log N(H I/cm^{-2}) $\simeq$ 14.2 – 14.8 and Doppler parameters between 140 and 430 km s^{-1}.

3.5.5.2 Results from SOAR

In the direction perpendicular to the radio axis, we detect the Lyα emission showing an asymmetric spatial distribution, being more extended towards the E (see the 2-D spectrum of the Lyα spectral region in Fig. 3.5a, see also the spatial variation of the Lyα flux in Fig. 3.5b). In Figure 3.5d, we show the integrated 1-D spectrum of the Lyα profile. In addition to Lyα, we also detected the C IV and He II emission lines (see Table 3.2). In Figures 3.5e and 3.5f, we show the spatial variations of FWHM and velocity of the extended Lyα nebula emission. The extended emission line shows line widths in the range FWHM = 1700 – 3890 km s^{-1} while the velocity offset is ranging from -670 km s^{-1} to 292 km s^{-1}. As in the previous objects, we find a correlation between the FWHM and the velocity offset of Lyα, such that regions with higher FWHM also tend to have a larger blueshift (see Fig. 3.5g). The result indicates that there is a negative relationship between the parameters with ρ = - 0.60 and p-value = 1.9 × 10^{-3}.

The spatial profile of the radio galaxy PKS 1138–262 (FWHM = 4.81 ± 0.31″) is spatially resolved compared with the seeing disk FWHM = 1.76 ± 0.02. The emission line shows an excess above the seeing disk at $\lesssim$ 5.4″, which is particularly obvious towards the East (see Fig. 3.5c), confirming that Lyα is dominated by extended emission. The intrisic FWHM for Lyα will be 4.48 ± 0.33″or 38 ± 3 kpc. None of the other UV emission lines are found to be extended in this spectrum.

Unlike Pentericci et al. (1997), only a single absorption feature is detected in the spectrum of PKS 1138–262 (see Fig. 3.5a), which is likely due to the lower resolution of our spectrum. Our best fit to the Lyα is shown in Fig. 3.5d. Table 3.3 lists the parameters of the best fitting model together with the diameter of the absorber, and the maximum detected radius. The absorber has a column density log N(H I/cm^{-2}) = 14.08 ± 0.10 with Doppler parameter b = 190 ± 43 km s^{-1}, and velocity offset -234 ± 28 km s^{-1}. In Figure 3.5h, we show the line of sight velocity of the H I absorber measured from the SOAR spectrum across its detected spatial

PKS 1138–262

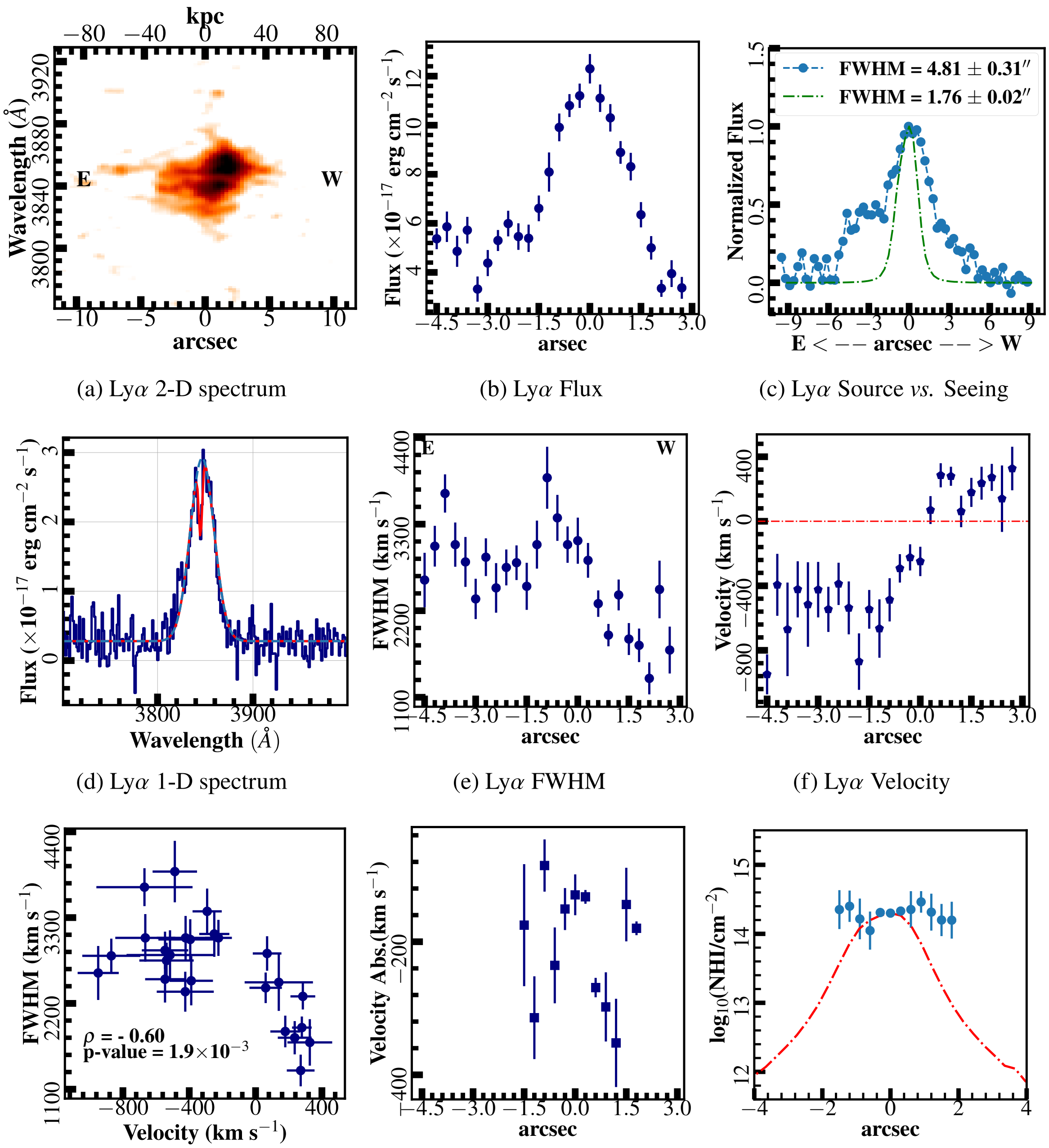

(a) Lyα 2-D spectrum (b) Lyα Flux (c) Lyα Source *vs.* Seeing

(d) Lyα 1-D spectrum (e) Lyα FWHM (f) Lyα Velocity

(g) Lyα FWHM *vs.* Velocity (h) Lyα Velocity Abs. (i) Lyα N(H I) *vs.* Seeing

Figure 3.5: Radio galaxy PKS 1138–262: (a) 2-D spectrum of the Lyα spectral region, (b) Spatial variation of the flux of the Lyα line, (c) Lyα spatial profile (blue circle with dashed lines) compared with the seeing (green dot dashed lines) and (d) 1-D spectrum of the Lyα spectral region extracted from the SOAR long-slit. The Lyα emission-line was extracted by summing over a 3″ region of the slit length. Spatial variations of (e) FWHM, (f) Velocity, (g) Variation of FWHM as a function of the velocity offset of Lyα with ρ and p-value representing the Spearman's rank correlation coefficient and t-distribution, respectively, (h) Velocity of the H I absorber and (i) Spatial profile of the H I column density (blue circle points) compared the seeing (red dot dashed lines), both on a logarithmic scale. In addition, the seeing profile has been normalised and shifted in order to allow the comparison.

extent. The absorbing gas appears blueshifted from the systemic velocity. The absorber is detected extending over across 3.3″ (or 28 kpc) in the direction perpendicular to the radio axis of the galaxy. In addition, the Lyα absorption feature is clearly spatially extended compared to the seeing profile (see Fig. 3.5i). Using the column density and extent of the absorber, we estimate the neutral mass to be log $(M_{\rm H\,I}/M_{\odot}) \gtrsim 3.4$.

3.6 Discussion

3.6.1 Gas Dynamics

Several scenarios have been suggested in order to explain the observed kinematic properties of the giant nebulae associated with HzRGs, including outflows resulting from jet-gas interactions, AGN or starburst driven super-winds (e.g. Villar-Martín et al., 1999a, 2000; Jarvis et al., 2003; Humphrey et al., 2006, 2008a; Nesvadba et al., 2006, 2008b; Swinbank et al., 2015; Cai et al., 2017; Nesvadba et al., 2017a), gas infalling/inflow (e.g. Humphrey et al., 2007; Villar-Martín et al., 2007b; Humphrey et al., 2013a; Roche et al., 2014; Silva et al., 2018b) or rotation (e.g. van Ojik et al., 1996; Villar-Martín et al., 2003, 2006; Arrigoni Battaia et al., 2018). Clearly, by studying the gas dynamics of the Lyα nebulae it should be possible to obtain information about their origins.

For 3 out of 5 radio galaxies (e.g. MRC 0406–244, TN J0920–0712 and PKS 1138–262), the kinematic properties of the Lyα emission line show a resemblance to rotation curves (see Figs. 3.2, 3.4 and 3.5). However, gas dynamics dominated by the large-scale gravitational potential of the host galaxy ought to show smooth velocity gradients and rather uniform line widths with FWHMs of a few $\times 100$ km s^{-1}. Given the large values of FWHM we measure in the extended Lyα emitting gas, it seems unlikely that rotation dominates the gas dynamics in these specific regions.

We note that most of the objects show a correlation between the FWHM and the velocity offset of Lyα (see Section 2.3), suggesting that bulk radial motion, rather than rotation or random motion, dominates the gas dynamics in these regions. Furthermore, the fact that this trend does not appear to correlate with the presence (or absence) of strong Lyα H I absorption suggests that the trend is not caused by the superposition of an extended absorption system. Given also the facts that the perturbed gas is spatially extended and detected on both sides of the nucleus, and that the most perturbed regions shows usually a blueshifted gas with respect to the systemic velocity, it would be natural to conclude that outflows dominate the kinematics of this gas. However, this interpretation effectively ignores line radiative transfer effects, which can have a significant effect on the observed kinematics of resonant lines such as Lyα. Indeed, if the

Lyα kinematics are strongly affected by resonant scattering, the correlation between FWHM and blueshift may also be explained by the *infall* of gas (see Dijkstra et al., 2006b; Verhamme et al., 2006). In other words, we argue that radial motion appears to dominate the bulk dynamics of this extended gas, but due to degeneracies inherent in the use of Lyα to study gas kinematics, we are unable to discriminate between the infall and outflow scenarios.

In the case of 4C–00.54, it seems plausible that due to jet precession (see Pentericci et al., 1997), the slit position angle used might intersect gas that has been disturbed by the radio jets. It is, however, unexpected that the ionized gas in the nucleus has lower FWHM than the extended gas outside the ionization cones. We should also expect the jets to interact with and perturb gas in the nuclear region of the galaxy, but this not seen in our data. On the other hand, if the jets are not responsible for the high FWHM, we suggest this might be a result of scattering of Lyα photons that were originally produced along the radio axis or within the ionization cones, by neutral gas in regions that are predominantly neutral due to not being illuminated by the AGN. In this scenario, the emergent velocity profile of the scattered Lyα would have a velocity profile that has been artificially broadened as a result of the kinematic diversity of the Lα emitting regions in the radio galaxy's extended gas halo. Another possibility might be that Lyα emitted by highly turbulent gas associated with jet-gas interactions is being preferentially scattered by neutral hydrogen within the extended regions in our slit. However, detailed numerical modeling of Lyα radiative transfer within the gas halo would be needed to explore this possible effect in more detail.

The radio galaxy MRC 0030–219 has a single and compact radio source, which is much less extended than the Lyα emission line gas detected. Given the sizes involved between the radio source and the emission line gas, we suggest that jets seem unlikely to be responsible for such turbulence. However, we are unable to definitely say what kind of motion is dominating the gas (i.e. infall, outflow or rotation) or if the observed properties observed are a consequence of the resonant scattering within the nebula.

Lyα is particularly sensitive to radiative transfer effects. Given this nature, the best way to avoid any possible uncertainty on this issue would be to compare the kinematic properties of Lyα with lines that are not affected by radiative transfer effects, such as He II λ 1640 or optical forbidden lines such as [O III] $\lambda\lambda$ 4959,5007. Although we can not neglect the contribution from radiative transfer effects, without other emission lines we are not able to say whether the high FWHM of Lyα is dominated by these effects or is instead due to extreme motions in the extended gas.

3.6.2 The radial gradient of Lyα/HeII in 4C–00.54

Previous investigations using long-slit spectroscopy along the radio axis or perpendicular to the radio axis of other HzRGs have shown that line ratios involving Lyα emission line can vary significantly (e.g. Humphrey et al., 2008b; Morais et al., 2017).

We find a significant variation in Lyα/He II flux ratio (see Fig. 3.3e). The ratio shows a radial increase from 5.0 ± 0.3 near the spatial axis origin, up to 16.3 ± 1.9 (r = - 0.9″) and 17.2 ± 1.3 (r = + 1.5″). Such a variation suggests evidence for some process in which the Lyα is depressed in the centre with this effect becoming less important when moving far from the centre. As it moves out from the centre, we note that the flux ratio reaches values that are typically seen in other HzRGs (Lyα/He II = 15 – 20; Villar-Martín et al. 2007a).

Using only the Lyα/He II flux ratio, it is not easy to discriminate what kind of effects might be responsible for the large variation observed. However, we suggest that it may be a consequence of effects such as (i) absorption of Lyα, presumably by H I or interstellar dust (see Röttgering et al., 1997; van Ojik et al., 1997), (ii) resonant scattering of Lyα photons (see Dijkstra and Loeb, 2008; Hayes et al., 2011; Steidel et al., 2011) and (iii) enhanced emission of Lyα, which can be produced by a low ionization parameter, a relatively soft ionizing spectral energy distribution (SED) or a low gas metallicity (see Villar-Martín et al., 2007a; Humphrey et al., 2019).

Interestingly, higher FWHM are one of the possible signatures of Lyα resonance scattering. If this is true, then the observed Lyα might be a result of resonant scattering strongly affecting the regions across the nebula.

3.6.3 The nature of the HI Absorbers

A new perspective about the gaseous environment of HzRGs was opened up by Röttgering et al. (1995a) and van Ojik et al. (1997) with the discovery of associated, spatially extended H I absorbers. With the slit positioned along the radio axis, a number of investigations have shown that the H I absorbers are typically detected with column densities between log N(H I/cm^{-2}) = 13 – 19 and Doppler width b = 20 – 874 km s^{-1} (e.g. Röttgering et al., 1995a; van Ojik et al., 1997; Binette et al., 2000; Jarvis et al., 2003; Wilman et al., 2004). In addition, previous work has shown that the absorbers are extended over tens or even a few hundred kpc, leading to H I mass estimates of up to log $(M_{\rm H\,I}/M_{\odot}) \sim 9$. In addition, it has been argued that the extended absorbers are (i) in outflow; (ii) partly ionized based on detection of C IV and other lines in a few cases; (iii) probably located outside the Lyα halos based on covering factor ~ 1 and the fact that the absorbers appear to completely cover the (detected) extended Lyα emission (e.g. Binette et al., 2000). Based on these properties, it has been argued that the absorbing gas is

Table 3.3: Lyα absorption features best fit parameters. Column (1) gives the object name. Column (2) gives the redshift for the Lyα emission Gaussian. Column (3) gives the redshift for the Lyα absorption. Column (4) gives the column density (N(H I)). Column (5) gives the Doppler width b. Column (6) gives the velocity shift of the absorber with respect to He II emission line. Column (7) gives the maximum diameter detected of the absorbers. Column (8) gives the maximum radius of the absorbers. We note that the radius over which we detect the absorber only gives us a lower limit to the radius of the shell because the absorption feature can not be detected where the background Lyα *emission* is weak or absent. In addition, without information on the ionization fraction of hydrogen, the H I column density only gives a lower limit on the total hydrogen column density. Moreover, because of the degeneracy discussed by Silva et al. (2018b) we also note that our column density estimate is likely a lower limit of the true column. Thus, our mass estimates are lower limits.

Object	Lyα emission redshift (z_{em})	Absorption redshift (z_{abs})	Column Density (cm^{-2})	Doppler Parameter (km s^{-1})	Δv (km s^{-1})	D (kpc)	R$_{max}$ (kpc)
(1)	(2)	(3)	(4)	(5)	(6)	(7)	(8)
MRC 0406–244	2.42287 ± 0.00015	2.42219 ± 0.00009	(6.46 ± 0.38)×10^{14}	250 ± 11	-184 ± 8	35	23
TN J0920–0712	2.75450 ± 0.00010	2.75385 ± 0.00010	(1.70 ± 0.10)×10^{14}	185 ± 10	-232 ± 6	27	17
PKS 1138–262	2.16430 ± 0.00032	2.16284 ± 0.00003	(1.21 ± 0.29)×10^{14}	190 ± 43	-234 ± 28	28	15

part of an expanding shell that surrounds the HzRG and its Lyα halo, produced by feedback activity (e.g. Binette et al., 2000).

However, single-slit observations did not provide information about the two-dimensional distribution of the absorbing gas, leaving open the possibility that the absorbers do not cover the entire Lyα halo, and are only present along the radio/optical axis of the HzRGs. A crucial test of the shell hypothesis is the detection of extended H I absorbers in the direction perpendicular to the radio/optical axis.

To address this issue, in recent years three HzRGs with extended H I absorbers were studied with IFU spectroscopy, and in each case the absorber was found to cover the full spatial extent of the Lyα halo (MRC 2025–218: Humphrey et al. 2008a; TN J1338–1942: Swinbank et al. 2015; MRC 0943-242: Gullberg et al. 2016; Silva et al. 2018b). Furthermore, Silva et al. (2018b) were able to measure the radial velocity curve for the main absorber in front of MRC 0943–242, and found a radial gradient consistent with an expanding shell with a radius of at least several tens of kpc.

In this paper, we have studied the H I absorbers of a further 3 HzRGs, placing a long slit at large angles (>45°) to the radio axis, and detecting the H I absorber across the full spatial extent of the Lyα emission. In all three cases, the absorber is blueshifted relative to the systemic velocity across its full detected extent.

Taking our new results together with the three IFU studies mentioned above, we find that for all 6 of the extended absorbers for which the test has been undertaken, the absorbing gas is extended perpendicularly to the radio/optical axis of the HzRG. We conclude that when present around an HzRG, this type of extended HI absorbing structure commonly covers the entire Lyα halo. These properties are consistent with the absorbing gas being part of a large-scale, expanding shell surrounding the HzRG and its Lyα halo, as suggested by Binette et al. (2000).

3.7 Conclusions

Making use of the Goodman long-slit on the SOAR telescope, we have studied the properties of the extended Lyα halo and the large-scale H I absorbers structures of 5 HzRGs, in regions that are expected to have little influence from the radiation field of the active nucleus or the radio jets, to examine the global properties of these two gaseous components.

We find spatially extended gas with high line widths (FWHM = 1000 – 2500 km s^{-1}), suggestive of turbulent motion. In addition, we find a correlation between the FWHM and the velocity offset of Lyα, such that regions with higher FWHM are more blueshifted. Based on this result, we conclude that an outflowing gas or an infalling gas are the two scenarios consistent with the kinematic properties of the radio galaxies, depending on the level of resonant scattering of the Lyα photons within the nebula but also on the gas geometry, H I distribution and column density.

Studying the H I absorbers of 3 HzRGs with the long slit placed at a large angle to the radio axis (>45°), we have detected the H I absorber across the full spatial extent of the Lyα emission. In all three cases, the absorber is blueshifted relative to the systemic velocity across its full detected extent. Our new results show that the extended H I absorbers associated with HzRGs, when present, cover the entire Ly-alpha halo, which is consistent with previous IFU results and also consistent with the absorbing gas being part of a giant, expanding shell of gas enveloping the HzRG and its Lyα halo.

Finally, we comment that our work shows the potential capability of the Goodman Spectrograph on the SOAR 4.1 m telescope to observe objects at high-redshift (z > 2).

Chapter 4

Carbon-loud SDSS BOSS QSO2s at $z > 2$: High density gas or secondary production of Carbon?

4.1 Abstract

We study the ultraviolet emission line ratios of a sample of 145 Type 2 quasars from SDSS BOSS, and compare against a grid of AGN photoionization models with a range in gas density, gas chemical abundances, and ionization parameter. Most of the quasars are "carbon-loud", with C IV/He II ratios that are unusually high for the narrow-line region, implying higher than expected gas density ($>10^6$ cm^{-3}) and/or significantly super-Solar relative carbon abundance. We also find that Solar or super-Solar nitrogen abundance and metallicity are required in the majority of our sample, with potentially significant variation between objects. Compared to radio galaxies at similar redshifts (HzRGs; z > 2), the QSO2s are offset to higher N V/He II, C IV/He II and C III]/He II, suggesting systematically higher gas density and/or systematically higher C and N abundances. We find no evidence for a systematic difference in the N/C abundance ratio between the two types of objects. Scatter in the N IV]/C IV ratio implies a significant scatter in the N/C abundance ratio among the QSO2s and HzRGs, consistent with differences in the chemical enrichment histories between objects. Interestingly, we find that adopting secondary behaviour for both N and C alleviates the long-standing "N IV] problem". A subset of the QSO2s and HzRGs also appear to be "silicon-loud", with Si III] relative fluxes suggesting Si/C and Si/O are an order of magnitude above their Solar values. Finally, we propose new UV-line criteria to select genuine QSO2s with low-density narrow line regions.

4.2 Introduction

High-z quasars (QSOs, z > 2) or more generally active galactic nuclei (AGNs) are among the byproducts of galaxy formation. They are powered by the accretion of material onto a central supermassive black hole (SMBH), and their study provides powerful tools for understanding SMBH growth (e.g. Mortlock et al., 2011; Wu et al., 2015), the re-ionization process (e.g. Fan et al., 2006a,b), and chemical enrichment history (e.g. Hamann et al., 2002; Dietrich et al., 2003; Baldwin et al., 2003; Nagao et al., 2006b,a; Xu et al., 2018) during a poorly understood early phase of galaxy assembly.

Among the notable observational characteristic of AGNs is the presence of emission lines with widths upwards of 1000 km s^{-1} (e.g. Villar-Martín et al., 1999a, 2003; Humphrey et al., 2006; Villar-Martín et al., 2007b; Humphrey et al., 2008b,a; Morais et al., 2017; Silva et al., 2018b,a) and far in excess of any other known class of galaxy. These broad lines are thought to arise in gas clouds of high density (i.e., $n_H \gtrsim 10^6$ cm^{-3}) situated close to the SMBHs (broad line region or BLR), which are photoionized by the radiation field from the accretion disk of the SMBH. On the other hand, when the BLR is obscured by the putative dusty torus, the observer is able to see narrow lines that arise in low density gas clouds (i.e., $n_H \lesssim 10^6$ cm^{-3}) located several parsecs or more from the AGN (narrow line region or NLR). The ultraviolet and optical emission lines from these regions are widely used to study the dynamics, ionization, and chemical abundances of the gas in and around AGNs (e.g. Hamann and Ferland, 1993; Villar-Martín et al., 1997; Ferland et al., 1996; Hamann and Ferland, 1999; Villar-Martín et al., 1999a,b, 2000; Dietrich and Wilhelm-Erkens, 2000; De Breuck et al., 2000a; Dietrich and Hamann, 2001; Hamann et al., 2002; Baldwin et al., 2003; Villar-Martín et al., 2003; Nagao et al., 2006b,a; Jiang et al., 2007; Humphrey et al., 2008b; Juarez et al., 2009; Humphrey et al., 2009; Morais et al., 2017; Silva et al., 2018b; Xu et al., 2018).

The gas phase metallicity in AGNs has been studied extensively, particularly in the case of the BLR of quasars. Using fluxes of several UV emission lines within the framework of photoionization models, previous works have reported that the BLR metallicity is typically higher than the solar value ($Z/Z_\odot \simeq 4$ to 8; e.g. Dietrich and Wilhelm-Erkens 2000; Dietrich and Hamann 2001; Hamann et al. 2002; Dietrich et al. 2003; Nagao et al. 2006a; Jiang et al. 2007; Juarez et al. 2009; Xu et al. 2018), reaching as much as $Z/Z_\odot \simeq 15$ in extreme cases (e.g. Baldwin et al., 2003; Bentz et al., 2004). Although the gas that makes up the BLR represents only a tiny fraction of the total gas in the host galaxy, it has been concluded that intense star formation at an early epoch is required to explain such high levels of chemical enrichment in many cases (Dietrich and Hamann, 2001; Hamann et al., 2002; Baldwin et al., 2003; Dietrich et al., 2003; Simon and Hamann, 2010; Xu et al., 2018).

Another possibility presented by the literature is to explore the gas phase metallicity in NLRs. In contrast to BLRs, the size of these regions are comparable to the size of their host galaxies which makes it a good tracer of chemical properties on galactic scales. However, as only a few optically-selected high-z type II quasars (or QSO2s) have been discovered, the literature has as main target the study of the Extended Emission Line Regions (EELR) of HzRGs, name commonly used for the most extended NLRs which have gas density lower than the less extended NLRs ($n_H \lesssim 100\ cm^{-3}$) and sizes that extend to several hundred kpc (Fosbury et al., 1982; di Serego Alighieri, 1988; McCarthy et al., 1990b; van Ojik et al., 1997; Pentericci et al., 1998; Francis et al., 2001; Reuland et al., 2003; Humphrey et al., 2013a; Cantalupo et al., 2014; Swinbank et al., 2015; Borisova et al., 2016; Cai et al., 2017). There have been a number of attempts at estimating the chemical abundances in the EELR of HzRGs, where the rest-frame UV lines have been widely used. For example, using the flux ratios N v/He ii and N v/C iv of two HzRGs at z ~ 2.5, Villar-Martín et al. (1999b) find large flux ratios values suggesting that N is overabundant in the ionized gas of these objects. By focusing on the same flux ratios and using sequences in metallicity, De Breuck et al. (2000a) and Vernet et al. (2001) reported nitrogen abundances in the range $0.4 \lesssim Z/Z_{\odot} \lesssim 4.0$ or possibly even much higher. Given the correlation defined by the sample, they suggest a metallicity evolution in nitrogen abundance. Based on rest-frame optical spectra obtained by sensitive near-infrared spectroscopy, Iwamuro et al. (2003) report that HzRGs tend to show sub-solar metallicities ($Z/Z_{\odot} \sim 0.2$), significantly lower than values previously reported. Such a disagreement with previous results must surely be due to the use of different modelling methodologies or different set of lines which can give significantly different metallicity estimates. An additional tool for the metallicity determination is the N iv] diagram. This diagram poses a problem in that photoionization models imply it should be less sensitive to ionization parameter (U) than the N v diagram. However, the models systematically overpredict N iv]/He ii and N iv]/C iv by a factor of ~ 2 (e.g. Vernet et al., 2001; Humphrey et al., 2008b). Taken at face value, the observed N iv] flux ratios would imply lower N abundance than the N v flux ratios by a factor of ~ 2. By using a large set of lines, Silva et al. (2018b) report a high gas metallicity ($Z/Z_{\odot} = 2.1$) for the EELR of the HzRG MRC 0943–242. In addition, they find a substantial range in ionization level across the object, validated by the analysis of the 2D ionization properties, with a clear spatial correlation between the radio hotspots and UV emission lines indicative of relatively low ionization.

In this paper, we present a study of the UV emission lines of a sample of 145 Type II quasars from SDSS BOSS (Alexandroff et al., 2013) in the redshift range 2.0 < z < 4.3, and compare against a grid of AGN photoionization models in order to obtain new information about the ionization conditions and chemical enrichment history of Type II quasars at high-z. In addition, we use rest-frame optical emission line fluxes from the literature (Greene et al., 2014), which partially overlaps with the SDSS BOSS sample of Type II quasars. To complement our study making comparisons of two different populations of objects, we also use emission line fluxes of HzRGs from the literature (Cimatti et al., 1998; Vernet et al., 2001; Humphrey et al., 2008b).

The paper is organized as follows. In §4.3, we describe the sample and data used in this study. In §2.5, we describe the methods for measuring the emission line parameters we use in our analysis. In §4.5, we present the photoionization model grid used to build our diagnostic diagrams, and in §2.6 we describe and discuss the results of our comparison between the data and models. Finally, in §2.7 we summarize our conclusions.

4.3 Sample and Emission Line Data

4.3.1 SDSS BOSS QSO2s

The objects studied in this paper are a sub-sample of quasars from the spectroscopic quasar sample of the Baryon Oscillation Spectroscopic Survey (BOSS) of the Sloan Digital Sky Survey III (SDSS) Data Release 9 (see Gunn et al. 2006; Alexandroff et al. 2013 and references therein). Alexandroff et al. (2013) Selected 452 candidate Type II quasars in the redshift range 2.0 < z < 4.3, using selection criteria that included 5σ detections in both Lyα and C IV, with which both lines also required have FWHM < 2000 km s^{-1}. These authors further refined their Type II quasar candidate sample by removing the two main contaminants in their original sample, narrow line Seyfert 1 (NLS1) galaxies and broad absorption line (BAL) quasars, and then splitting the remaining objects into two categories: i) those with the characteristics of an obscured quasar, i.e., narrow emission lines, no associated absorption and weak continuum (Class A; 145 objects); and ii) those with one or more characteristics of an unobscured quasar, i.e., a broad (BLR) component to an emission line, a BAL, or a strong blue continuum (Class B; 307 objects). In this study, we consider only the 145 Type II Class A quasar candidates of Alexandroff et al. (2013), in order to avoid unnecessary contamination from unobscured objects.

In addition, we make use of rest-frame optical line fluxes of Type II quasar candidates published by Greene et al. (2014), who used Triplespec on the Apache Point Observatory 3.5m Telescope (APO), Folded-port Infrared Echellete (FIRE) on the 6.5m Baad-Magellan Telescope, and the Gemini Near-Infrared Spectrograph (GNIRS) on the Gemini North 8.1m Telescope. The sample of Greene et al. (2014) consists of 19 candidate QSO2s at 2.0 < z < 3.4 (see Greene et al., 2014, Table 2); here we use the line fluxes of the 16 quasars which are also present in the Class A subsample discussed above.

4.3.2 Radio Galaxies at $2.27 \leq z \leq 3.56$

As a comparison sample, we used emission line fluxes of HzRGs at $2.27 \leq z \leq 3.56$ from the literature (see Table 4.1). The objects were observed using the Low Resolution Imaging Spectrometer (LRIS) in spectropolarimetry mode at the Keck II 10m telescope, the Infrared Spectrometer and Array Camera (ISAAC) in long-slit mode and Focal Reducer and Spectrograph (FORS1) at the Very Large Telescope (VLT), OH Airglow Suppressor (OHS) spectrograph mounted on the Subaru telescope and ESO Multi-Mode Instrument (EMMI) at the New Technology Telescope (NTT). The line flux measurements and more detailed information on the observation are given by Cimatti et al. (1998), Vernet et al. (2001) and Humphrey et al. (2008b). Humphrey et al. also presented near-IR spectroscopy for a partially overlapping sample of HzRGs in a similar redshift range, which we make use of 11 of the 16 HzRGs in this sample. A number of previous publications have presented further analyses of these objects (e.g. McCarthy et al., 1992; Röttgering et al., 1995b; Knopp and Chambers, 1997; Cimatti et al., 1998; Villar-Martín et al., 1999b; Pentericci et al., 1999; Overzier et al., 2001; Pentericci et al., 2001; Villar-Martín et al., 2002; Iwamuro et al., 2003; Egami et al., 2003; Villar-Martín et al., 2003; Humphrey et al., 2006; Broderick et al., 2007; Humphrey et al., 2007; Gullberg et al., 2016; Morais et al., 2017; Silva et al., 2018a).

In the special case of the radio galaxy MRC 0943–242 (z = 2.92), we have used the UV and optical lines from the X-SHOOTER study of Silva et al. (2018b). However, given that some UV emission lines were not detected by the X-SHOOTER instrument we also make use of the UV emission lines from Vernet et al. (2001) in order to complement the X-SHOOTER data.

Two of the HzRGs in this sample appear to be intermediate objects. MRC 2025–218 (z = 2.63) appears to be a broad line radio galaxy (BLRG), on account of its broad C IV (e.g. Villar-Martín et al., 1999b) and Hα (e.g. Larkin et al., 2000; Humphrey et al., 2008b) lines. In addition, MRC 1558-003 (z = 2.57) shows broad (FWHM = 12000 km s^{-1}) Hα (Humphrey et al., 2008b), while its permitted UV lines remain narrow (e.g., FWHM$\sim$1000 km s^{-1}), but as this paper focuses on the UV lines we classify it as a Type 2 radio galaxy.

4.4 Data Analysis

For the purpose of fitting the emission line parameters (e.g. flux and wavelength) we created a PYTHON routine that minimizes the sum of the squares of the difference between the model and data using the LMFIT algorithm (Newville et al., 2014). Gaussian line profiles were used for the fits with the number of components changing according to the emission line or when a single component inadequately represented an emission line. The continuum was modeled on a line-by-line basis using a single power law.

For doublets, such as C IV $\lambda\lambda$1548,1551 (hereafter C IV) or N V $\lambda\lambda$1239,1243 (hereafter N V), we use a single Gaussian for each doublet component, with both components constrained to have equal FWHM, and a fixed wavelength separation corresponding to the theoretical value. In the case of resonant lines, we adopt a fixed flux ratio of blue:red = 2:1 corresponding to the optically thin case. We have repeated our fits using optically-thick (blue:red ~ 1:1) and find no significant difference to the summed flux of the two doublet components.

In the case of density sensitive doublets such as Si III] $\lambda\lambda$1883,1892 (hereafter Si III]) and C III] $\lambda\lambda$1907,1909 (hereafter C III]), we adopt the low density flux ratio (blue:red $\gtrsim$ 1:1). Repeating our fits using a doublet ratio corresponding to high (BLR) density made no significant differences to our flux measurements of sum of the doublet flux.

In the special cases where multiple lines are blended together, such as O VI $\lambda\lambda$1032,1038 + C II λ1037 (hereafter O VI+C II) or Si IV $\lambda\lambda$1393,1402 + O IV]$\lambda\lambda$1401,1407 (hereafter Si IV+O IV]), each line was fitted with a single Gaussian, with all lines constrained to have equal FWHM, and a fixed wavelength separation corresponding to the theoretical value. However, the flux ratio between different species was allowed to vary freely. In such cases, we provide the flux of the summed blend.

The forbidden emission line [Ne IV] λ1602 (hereafter [Ne IV]1602) was detected only in 3 objects (see Fig. 4.9), but considering its importance as a diagnostic of electron density when used together with [Ne IV] λ2422, we have estimated its 3σ upper limit in cases where the 2422 Å line was detected.

Throughout this work we shall abbreviate the other emission lines as follows: Lyα for Lyα λ1216, O I for O I λ1304, N IV] for N IV] λ1487, He II for He II λ1640, O III] for O III] λ1661, [Ne IV] for [Ne IV] λ2422 (see Figures 4.10 and 4.11 showing the detection), Mg II for Mg II $\lambda\lambda$2796, 2803 (see Table 4.2), Hβ for Hβ λ4863, [O III] for [O III] λ5007, [N II] for [N II] λ6585 and Hα for Hα λ6565.

4.5 Photoionization Models

In order to characterize the chemical abundances, density and ionization properties of the observed emission line gas, a grid of photoionization models was computed using the multipurpose code MAPPINGS Ie (Binette et al., 1985; Ferruit et al., 1997). In the interest of simplicity, we have adopted a single-slab, radiation bounded and isochoric geometry. The main input parameters were:

- Spectral energy distribution (SED)[1] of the photoionizing continuum radiation, set to α = - 1.0 with high-energy cut-off of 1.0×10^3 eV. A hard ionizing continuum has previously provided a good fit to the UV line ratios of HzRGs (e.g. Villar-Martín et al., 1997).

- Hydrogen density $n_H = 10^2$ cm^{-3}, 10^4 cm^{-3}, 10^6 cm^{-3}, 10^7 cm^{-3} or 10^8 cm^{-3}.

- Ionization parameter[2] (U), defined as the ratio of the ionizing photon density to the hydrogen density at the irradiated surface of a cloud. It was set to vary from $U = 2{\times}10^{-3}$ to 1.0.

- Gas metallicity $Z/Z_{\odot}$, which we define as the O/H abundance ratio divided by its Solar value as determined by Asplund et al. (2006), and for which use the values $Z/Z_{\odot}$ = 0.5, 1.0, 2.0, 3.0, 4.0, or 5.0. We adopt the abundances of Asplund et al. (2006) for our default Solar abundances set.

For the chemical composition of gas, we have used four different schemes to vary the abundances of N, C, Si with O/H:

- Secondary N behaviour, such that N/H $\propto$ O/H at $Z/Z_{\odot} < 0.3$ and N/O $\propto$ O/H at $Z/Z_{\odot} \geq$ 0.3, to take into account its expected secondary behaviour at moderate to high metallicity (Villar-Martín et al. 1999b; Henry et al. 2000), with all other metals fixed at their Solar abundance relative to O (see the abundances in Table 4.3).

- Secondary N and secondary C (Nicholls et al., 2017) with all other metals fixed at their Solar abundance relative to O, such that N/O $\propto$ N/C $\propto$ O/H at $Z/Z_{\odot} \geq 0.3$ (see the abundances in Table 4.4).

- secondary N with Si/O = 10 $\times$ Solar, with all other metals (including C) fixed at their Solar abundance relative to O (see the abundances in Table 4.5).

- Secondary N and secondary C, with Si/O = 10 $\times$ Solar, and all other metals fixed at their Solar abundance relative to O (see the abundances in Table 4.6).

[1]The ionizing continuum is characterized as a power law with $S_\nu \propto \nu^\alpha$ where ν is frequency (Hz) and S_ν is the flux density (erg s^{-1} Hz^{-1}).

[2]We adopt the definition $Q/(4\pi r^2 n_H c)$, where Q is the isotropic ionizing photon number luminosity of the source, r is the distance of the cloud from the ionizing source, n_H is the hydrogen density and c is the speed of light.

4.6 Results and Discussion

4.6.1 The diagnostic diagrams

In Figures 4.1 to 4.8 and 4.12 to 4.25, we show diagnostic diagrams with our grid of photoionization models and observed emission line ratios of the QSO2s and HzRGs. In these Figures, each line represents a sequence in ionization parameter U at fixed values of n_H and Z. The six panels in each figure each show the models at a different gas metallicity Z. The measured line ratios of the type II quasars are shown by purple filled diamonds (C IV/He II < 4) or yellow filled circles (C IV/He II > 4). The HzRGs are shown by blue filled triangles; however, for the special case of the BLRG 2025–218, we use instead a red filled triangle. Arrows indicate 3σ upper or lower limits (see for example Figs. 4.20 and 4.21).

4.6.2 Gas chemical abundances

4.6.2.1 Nitrogen abundance

Nitrogen is mainly produced by the CN cycle of the CNO reactions which catalyze hydrogen burning in stars. It is mostly a secondary element being synthesized from the C and O already present in the stars, and the increase in the abundance of N should be proportional to the initial C and O content, which will be proportional to the square of the metal content in a galaxy (Hamann and Ferland, 1992; Matteucci and Padovani, 1993; Matteucci, 1996; Chiappini et al., 2003; Nicholls et al., 2017). As such, line ratios involving N are valuable tracers of chemical enrichment, since this element is selectively enhanced by secondary processing in stellar populations.

The study of the gas metallicity using nitrogen lines (more specifically N V) over C IV or He II has been applied to the BLRs and NLRs of high-z quasars (e.g. Hamann and Ferland, 1993; Ferland et al., 1996; Hamann and Ferland, 1999; Dietrich and Wilhelm-Erkens, 2000; Dietrich and Hamann, 2001; Hamann et al., 2002; Baldwin et al., 2003; Nagao et al., 2006b,a; Xu et al., 2018) and also HzRGs (e.g. van Ojik et al., 1994; Villar-Martín et al., 1997, 1999b; De Breuck et al., 2000a; Vernet et al., 2001; Overzier et al., 2001; Humphrey et al., 2008b; Morais et al., 2017; Silva et al., 2018b). Such studies have generally concluded that the BLR or NLR of many high-z quasars and HzRGs have Solar or super-Solar gas metallicities.

Looking first at the N V-diagram (Fig. 4.1 and 4.2), the observational data shows an order of magnitude range in N V/C IV and N V/He II, with the QSO2s and HzRGs defining two parallel correlations, with the QSO2s offset to higher values of N V/He II for a given N V/C IV. In this diagram, there is a degeneracy between nitrogen abundance and U, such that a sequence in U can mimic a sequence in nitrogen abundance, and vice versa (see also Humphrey et al., 2008b).

The trend defined by the QSO2 sample runs parallel to the loci of varying U and varying metallicity, suggesting that U and/or metallicity varies significantly between the quasars. Based on their position relative to the models, QSO2s at the low N v/He II and N v/C IV end of the trend require N/H of at least 0.25×Solar, corresponding to O/H = 0.5×Solar if our adopted relation between N/H and O/H is correct (Fig. 4.1 and 4.2, top left panel)[3].

Conversely, to explain the QSOs at the high N v/He II and N v/C IV trend we find that a combination of high gas density ($n_H \gtrsim 10^7$ cm^{-3}) and N/H $\gtrsim$ 16×Solar is required, corresponding to O/H $\gtrsim$ 4×Solar. A potential alternative to $n_H \gtrsim 10^7$ cm^{-3} could be that this subset of quasars have a nitrogen abundance that is a factor of $\gtrsim$2 higher than assumed in our highest metallicity models. While there is potentially a large variation in N/H throughout the QSO2 sample, from N/H ~ 0.25 to N/H ~ 16×Solar, the degeneracy between U and N/H inherent to the N v-diagram means that the QSO2 data are also compatible with a range in U and a smaller (or no) variation in N/H between objects. For instance, our sequence in U with 4×Solar metallicity is able to reproduce the full range of N v/He II and N v/C IV shown by the quasars.

When using secondary behaviour for carbon, the N v-diagram changes such that even at high-U and high metallicity, the models fail to reproduce the positions of the ~ 30% of QSO2 with the highest values of N v/C IV (Fig. 4.2). This is because our adopted secondary behaviour of C and N results in a constant Solar N/C abundance ratio at all values of gas metallicity, preventing the supersolar N/C ratios that give rise to the highest N v/C IV line ratios in Fig. 4.1. Nevertheless, Fig. 4.1 and Fig. 4.2 give consistent results in terms of N v/He II and the N/H abundance ratio, because this ratio is unaffected by the choice between using the primary or secondary behaviour of carbon.

In Figs. 4.3 and 4.4 we show the N v/C IV *vs.* C IV/C III] diagram, which one might expect to provide information about the possible degeneracy between N abundance and U. However, no obvious correlation is seen between the N v/C IV ratio and the U-sensitive C IV/C III] ratio. The observed CIV/CIII] ratio varies by more than an order of magnitude in the QSO2 sample, suggesting significant variation in U between objects. However, the degeneracy between U, metallicity and density in this diagram makes it challenging to determine the extent to which U might vary in the sample, or whether U genuinely varies at all. Given the complex behaviour of the U-sequences, which are highly dependent on the density and metallicity of the gas we suggest that at least two out of U, Z and n_H vary significantly in the QSO2 sample, in order to produce the observed distribution of points in this diagram.

The observed flux ratio N IV]/C IV (see Figs. 4.5 and 4.6) shows significant scatter perpendicular to the model loci, which is difficult to explain by variation in U or n_H, and which

[3]Strictly speaking, using N v/He II in this way we obtain the N/He ratio, which we use as a proxy for N/H assuming He/H = 0.085.

strongly suggests a significant variation in the N/C abundance ratio between objects. However, it is unclear whether the relative variation is due to differences in the ISM abundance ratio, differential depletion of N and C into dust grains, or interstellar absorption of C IV. Previous modeling which used primary carbon behaviour systematically overpredicted N IV]/He II and N IV]/C IV by a factor of ~ 2 (e.g. Vernet et al., 2001; Humphrey et al., 2008b) but, interestingly, using secondary behaviour for both N and C appears to alleviate this problem involving this so-called N IV]-problem.

Another interesting result from our models is that when secondary behaviour is adopted for carbon, the N/C abundance ratio (and consequently the N V/C IV and N IV]/C IV flux ratios) ceases to be a useful metallicity indicator. This is because, at least in the scheme we have adopted for the secondary behaviour of N and C, the N/C abundance ratio remains constant across the full range of gas metallicity.

Although the gas phase metallcity of the HzRGs has been examined in several previous studies (Villar-Martín et al., 1999b; Vernet et al., 2001; Humphrey et al., 2008b), we revisit this topic here in light of our new analysis and models. Consistent with previous authors (Villar-Martín et al., 1999b; Vernet et al., 2001; Humphrey et al., 2008b), we find that the HzRGs require N/H $\gtrsim$ 0.25 ×Solar, implying gas metallicity $\gtrsim$ 0.5×Solar, with some objects requiring Solar or super-Solar N/H, and by implication in our N abundance variation scheme, Solar or Super-solar metallicity. However, as argued by Humphrey et al. (2008b), the positions of the HzRGs in the N V-diagram are also consistent with little or no variation in N/H, and a range in ionization parameter U. We argue that the vertical offset between the QSO2s and HzRGs implies that the QSO2s typically have significantly higher gas density (at least 2 orders of magnitude), and/or that the QSO2s have significantly higher N/H (a factor of ~ 4) than the HzRGs. On the other hand, we note that there is no evidence for a systematic difference in the N/C abundance ratio between the QSO2s and the HzRGs.

4.6.2.2 Carbon abundance

Carbon is also a product of the CNO cycle which can be produced by stars of all masses. Although it is substantially produced in low and intermediate mass stars where the bulk of nitrogen also originates, carbon is also expected to derive from supernovae as is also the case for the so-called α-elements (e.g. O, Ne, Mg; Matteucci and Padovani 1993; Matteucci 1996).

In Figures 4.7 and 4.8, we show the C IV-diagram. The observtional data shows an order of magnitude range in C IV/He II and C IV/C III], with some QSO2s showing very high values of C IV/He II (> 10). Although some of this variation could be due to the presence of a range in U in the sample, the large dispersion in C IV/He II at a given value of C IV/C III] appears inconsistent with being due to variation in U alone. We argue that at least two out of U, Z ,C/H, or n_H would

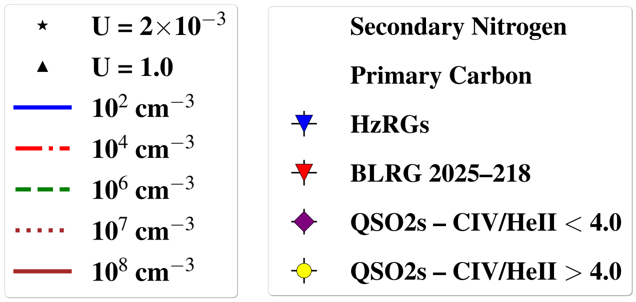

(a) Legend

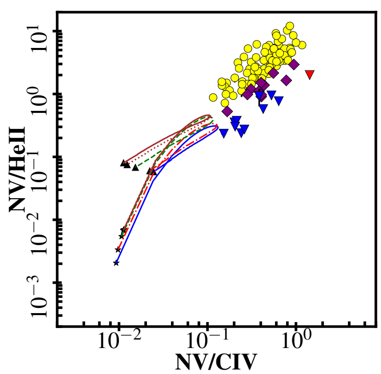

(b) Z/Z$_{\odot}$ = 0.5

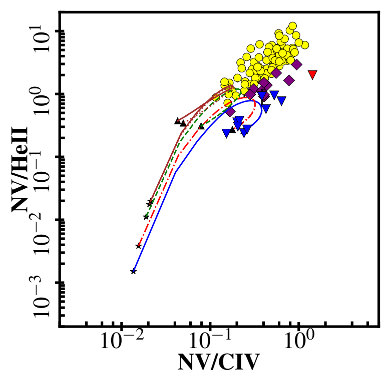

(c) Z/Z$_{\odot}$ = 1.0

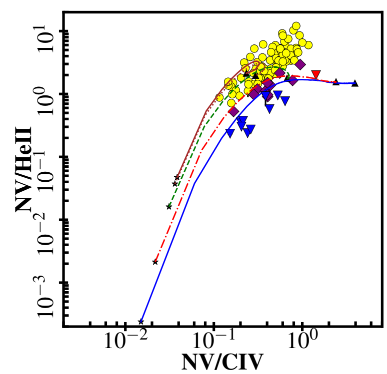

(d) Z/Z$_{\odot}$ = 2.0

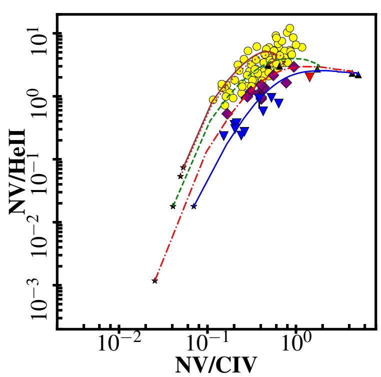

(e) Z/Z$_{\odot}$ = 3.0

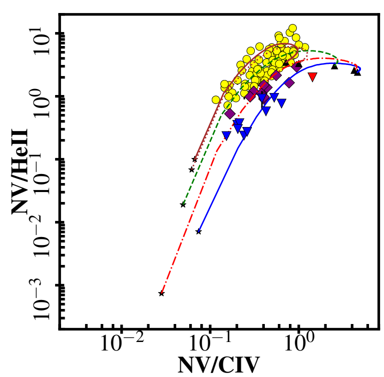

(f) Z/Z$_{\odot}$ = 4.0

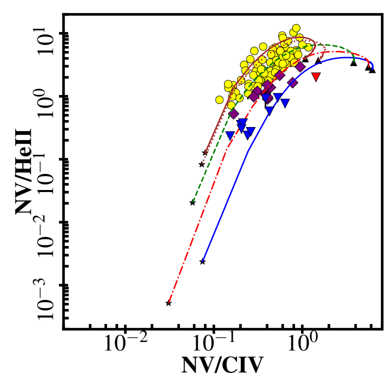

(g) Z/Z$_{\odot}$ = 5.0

Figure 4.1: Comparison of the observed emission line ratios from the SDSS type II quasars divided in objects with C IV/He II < 4 and C IV/He II > 4 (purple filled diamond and yellow filled circles, respectively), and Keck II HzRGs from Vernet et al. (2001) (blue filled triangles) with photoionization models using ionizing continuum power law index α = -1.0. Each diagram presents a different gas metallicity, i.e., Z/Z$_{\odot}$ = 0.5, 1.0, 2.0, 3.0, 4.0, 5.0. Curves with different colors represent the hydrogen gas density (n$_{H}$) described in 4.1a. At the end of each sequence, a solid black triangle corresponds to the lowest ionization parameter (U = 2×10^{-3}) while the solid black star corresponds to the maximum value of the ionization parameter (U = 1.0).

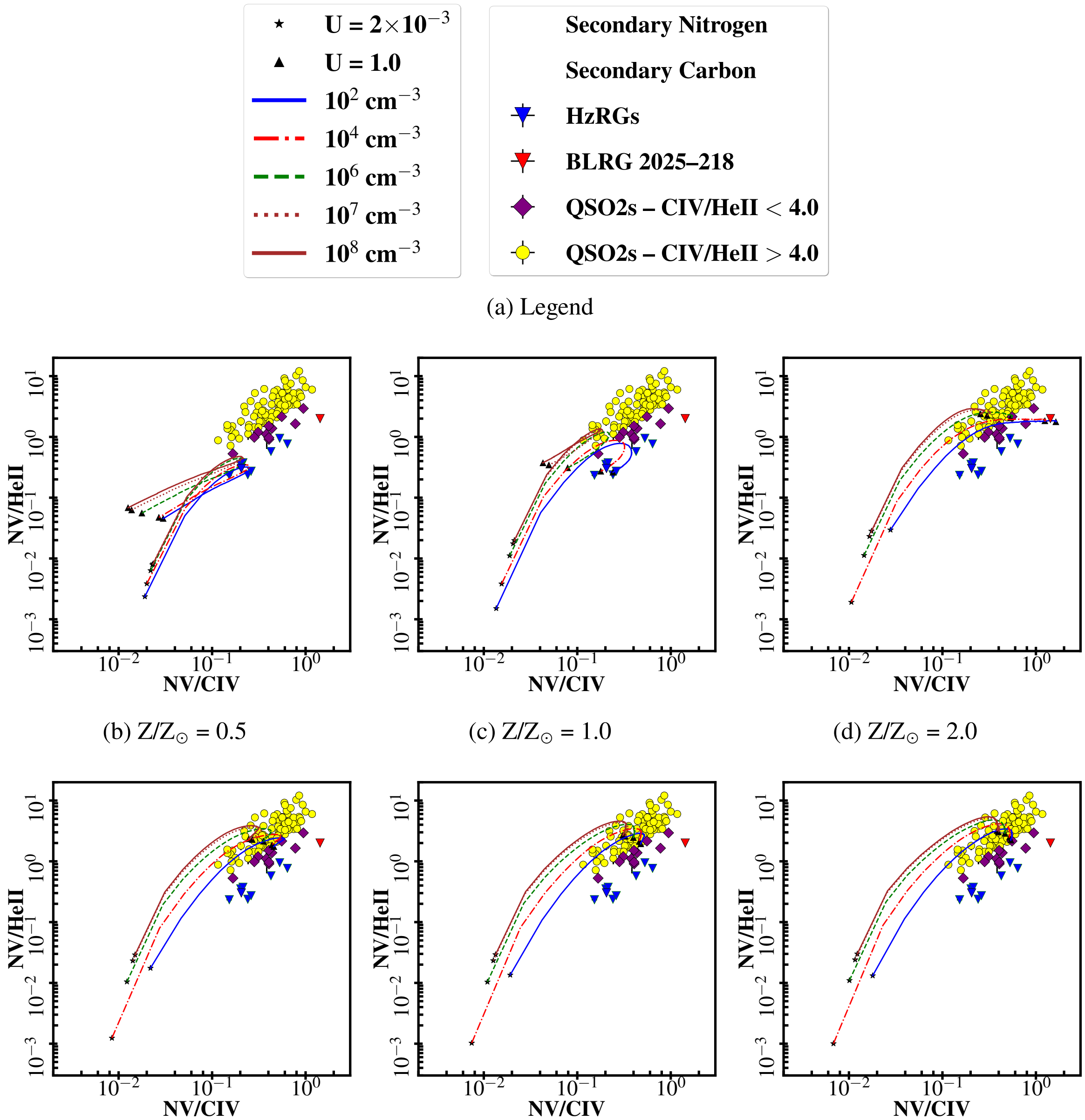

(a) Legend

(b) $Z/Z_{\odot}$ = 0.5 (c) $Z/Z_{\odot}$ = 1.0 (d) $Z/Z_{\odot}$ = 2.0

(e) $Z/Z_{\odot}$ = 3.0 (f) $Z/Z_{\odot}$ = 4.0 (g) $Z/Z_{\odot}$ = 5.0

Figure 4.2: Comparison of the observed emission line ratios from the SDSS type II quasars divided in objects with C IV/He II < 4 and C IV/He II > 4 (purple filled diamond and yellow filled circles, respectively), and Keck II HzRGs from Vernet et al. (2001) (blue filled triangles) with photoionization models using ionizing continuum power law index α = -1.0. Nitrogen and Carbon are a secondary elements in which their abundances are proportional to the square of the metallicity. Each diagram presents a different gas metallicity, i.e., $Z/Z_{\odot}$ = 0.5, 1.0, 2.0, 3.0, 4.0, 5.0. Curves with different colors represent the hydrogen gas density (n_H) described in 4.2a. At the end of each sequence, a solid black triangle corresponds to the lowest ionization parameter (U = 2×10^{-3}) while the solid black star corresponds to the maximum value of the ionization parameter (U = 1.0).

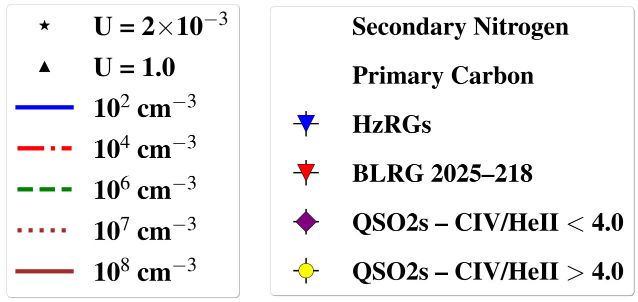

(a) Legend

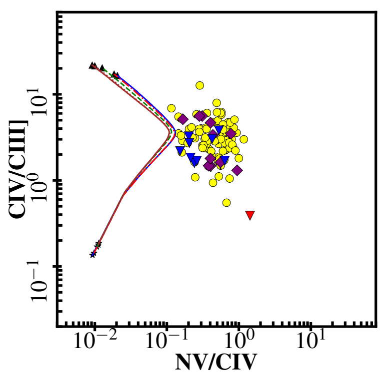

(b) $Z/Z_\odot$ = 0.5

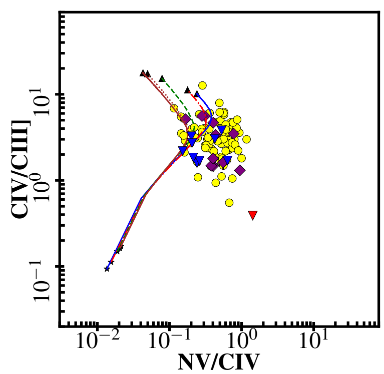

(c) $Z/Z_\odot$ = 1.0

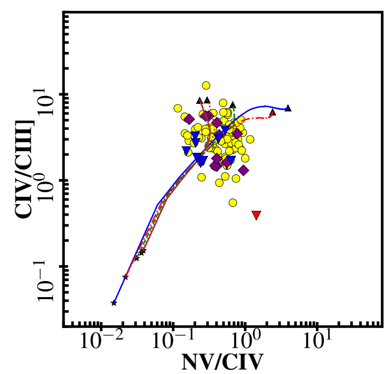

(d) $Z/Z_\odot$ = 2.0

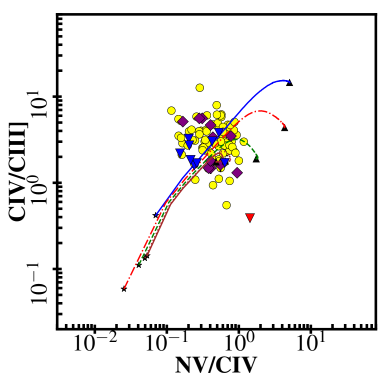

(e) $Z/Z_\odot$ = 3.0

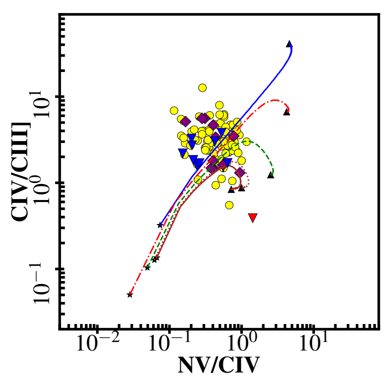

(f) $Z/Z_\odot$ = 4.0

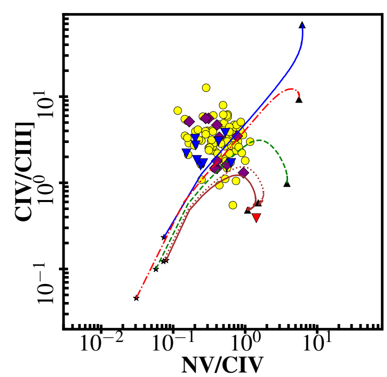

(g) $Z/Z_\odot$ = 5.0

Figure 4.3: Comparison of the observed emission line ratios from the SDSS type II quasars divided in objects with C IV/He II < 4 and C IV/He II > 4 (purple filled diamond and yellow filled circles, respectively), and Keck II HzRGs from Vernet et al. (2001) (blue filled triangles) with photoionization models using ionizing continuum power law index α = -1.0. Each diagram presents a different gas metallicity, i.e., $Z/Z_\odot$ = 0.5, 1.0, 2.0, 3.0, 4.0, 5.0. Curves with different colors represent the hydrogen gas density (n_H) described in 4.3a. At the end of each sequence, a solid black triangle corresponds to the lowest ionization parameter (U = 2×10^{-3}) while the solid black star corresponds to the maximum value of the ionization parameter (U = 1.0).

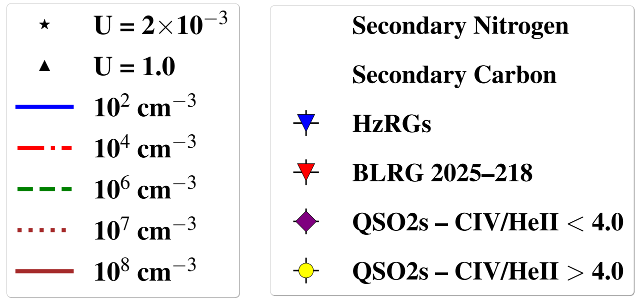

(a) Legend

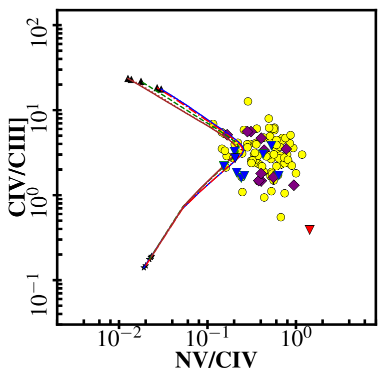

(b) $Z/Z_{\odot}$ = 0.5

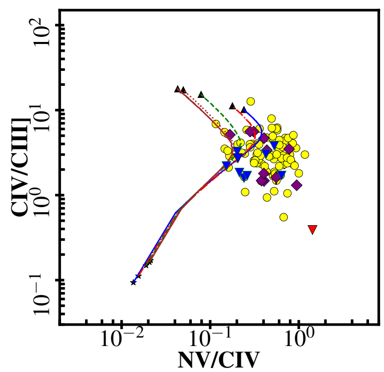

(c) $Z/Z_{\odot}$ = 1.0

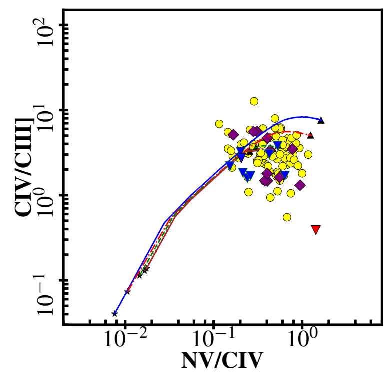

(d) $Z/Z_{\odot}$ = 2.0

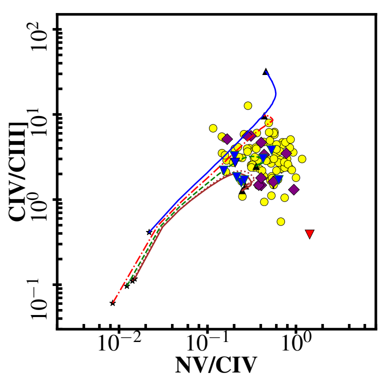

(e) $Z/Z_{\odot}$ = 3.0

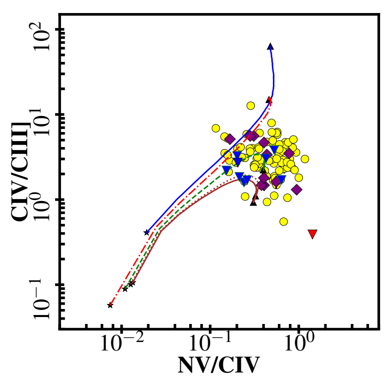

(f) $Z/Z_{\odot}$ = 4.0

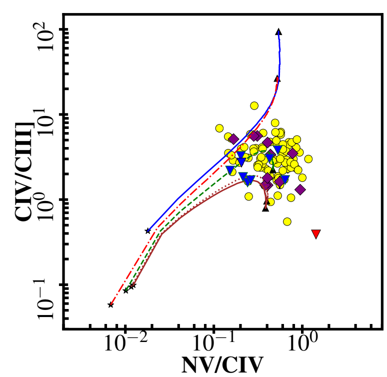

(g) $Z/Z_{\odot}$ = 5.0

Figure 4.4: Comparison of the observed emission line ratios from the SDSS type II quasars divided in objects with C IV/He II < 4 and C IV/He II > 4 (purple filled diamond and yellow filled circles, respectively), and Keck II HzRGs from Vernet et al. (2001) (blue filled triangles) with photoionization models using ionizing continuum power law index α = -1.0. Carbon is a secondary element in which its abundance is proportional to the square of the metallicity. Each diagram presents a different gas metallicity, i.e., $Z/Z_{\odot}$ = 0.5, 1.0, 2.0, 3.0, 4.0, 5.0. Curves with different colors represent the hydrogen gas density (n_H) described in 4.4a. At the end of each sequence, a solid black triangle corresponds to the lowest ionization parameter (U = 2×10^{-3}) while the solid black star corresponds to the maximum value of the ionization parameter (U = 1.0).

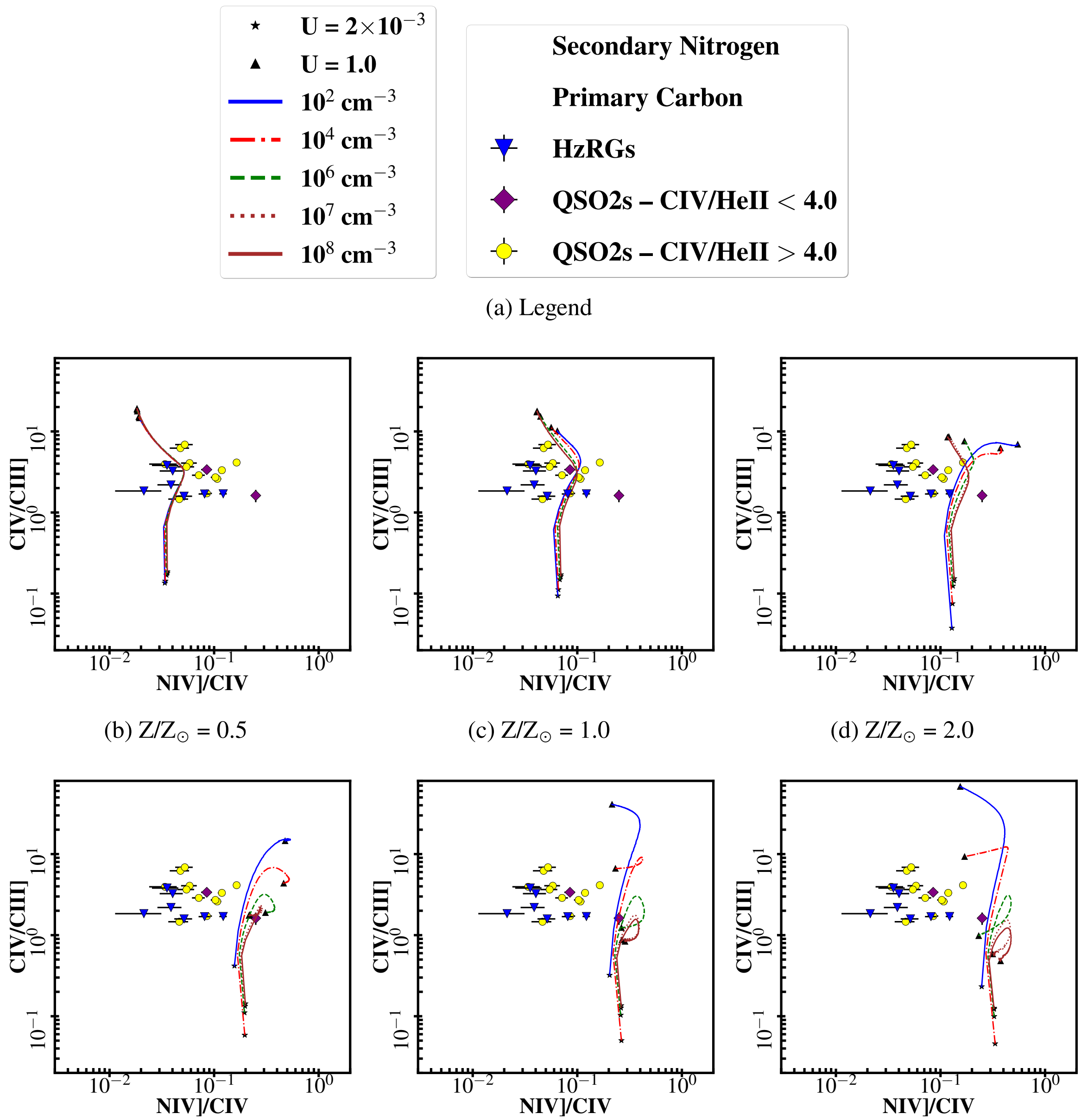

(a) Legend

(b) $Z/Z_{\odot}$ = 0.5 (c) $Z/Z_{\odot}$ = 1.0 (d) $Z/Z_{\odot}$ = 2.0

(e) $Z/Z_{\odot}$ = 3.0 (f) $Z/Z_{\odot}$ = 4.0 (g) $Z/Z_{\odot}$ = 5.0

Figure 4.5: Comparison of the observed emission line ratios from the SDSS type II quasars divided in objects with C IV/He II < 4 and C IV/He II > 4 (purple filled diamond and yellow filled circles, respectively), and Keck II HzRGs from Vernet et al. (2001) (blue filled triangles) with photoionization models using ionizing continuum power law index α = -1.0. Each diagram presents a different gas metallicity, i.e., $Z/Z_{\odot}$ = 0.5, 1.0, 2.0, 3.0, 4.0, 5.0. Curves with different colors represent the hydrogen gas density (n_H) described in 4.5a. At the end of each sequence, a solid black triangle corresponds to the lowest ionization parameter (U = $2{\times}10^{-3}$) while the solid black star corresponds to the maximum value of the ionization parameter (U = 1.0).

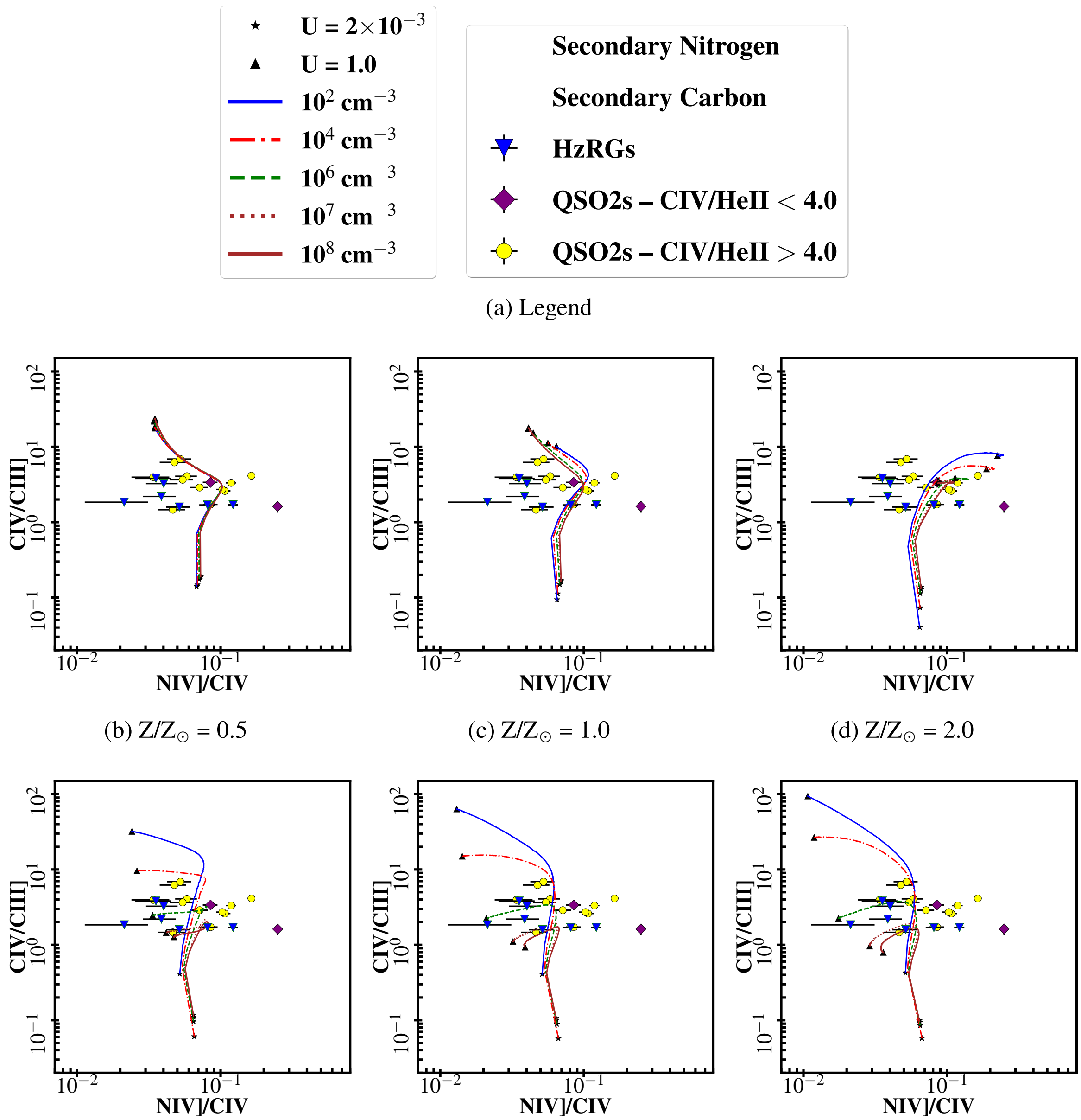

(a) Legend

(b) $Z/Z_\odot$ = 0.5 (c) $Z/Z_\odot$ = 1.0 (d) $Z/Z_\odot$ = 2.0

(e) $Z/Z_\odot$ = 3.0 (f) $Z/Z_\odot$ = 4.0 (g) $Z/Z_\odot$ = 5.0

Figure 4.6: Comparison of the observed emission line ratios from the SDSS type II quasars divided in objects with C IV/He II < 4 and C IV/He II > 4 (purple filled diamond and yellow filled circles, respectively), and Keck II HzRGs from Vernet et al. (2001) (blue filled triangles) with photoionization models using ionizing continuum power law index α = -1.0. Carbon is a secondary element in which its abundance is proportional to the square of the metallicity. Each diagram presents a different gas metallicity, i.e., $Z/Z_\odot$ = 0.5, 1.0, 2.0, 3.0, 4.0, 5.0. Curves with different colors represent the hydrogen gas density (n_H) described in 4.6a. At the end of each sequence, a solid black triangle corresponds to the lowest ionization parameter (U = 2×10^{-3}) while the solid black star corresponds to the maximum value of the ionization parameter (U = 1.0).

need to have a significant variation in order to simultaneously explain the distribution of the observational data in this diagram. Looking at those objects with high C IV/He II flux ratios, we find that using primary behaviour of C, a combination of high gas density ($n_H \gtrsim 10^6$ cm^{-3}) and Z/Z$_\odot$ > 2.0 appears to provide the best fit to the high flux ratio (see Fig. 4.7), however due to the degeneracy in C IV/He II we are unable to explain the highest flux ratios.

In the case of primary C behaviour, C IV/He II peaks at subsolar Z (Z/Z$_\odot$ ~ 0.3), and it gets lower as it moves to higher Z or lower Z. That means essentially any measured value of C IV/He II corresponds to two different possible values of Z, and the lower the measured value of C IV/He II, the more separated the two corresponding values of Z are.

Using secondary behaviour of C we find that a combination of intermediate gas density (n_H < 10^6 cm^{-3}) and Z/Z$_\odot \gtrsim$ 4.0 is required. In addition, C IV/He II does appear to show a simple relationship with Z, such that higher Z results in higher C IV/He II ratios.

The HzRGs have systematically weaker C IV/He II (versus UV and rest-frame optical lines) than most of the QSO2s. On the other hand, we note that there is no evidence for a systematic difference in the C IV/C III] ratio between the QSO2s and the HzRGs. Using primary behaviour of C, a combination of low gas density (n_H = 10^2 cm^{-3}) and Z/Z$_\odot$ > 2.0 appears to provide the best fit to the observed flux ratios. In the case of secondary C behaviour we note that, with exception of the diagram with Z/Z$_\odot$ = 0.5, the U-sequences with n_H = 10^2 cm^{-3} predict very high C IV/He II ratio compared with the observed C IV/He II ratio of the HzRGs.

4.6.2.3 Silicon abundance

The abundance of Si relative to other metals is particularly interesting because its behaviour deviates somewhat from that of O and other α-elements. In addition to being produced by short-lived massive stars, Si is also produced on very long timescales (~ 1 Gyr) by Type Ia supernovae, which means the Si abundance can in principle continue to increase long after star formation and O-production has ceased (e.g. Matteucci and Padovani, 1993).

In Figs. 4.12 and 4.13, we compare the observed flux ratios of Si III]/C III] and C IV/C III] with the prediction of the photoionization models. Our models using the Solar Si/O abundance ratio fail to explain the observed Si III]/C III] flux ratios of the quasars and radio galaxies that are detected in SiIII], with the observed ratios being a factor of ~10 higher than produced in these models. On the other hand, our models with a Si/O abundance ratio of 10 × Solar dramatically reduce this discrepancy, suggesting that Si/O and Si/C are an order of magnitude (or more) above their Solar values (see Figs. 4.14 and 4.15). The C IV/He II vs. Si III]/O III] diagram is consistent with this. We find no systematic difference in the Si III]/C III] or Si III]/O III] flux ratios between the QSO2s and HzRG samples.

These results are independent of whether the primary or secondary behaviour of carbon is

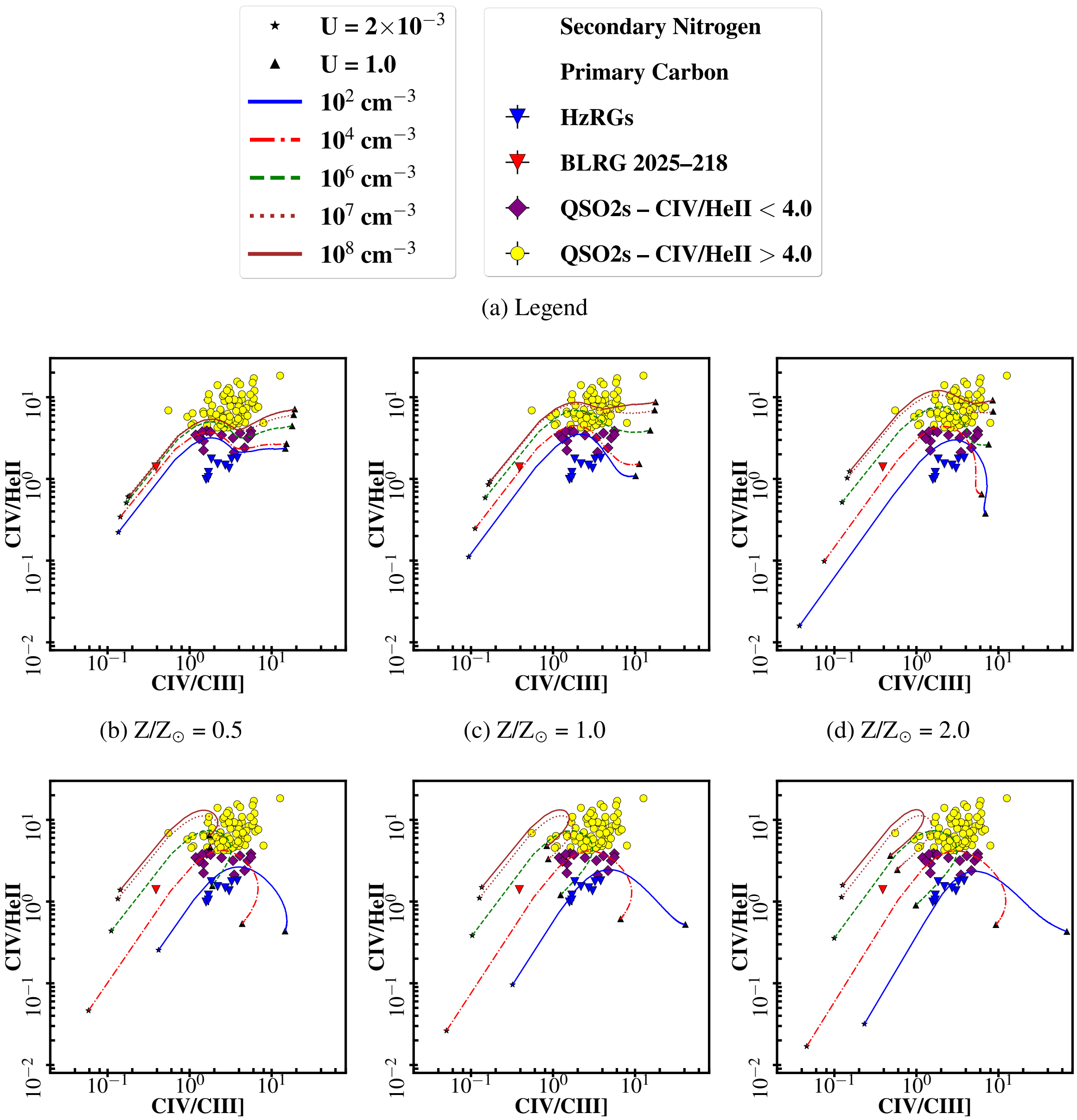

(a) Legend

(b) $Z/Z_\odot$ = 0.5 (c) $Z/Z_\odot$ = 1.0 (d) $Z/Z_\odot$ = 2.0

(e) $Z/Z_\odot$ = 3.0 (f) $Z/Z_\odot$ = 4.0 (g) $Z/Z_\odot$ = 5.0

Figure 4.7: Comparison of the observed emission line ratios from the SDSS type II quasars divided in objects with C IV/He II < 4 and C IV/He II > 4 (purple filled diamond and yellow filled circles, respectively), and Keck II HzRGs from Vernet et al. (2001) (blue filled triangles) with photoionization models using ionizing continuum power law index α = -1.0. Each diagram presents a different gas metallicity, i.e., $Z/Z_\odot$ = 0.5, 1.0, 2.0, 3.0, 4.0, 5.0. Curves with different colors represent the hydrogen gas density (n_H) described in 4.7a. At the end of each sequence, a solid black triangle corresponds to the lowest ionization parameter (U = 2×10^{-3}) while the solid black star corresponds to the maximum value of the ionization parameter (U = 1.0).

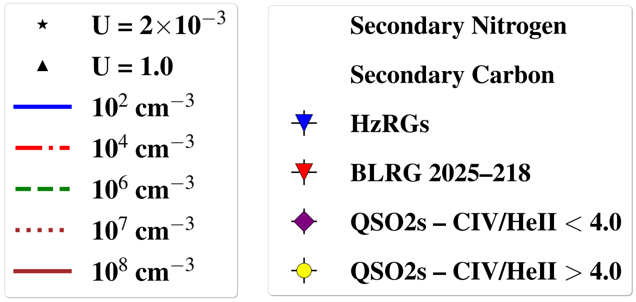

(a) Legend

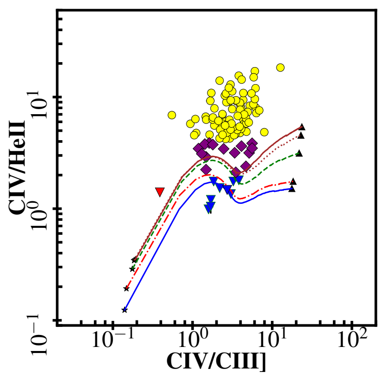

(b) $Z/Z_{\odot}$ = 0.5

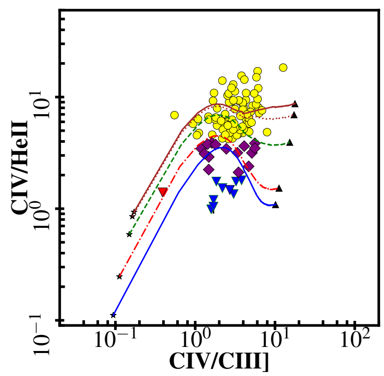

(c) $Z/Z_{\odot}$ = 1.0

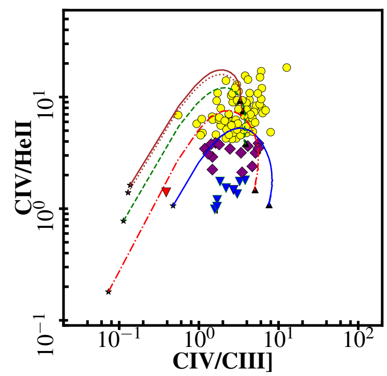

(d) $Z/Z_{\odot}$ = 2.0

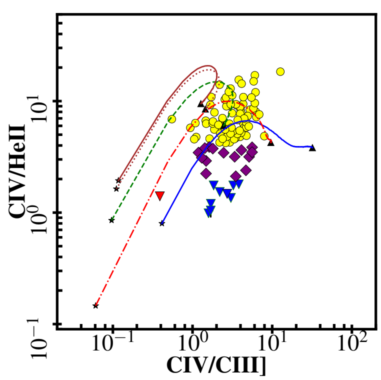

(e) $Z/Z_{\odot}$ = 3.0

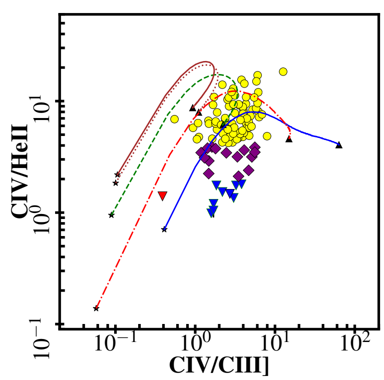

(f) $Z/Z_{\odot}$ = 4.0

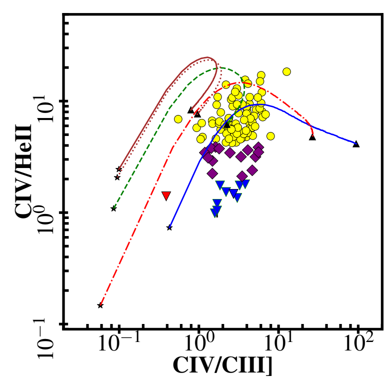

(g) $Z/Z_{\odot}$ = 5.0

Figure 4.8: Comparison of the observed emission line ratios from the SDSS type II quasars divided in objects with C IV/He II < 4 and C IV/He II > 4 (purple filled diamond and yellow filled circles, respectively), and Keck II HzRGs from Vernet et al. (2001) (blue filled triangles) with photoionization models using ionizing continuum power law index α = -1.0. Carbon is a secondary element in which its abundance is proportional to the square of the metallicity. Each diagram presents a different gas metallicity, i.e., $Z/Z_{\odot}$ = 0.5, 1.0, 2.0, 3.0, 4.0, 5.0. Curves with different colors represent the hydrogen gas density (n_H) described in 4.8a. At the end of each sequence, a solid black triangle corresponds to the lowest ionization parameter (U = 2×10^{-3}) while the solid black star corresponds to the maximum value of the ionization parameter (U = 1.0).

used. It is also important to be aware that these results only apply to quasars or radio galaxies for which Si III] emission has been detected and, as such, there may be a bias towards the presence of objects with very high Si abundances in these diagrams.

4.6.3 Gas Density

As mentioned already in Section 4.6.2, a subset of the QSO2s show very high values of C IV/He II and N V/He II, with one possible explanation being that their NLR has a relatively high gas density (e.g., $\gtrsim 10^6$ cm^{-3}), although very high N and C abundances may also explain the ratios. Here, we consider new line ratio diagnostics to break the degeneracy between density and abundance effects, and discuss which of the two effects is most likely the cause of the very high C IV/He II and N V/He II ratios.

For this, we propose three additional density-sensitive ratios: [Ne IV]2422/C IV, [Ne IV]2422/He II, and [Ne IV]1602/[Ne IV]2422. New diagnostic diagrams using these ratios are shown in Figs. 4.20 – 4.25. The line [Ne IV]2422 is often detected in photoionized regions associated with AGNs at high-z (e.g. Vernet et al., 2001), and as a forbidden line (critical density = 1.0×10^6 cm^{-3} for T_e = 10^4 K) it becomes collisionally de-excited at $n_e \gtrsim 10^6$ cm^{-3}. This means its flux ratio to permitted lines (e.g., [Ne IV]2422/C IV or [Ne IV]2422/He II) decreases as density increases.

Similarly, the forbidden line [Ne IV]1602, with a critical density of 1.0×10^8 cm^{-3} (for T_e = 10^4 K), also suffers collisional de-excitation at densities of $\gtrsim 10^8$ cm^{-3}, and its ratio to permitted lines also decreases as density increases. However, this line is usually very weak and thus detections are rare (e.g. Vernet et al., 2001), although the advent of the next generation of extremely large telescopes should make detection of this line in type 2 active galaxies more commonplace.

In addition, the ratio between [Ne IV]1602 and [Ne IV]2422 is sensitive to density because the two lines have different critical densities, with collisional de-excitation of [Ne IV]2422 starting at lower densities than [Ne IV]1602. As a result, the [Ne IV]1602/[Ne IV]2422 flux ratio increases as density increases.

In Figs. 4.24 and 4.25 we show C IV/He II *vs.* [Ne IV]2422/He II. When using the primary behaviour of carbon (Fig. 4.24), we find that the models fail to reach the positions of most of the plotted QSO2s, which lie above and/or to the right of the models. Although high densities do produce sufficiently high values of C IV/He II, this comes at the cost of a substantial decrease in [Ne IV]2422/He II due to collisional de-excitation of the [Ne IV] line. In other words, C IV/He II and [Ne IV]2422/He II are simultaneously too high to be explained by these models, regardless of which density or metallicity is used.

However, we find that when using secondary behaviour for carbon (Fig. 4.25), our high metallicity models ($Z/Z_{\odot} \gtrsim 2$) produce much higher CIV/HeII ratios even at low gas density ($\lesssim 10^4$ cm^{-3}), allowing the positions of the QSO2s to be generally well reproduced in this diagram. We obtain essentially the same result from the C IV/He II *vs.* [Ne IV]2422/C IV diagram (see Figs. 4.22 and 4.23).

In the C IV/He II *vs.* [Ne IV]1602/[Ne IV]2422 diagram (Fig. 4.20 and 4.21), most of the QSO2s have upper limits on the [Ne IV]1602/[Ne IV]2422 ratio which imply $n_e \lesssim 10^6$ cm^{-3}. However, there are two QSO2s where [Ne IV]1602 was detected and [Ne IV]2422 was not, and their lower limits on [Ne IV]1602/[Ne IV]2422 requires $n_e \gtrsim 10^6$ cm^{-3}, implying these two are intermediate or high density objects.

Overall, the positions of the HzRGs in the C IV/He II *vs.* [Ne IV]2422/He II and C IV/He II *vs.* [Ne IV]2422/C IV diagrams are well explained using models with $n_e \lesssim 10^4$ cm^{-3}, consistent with previous conclusions about the gas density in the extended gas of HzRGs (e.g. De Breuck et al., 2000a; Vernet et al., 2001; Humphrey et al., 2008b). Furthermore, we find that the single HzRG which has a measurement of both [Ne IV]1602 and [Ne IV]2422 (TXS 0828+193; Vernet et al. 2001) lies very close to the n_e = 100 cm^{-3} density models, consistent with a low gas density.

Interestingly, in the C IV/He II *vs.* [Ne IV]2422/He II diagram (Figs. 4.24 and 4.25) the HzRGs and QSO2s show no systematic difference in [Ne IV]2422/He II, suggesting the NLR of the plotted QSO2s and the HzRGs have similar gas densities. The systematic vertical offset of the QSO2s above the HzRGs then suggests that the QSO2s have substantially higher carbon abundance.

Of course, the conclusions derived from the [Ne IV] lines apply only to the objects for which we have detected one such line, and it is plausible that many other QSO2s in this sample are undetected in [Ne IV] as a result of collisional de-excitation in high-density gas. Nonetheless, this analysis shows that at least some of the QSO2s in this sample, including some objects with very high C IV/He II, have low density NLRs with high carbon abundances. On the other hand, at least two of the QSO2s do appear to have intermediate or high density ($n_e \gtrsim 10^6$ cm^{-3}), and thus it is likely that this sample of QSOs encompasses objects with a wide range in gas density.

Investigating the possible correlation between the C IV/He II flux ratio and the FWHM of the C IV emission line, we find that the Spearman correlation (ρ) and the t-distribution (p-value) indicate a reasonable positive relationship between the C IV/He II flux ratio and $FWHM_{CIV}$ with $\rho = 0.47$ and p-value = 9.01×10^{-7} (see Fig. 4.26). The diagram shows that there is a correlation between higher $FWHM_{CIV}$ and higher C IV/He II flux ratio, which is consistent with some of the QSOs having a contribution from a region with density and kinematic properties intermediate between the classical NLR and BLR. A possible alternative explanation is that outflows are present in some objects, broadening C IV and enhancing the C IV/He II due to shock ionization.

4.7 Revised selection criteria for QSO2s with low density NLR

In the previous sections we found that a significant fraction (71%) of the 145 Class A candidate QSO2s selected by Alexandroff et al. (2013) show UV line ratios consistent with intermediate/high gas densities. Here we propose refined selection criteria for QSO2s, using density-sensitive UV line flux ratios.

- Class 1: Highly likely QSO candidates with C IV/He II < 4 and [Ne IV]2422/He II > 0.4 and [Ne IV]2422/C IV > 0.1 consistent with low electron density (see Figs. 4.27a and 4.27b). One object (0.7%) from the QSO2 sample meets these requirements (SDSSJ213557.35-032130.0; see Table 4.7).

- Class 2: Good QSO candidates with C IV/He II < 4, but have no useful information from [Ne IV] ([Ne IV] not detected and the [Ne IV]2422/He II and [Ne IV]2422/C IV upper limits are consistent with [Ne IV]2422/He II > 0.4 and [Ne IV]2422/C IV > 0.1; see Figs. 4.27a and 4.27b). Fourteen objects (9.7%) from the QSO2 sample meet these requirements (see Table 4.7).

- Class 3: Quasars with [Ne IV]2422/He II and [Ne IV]2422/C IV ratios consistent with low densities, but with C IV/He II > 4 consistent with high gas density and/or high carbon abundance. As discussed in section 4.6.3, such objects could be objects with an intermediate orientation such that the low density NLR and more central intermediate/high density are both observed. On the other hand, they may be QSO2s with a low density NLR and a high carbon abundance. Six objects (4.1%) from the QSO2 sample meet these requirements (see Table 4.7).

- Class 4: Ambiguous, potentially intermediate/high density objects. QSOs with C IV/He II > 4 but [Ne IV]2422/He II < 0.4 and [Ne IV]2422/C IV < 0.1 (or no information about [Ne IV]2422; see Figs. 4.27a and 4.27b). A few objects appear consistent with this criterion, including those two using [Ne IV]2422/He II and [Ne IV]2422/C IV upper limits. However, by rejecting those QSOs that have CIV/HeII > 4 but no information about [Ne IV]2422/He II or [Ne IV]2422/C IV, it is possible that some QSO2s with genuine low density NLRs and high carbon abundance are being rejected alongside high density objects. Seventy-seven objects (53%) from the QSO2 sample meet these requirements (see Table 4.7 and 4.8).

- Class 5: Likely intermediate or high density objects. QSOs with [Ne IV]1602/[Ne IV]2422 > 0.5 (see Fig. 4.27c). Two objects (1.4%) from the QSO2 sample meet these requirements (see Table 4.8).

4.8 Conclusions

We have studied the ultraviolet emission line ratios of a sample of 145 Type 2 quasars from SDSS BOSS, and have compared them against powerful radio galaxies at z ~ 2.5 and against a grid of AGN photoionization models. The main results are as follows:

- Some QSO2s show very high CIV/HeII (> 10), consistent with BLR densities (>10^7 cm^{-3}) or supersolar C/O (i.e., secondary carbon).
- Where [NeIV] λ2422 has been detected (15 QSO2s), gas densities < 10^6 cm^{-3} are implied. Two further objects show [NeIV] λ1602 / [NeIV] λ2422 ratios that imply densities > 10^6 cm^{-3}.
- Solar or supersolar nitrogen abundances and gas metallicities are required in most of the quasars (e.g. the NV/HeII ratio).
- The degeneracy between high density and high C abundance appears to be broken using the CIV/HeII vs [NeIV]/HeII diagram. Both ratios are density sensitive, but the cloud of QSO2s is positioned where none of the models that use primary C can reach. However, models using secondary C can reach the cloud of QSO2s at supersolar metallicities.
- We compare the UV emission line ratios of the QSO2s to high-redshift radio galaxies at z > 2 (HzRGs), and find that the QSO2s are systematically offset to higher CIV/HeII, CIII]/HeII and NV/HeII suggesting systematically higher gas density and/or systematically higher C and N abundances. However, we find no evidence for a systematic difference in the N/C abundance ratio between the two types of object.
- Scatter in the NIV]/CIV ratio implies a significant scatter in the N/C abundance ratio in the QSO2s and HzRGs, although it is unclear whether the scatter is due to differences in the ISM abundance ratio or differential depletion of N and C into dust grains. Interestingly, we also find that adopting secondary behaviour for both N and C alleviates the "NIV] problem" reported by a number of previous studies.
- Using secondary behaviour of carbon reported by Nicholls et al. (2017) (in addition to Nitrogen) we note that NV/CIV and NIV]/CIV stops being a useful metallicity indicator,

but is still an indicator of U and the N/C ratio. For a given U, a dustier QSO ought to have a higher NV/CIV due to greater depletion of C than N (we think this might give a nice explanation of the polarization - NV/CIV correlation seen in HzRGs).

- A subset of the QSO2s and HzRGs appear to be "Silicon-loud", with SiIII] relative fluxes suggesting Si/C and Si/O are an order of magnitude above their Solar values (see Figs. from 4.12 to 4.19).

- Finally, we propose new UV-line based criteria to select genuine type 2 quasars with low-density narrow line regions.

Table 4.1: List of flux ratios measurements of the rest-frame UV and optical of HzRGs from the literature. See §4.3.2 for more details.

	4C+03.24[a]	0828+193[a,b]	4C+23.56a[a,b]	0731+438[a]	4C–00.54[a,b]	4C+48.48[a]	0211–122[a,b]	4C+40.36[a,b]	0406–244[b]	1558–003[b]	2025–218[b]	2104–242[b]	0943–242[a,c]
Flux ratio	z = 3.56	z = 2.57	z = 2.48	z = 2.43	z =2.36	z = 2.34	z = 2.34	z = 2.27	z = 2.44	z = 2.53	z = 2.63	z = 2.49	z = 2.92
(OVI+CII)/HeII	–	–	–	–	–	–	–	–	–	–	–	–	0.77 ± 0.12
Lyα/HeII	48.90 ± 12.30	8.40 ± 0.20	5.20 ± 0.40	14.10 ± 0.20	12.20 ± 0.30	13.20 ± 0.90	0.57 ± 0.02	14.68 ± 1.17	5.83 ± 0.59	15.44 ± 0.61	16.00 ± 3.77	13.00 ± 1.64	9.90 ± 0.43
NV/HeII	0.90 ± 0.30	0.4 ± 0.1	0.80 ± 0.10	0.23 ± 0.02	0.60 ± 0.10	0.27 ± 0.08	0.95 ± 0.09	0.40 ± 0.08	< 0.17	0.46 ± 0.10	2.00 ± 0.57	0.32 ± 0.04	0.30 ± 0.06
(SiIV+OIV])/HeII	1.20 ± 0.60	0.30	0.10	0.32 ± 0.01	0.50	0.30	0.20	0.30	0.25 ± 0.09	0.41 ± 0.10	–	0.39 ± 0.05	4.04
NIV]/HeII	–	0.07 ± 0.01	0.15 ± 0.04	0.06 ± 0.01	–	0.08 ± 0.02	0.06 ± 0.01	0.04 ± 0.01	< 0.08	0.14 ± 0.04	–	–	1.09 ± 0.14
CIV/HeII	2.40 ± 0.70	1.80 ± 0.10	1.20 ± 0.10	1.53 ± 0.04	1.40 ± 0.10	1.04 ± 0.07	1.80 ± 0.07	1.80 ± 0.14	0.75 ± 0.10	2.67 ± 0.14	1.40 ± 0.49	0.80 ± 0.13	1.47 ± 0.11
[NeIV]1602/HeII	–	0.02	–	–	–	–	–	–	–	–	–	–	–
OIII]/HeII	–	0.18	0.30	0.20	0.17	0.11	0.08	0.16 ± 0.01	0.17 ± 0.08	0.43 ± 0.08	–	0.1 ± 0.03	3.45
SiIII]/HeII	–	0.18	–	0.09	–	–	–	–	–	0.13 ± 0.03	1.80 ± 1.25	–	0.05
CIII]/HeII	–	0.5 ± 0.1	0.7 ± 0.1	0.70 ± 0.02	0.45 ± 0.03	0.62 ± 0.04	0.50 ± 0.03	0.95 ± 0.17	0.75 ± 0.10	0.75 ± 0.10	3.60 ± 1.40	–	0.54 ± 0.04
[NeIV]2422/HeII	–	0.50	0.90	0.60	1.00	0.60	0.30	0.50	0.83 ± 0.26	0.56 ± 0.11	–	–	–
[OIII]5008/Hα	–	–	3.40 ± 0.31	–	3.43 ± 0.29	–	3.27 ± 0.56	3.69 ± 0.06	–	4.80 ± 1.47	1.60 ± 0.57	4.00 ± 0.64	–
[OIII]5008/Hβ	–	9.53 ± 0.58	9.71 ± 4.20	–	> 17.15	–	> 6.54	10.85 ± 1.61	12.6 ± 0.89	8.00 ± 2.71	> 5.33	13.33 ± 4.75	–
[NII]/Hα	–	–	0.21 ± 0.07	–	0.29 ± 0.05	–	< 0.2	1.6	–	0.70 ± 0.29	0.60 ± 0.27	0.30 ± 0.06	–
[OII]3728/[OIII]5008	–	0.18 ± 0.01	0.27 ± 0.06	–	0.15 ± 0.03	–	0.12 ± 0.03	0.39 ± 0.02	0.21 ± 0.02	0.31 ± 0.05	< 1.50	0.15 ± 0.03	0.32 ± 0.01

References: [a]Vernet et al. (2001), [b]Humphrey et al. (2008b), [c]Silva et al. (2018b).

Table 4.2: List of the first forty type II quasars followed by the detected emission lines. The line fluxes obtained with the fitting routine are measured in $\times 10^{-17}$ erg cm^{-2} s^{-1} . See §2.5 for more details.

SDSS name	z	Class	OVI+CII	Lyα	NV	OI	SiIV+OIV{}	NIV{}	CIV	{[}NeIV{]}1602	HeII	OIII{}	SiIII{}	CIII{}	{[}NeIV{]}2422	MgII
J011506.65-015307.0	2.33	4		587.7 ± 11.8	44.7 ± 3.9	26.4 ± 2.9	9.3 ± 1.9		149.8 ± 4.8		17.9 ± 2.2		10.6 ± 0.7	37.3 ± 0.7		
J022051.68-012403.3	2.60	4		1171.7 ± 18.3	130.3 ± 4.8	22.6 ± 3.9	36.0 ± 4.8		203.7 ± 7.2		21.6 ± 3.3			47.1 ± 2.7		
J075119.09+130202.4	2.64	4		558.4 ± 3.8	68.4 ± 4.5	28.5 ± 3.8	38.1 ± 3.8		129.6 ± 5.2		27.2 ± 3.9			116.6 ± 5.0		
J075656.49+362507.4	2.87	5	104.9 ± 7.1	912.9 ± 16.6	122.5 ± 4.9	26.6 ± 3.2	20.7 ± 1.9		195.9 ± 0.3	<17.2	31.3 ± 4.2		82.8 ± 2.3	45.0 ± 0.7	13.5 ± 1.6	
J081950.96+111507.9	2.81	4	94.5 ± 4.4	787.0 ± 13.7	56.7 ± 3.5	5.9 ± 1.9	38.3 ± 2.0		161.8 ± 4.4		20.7 ± 3.3			39.5 ± 3.0		
J084005.00+344832.1	2.55	4		648.7 ± 5.4	27.1 ± 2.3	21.3 ± 2.5	8.5 ± 1.5	11.8 ± 1.8	164.6 ± 9.8		18.1 ± 2.1	21.8 ± 1.9	13.7 ± 0.7	57.1 ± 0.5		
J095118.93+450432.4	2.45	5		1396.5 ± 19.6	45.3 ± 3.6	46.5 ± 3.9	51.5 ± 4.8		288.8 ± 5.8	<17.5	34.5 ± 5.0			55.2 ± 2.7	16.5 ± 1.1	77.4 ± 11.6
J100250.98+382532.3	2.73		129.6 ± 9.0	688.9 ± 13.8	96.8 ± 4.5	16.8 ± 1.6			188.1 ± 3.7	<38.4	20.3 ± 2.7	12.9 ± 3.4		112.4 ± 5.1	14.5 ± 1.0	
J100916.93+031128.9	2.69	4	169.5 ± 11.5	659.4 ± 10.6	136.9 ± 5.1	14.9 ± 3.2	24.7 ± 2.8		147.0 ± 3.0		16.0 ± 2.4			41.0 ± 3.0		
J112230.35+341538.0	2.40	5		639.1 ± 9.6	52.9 ± 3.4		32.1 ± 4.5		148.4 ± 2.7	<15.1	31.1 ± 3.5			37.6 ± 3.1	12.7 ± 1.8	
J114542.07+401318.4	3.30	4	129.6 ± 6.2	684.4 ± 3.7	134.0 ± 3.4		22.2 ± 3.6	11.2 ± 2.1	234.4 ± 2.2		29.2 ± 2.0	9.9 ± 2.0		37.7 ± 3.2		
J125148.53+060027.4	2.27	4		766.0 ± 10.7	87.2 ± 5.7	39.2 ± 4.5	39.8 ± 4.4		169.4 ± 0.3		29.4 ± 3.2	19.7 ± 3.2		38.2 ± 3.7		43.9 ± 3.6
J135531.46+072950.6	3.15	5	112.9 ± 6.0	867.0 ± 17.2	58.1 ± 3.3	34.7 ± 3.4	43.9 ± 5.6		151.7 ± 2.6	<22.8	27.3 ± 3.4	28.6 ± 4.0		65.5 ± 6.2	12.0 ± 0.7	
J150549.73+074309.0	3.32	4	319.6 ± 8.6	1314.3 ± 11.0	276.5 ± 4.1	28.9 ± 3.0	51.2 ± 4.5		392.7 ± 3.2		67.8 ± 3.8	29.0 ± 3.7		83.4 ± 5.1		
J153306.06+322649.6	2.71	4	160.2 ± 11.3	657.8 ± 9.1	137.8 ± 4.6	19.1 ± 1.1	47.3 ± 3.1		232.4 ± 9.6		15.0 ± 2.8	17.5 ± 3.5	24.0 ± 0.7	61.1 ± 0.7		
J160900.01+190534.8	2.54	4	204.2 ± 14.1	1791.3 ± 8.6	76.4 ± 3.6	65.6 ± 3.0	29.7 ± 1.8	12.8 ± 1.8	375.7 ± 6.9		42.3 ± 3.1	45.4 ± 3.9		95.1 ± 3.0		58.1 ± 8.1
J161059.96+260321.5	2.28	2		703.5 ± 12.8	59.2 ± 6.4	44.2 ± 6.2	38.6 ± 6.2		190.8 ± 3.5		49.5 ± 9.4	16.3 ± 2.8		34.1 ± 3.6		44.1 ± 3.3
J162812.51+233734.8	2.39	4		998.7 ± 11.2	106.4 ± 3.6	63.4 ± 4.1	75.2 ± 4.2	13.2 ± 1.3	283.2 ± 1.8		42.5 ± 5.2	34.5 ± 4.3		193.5 ± 1.7		209.7 ± 13.9
J163343.85+261026.2	3.07	4	50.8 ± 3.6	794.6 ± 9.4	54.0 ± 2.8	44.8 ± 3.4			123.3 ± 0.3	24.1 ± 2.8	21.4 ± 3.4		17.2 ± 1.8	149.1 ± 1.8	<17.8	
J222946.61+005540.5	2.37	4		943.4 ± 17.1	80.5 ± 4.3				153.6 ± 2.8		17.1 ± 1.6		12.2 ± 0.8	57.8 ± 0.8		
J001040.82+004550.5	2.72	3	63.7 ± 4.8	256.1 ± 3.9	34.3 ± 2.6		11.6 ± 1.7		69.9 ± 0.5		16.4 ± 3.0		9.0 ± 0.6	23.8 ± 0.5	12.4 ± 1.6	
J001738.55-011838.7	3.22			177.6 ± 4.9	16.7 ± 1.9				31.4 ± 3.1							
J001814.72+023258.8	2.90	2	16.7 ± 2.0	237.0 ± 3.6					25.3 ± 2.7		7.3 ± 1.5			21.3 ± 2.2		
J003605.26+001618.7	2.94			82.8 ± 3.9	15.2 ± 2.5				19.8 ± 2.2					10.8 ± 1.8		
J004423.20+035715.5	2.22	4		560.6 ± 17.3	17.9 ± 3.9				72.1 ± 2.4		11.4 ± 2.0	12.5 ± 2.6		66.4 ± 2.4		
J004600.48+000543.6	2.46	4		267.3 ± 5.8	33.9 ± 2.9		14.6 ± 1.6		50.3 ± 2.5		7.3 ± 2.0			91.4 ± 1.1		25.8 ± 1.2
J004728.77+004020.3	3.06		101.6 ± 5.5	224.8 ± 7.1	36.0 ± 3.4				94.4 ± 6.0							
J012552.08-015218.3	3.18	4	83.1 ± 5.5	116.5 ± 2.5	85.0 ± 2.5		34.3 ± 3.6		107.2 ± 2.3		8.3 ± 1.7			35.7 ± 3.6		
J013747.84+000612.7	2.82		92.2 ± 7.2	567.8 ± 1.1	43.9 ± 3.3	30.1 ± 3.0			121.6 ± 3.0							
J014607.15+121119.9	3.14	4	67.6 ± 3.5	523.8 ± 7.3	60.9 ± 3.8	34.9 ± 3.2		8.3 ± 1.5	97.2 ± 2.6		8.9 ± 1.2			56.5 ± 2.1		
J014841.83+055024.2	2.66			233.2 ± 3.0					19.3 ± 1.9					8.5 ± 1.6		
J015458.32+015720.2	2.89		33.2 ± 4.0	187.1 ± 4.6					28.7 ± 2.7							
J015700.14+073116.0	3.05	4	83.7 ± 5.2	590.1 ± 3.4	40.4 ± 3.0				112.0 ± 3.5		6.6 ± 1.2			18.5 ± 1.8		
J020245.82+000848.4	2.22	4		352.8 ± 8.2					75.0 ± 2.5		10.4 ± 1.2			11.9 ± 2.5		
J020643.64+010403.3	2.66	4	69.3 ± 9.9	465.6 ± 10.7	91.8 ± 7.4	65.9 ± 6.1			123.2 ± 5.6		27.1 ± 5.0	22.2 ± 4.9	29.1 ± 1.5	117.3 ± 1.4		
J020728.19+033833.5	2.76	4	103.6 ± 6.1	404.2 ± 8.6	128.2 ± 1.9	18.4 ± 2.1	40.2 ± 2.7		150.7 ± 4.5		23.8 ± 3.7	23.5 ± 3.7	29.5 ± 0.7	64.5 ± 0.7		
J021834.53-033518.4	3.02			157.4 ± 5.0	16.4 ± 2.1				37.0 ± 3.7							
J022447.84+032452.0	2.53			249.8 ± 1.3	22.9 ± 2.8				28.6 ± 1.3							
J023210.88+002835.1	2.29			51.8 ± 2.9	22.4 ± 2.8				18.2 ± 0.9					9.1 ± 1.6		57.0 ± 9.0
J023337.89+002303.7	2.83			145.4 ± 6.5	8.9 ± 1.6	3.2 ± 0.3			19.1 ± 1.5							

Table 4.3: Set of chemical abundances used in MAPPINGS Ie. The abundances were obtained using primary behaviour of C (herefater PC).

$Z/Z_\odot$	0.5	1.0	2.0	3.0	4.0	5.0
H	1.0	1.0	1.0	1.0	1.0	1.0
He	8.5×10^{-2}	8.5×10^{-2}	8.5×10^{-2}	8.5×10^{-2}	8.5×10^{-2}	8.5×10^{-2}
C	1.35×10^{-4}	2.7×10^{-4}	5.4×10^{-4}	8.1×10^{-4}	1.08×10^{-3}	1.35×10^{-3}
N	1.7×10^{-5}	6.8×10^{-5}	2.72×10^{-4}	6.12×10^{-4}	1.088×10^{-3}	1.7×10^{-3}
O	2.45×10^{-4}	4.9×10^{-4}	9.8×10^{-4}	1.47×10^{-3}	1.96×10^{-3}	2.45×10^{-3}
Ne	4.25×10^{-5}	8.5×10^{-5}	1.7×10^{-4}	2.55×10^{-4}	3.4×10^{-4}	4.25×10^{-4}
Fe	1.6×10^{-5}	3.2×10^{-5}	6.4×10^{-5}	9.6×10^{-5}	1.28×10^{-4}	1.6×10^{-4}
Mg	2.0×10^{-5}	4.0×10^{-5}	8.0×10^{-5}	1.2×10^{-4}	1.6×10^{-4}	2.0×10^{-4}
Si	1.6×10^{-5}	3.2×10^{-5}	6.4×10^{-5}	9.6×10^{-5}	1.28×10^{-4}	1.6×10^{-4}
S	6.5×10^{-6}	1.3×10^{-5}	2.6×10^{-5}	3.9×10^{-5}	5.2×10^{-5}	6.5×10^{-5}
Ca	1.1×10^{-6}	2.2×10^{-6}	4.4×10^{-6}	6.6×10^{-6}	8.8×10^{-6}	1.1×10^{-5}
Ar	1.25×10^{-6}	2.5×10^{-6}	5.0×10^{-6}	7.5×10^{-6}	1.0×10^{-5}	1.25×10^{-5}

Table 4.4: Set of chemical abundances used in MAPPINGS Ie. The abundances were obtained using secondary behaviour of C (herefater SC).

$Z/Z_\odot$	0.5	1.0	2.0	3.0	4.0	5.0
H	1.0	1.0	1.0	1.0	1.0	1.0
He	8.5×10^{-2}	8.5×10^{-2}	8.5×10^{-2}	8.5×10^{-2}	8.5×10^{-2}	8.5×10^{-2}
C	6.75×10^{-5}	2.7×10^{-4}	1.08×10^{-3}	2.43×10^{-3}	4.32×10^{-3}	6.75×10^{-3}
N	1.7×10^{-5}	6.8×10^{-5}	2.72×10^{-4}	6.12×10^{-4}	1.088×10^{-3}	1.7×10^{-3}
O	2.45×10^{-4}	4.9×10^{-4}	9.8×10^{-4}	1.47×10^{-3}	1.96×10^{-3}	2.45×10^{-3}
Ne	4.25×10^{-5}	8.5×10^{-5}	1.7×10^{-4}	2.55×10^{-4}	3.4×10^{-4}	4.25×10^{-4}
Fe	1.6×10^{-5}	3.2×10^{-5}	6.4×10^{-5}	9.6×10^{-5}	1.28×10^{-4}	1.6×10^{-4}
Mg	2.0×10^{-5}	4.0×10^{-5}	8.0×10^{-5}	1.2×10^{-4}	1.6×10^{-4}	2.0×10^{-4}
Si	1.6×10^{-5}	3.2×10^{-5}	6.4×10^{-5}	9.6×10^{-5}	1.28×10^{-4}	1.6×10^{-4}
S	6.5×10^{-6}	1.3×10^{-5}	2.6×10^{-5}	3.9×10^{-5}	5.2×10^{-5}	6.5×10^{-5}
Ca	1.1×10^{-6}	2.2×10^{-6}	4.4×10^{-6}	6.6×10^{-6}	8.8×10^{-6}	1.1×10^{-5}
Ar	1.25×10^{-6}	2.5×10^{-6}	5.0×10^{-6}	7.5×10^{-6}	1.0×10^{-5}	1.25×10^{-5}

Table 4.5: Set of chemical abundances used in MAPPINGS Ie. The abundances were obtained using primary carbon with Si/O=10xSolar (or PCSi10).

$Z/Z_\odot$	0.5	1.0	2.0	3.0	4.0	5.0
H	1.0	1.0	1.0	1.0	1.0	1.0
He	8.5×10^{-2}	8.5×10^{-2}	8.5×10^{-2}	8.5×10^{-2}	8.5×10^{-2}	8.5×10^{-2}
C	1.35×10^{-4}	2.7×10^{-4}	1.08×10^{-3}	2.43×10^{-3}	4.32×10^{-3}	6.75×10^{-3}
N	1.7×10^{-5}	6.8×10^{-5}	2.72×10^{-4}	6.12×10^{-4}	1.088×10^{-3}	1.7×10^{-3}
O	2.45×10^{-4}	4.9×10^{-4}	9.8×10^{-4}	1.47×10^{-3}	1.96×10^{-3}	2.45×10^{-3}
Ne	4.25×10^{-5}	8.5×10^{-5}	1.7×10^{-4}	2.55×10^{-4}	3.4×10^{-4}	4.25×10^{-4}
Fe	1.6×10^{-5}	3.2×10^{-5}	6.4×10^{-5}	9.6×10^{-5}	1.28×10^{-4}	1.6×10^{-4}
Mg	2.0×10^{-5}	4.0×10^{-5}	8.0×10^{-5}	1.2×10^{-4}	1.6×10^{-4}	2.0×10^{-4}
Si	1.6×10^{-4}	3.2×10^{-4}	6.4×10^{-4}	9.6×10^{-4}	1.28×10^{-3}	1.6×10^{-3}
S	6.5×10^{-6}	1.3×10^{-5}	2.6×10^{-5}	3.9×10^{-5}	5.2×10^{-5}	6.5×10^{-5}
Ca	1.1×10^{-6}	2.2×10^{-6}	4.4×10^{-6}	6.6×10^{-6}	8.8×10^{-6}	1.1×10^{-5}
Ar	1.25×10^{-6}	2.5×10^{-6}	5.0×10^{-6}	7.5×10^{-6}	1.0×10^{-5}	1.25×10^{-5}

Table 4.6: Set of chemical abundances used in MAPPINGS Ie. The abundances were obtained using secondary carbon with Si/O=10xSolar (or SCSi10).

$Z/Z_\odot$	0.5	1.0	2.0	3.0	4.0	5.0
H	1.0	1.0	1.0	1.0	1.0	1.0
He	8.5×10^{-2}	8.5×10^{-2}	8.5×10^{-2}	8.5×10^{-2}	8.5×10^{-2}	8.5×10^{-2}
C	6.75×10^{-5}	2.7×10^{-4}	1.08×10^{-3}	2.43×10^{-3}	4.32×10^{-3}	6.75×10^{-3}
N	1.7×10^{-5}	6.8×10^{-5}	2.72×10^{-4}	6.12×10^{-4}	1.088×10^{-3}	1.7×10^{-3}
O	2.45×10^{-4}	4.9×10^{-4}	9.8×10^{-4}	1.47×10^{-3}	1.96×10^{-3}	2.45×10^{-3}
Ne	4.25×10^{-5}	8.5×10^{-5}	1.7×10^{-4}	2.55×10^{-4}	3.4×10^{-4}	4.25×10^{-4}
Fe	1.6×10^{-5}	3.2×10^{-5}	6.4×10^{-5}	9.6×10^{-5}	1.28×10^{-4}	1.6×10^{-4}
Mg	2.0×10^{-5}	4.0×10^{-5}	8.0×10^{-5}	1.2×10^{-4}	1.6×10^{-4}	2.0×10^{-4}
Si	1.6×10^{-4}	3.2×10^{-4}	6.4×10^{-4}	9.6×10^{-4}	1.28×10^{-3}	1.6×10^{-3}
S	6.5×10^{-6}	1.3×10^{-5}	2.6×10^{-5}	3.9×10^{-5}	5.2×10^{-5}	6.5×10^{-5}
Ca	1.1×10^{-6}	2.2×10^{-6}	4.4×10^{-6}	6.6×10^{-6}	8.8×10^{-6}	1.1×10^{-5}
Ar	1.25×10^{-6}	2.5×10^{-6}	5.0×10^{-6}	7.5×10^{-6}	1.0×10^{-5}	1.25×10^{-5}

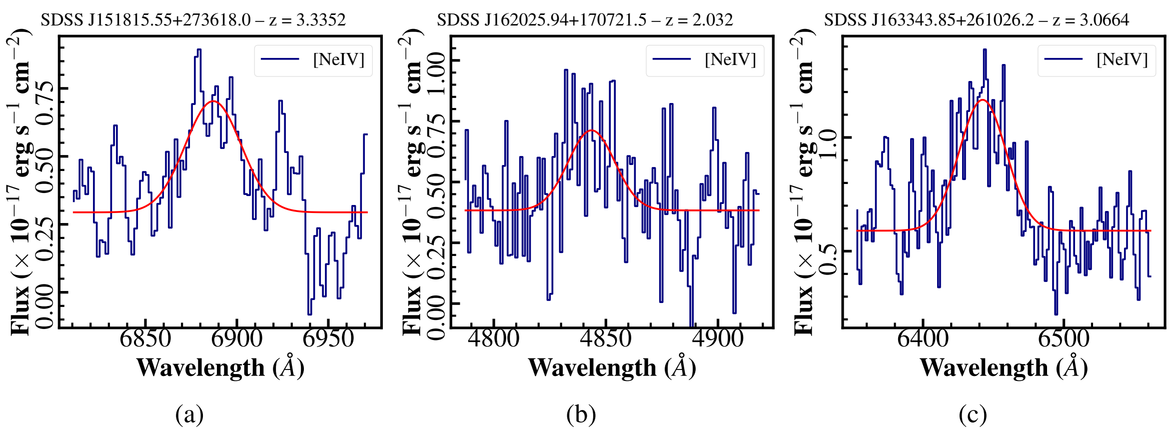

Figure 4.9: Spectra of the emission line [Ne IV] λ 1602 detected in some type II quasars.

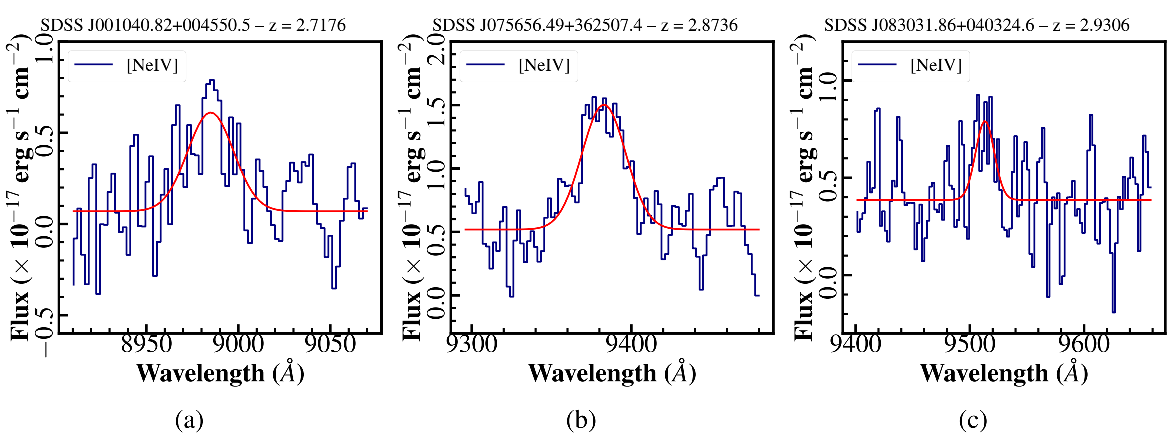

Figure 4.10: Spectra of the emission line [Ne IV] λ 2422 detected in some type II quasars.

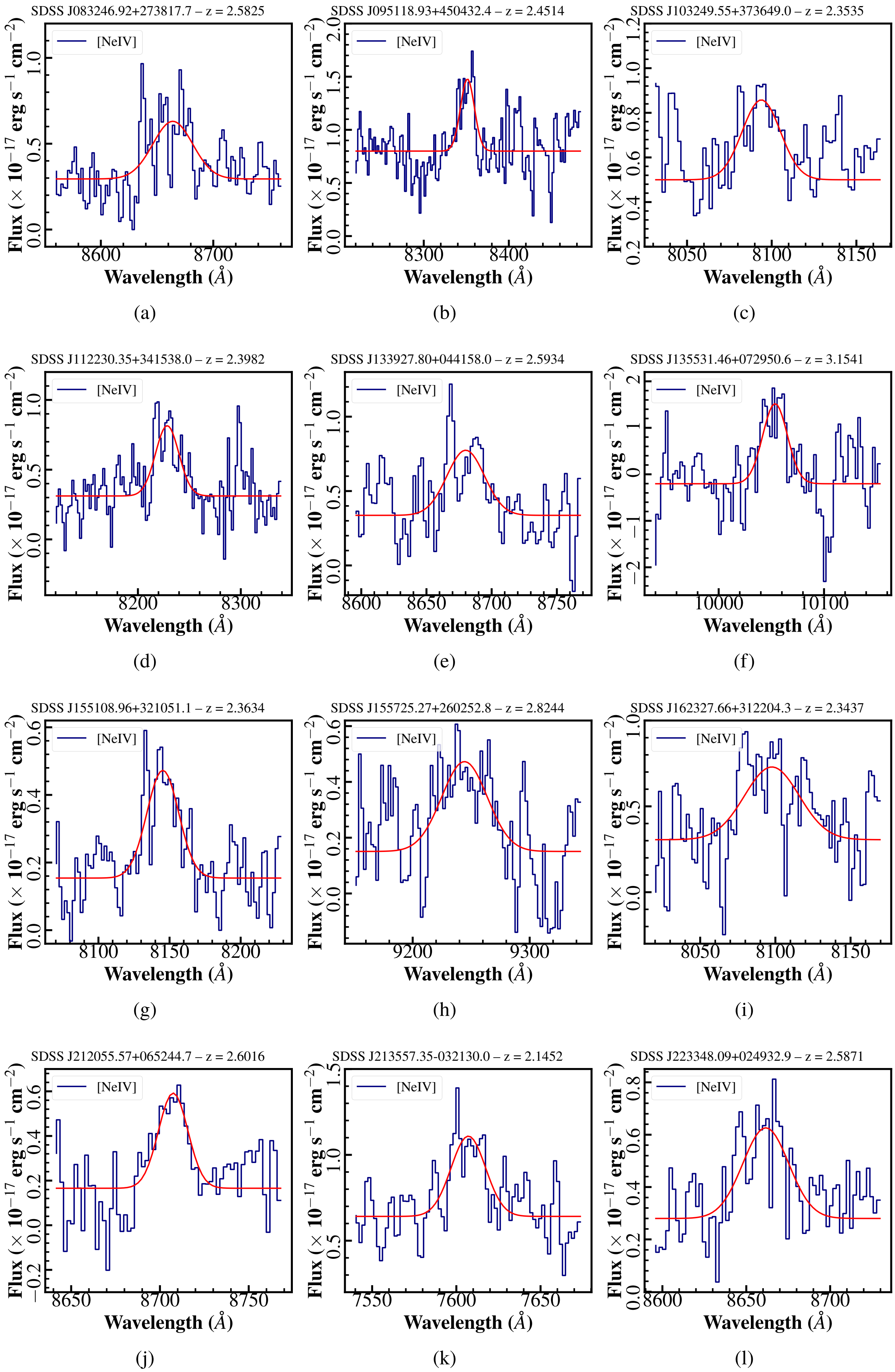

Figure 4.11: (continued).

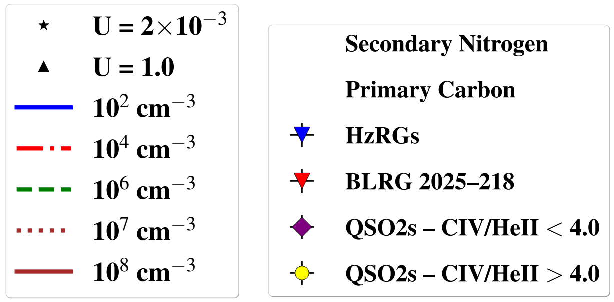

(a) Legend

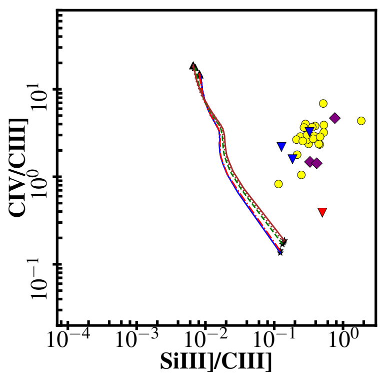

(b) Z/Z$_\odot$ = 0.5

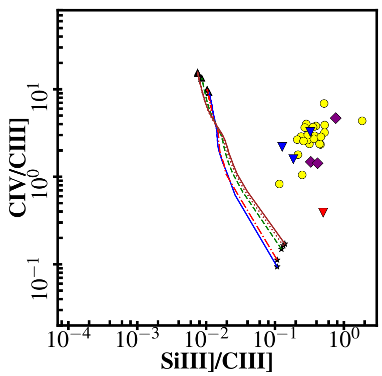

(c) Z/Z$_\odot$ = 1.0

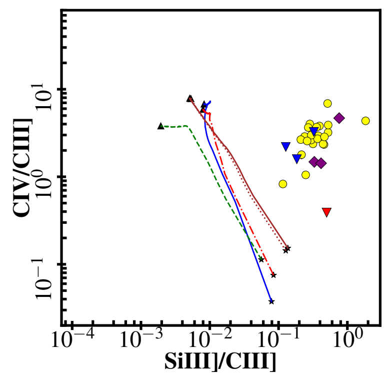

(d) Z/Z$_\odot$ = 2.0

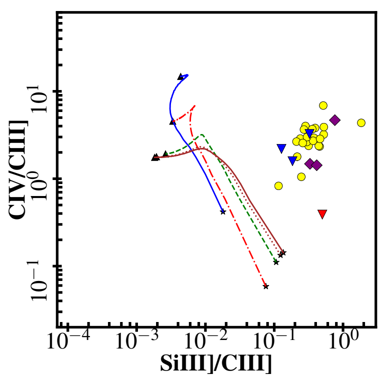

(e) Z/Z$_\odot$ = 3.0

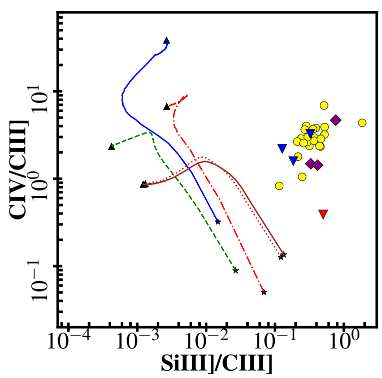

(f) Z/Z$_\odot$ = 4.0

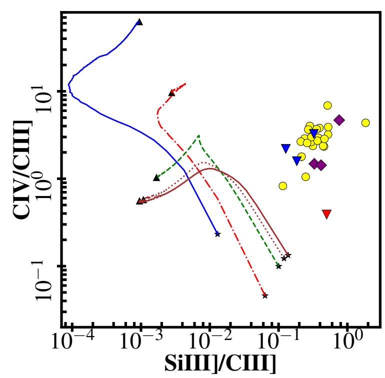

(g) Z/Z$_\odot$ = 5.0

Figure 4.12: Comparison of the observed emission line ratios from the SDSS type II quasars divided in objects with C IV/He II < 4 and C IV/He II > 4 (purple filled diamond and yellow filled circles, respectively), and Keck II HzRGs from Vernet et al. (2001) (blue filled triangles) with photoionization models using ionizing continuum power law index α = -1.0. Each diagram presents a different gas metallicity, i.e., Z/Z$_\odot$ = 0.5, 1.0, 2.0, 3.0, 4.0, 5.0. Curves with different colors represent the hydrogen gas density (n$_H$) described in 4.12a. At the end of each sequence, a solid black triangle corresponds to the lowest ionization parameter (U = 2×10^{-3}) while the solid black star corresponds to the maximum value of the ionization parameter (U = 1.0).

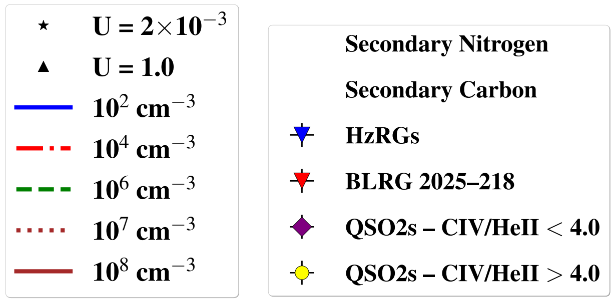

(a) Legend

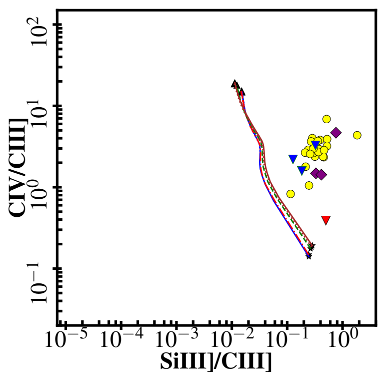

(b) Z/Z$_\odot$ = 0.5

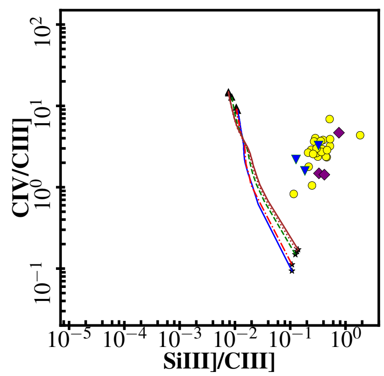

(c) Z/Z$_\odot$ = 1.0

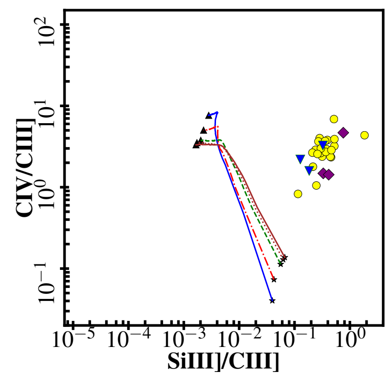

(d) Z/Z$_\odot$ = 2.0

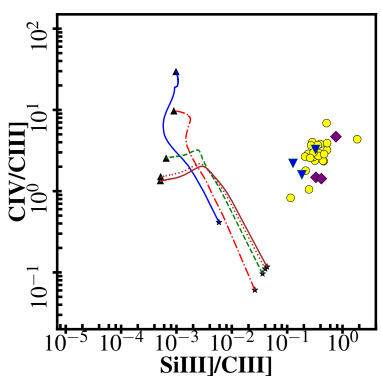

(e) Z/Z$_\odot$ = 3.0

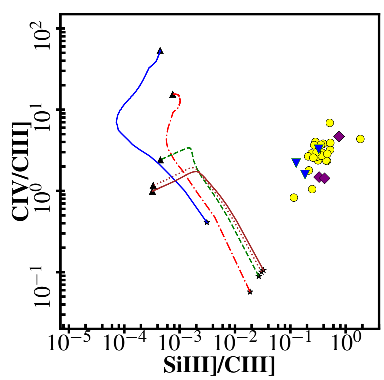

(f) Z/Z$_\odot$ = 4.0

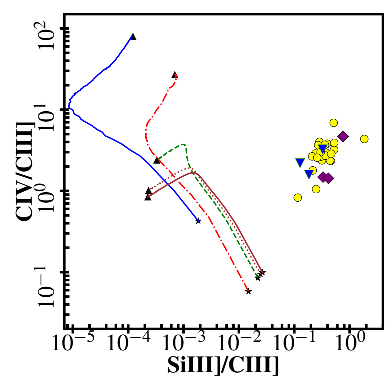

(g) Z/Z$_\odot$ = 5.0

Figure 4.13: Comparison of the observed emission line ratios from the SDSS type II quasars divided in objects with C IV/He II < 4 and C IV/He II > 4 (purple filled diamond and yellow filled circles, respectively), and Keck II HzRGs from Vernet et al. (2001) (blue filled triangles) with photoionization models using ionizing continuum power law index α = -1.0. Carbon is a secondary element in which its abundance is proportional to the square of the metallicity. Each diagram presents a different gas metallicity, i.e., Z/Z$_\odot$ = 0.5, 1.0, 2.0, 3.0, 4.0, 5.0. Curves with different colors represent the hydrogen gas density (n_H) described in 4.13a. At the end of each sequence, a solid black triangle corresponds to the lowest ionization parameter (U = 2×10^{-3}) while the solid black star corresponds to the maximum value of the ionization parameter (U = 1.0).

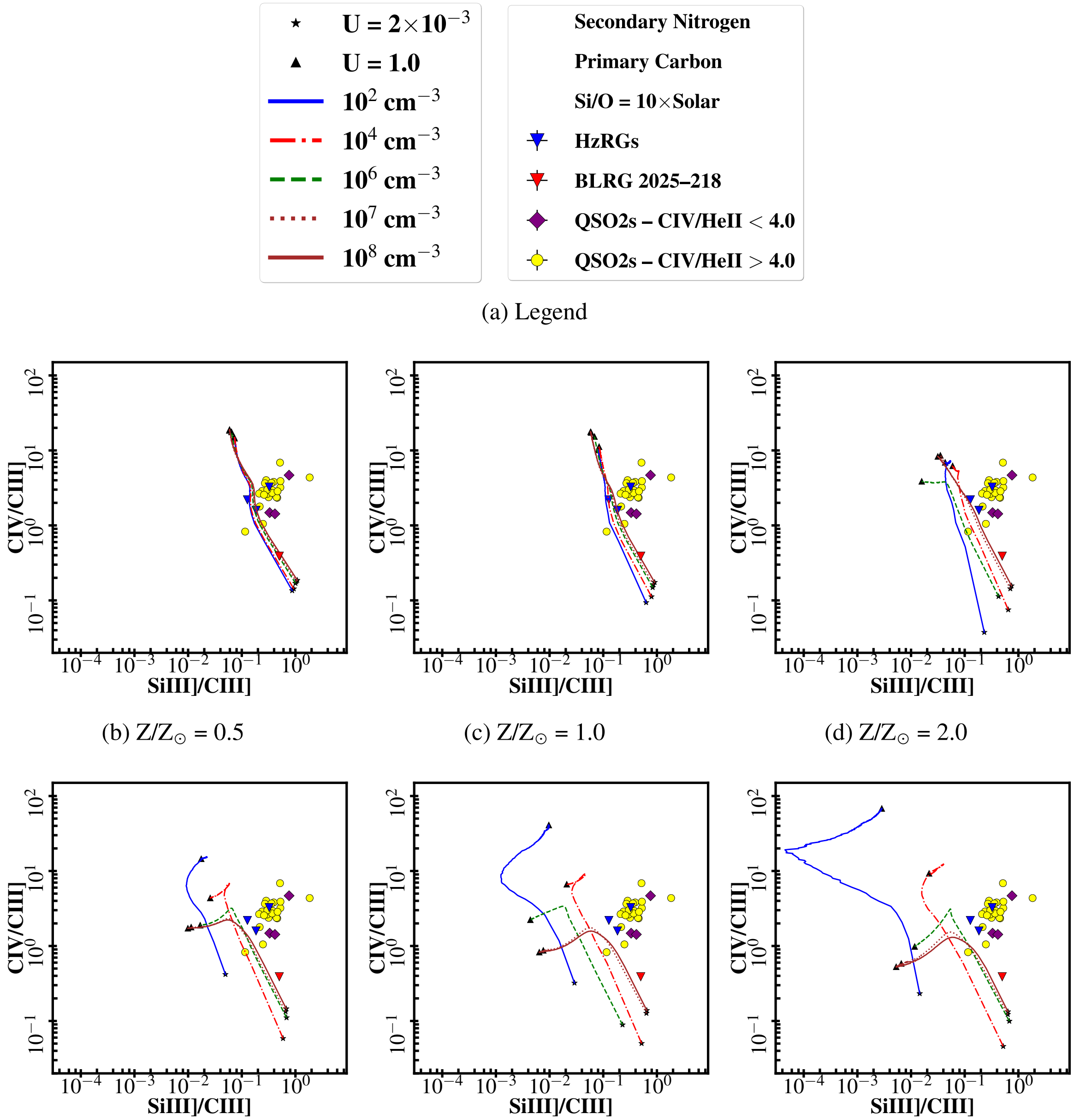

(a) Legend

(b) $Z/Z_{\odot}$ = 0.5 (c) $Z/Z_{\odot}$ = 1.0 (d) $Z/Z_{\odot}$ = 2.0

(e) $Z/Z_{\odot}$ = 3.0 (f) $Z/Z_{\odot}$ = 4.0 (g) $Z/Z_{\odot}$ = 5.0

Figure 4.14: Comparison of the observed emission line ratios from the SDSS type II quasars divided in objects with C IV/He II < 4 and C IV/He II > 4 (purple filled diamond and yellow filled circles, respectively), and Keck II HzRGs from Vernet et al. (2001) (blue filled triangles) with photoionization models using ionizing continuum power law index α = -1.0. Each diagram presents a different gas metallicity, i.e., $Z/Z_{\odot}$ = 0.5, 1.0, 2.0, 3.0, 4.0, 5.0. In addition, at each of the gas metallicities shown in this Figure, the abundance of Si was increased by a factor of 10, resulting in a Si/O abundance ratio ten times its Solar value. Curves with different colors represent the hydrogen gas density (n_H) described in 4.14a. At the end of each sequence, a solid black triangle corresponds to the lowest ionization parameter (U = 2×10^{-3}) while the solid black star corresponds to the maximum value of the ionization parameter (U = 1.0).

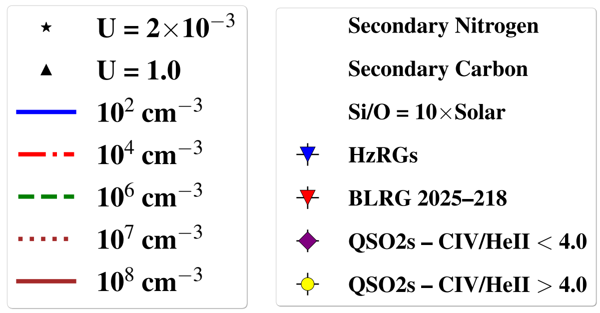

(a) Legend

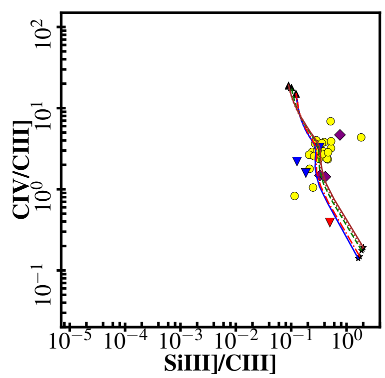

(b) $Z/Z_{\odot}$ = 0.5

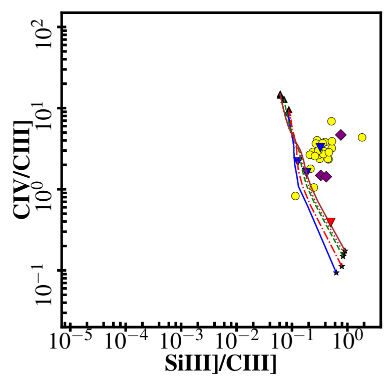

(c) $Z/Z_{\odot}$ = 1.0

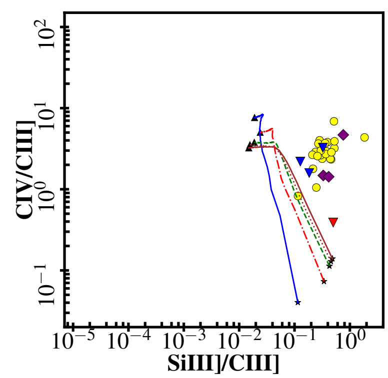

(d) $Z/Z_{\odot}$ = 2.0

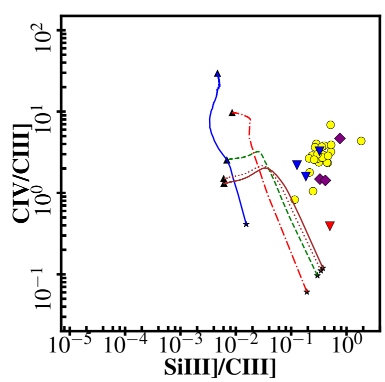

(e) $Z/Z_{\odot}$ = 3.0

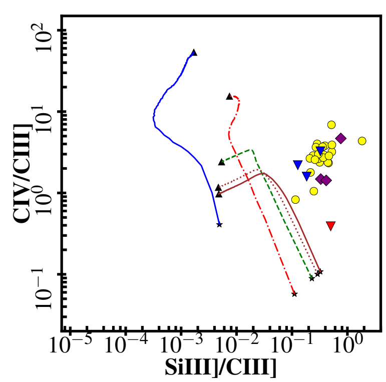

(f) $Z/Z_{\odot}$ = 4.0

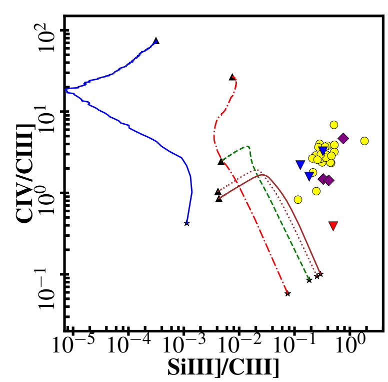

(g) $Z/Z_{\odot}$ = 5.0

Figure 4.15: Comparison of the observed emission line ratios from the SDSS type II quasars divided in objects with C IV/He II < 4 and C IV/He II > 4 (purple filled diamond and yellow filled circles, respectively), and Keck II HzRGs from Vernet et al. (2001) (blue filled triangles) with photoionization models using ionizing continuum power law index α = -1.0. Each diagram presents a different gas metallicity, i.e., $Z/Z_{\odot}$ = 0.5, 1.0, 2.0, 3.0, 4.0, 5.0. Carbon is a secondary element in which its abundance is proportional to the square of the metallicity and at each of the gas metallicities shown in this Figure, the abundance of Si was increased by a factor of 10, resulting in a Si/O abundance ratio ten times its Solar value. Curves with different colors represent the hydrogen gas density (n_H) described in 4.15a. At the end of each sequence, a solid black triangle corresponds to the lowest ionization parameter ($U = 2{\times}10^{-3}$) while the solid black star corresponds to the maximum value of the ionization parameter (U = 1.0).

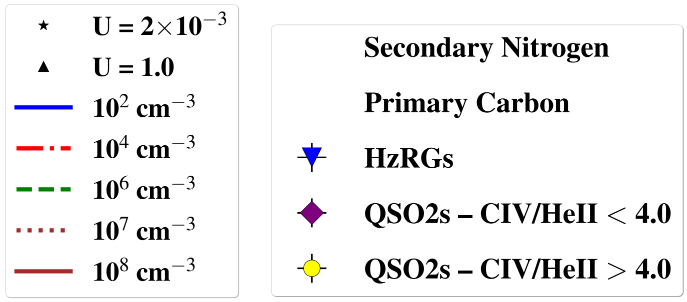

(a) Legend

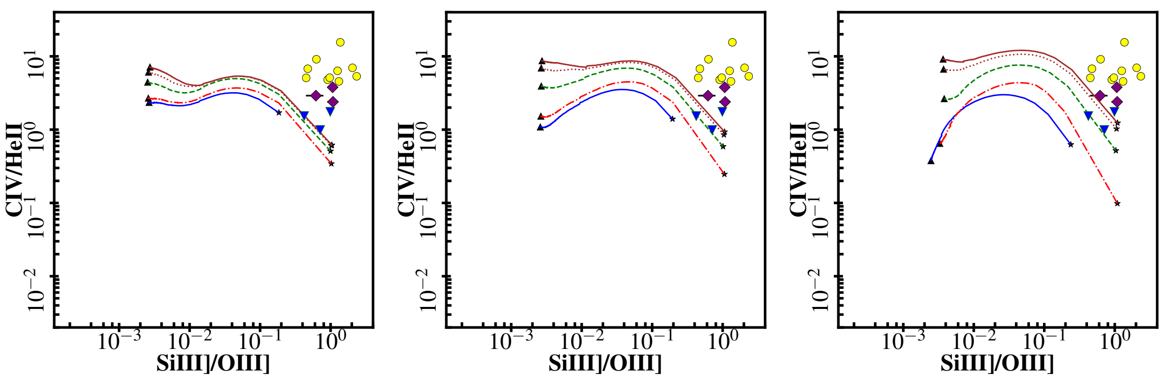

(b) $Z/Z_\odot$ = 0.5 (c) $Z/Z_\odot$ = 1.0 (d) $Z/Z_\odot$ = 2.0

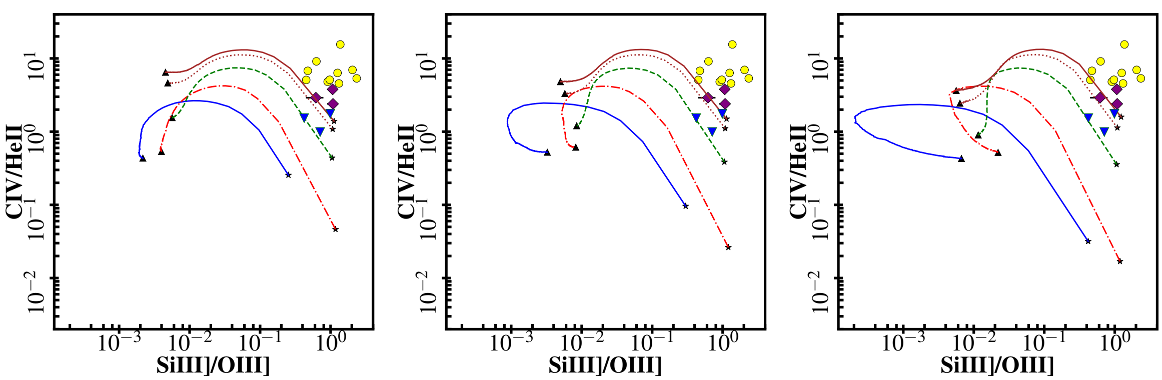

(e) $Z/Z_\odot$ = 3.0 (f) $Z/Z_\odot$ = 4.0 (g) $Z/Z_\odot$ = 5.0

Figure 4.16: Comparison of the observed emission line ratios from the SDSS type II quasars divided in objects with C IV/He II < 4 and C IV/He II > 4 (purple filled diamond and yellow filled circles, respectively), and Keck II HzRGs from Vernet et al. (2001) (blue filled triangles) with photoionization models using ionizing continuum power law index α = -1.0. Each diagram presents a different gas metallicity, i.e., $Z/Z_\odot$ = 0.5, 1.0, 2.0, 3.0, 4.0, 5.0. Curves with different colors represent the hydrogen gas density (n_H) described in 4.16a. At the end of each sequence, a solid black triangle corresponds to the lowest ionization parameter (U = $2{\times}10^{-3}$) while the solid black star corresponds to the maximum value of the ionization parameter (U = 1.0).

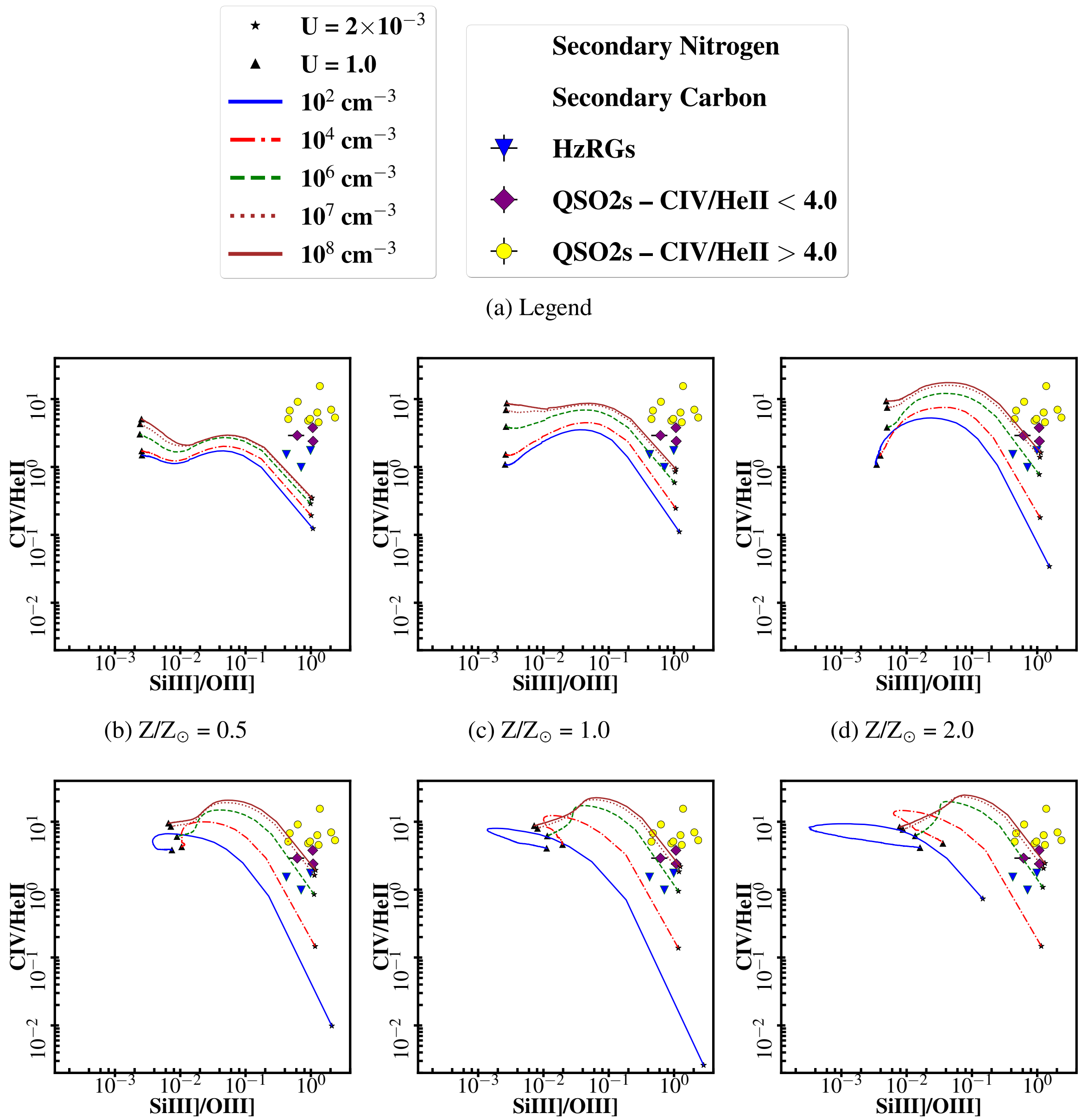

(a) Legend

(b) $Z/Z_{\odot}$ = 0.5 (c) $Z/Z_{\odot}$ = 1.0 (d) $Z/Z_{\odot}$ = 2.0

(e) $Z/Z_{\odot}$ = 3.0 (f) $Z/Z_{\odot}$ = 4.0 (g) $Z/Z_{\odot}$ = 5.0

Figure 4.17: Comparison of the observed emission line ratios from the SDSS type II quasars divided in objects with C IV/He II < 4 and C IV/He II > 4 (purple filled diamond and yellow filled circles, respectively), and Keck II HzRGs from Vernet et al. (2001) (blue filled triangles) with photoionization models using ionizing continuum power law index α = -1.0. Carbon is a secondary element in which its abundance is proportional to the square of the metallicity. Each diagram presents a different gas metallicity, i.e., $Z/Z_{\odot}$ = 0.5, 1.0, 2.0, 3.0, 4.0, 5.0. Curves with different colors represent the hydrogen gas density (n_H) described in 4.17a. At the end of each sequence, a solid black triangle corresponds to the lowest ionization parameter (U = 2×10^{-3}) while the solid black star corresponds to the maximum value of the ionization parameter (U = 1.0).

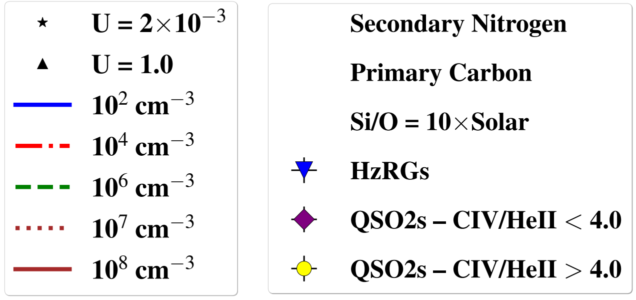

(a) Legend

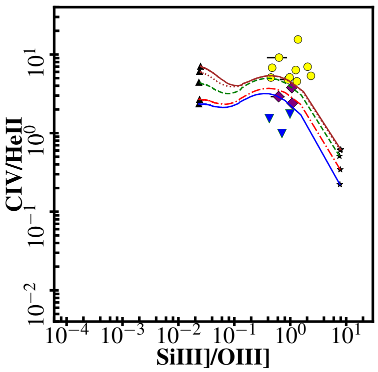

(b) Z/Z$_{\odot}$ = 0.5

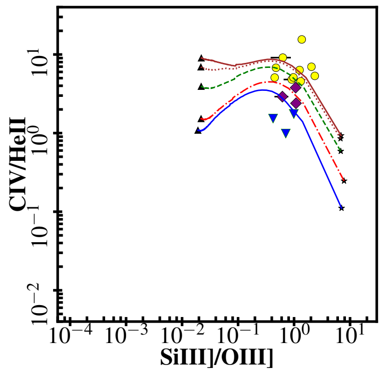

(c) Z/Z$_{\odot}$ = 1.0

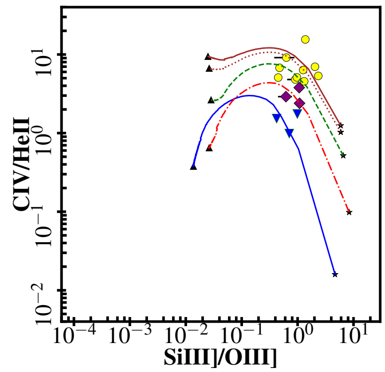

(d) Z/Z$_{\odot}$ = 2.0

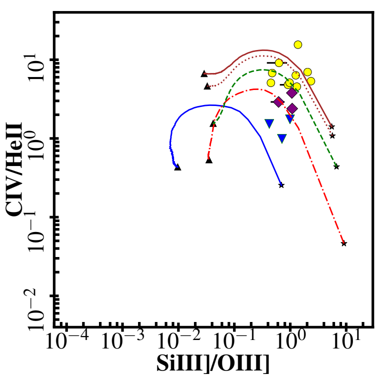

(e) Z/Z$_{\odot}$ = 3.0

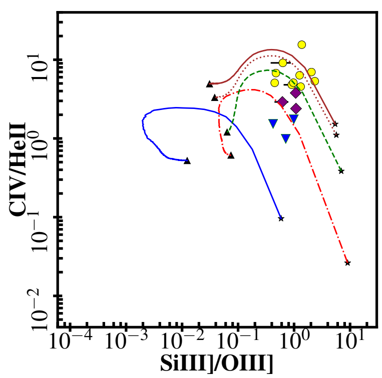

(f) Z/Z$_{\odot}$ = 4.0

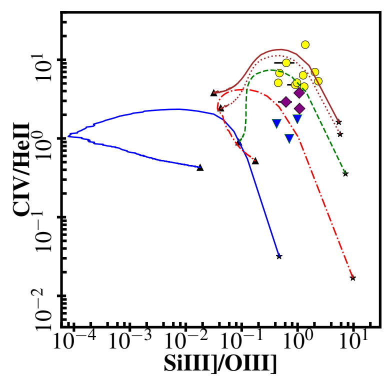

(g) Z/Z$_{\odot}$ = 5.0

Figure 4.18: Comparison of the observed emission line ratios from the SDSS type II quasars divided in objects with C IV/He II < 4 and C IV/He II > 4 (purple filled diamond and yellow filled circles, respectively), and Keck II HzRGs from Vernet et al. (2001) (blue filled triangles) with photoionization models using ionizing continuum power law index α = -1.0. Each diagram presents a different gas metallicity, i.e., Z/Z$_{\odot}$ = 0.5, 1.0, 2.0, 3.0, 4.0, 5.0. In addition, at each of the gas metallicities shown in this Figure, the abundance of Si was increased by a factor of 10, resulting in a Si/O abundance ratio ten times its Solar value. Curves with different colors represent the hydrogen gas density (n$_{H}$) described in 4.18a. At the end of each sequence, a solid black triangle corresponds to the lowest ionization parameter (U = 2×10^{-3}) while the solid black star corresponds to the maximum value of the ionization parameter (U = 1.0).

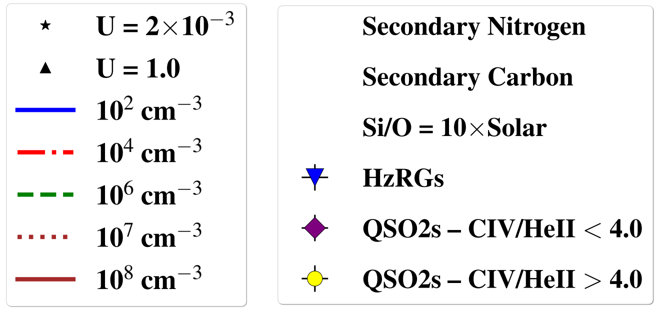

(a) Legend

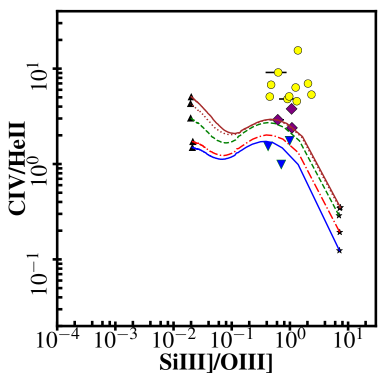

(b) $Z/Z_{\odot}$ = 0.5

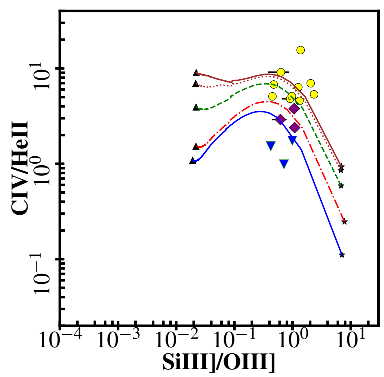

(c) $Z/Z_{\odot}$ = 1.0

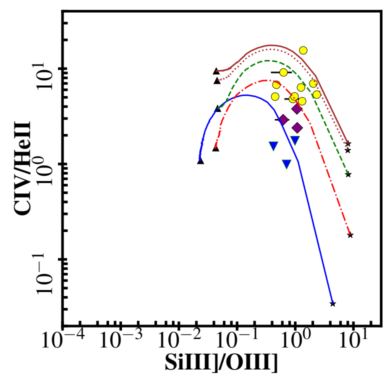

(d) $Z/Z_{\odot}$ = 2.0

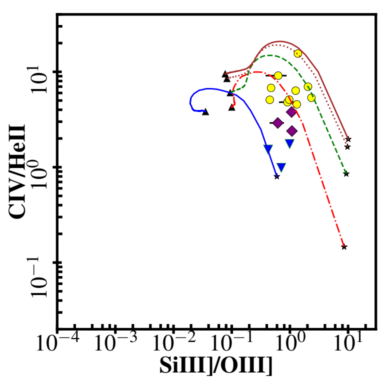

(e) $Z/Z_{\odot}$ = 3.0

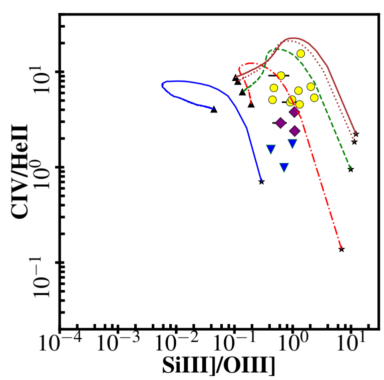

(f) $Z/Z_{\odot}$ = 4.0

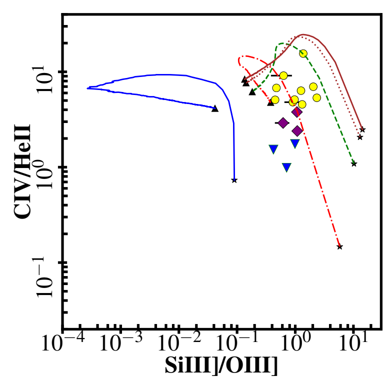

(g) $Z/Z_{\odot}$ = 5.0

Figure 4.19: Comparison of the observed emission line ratios from the SDSS type II quasars divided in objects with C IV/He II < 4 and C IV/He II > 4 (purple filled diamond and yellow filled circles, respectively), and Keck II HzRGs from Vernet et al. (2001) (blue filled triangles) with photoionization models using ionizing continuum power law index α = -1.0. Each diagram presents a different gas metallicity, i.e., $Z/Z_{\odot}$ = 0.5, 1.0, 2.0, 3.0, 4.0, 5.0. Carbon is a secondary element in which its abundance is proportional to the square of the metallicity and at each of the gas metallicities shown in this Figure, the abundance of Si was increased by a factor of 10, resulting in a Si/O abundance ratio ten times its Solar value. Curves with different colors represent the hydrogen gas density (n_H) described in 4.19a. At the end of each sequence, a solid black triangle corresponds to the lowest ionization parameter ($U = 2{\times}10^{-3}$) while the solid black star corresponds to the maximum value of the ionization parameter (U = 1.0).

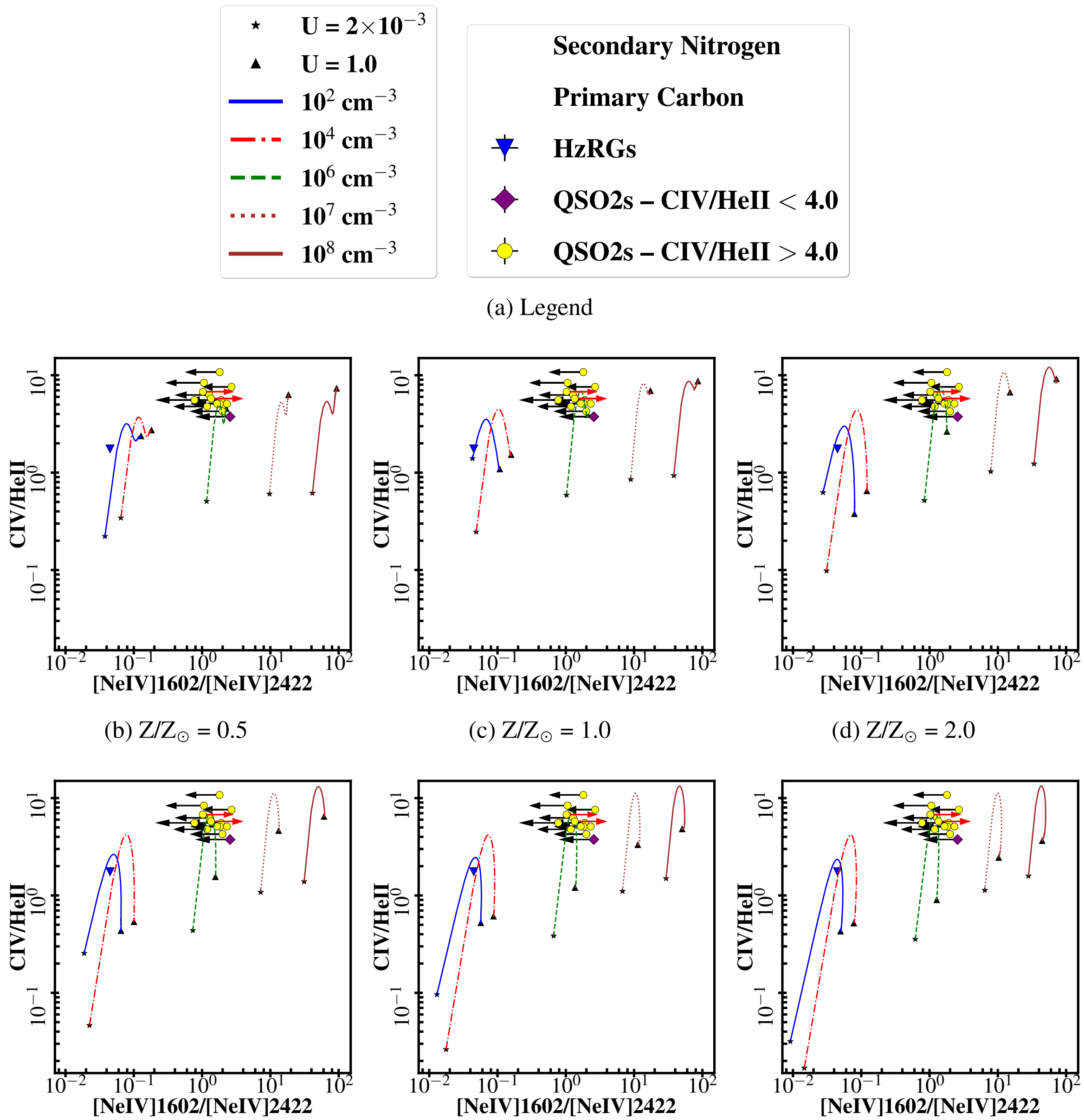

(a) Legend

(b) Z/Z$_\odot$ = 0.5 (c) Z/Z$_\odot$ = 1.0 (d) Z/Z$_\odot$ = 2.0

(e) Z/Z$_\odot$ = 3.0 (f) Z/Z$_\odot$ = 4.0 (g) Z/Z$_\odot$ = 5.0

Figure 4.20: Comparison of the observed emission line ratios from the SDSS type II quasars divided in objects with C IV/He II < 4 and C IV/He II > 4 (purple filled diamond and yellow filled circles, respectively), and Keck II HzRGs from Vernet et al. (2001) (blue filled triangles) with photoionization models using ionizing continuum power law index α = -1.0. Each diagram presents a different gas metallicity, i.e., Z/Z$_\odot$ = 0.5, 1.0, 2.0, 3.0, 4.0, 5.0. The black arrows represent the estimated 3σ upper limit for the emission line [Ne IV] λ 1602 while the red arrows represent the estimated 3σ upper limit for the emission line [Ne IV] λ 2422. Curves with different colors represent the hydrogen gas density (n$_H$) described in 4.20a. At the end of each sequence, a solid black triangle corresponds to the lowest ionization parameter (U = 2×10^{-3}) while the solid black star corresponds to the maximum value of the ionization parameter (U = 1.0).

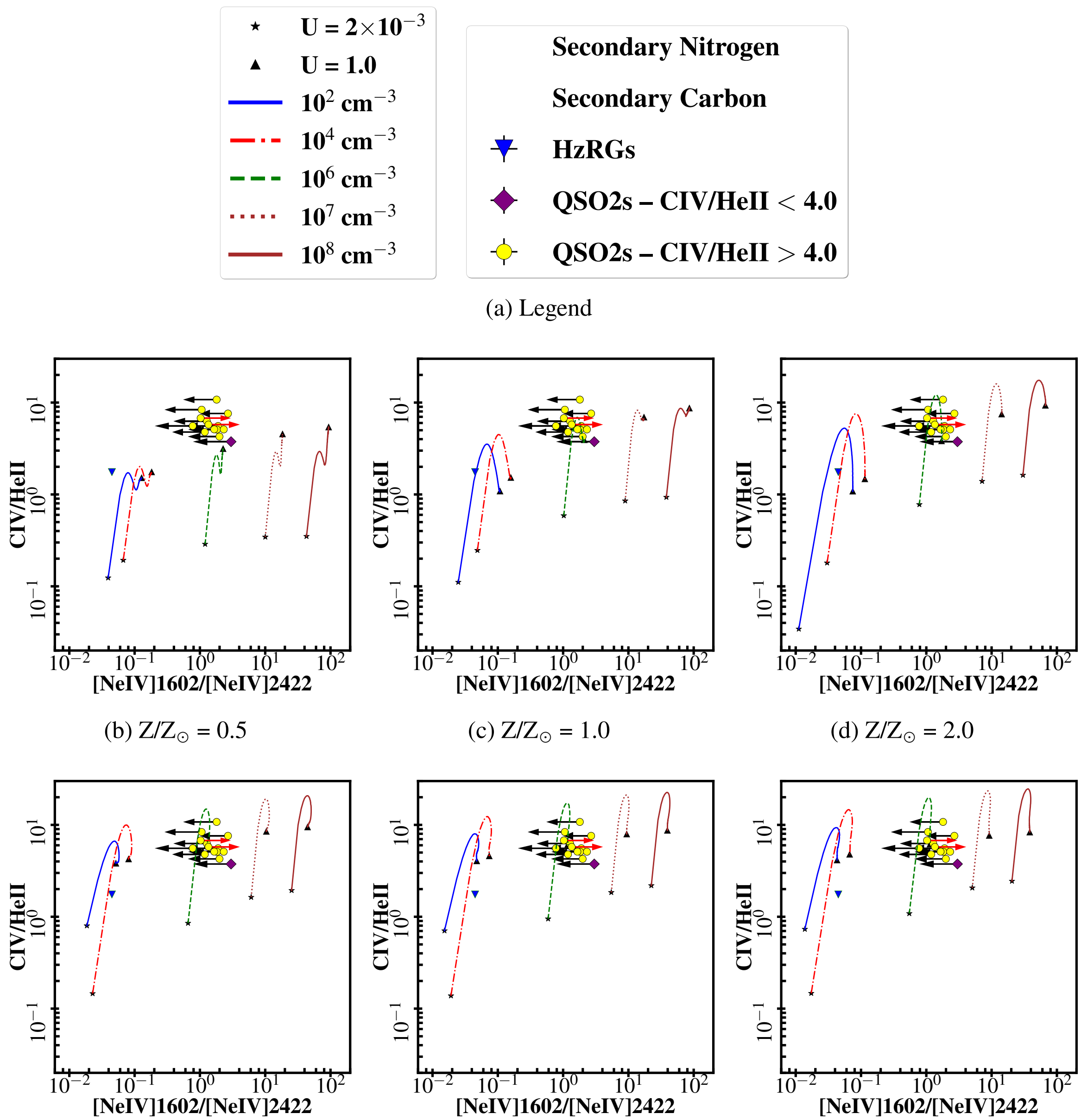

(a) Legend

(b) $Z/Z_\odot$ = 0.5 (c) $Z/Z_\odot$ = 1.0 (d) $Z/Z_\odot$ = 2.0

(e) $Z/Z_\odot$ = 3.0 (f) $Z/Z_\odot$ = 4.0 (g) $Z/Z_\odot$ = 5.0

Figure 4.21: Comparison of the observed emission line ratios from the SDSS type II quasars divided in objects with C IV/He II < 4 and C IV/He II > 4 (purple filled diamond and yellow filled circles, respectively), and Keck II HzRGs from Vernet et al. (2001) (blue filled triangles) with photoionization models using ionizing continuum power law index α = -1.0. Carbon is a secondary element in which its abundance is proportional to the square of the metallicity. Each diagram presents a different gas metallicity, i.e., $Z/Z_\odot$ = 0.5, 1.0, 2.0, 3.0, 4.0, 5.0.The black arrows represent the estimated 3σ upper limit for the emission line [Ne IV] λ 1602 while the red arrows represent the estimated 3σ upper limit for the emission line [Ne IV] λ 2422. Curves with different colors represent the hydrogen gas density (n_H) described in 4.21a. At the end of each sequence, a solid black triangle corresponds to the lowest ionization parameter ($U = 2\times10^{-3}$) while the solid black star corresponds to the maximum value of the ionization parameter (U = 1.0).

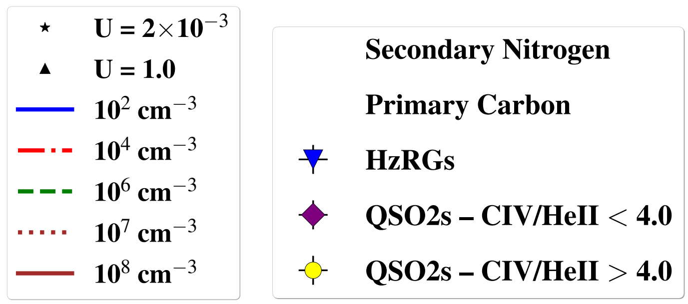

(a) Legend

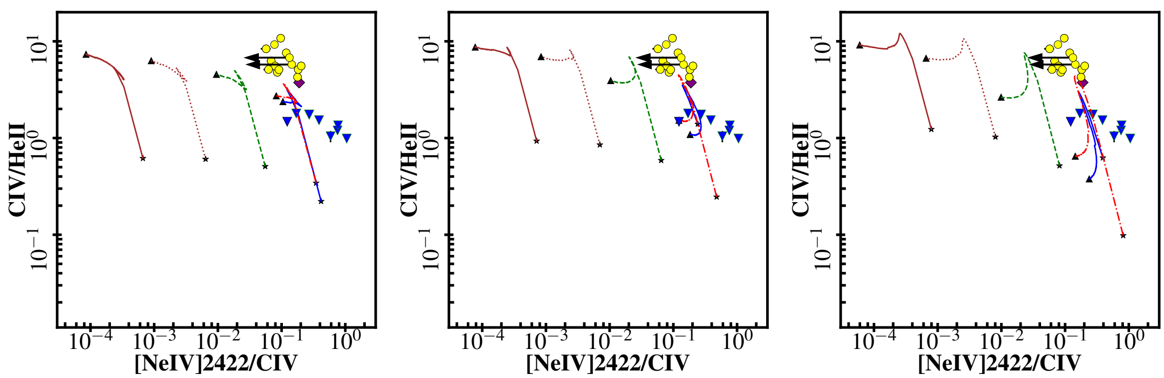

(b) $Z/Z_{\odot}$ = 0.5 (c) $Z/Z_{\odot}$ = 1.0 (d) $Z/Z_{\odot}$ = 2.0

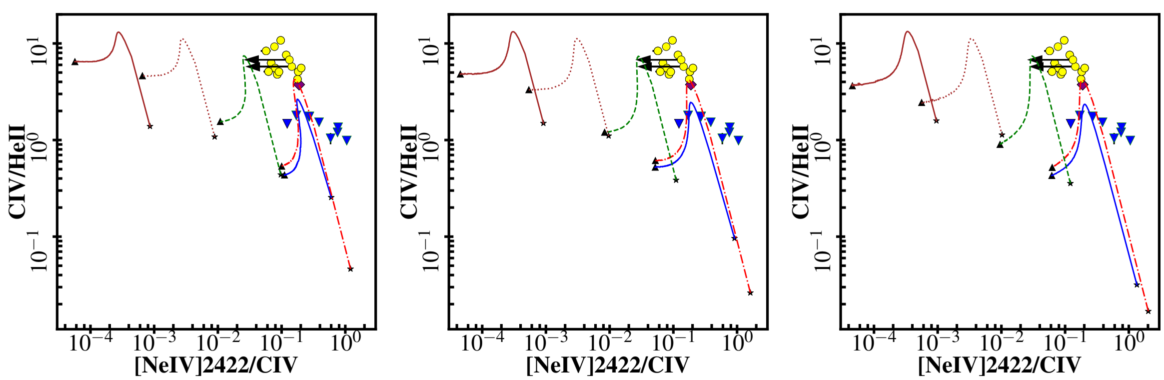

(e) $Z/Z_{\odot}$ = 3.0 (f) $Z/Z_{\odot}$ = 4.0 (g) $Z/Z_{\odot}$ = 5.0

Figure 4.22: Comparison of the observed emission line ratios from the SDSS type II quasars divided in objects with C IV/He II < 4 and C IV/He II > 4 (purple filled diamond and yellow filled circles, respectively), and Keck II HzRGs from Vernet et al. (2001) (blue filled triangles) with photoionization models using ionizing continuum power law index α = -1.0. Each diagram presents a different gas metallicity, i.e., $Z/Z_{\odot}$ = 0.5, 1.0, 2.0, 3.0, 4.0, 5.0. Curves with different colors represent the hydrogen gas density (n_H) described in 4.22a. At the end of each sequence, a solid black triangle corresponds to the lowest ionization parameter (U = 2×10^{-3}) while the solid black star corresponds to the maximum value of the ionization parameter (U = 1.0).

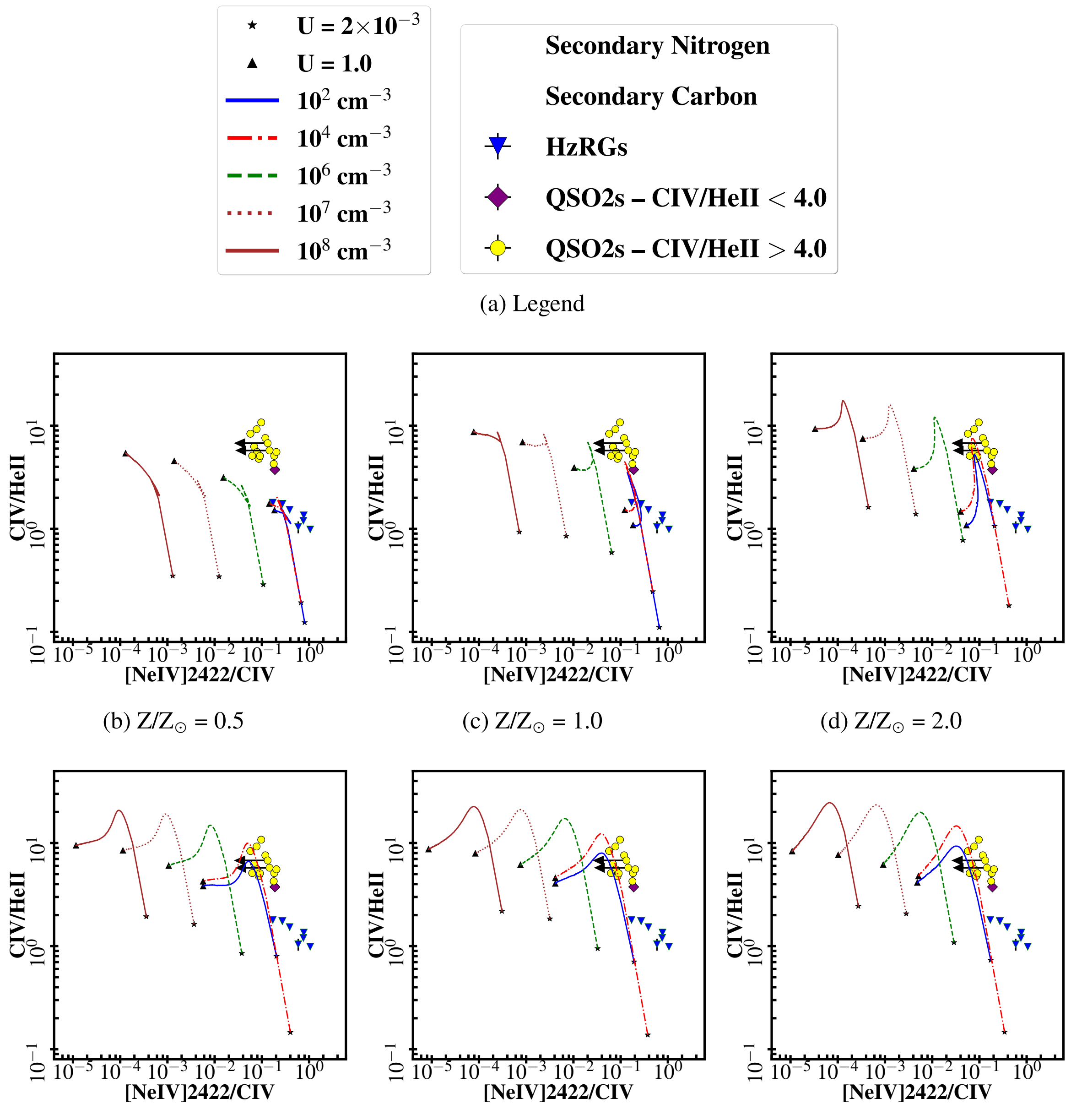

(a) Legend

(b) Z/Z$_\odot$ = 0.5 (c) Z/Z$_\odot$ = 1.0 (d) Z/Z$_\odot$ = 2.0

(e) Z/Z$_\odot$ = 3.0 (f) Z/Z$_\odot$ = 4.0 (g) Z/Z$_\odot$ = 5.0

Figure 4.23: Comparison of the observed emission line ratios from the SDSS type II quasars divided in objects with C IV/He II < 4 and C IV/He II > 4 (purple filled diamond and yellow filled circles, respectively), and Keck II HzRGs from Vernet et al. (2001) (blue filled triangles) with photoionization models using ionizing continuum power law index α = -1.0. Carbon is a secondary element in which its abundance is proportional to the square of the metallicity. Each diagram presents a different gas metallicity, i.e., Z/Z$_\odot$ = 0.5, 1.0, 2.0, 3.0, 4.0, 5.0. Curves with different colors represent the hydrogen gas density (n$_H$) described in 4.23a. At the end of each sequence, a solid black triangle corresponds to the lowest ionization parameter (U = 2×10^{-3}) while the solid black star corresponds to the maximum value of the ionization parameter (U = 1.0).

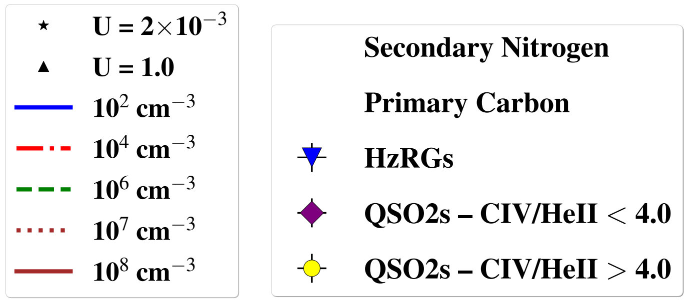

(a) Legend

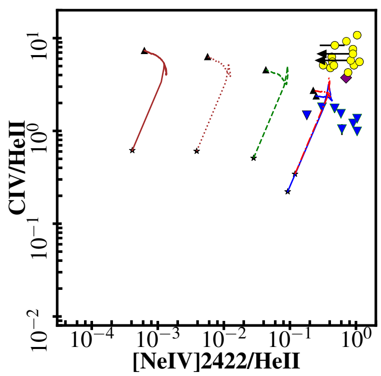

(b) $Z/Z_{\odot}$ = 0.5

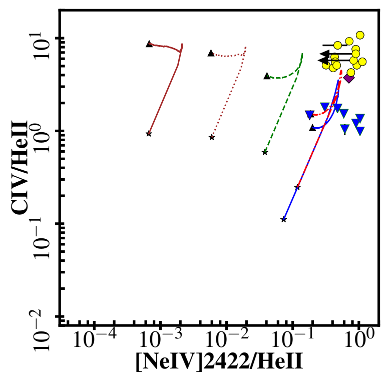

(c) $Z/Z_{\odot}$ = 1.0

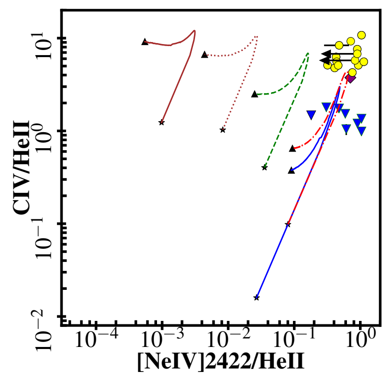

(d) $Z/Z_{\odot}$ = 2.0

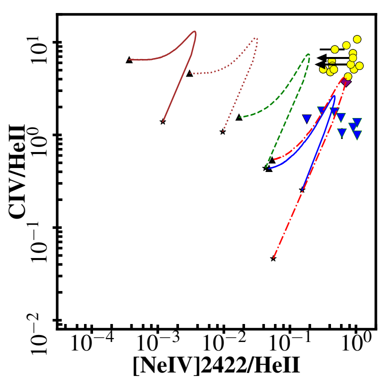

(e) $Z/Z_{\odot}$ = 3.0

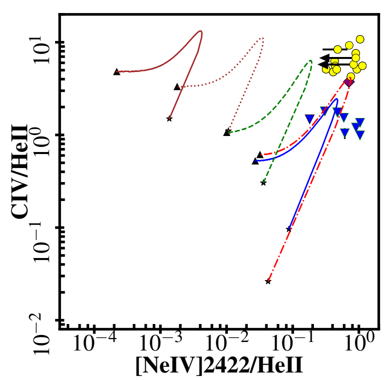

(f) $Z/Z_{\odot}$ = 4.0

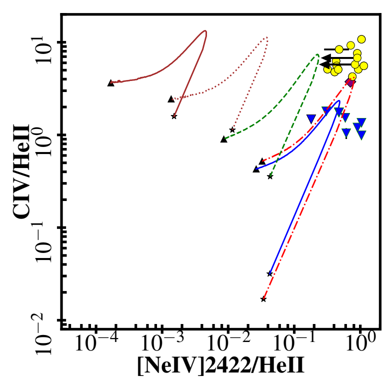

(g) $Z/Z_{\odot}$ = 5.0

Figure 4.24: Comparison of the observed emission line ratios from the SDSS type II quasars divided in objects with C IV/He II < 4 and C IV/He II > 4 (purple filled diamond and yellow filled circles, respectively), and Keck II HzRGs from Vernet et al. (2001) (blue filled triangles) with photoionization models using ionizing continuum power law index α = -1.0. Each diagram presents a different gas metallicity, i.e., $Z/Z_{\odot}$ = 0.5, 1.0, 2.0, 3.0, 4.0, 5.0. Curves with different colors represent the hydrogen gas density (n_H) described in 4.24a. At the end of each sequence, a solid black triangle corresponds to the lowest ionization parameter (U = 2×10^{-3}) while the solid black star corresponds to the maximum value of the ionization parameter (U = 1.0).

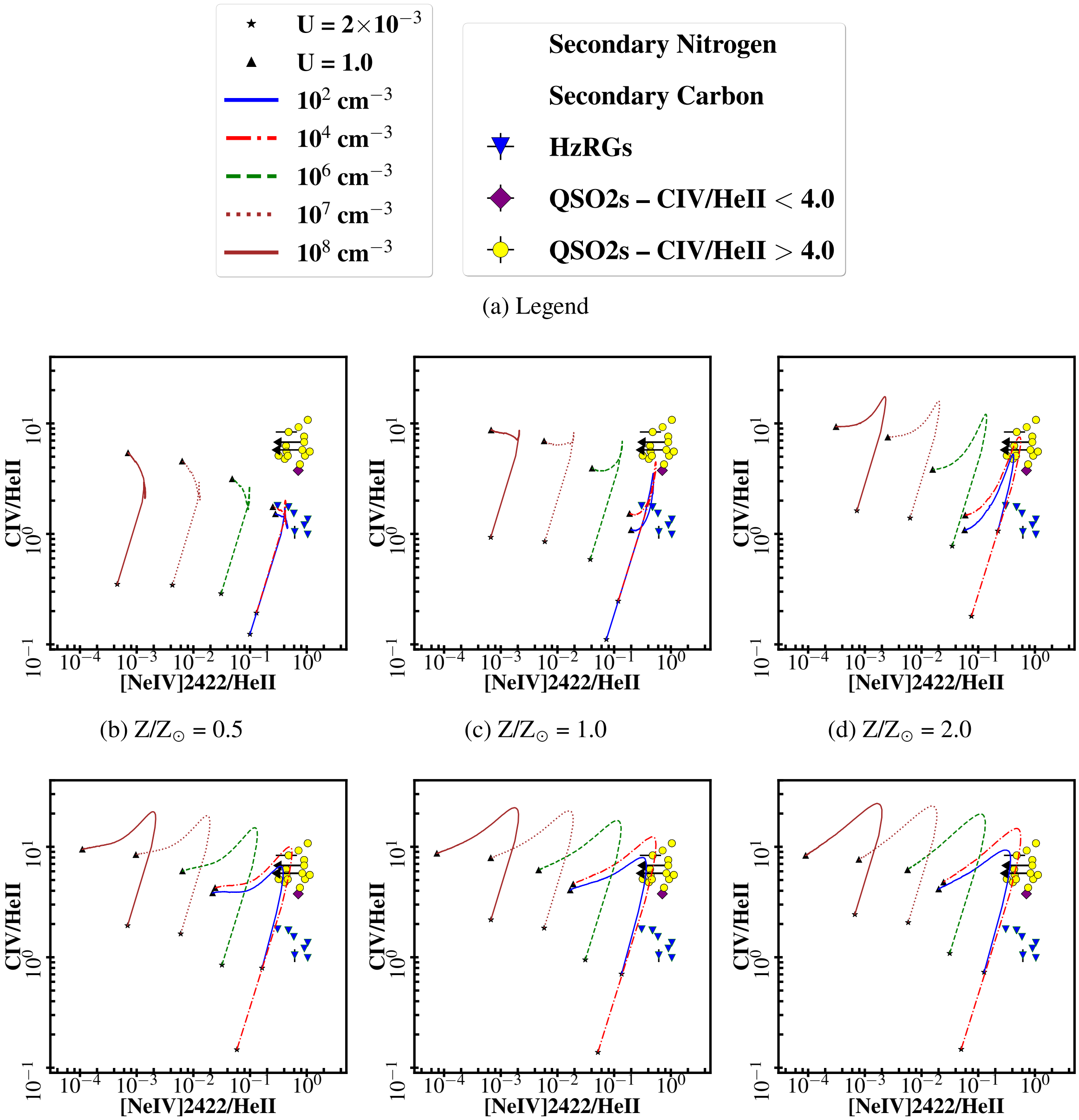

(a) Legend

(b) $Z/Z_{\odot}$ = 0.5 (c) $Z/Z_{\odot}$ = 1.0 (d) $Z/Z_{\odot}$ = 2.0

(e) $Z/Z_{\odot}$ = 3.0 (f) $Z/Z_{\odot}$ = 4.0 (g) $Z/Z_{\odot}$ = 5.0

Figure 4.25: Comparison of the observed emission line ratios from the SDSS type II quasars divided in objects with C IV/He II < 4 and C IV/He II > 4 (purple filled diamond and yellow filled circles, respectively), and Keck II HzRGs from Vernet et al. (2001) (blue filled triangles) with photoionization models using ionizing continuum power law index α = -1.0. Each diagram presents a different gas metallicity, i.e., $Z/Z_{\odot}$ = 0.5, 1.0, 2.0, 3.0, 4.0, 5.0. Carbon is a secondary element in which its abundance is proportional to the square of the metallicity. Curves with different colors represent the hydrogen gas density (n_H) described in 4.25a. At the end of each sequence, a solid black triangle corresponds to the lowest ionization parameter (U = 2×10^{-3}) while the solid black star corresponds to the maximum value of the ionization parameter (U = 1.0).

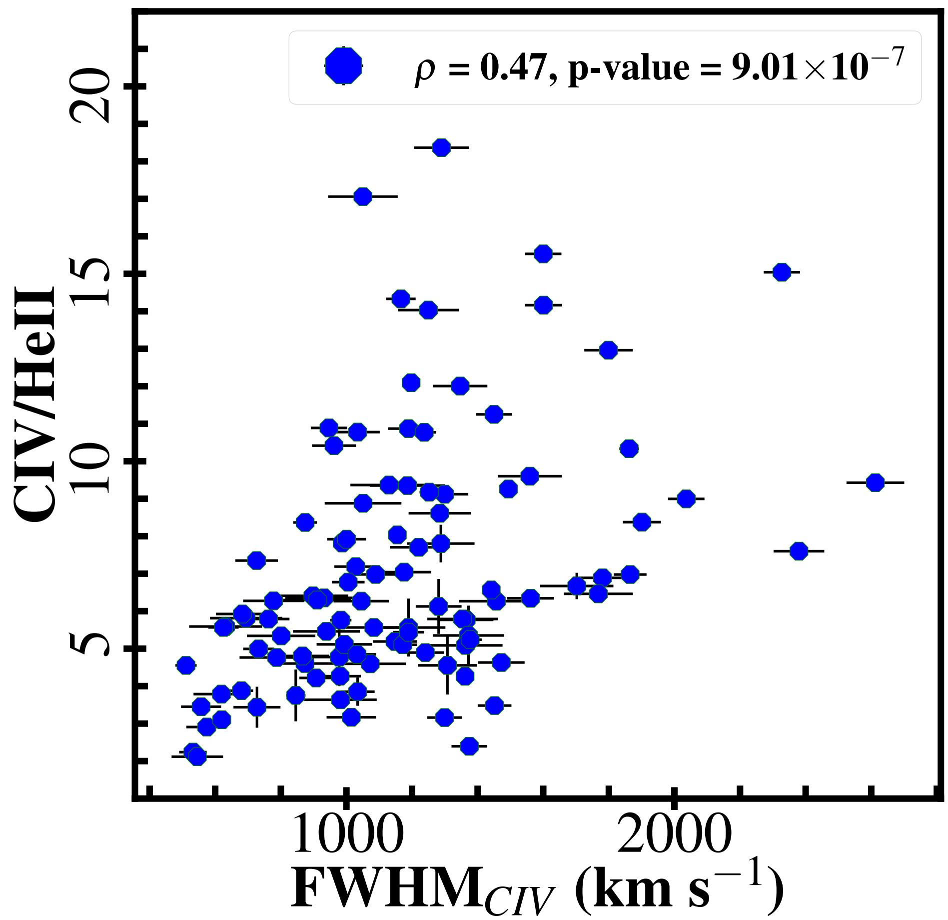

Figure 4.26: Variation of C IV/He II flux ratio as a function of the FWHM of C IV with ρ and p-value representing the Spearman's rank correlation coefficient and t-distribution, respectively.

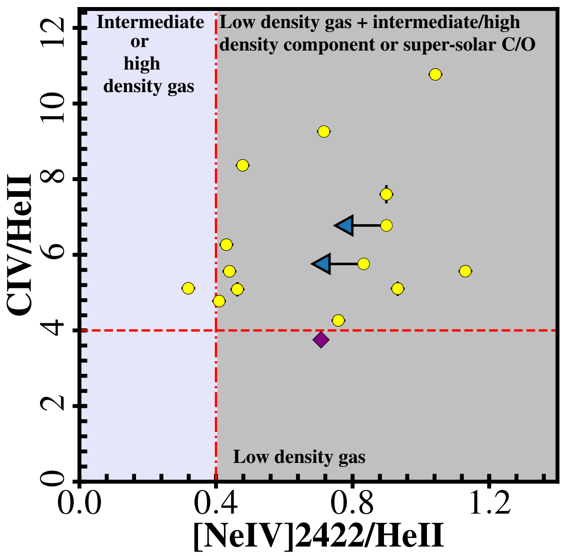

(a) [Ne IV]2422/He II vs. C IV/He II

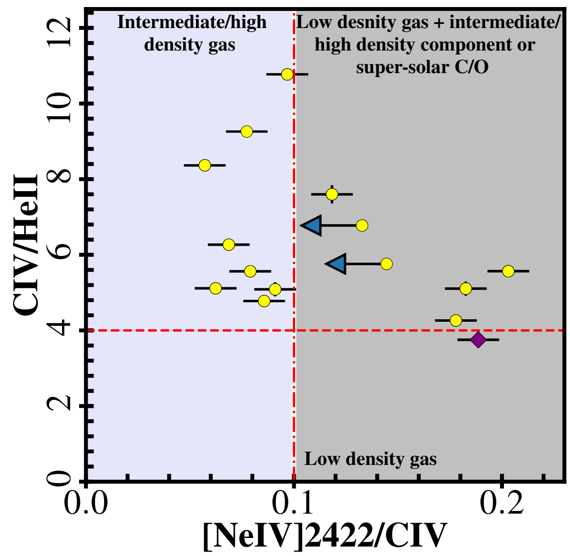

(b) [Ne IV]2422/C IV vs. C IV/He II

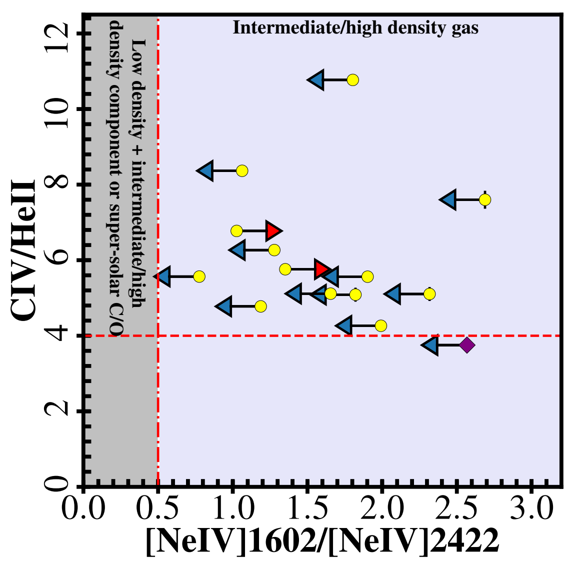

(c) [Ne IV]1602/[Ne IV]2422 vs. C IV/He II

Figure 4.27: Proposed new criteria to the QSO2s sample to produce our revised list of QSO2s.

Table 4.7: List of objects separated according to the selection criteria presented in §4.7.

SDSS name	z	NV/HeII	CIV/HeII	[NeIV]2422/HeII	[NeIV]2422/CIV	[NeIV]1602/[NeIV]2422	$FWHM_{CIV}$ (km s^{-1})
				Class 1			
J213557.35-032130.0	2.15	1.51 ± 0.11	3.75 ± 0.29	0.71 ± 0.20	0.19 ± 0.02	< 2.57	846 ± 115
				Class 2			
J161059.96+260321.5	2.28	1.19 ± 0.19	3.85 ± 0.38	–	–	–	1034 ± 87
J001814.72+023258.8	2.90		3.45 ± 0.54	–	–	–	557 ± 47
J074725.50+160053.7	2.83	0.53 ± 0.09	3.16 ± 0.19	–	–	–	1300 ± 67
J080826.02+435652.1	2.85	–	3.44 ± 0.55	–	–	–	727 ± 62
J081257.15+181916.8	2.38	0.91 ± 0.35	2.24 ± 0.33	–	–	–	532 ± 38
J094308.14+380923.0	3.12	1.64 ± 0.17	2.12 ± 0.27	–	–	–	545 ± 116
J101448.79+451444.7	2.28	2.16 ± 0.06	3.88 ± 0.49	–	–	–	680 ± 69
J113351.03+400851.1	3.00	1.11 ± 0.08	2.91 ± 0.20	–	–	–	574 ± 46
J114703.82+382727.2	2.26	2.94 ± 0.47	3.10 ± 0.65	–	–	–	620 ± 111
J122214.45+374837.9	3.16	0.98 ± 0.13	3.48 ± 0.44	–	–	–	1452 ± 41
J124302.62+421245.3	2.41	0.97 ± 0.29	2.39 ± 0.22	–	–	–	1375 ± 76
J141853.65+034005.2	3.19	–	3.79 ± 0.34	–	–	–	619 ± 74
J152051.00+252830.1	3.77	1.38 ± 0.27	3.17 ± 0.47	–	–	–	1015 ± 86
J161353.27+201526.5	2.97	–	3.64 ± 0.36	–	–	–	982 ± 56
				Class 3			
J001040.82+004550.5	2.72	2.09 ± 0.28	4.26 ± 0.16	0.76 ± 0.15	0.18 ± 0.09	< 1.99	1362 ± 98
J155108.96+321051.1	2.36	0.88 ± 0.36	7.60 ± 0.61	0.90 ± 0.11	0.12 ± 0.06	< 2.69	2380 ± 121
J155725.27+260252.8	2.82	4.58 ± 0.43	5.10 ± 0.17	0.93 ± 0.10	0.18 ± 0.03	< 2.32	1172 ± 85
J212055.57+065244.7	2.60	1.80 ± 0.32	5.57 ± 0.27	1.13 ± 0.05	0.20 ± 0.02	< 0.78	625 ± 75
J163343.85+261026.2	3.07	2.52 ± 0.22	5.76 ± 0.08	< 0.83	< 0.14	> 1.35	983 ± 52
J162025.94+170721.5	2.03	2.03 ± 0.18	6.77 ± 0.11	< 0.90	< 0.13	> 1.03	1005 ± 74
				Class 4			
J162327.66+312204.3	2.34	6.00 ± 0.50	5.11 ± 0.81	0.32 ± 0.10	0.06 ± 0.02	–	994 ± 90
J011506.65-015307.0	2.33	2.50 ± 0.79	8.37 ± 0.19	–	–	–	1901 ± 64
J022051.68-012403.3	2.60	6.03 ± 0.46	9.43 ± 0.20	–	–	–	2613 ± 74
J075119.09+130202.4	2.64	2.51 ± 0.13	4.76 ± 0.33	–	–	–	788 ± 88
J081950.96+111507.9	2.81	2.74 ± 0.05	7.82 ± 0.34	–	–	–	987 ± 49
J084005.00+344832.1	2.55	1.50 ± 0.13	9.12 ± 0.80	–	–	–	1300 ± 107
J100916.93+031128.9	2.69	8.55 ± 0.14	9.18 ± 0.26	–	–	–	1252 ± 39
J114542.07+401318.4	3.30	4.59 ± 0.65	8.03 ± 0.06	–	–	–	1155 ± 91
J125148.53+060027.4	2.27	2.97 ± 0.81	5.77 ± 0.09	–	–	–	1365 ± 53
J150549.73+074309.0	3.32	4.08 ± 0.08	5.79 ± 0.85	–	–	–	1354 ± 20
J153306.06+322649.6	2.71	9.21 ± 0.62	15.53 ± 0.41	–	–	–	1600 ± 25
J160900.01+190534.8	2.54	1.81 ± 0.17	8.88 ± 0.26	–	–	–	1051 ± 113
J162812.51+233734.8	2.39	2.51 ± 0.69	6.67 ± 0.35	–	–	–	1702 ± 99
J163343.85+261026.2	3.07	2.52 ± 0.52	5.76 ± 0.08	–	–	–	983 ± 52
J222946.61+005540.5	2.37	4.71 ± 0.63	9.00 ± 0.68	–	–	–	2036 ± 103
J004423.20+035715.5	2.22	1.58 ± 0.44	6.35 ± 0.19	–	–	–	931 ± 25
J004600.48+000543.6	2.46	4.65 ± 0.47	6.89 ± 0.27	–	–	–	1781 ± 29
J012552.08-015218.3	3.18	10.28 ± 0.44	12.96 ± 0.37	–	–	–	1799 ± 120
J014607.15+121119.9	3.14	6.82 ± 0.25	10.89 ± 0.24	–	–	–	947 ± 107
J015700.14+073116.0	3.05	6.16 ± 0.41	17.06 ± 0.78	–	–	–	1050 ± 102
J020245.82+000848.4	2.22	–	7.19 ± 0.04	–	–	–	1029 ± 35
J020643.64+010403.3	2.66	3.39 ± 0.46	4.55 ± 0.12	–	–	–	511 ± 84
J020728.19+033833.5	2.76	5.39 ± 0.52	6.34 ± 0.22	–	–	–	1562 ± 35
J024525.95+025310.7	3.18	2.79 ± 0.26	4.63 ± 0.10	–	–	–	1472 ± 25
J025339.00+042154.5	2.85	7.53 ± 0.45	10.87 ± 0.63	–	–	–	1189 ± 49
J073637.54+225917.4	2.27	3.43 ± 0.70	7.92 ± 0.64	–	–	–	1000 ± 72
J073851.85+422010.9	2.19	1.80 ± 0.37	5.35 ± 0.80	–	–	–	1372 ± 46
J080428.80+111906.6	2.59	2.12 ± 0.32	4.90 ± 0.16	–	–	–	1240 ± 64
J081812.72+223755.3	2.46	3.74 ± 0.16	7.35 ± 0.21	–	–	–	726 ± 78
J082530.67+120658.4	2.35	3.31 ± 0.06	4.99 ± 0.06	–	–	–	733 ± 91
J082550.58+332543.1	2.87	3.99 ± 0.41	5.81 ± 0.56	–	–	–	694 ± 67
J083851.81+022907.1	2.87	1.36 ± 0.24	9.37 ± 0.05	–	–	–	1130 ± 45
J084949.57+044330.9	3.10	1.14 ± 0.12	6.41 ± 0.49	–	–	–	898 ± 47
J090612.64+030900.4	2.50	4.92 ± 0.46	8.61 ± 0.45	–	–	–	1285 ± 55
J091025.50+042944.4	3.78	4.43 ± 0.54	5.19 ± 0.16	–	–	–	1148 ± 52

Table 4.8: continued.

SDSS name	z	NV/HeII	CIV/HeII	[NeIV]2422/HeII	[NeIV]2422/CIV	[NeIV]1602/[NeIV]2422	FWHM$_{CIV}$ (km s^{-1})
Class 4							
J091357.87+005530.7	3.21	5.37 ± 0.49	9.60 ± 0.64	–	–	–	1559 ± 68
J094826.45+035834.5	2.27	2.16 ± 0.18	7.70 ± 0.03	–	–	–	1221 ± 74
J095819.35+013530.5	3.06	2.34 ± 0.19	6.98 ± 0.23	–	–	–	1865 ± 41
J100133.85+415107.9	2.36	3.22 ± 0.70	10.33 ± 0.20	–	–	–	1862 ± 97
J100210.53+381245.0	2.94	5.96 ± 0.36	12.01 ± 0.70	–	–	–	1347 ± 57
J104133.36+393325.4	2.43	3.88 ± 0.52	15.04 ± 0.72	–	–	–	2328 ± 57
J105324.11+445444.4	2.31	4.91 ± 0.18	6.46 ± 0.23	–	–	–	1768 ± 41
J105344.18+395402.3	3.23	3.49 ± 0.28	5.46 ± 0.59	–	–	–	939 ± 53
J114856.13+012731.6	2.33	3.51 ± 0.35	6.27 ± 0.29	–	–	–	778 ± 43
J115335.78+051221.8	3.07	0.72 ± 0.17	4.55 ± 0.38	–	–	–	1308 ± 113
J115411.95+040556.4	3.32	2.96 ± 0.13	5.56 ± 0.62	–	–	–	1084 ± 65
J115510.34+044455.4	2.43	5.24 ± 0.25	7.04 ± 0.17	–	–	–	1176 ± 119
J115947.86+351418.6	2.47	4.21 ± 0.49	6.98 ± 0.29	–	–	–	1089 ± 28
J133059.32+014610.3	2.34	5.15 ± 0.41	5.92 ± 0.15	–	–	–	683 ± 101
J133417.04+362753.0	2.29	3.16 ± 0.13	14.33 ± 0.25	–	–	–	1166 ± 109
J140625.75+042919.4	3.38	2.32 ± 0.17	6.27 ± 0.09	–	–	–	1457 ± 39
J144441.05-001343.4	2.55	5.27 ± 0.37	18.37 ± 0.36	–	–	–	1290 ± 95
J150145.46+360148.4	2.19	4.12 ± 0.15	5.59 ± 0.02	–	–	–	632 ± 99
J150451.51+202507.4	3.81	2.68 ± 0.29	7.80 ± 0.50	–	–	–	1288 ± 66
J151544.01+175753.0	2.40	3.43 ± 0.22	4.22 ± 0.20	–	–	–	908 ± 53
J151747.00+005550.7	2.66	1.12 ± 0.18	4.60 ± 0.13	–	–	–	874 ± 55
J151815.55+273618.0	3.34	8.45 ± 0.32	14.03 ± 0.19	–	–	–	1250 ± 73
J152105.83+182318.3	2.66	0.94 ± 0.10	4.80 ± 0.42	–	–	–	866 ± 37
J155200.53+175722.7	2.70	–	5.34 ± 0.18	–	–	–	801 ± 96
J160103.85+195436.2	2.45	3.39 ± 0.18	6.30 ± 0.14	–	–	–	911 ± 31
J160158.53+260926.1	2.79	5.27 ± 0.42	9.35 ± 0.27	–	–	–	1186 ± 81
J161343.40+314524.8	3.21	1.56 ± 0.24	10.78 ± 0.40	–	–	–	1034 ± 110
J161447.97+354221.2	3.30	1.76 ± 0.26	4.27 ± 0.11	–	–	–	981 ± 92
J162025.94+170721.5	2.03	4.45 ± 0.48	6.77 ± 0.21	–	–	–	1005 ± 74
J162500.57+165705.8	2.20	2.65 ± 0.35	5.24 ± 0.31	–	–	–	1377 ± 76
J162651.76+293111.3	2.48	1.43 ± 0.19	5.79 ± 0.26	–	–	–	762 ± 72
J162806.01+331551.1	2.43	3.28 ± 0.25	5.44 ± 0.18	–	–	–	1189 ± 113
J165525.54+322936.9	2.72	2.56 ± 0.14	11.25 ± 0.38	–	–	–	1450 ± 65
J170110.12+301502.9	3.27	6.57 ± 0.25	6.57 ± 0.17	–	–	–	1441 ± 109
J170558.64+273624.8	2.45	5.58 ± 0.21	12.09 ± 0.29	–	–	–	1197 ± 47
J171908.90+310438.6	2.32	0.99 ± 0.16	6.13 ± 0.37	–	–	–	1281 ± 83
J213843.08-010133.6	2.80	1.44 ± 0.17	4.60 ± 0.26	–	–	–	1073 ± 47
J215341.33+041132.7	2.42	2.39 ± 0.22	4.85 ± 0.17	–	–	–	1032 ± 70
J225607.63+052520.2	3.15	4.62 ± 0.33	10.42 ± 0.30	–	–	–	962 ± 71
J230451.68+005135.1	4.17	12.09 ± 0.29	14.16 ± 0.34	–	–	–	1601 ± 66
Class 5							
J163343.85+261026.2	3.07	2.52 ± 0.42	5.76 ± 0.08	< 0.83	< 0.14	> 1.35	983 ± 52
J162025.94+170721.5	2.03	4.45 ± 0.48	6.77 ± 0.21	< 0.90	< 0.13	> 1.03	1005 ± 74

Chapter 5

Conclusions and Future work

5.1 Conclusions

This thesis presents a detailed study of the giant Lyα emitting nebulae and the giant H I absorbers associated with HzRGs or HzQSOs ($z > 2$). Rest-frame UV and optical emission lines from a wide variety of species have been used to explore the dynamics and line profiles of the emitting and absorbing gas, as well as their chemical enrichment. In addition to the one-dimensional information provided by the long-slit instruments, this work also presents Lyα nebula with full two-dimensional information from integral field spectroscopy over their full detectable extent, as required to truly understand the origins, morphology and dynamics of both gaseous structures, extracting new information about feedback processes that operate on these massive objects and their high-redshift progenitors.

In Chapter 2 of the thesis, the emphasis was on using observations from MUSE, X-SHOOTER and other instruments to study the kinematic, chemical and excitation properties of the giant Lyα emitting halo and the giant H I absorber associated with the $z = 2.92$ radio galaxy MRC 0943–242. The spatially resolved structure of the Lyα emitting nebula reveals an extended emission line halo with a major axis well aligned with the position angle of the radio source. In agreement with previous kinematic studies of this galaxy, the extended emission line halo shows a central, extended region of kinematically turbulent gas almost reaching the radio hotspots, with kinematically more quiescent gas located at larger radii. The velocity maps and velocity curves revealed the kinematic turbulent gas consistent with a transition from redshifted to blueshifted velocities, with the largest FWHM spatially coincident with the highest relative blueshifted near the positions of the radio hotspots in Lyα, C IV, He II and C III]. Based on clear evidence for jet gas interactions strongly affecting the kinematic properties of the giant Lyα emitting gas, it is suggested that both outflows and inflows induced by radio-mode feedback are the best mechanisms to explain the dynamics of the emitting gas. In addition, the fact that much of the kinematically perturbed gas is redshifted suggests that the inflow of gas driven by radio-mode feedback must be due to (1) jets entraining gas from the ISM of the galaxy, dragging gas in towards the jet as well as along the velocity vector of the jet or (2) a backflow of material from the radio hotspots which cycles material back into the host galaxy, producing the observed redshifted velocities of the kinematically perturbed gas. This scenario leads us to speculate that the radio galaxy could be in a phase of positive radio-mode feedback where fuel is cycled back into the central regions of the galaxy inducing star formation and feeding the AGN rather than quenching star-formation and starving the AGN of fuel.

Maps of several UV line ratios show large variation suggesting a substantial range in ionization level across the radio galaxy MRC 0943–242. The emission line ratios show regions with relatively low values of C IV/He II and C IV/C III], and high values of C III]/He II, spatially associated with the radio hotspots and consistent with lower ionization parameter. There is no direct spatial correlation between the Lyα/He II ratio and the radio hotspots, although it is still possible to see relatively low values spatially coincident with a region of kinematically quiescent gas in the He II and C III] kinematic maps, suggesting that the Lyα escape fraction is much lower in regions that are not affected by radio-mode feedback.

The photoionization model with U = 0.018, α = -1.0, gas metallicity $Z/Z_{\odot}$ =2.1 and A_v = 0 provides the best overall fit to the X-SHOOTER emission lines, consistent with conclusions obtained from smaller subsets of the UV lines by previous authors. The distribution of data points in diagnostic diagrams involving the MUSE UV emission lines such as C IV, He II and C III] is consistent with a large variation in ionization state throughout the extended ionized halo. The spaxels with relatively low values of C IV/C III], which are close to the radio hotspots, have different ionization conditions to the rest of the nebula, although degeneracies between models make it chalenging to determine the origin of this difference. With the line ratios in these spaxels also close to the shock models, it is suggested that the radio source may induce lower ionization where it most strongly interacts with the ISM, due to compression of gas or shock ionization.

The strong and spatially extended absorption feature in the profile of the Lyα line shows a strong degeneracy between the column density and the Doppler width. Although a broad range in column density yielding a reasonable fit to the data has been found, the fitting routine indicates that the best-fitting are located near each end of this range (log N(H I/cm^{-2}) = 15.20 and 19.63), with the highest column density in agreement with previous studies of the radio galaxy. The metal line column densities, derived from C IV, C II and C I, together with the H I column density indicate that the absorbing gas is mostly ionized and extremely metal poor (C/H < $0.013Z_{\odot}$ and O/H < $0.076Z_{\odot}$). In addition, the extended absorber shows a gradient in velocity with a significant decrease in blueshift outward from the central region of the galaxy, consistent with a large-scale expanding shell. Assuming the absorber is a spherical shell with R $\gtrsim$ 60 kpc and $N_H > 5\times10^{17}$ cm^{-2}, the estimated hard lower limit mass is $\log(M_H/M_\odot) \gtrsim 8.3$. However, assuming that the absorber is entirely neutral and using the high column density (log N(H I/cm^{-2}) = 19.63), the lower limit mass will be $\log(M_H/M_\odot) \gtrsim 10.2$.

In Chapter 3 of the thesis, the emphasis was on using observations from the Goodman long-slit spectrograph on the SOAR telescope, with the slit placed at large angles ($> 45^o$) to the radio axis, to study regions that are unlikely to be illuminated by the AGN. Investigating the properties of the extended Lyα nebulae of five HzRGs at $z > 2$, the results reveal that most of the objects show an asymmetric and extended spatial distribution (e.g. MRC 0406–244, 4C–00.54 and PKS 1138–262). Although other UV emission lines have been detected, none of them have shown to be extended in the SOAR spectra. For 3 out of 5 radio galaxies (e.g. MRC 0406–244, TNJ 0920–0712 and PKS 1138–262), there is a correlation between the FWHM and the velocity offset, suggesting that bulk radial motion dominates the gas dynamics. Within this framework, the correlation between the FWHM and blueshift was explained by: (i) Outflows, given that the most perturbed regions shows usually a blueshift with respect to the systemic velocity or (ii) Infall of gas in combination with Lyα radiative transfer effects. However, due to degeneracies inherent in the use of a resonant line Lyα to study gas kinematics, it was not possible to definitely discriminate between the infall and outflow scenarios.

In the case of the radio galaxy 4C-00.54, its SOAR spectrum has revealed a systematic increase in the blueshift and FWHM of the Lyα emission, outwards from the position of the AGN. This trend was interpreted as a consequence of scattering of Lyα photons that were originally produced along the radio axis or within the ionization cones, by neutral gas in regions that are predominantly neutral due to not being illuminated by the AGN. The Lyα/He II flux ratio shows a gradual increase outwards from the nucleus suggesting evidence for a radially increasing contribution from (i) absorption of Lyα (see Röttgering et al., 1997; van Ojik et al., 1997), (ii) resonant scattering of Lyα photons (see Dijkstra and Loeb, 2008; Hayes et al., 2011; Steidel et al., 2011) and (iii) enhanced emission of Lyα, which can be produced by a low ionization parameter, a relatively soft ionizing spectral energy distribution (SED) or a low gas metallicity (see Villar-Martín et al., 2007a; Humphrey et al., 2019).

Extended, blueshifted Lyα absorption was detected across the full spatial extent of the Lyα emission in 3 HzRGs (e.g. MRC 0406–244, TN J0920–0712 and PKS 1138–262). The new results obtained with the long-slit placed at large angles ($> 45^o$) indicate that the absorbing gas is extended perpendicularly to the radio/optical axis of the HzRG increasing the number of objects for which this test has been done. With minimum spatial extents ranging from $\gtrsim$ 27 kpc to $\gtrsim$ 35 kpc, the absorbing gas supports the idea that when present around a HzRG, this structure commonly covers the entire Lyα halo. In addition, the observed properties are consistent with the absorbing gas being part of a giant, expanding shell of gas surrounding the HzRG and its Lyα halo.

In Chapter 4 of the thesis, it is presented the modeling the UV line spectrum of a sample of 145 Type 2 quasars, with a view to understanding the gas properties of their narrow line regions. Comparing the emission line ratios against a grid of AGN photoionization models, it was found that solar or supersolar nitrogen abundances and gas metallicity are required in most of the quasars, with the strongest constraints coming from the N v/He II ratio. However, when using secondary behaviour for carbon, the models fail to reproduce the positions of some QSO2s with the highest values of N v/C IV because the adopted secondary behaviour of C and N results in a constant Solar N/C abundance ratio, preventing the supersolar N/C ratios that give rise to the highest N v/C IV. Scatter in the flux ratio N IV]/C IV suggests a significant variation in the N/C abundance ratio in the QSO2s and HzRGs, however it is unclear whether the scatter is due to differences in the ISM abundance ratio or differential depletion of N and C into dust grains. Adopting secondary behaviour for both N and C alleviates the N IV]-problem reported by a number of previous studies. Furthermore, it is found that when using secondary behaviour of C the N v/C IV and N IV]/C IV stop being useful metallicity indicators because the N/C abundance ratio remains constant (or nearly constant) across the full range of gas metallicity.

Some of the QSO2s show very high C IV/He II (> 10), consistent with a combination of high gas density ($\gtrsim 10^6$ cm^{-3}) and Z/Z$_\odot$ > 2.0 when assuming primary behaviour of C. However, due to degeneracies it has not been possible to determine which parameters (Z, C/H or n$_H$) are responsible for the very high C IV/He II ratios. Adopting instead the secondary behaviour of C, it has been found that the high C IV/He II flux ratio is consistent with a combination of low to intermediate gas density (< 10^6 cm^{-3}) and high gas metallicity Z/Z$_\odot \gtrsim 4.0$.

For comparison, the UV line ratios of a sample of HzRGs at z ~ 2.5 have been examined. It was found that a combination of low gas density (10^2 cm^{-3}) and Z/Z$_\odot$ > 2.0 appears to provide the best fit to the observed flux ratios of the HZRGs, using primary behaviour of C.

The Solar Si/O abundance ratio is usually assumed in photoionization models for active galaxies. However, our photoionization models using the Solar Si/O ratio produced Si III]/C III] flux ratios around an order of magnitude lower than their observed values. This discrepancy was dramatically reduced when the Si/O abundance ratio was increased to 10 times the Solar value. No systematic difference was found in the Si III]/C III] or Si III]/O III] flux ratios between the QSO2s and HzRG, suggesting that an order of magnitude overabundance of Si may be a common feature in the NLR / EELR of powerful active galaxies at z > 2.

Results derived from diagnostic diagrams using density sensitive [Ne IV] emission lines indicated that some QSO2s, including some objects with very high C IV/He II, have low density NLRs ($\lesssim 10^4$ cm^{-3}). On the other hand, the [Ne IV] ratios of two QSO2s imply intermediate or high gas density ($\gtrsim 10^6$ cm^{-3}), suggesting that there is a wide range of NLR gas density within the QSO2 sample.

In summary, this work has shown that the impact of jets on the gas dynamics of the HzRG MRC 0943–242 suggests that process related to the radio-mode feedback are drawing gas deeper into the potential well, which is speculated to give rise to a short-lived enhancement of star formation and the feeding of the AGN. In the long-run, the feedback is expected to suppress the star formation activity found in the host galaxy, and starve the AGN of fuel, which is consistent with the scenario in which the massive galaxy will evolve into a passive spheroidal system. This work has confirmed that there is a strong degeneracy between the column density and the Doppler width. Additionally, this work has shown that when present around a HzRG the blueshifted H I Lyα absorber is spatially extended parallel and perpendicular to the radio axis, consistent with a large scale expanding shell of gas covering the entire Lyα halo. Lastly, it has shown that if the emission lines can give hints on the chemical composition of the QSO2s environments, the results suggest that these objects are likely seen at the very end of the process, i.e., long after a star formation episode when a significant fraction of the stellar mass was assembled.

5.2 Future Work

The subject of exploring the Universe using Lyα as a tool has only begun, but it is increasing in popularity and it is quite imaginable that many new and interesting revelations about galaxy formation will come from this field in the future. A few aspects that I see as being crucial in understanding these galaxies, and which I hope to be able to work on are mentioned here.

- The combination of sensitivity, image quality and spectral resolution provided by MUSE will allow me to make a very significant step forward in assessing the morphology, kinematics and metal content of large-scale Lyα emitting gas and H I absorbers associated with high-redshift radio galaxies, shedding light on some of the key processes that drive the formation of the most massive galaxies. In addition, the very efficient single-target, intermediate-resolution and multi-wavelength X-shooter must be of great value given its broad application ranging from nearby intrinsically faint objects to bright sources at the edge of the Universe.

- The 2D spatial information of HzRGs such as MRC 0406–244, TN J0920–0712 and PKS 1138–262 would allow to characterize the properties of the extended Lyα halos and the large-scale H I absorbing structures of these objects. Based on the UV emission lines, the new results can add new information about gas infall / outflow scenarios, the distribution of the ionized and neutral gas, distribution of masses and the ionization mechanism (photoionization, shocks or shocks + precursor).

- The detailed analysis of the global properties of the extended Lyα halo associated with the radio galaxy 4C–00.54 will help to quantify the impact of the radio jets in the extended halo, to understand better the dynamics of the gas (infall / outflow scenarios) and also the spatial variation of the UV emission line ratios.
- Obtaining X-shooter observations of the sample used in Chapter 3, with the slit placed at large angle to the radio axis, allow to distinguish between gas infall and outlfow scenarios, but also confirmation of the conclusion that the absorbing gas is part of a extended, expanding shell of gas eveloping the HzRG.
- From the results of Chapter 4, future work will on this particular topic focus on further ionization mechanisms. Thus, dusty models, κ-distribution and shock ionization models must be taken into account. This will afford a wide examination of emission line ratios, helping to explain the high abundance of Si seen in a subset of QSO2s and HzRGs.

Bibliography

K. L. Adelberger, C. C. Steidel, J. A. Kollmeier, and N. A. Reddy. Possible Detection of Lyα Fluorescence from a Damped Lyα System at Redshift z ~ 2.8. *ApJ*, 637:74–79, January 2006. doi: 10.1086/497896.

Martez Ahmadi, B X. R. Alves, C J. Baker, William Bertsche, A Capra, Celeste Carruth, C L. Cesar, M Charlton, S Cohen, R Collister, S Eriksson, Andrew Evans, Nathan Evetts, J Fajans, T Friesen, M C. Fujiwara, David Gill, J S. Hangst, W Hardy, and J S. Wurtele. Observation of the 1s-2p lyman-α transition in antihydrogen. *Nature*, 561:1, 08 2018. doi: 10.1038/s41586-018-0435-1.

S. M. K. Alam and J. Miralda-Escudé. Self-Absorption of Ionizing Radiation and Extended Narrow-Line Emission in High-Redshift Quasi-stellar Objects. *ApJ*, 568:576–580, April 2002. doi: 10.1086/339031.

D. M. Alexander and R. C. Hickox. What drives the growth of black holes? *New Astron. Rev.*, 56:93–121, June 2012. doi: 10.1016/j.newar.2011.11.003.

R. Alexandroff, A. S. Strauss, J. E. Greene, N. L. Zakamska, and N. P. Ross. Candidate Type II Quasars at 2 < z < 4.3 in the Sloan Digital Sky Survey III. *MNRAS*, 1:26, August 2013.

M. G. Allen, B. A. Groves, M. A. Dopita, R. S. Sutherland, and L. J. Kewley. The MAPPINGS III Library of Fast Radiative Shock Models. *ApJS*, 178:20-55, September 2008. doi: 10.1086/589652.

A. Alonso-Herrero, P. G. Pérez-González, D. M. Alexander, G. H. Rieke, D. Rigopoulou, E. Le Floc'h, P. Barmby, C. Papovich, J. R. Rigby, F. E. Bauer, W. N. Brandt, E. Egami, S. P. Willner, H. Dole, and J.-S. Huang. Infrared Power-Law Galaxies in the Chandra Deep Field-South: Active Galactic Nuclei and Ultraluminous Infrared Galaxies. *ApJ*, 640:167–184, March 2006. doi: 10.1086/499800.

S. Antón, I. W. A. Browne, and M. J. Marchã. The colour of the narrow line Sy1-blazar 0324+3410. *A&A*, 490:583–587, November 2008. doi: 10.1051/0004-6361:20078926.

R. Antonucci. Unified models for active galactic nuclei and quasars. *ARA&A*, 31:473–521, 1993. doi: 10.1146/annurev.aa.31.090193.002353.

V. Antonuccio-Delogu and J. Silk. Active galactic nuclei activity: self-regulation from backflow. *MNRAS*, 405:1303–1314, June 2010. doi: 10.1111/j.1365-2966.2010.16532.x.

S. Arribas, E. Mediavilla, B. García-Lorenzo, and C. del Burgo. Stellar and Ionized-Gas Kinematics of the Seyfert 1 Galaxy NGC 3516. *ApJ*, 490:227–237, November 1997. doi: 10.1086/304849.

F. Arrigoni Battaia, J. X. Prochaska, J. F. Hennawi, A. Obreja, T. Buck, S. Cantalupo, A. A. Dutton, and A. V. Macciò. Inspiraling halo accretion mapped in Ly α emission around a z $\sim$ 3 quasar. *MNRAS*, 473:3907–3940, January 2018. doi: 10.1093/mnras/stx2465.

M. Asplund, N. Grevesse, and A. Jacques Sauval. The solar chemical composition. *Nuclear Physics A*, 777:1–4, October 2006. doi: 10.1016/j.nuclphysa.2005.06.010.

R. J. Assef, D. Stern, C. S. Kochanek, A. W. Blain, M. Brodwin, M. J. I. Brown, E. Donoso, P. R. M. Eisenhardt, B. T. Jannuzi, T. H. Jarrett, S. A. Stanford, C.-W. Tsai, J. Wu, and L. Yan. Mid-infrared Selection of Active Galactic Nuclei with the Wide-field Infrared Survey Explorer. II. Properties of WISE-selected Active Galactic Nuclei in the NDWFS Boötes Field. *ApJ*, 772:26, July 2013. doi: 10.1088/0004-637X/772/1/26.

H. Awaki, K. Koyama, H. Inoue, and J. P. Halpern. X-ray implications of a unified model of Seyfert galaxies. *PASJ*, 43:195–212, April 1991.

R. Bacon, M. Accardo, L. Adjali, H. Anwand, S. Bauer, I. Biswas, J. Blaizot, D. Boudon, S. Brau-Nogue, J. Brinchmann, P. Caillier, L. Capoani, C. M. Carollo, T. Contini, P. Couderc, E. Daguisé, S. Deiries, B. Delabre, S. Dreizler, J. Dubois, M. Dupieux, C. Dupuy, E. Emsellem, T. Fechner, A. Fleischmann, M. François, G. Gallou, T. Gharsa, A. Glindemann, D. Gojak, B. Guiderdoni, G. Hansali, T. Hahn, A. Jarno, A. Kelz, C. Koehler, J. Kosmalski, F. Laurent, M. Le Floch, S. J. Lilly, J.-L. Lizon, M. Loupias, A. Manescau, C. Monstein, H. Nicklas, J.-C. Olaya, L. Pares, L. Pasquini, A. Pécontal-Rousset, R. Pelló, C. Petit, E. Popow, R. Reiss, A. Remillieux, E. Renault, M. Roth, G. Rupprecht, D. Serre, J. Schaye, G. Soucail, M. Steinmetz, O. Streicher, R. Stuik, H. Valentin, J. Vernet, P. Weilbacher, L. Wisotzki, and N. Yerle. The MUSE second-generation VLT instrument. In *Ground-based and Airborne Instrumentation for Astronomy III*, volume 7735 of *Proc. SPIE*, page 773508, July 2010. doi: 10.1117/12.856027.

R. Bacon, J. Vernet, E. Borisova, N. Bouché, J. Brinchmann, M. Carollo, D. Carton, J. Caruana, S. Cerda, T. Contini, M. Franx, M. Girard, A. Guerou, N. Haddad, G. Hau, C. Herenz, J. C. Herrera, B. Husemann, T.-O. Husser, A. Jarno, S. Kamann, D. Krajnovic, S. Lilly, V. Mainieri, T. Martinsson, R. Palsa, V. Patricio, A. Pécontal, R. Pello, L. Piqueras, J. Richard, C. Sandin, I. Schroetter, F. Selman, M. Shirazi, A. Smette, K. Soto, O. Streicher, T. Urrutia, P. Weilbacher, L. Wisotzki, and G. Zins. MUSE Commissioning. *The Messenger*, 157: 13–16, September 2014.

J. N. Bahcall, S. Kirhakos, D. H. Saxe, and D. P. Schneider. Hubble Space Telescope Images of a Sample of 20 Nearby Luminous Quasars. *ApJ*, 479:642–658, April 1997. doi: 10.1086/303926.

J. A. Baldwin, F. Hamann, K. T. Korista, G. J. Ferland, M. Dietrich, and C. Warner. Chemical Abundances in Broad Emission Line Regions: The “Nitrogen-loud” Quasi-Stellar Object Q0353-383. *ApJ*, 583:649–658, February 2003. doi: 10.1086/345449.

D. R. Ballantyne. Obscuring Active Galactic Nuclei with Nuclear Starburst Disks. *ApJ*, 685: 787–800, October 2008. doi: 10.1086/591048.

L. A. Barnes, T. Garel, and G. G. Kacprzak. Ly-α and Mg II as Probes of Galaxies and Their Environment. *PASP*, 126:969, November 2014. doi: 10.1086/679178.

P. D. Barthel. Is every quasar beamed? *ApJ*, 336:606–611, January 1989. doi: 10.1086/167038.

Richard Barvainis, Joseph Lehár, Mark Birkinshaw, Heino Falcke, and Katherine M. Blundell. Radio variability of radio-quiet and radio-loud quasars. *The Astrophysical Journal*, 618(1): 108, 2005.

A. Baskin and A. Laor. Dust inflated accretion disc as the origin of the broad line region in active galactic nuclei. *MNRAS*, 474:1970–1994, February 2018. doi: 10.1093/mnras/stx2850.

L. Bassani, M. Dadina, R. Maiolino, M. Salvati, G. Risaliti, R. Della Ceca, G. Matt, and G. Zamorani. A Three-dimensional Diagnostic Diagram for Seyfert 2 Galaxies: Probing X-Ray Absorption and Compton Thickness. *ApJS*, 121:473–482, April 1999. doi: 10.1086/313202.

S. A. Baum and T. Heckman. Extended optical line emitting gas in powerful radio galaxies - What is the radio emission-line connection? *ApJ*, 336:702–721, January 1989. doi: 10.1086/167044.

M. Beck, C. Scarlata, M. Hayes, M. Dijkstra, and T. J. Jones. Spectropolarimetry Confirms Central Powering in a Lyα Nebula at z = 3.09. *ApJ*, 818:138, February 2016. doi: 10.3847/0004-637X/818/2/138.

V. Beckmann and C. Shrader. The AGN phenomenon: open issues. In *Proceedings of "An INTEGRAL view of the high-energy sky (the first 10 years)" - 9th INTEGRAL Workshop and celebration of the 10th anniversary of the launch (INTEGRAL 2012). 15-19 October 2012. Bibliotheque Nationale de France, Paris, France.*, page 69, 2012.

A. Beelen, A. Omont, N. Bavouzet, A. Kovács, G. Lagache, C. De Breuck, A. Weiss, K. M. Menten, J. W. Colbert, H. Dole, G. Siringo, and E. Kreysa. Submillimeter observations of the J2142-4423 Lyα protocluster at z = 2.38. *A&A*, 485:645–655, July 2008. doi: 10.1051/0004-6361:200809500.

M. C. Begelman and D. F. Cioffi. Overpressured cocoons in extragalactic radio sources. *ApJ*, 345:L21–L24, October 1989. doi: 10.1086/185542.

N. Bennert, G. Canalizo, B. Jungwiert, A. Stockton, F. Schweizer, C. Y. Peng, and M. Lacy. Evidence for Merger Remnants in Early-Type Host Galaxies of Low-Redshift QSOs. *ApJ*, 677:846–857, April 2008. doi: 10.1086/529068.

A. J. Benson, R. G. Bower, C. S. Frenk, C. G. Lacey, C. M. Baugh, and S. Cole. What Shapes the Luminosity Function of Galaxies? *ApJ*, 599:38–49, December 2003. doi: 10.1086/379160.

M. C. Bentz, P. B. Hall, and P. S. Osmer. Nitrogen-Enriched Quasars in the Sloan Digital Sky Survey First Data Release. *AJ*, 128:561–568, August 2004. doi: 10.1086/422346.

P. N. Best, M. S. Longair, and H. J. A. Roettgering. HST, radio and infrared observations of 28 3CR radio galaxies at redshift Z of about 1. I - The observations. *MNRAS*, 292:758, December 1997. doi: 10.1093/mnras/292.4.758.

P. N. Best, H. J. A. Röttgering, and M. S. Longair. Ionization, shocks and evolution of the emission-line gas of distant 3CR radio galaxies. *MNRAS*, 311:23–36, January 2000. doi: 10.1046/j.1365-8711.2000.03028.x.

P. N. Best, G. Kauffmann, T. M. Heckman, and Ž. Ivezić. A sample of radio-loud active galactic nuclei in the Sloan Digital Sky Survey. *MNRAS*, 362:9–24, September 2005. doi: 10.1111/j.1365-2966.2005.09283.x.

G. V. Bicknell, R. S. Sutherland, W. J. M. van Breugel, M. A. Dopita, A. Dey, and G. K. Miley. Jet-induced Emission-Line Nebulosity and Star Formation in the High-Redshift Radio Galaxy 4C 41.17. *ApJ*, 540:678–686, September 2000. doi: 10.1086/309343.

L. Binette, M. A. Dopita, and I. R. Tuohy. Radiative shock-wave theory. II - High-velocity shocks and thermal instabilities. *ApJ*, 297:476–491, October 1985. doi: 10.1086/163544.

L. Binette, J. D. Kurk, M. Villar-Martín, and H. J. A. Röttgering. A vestige low metallicity gas shell surrounding the radio galaxy 0943-242 at z=2.92. *AAP*, 356:23–32, April 2000.

L. Binette, R. J. Wilman, M. Villar-Martín, R. A. E. Fosbury, M. J. Jarvis, and H. J. A. Röttgering. Ionization of large-scale absorbing haloes and feedback events from high-redshift radio galaxies. *A&A*, 459:31–42, November 2006. doi: 10.1051/0004-6361:20065079.

L. Binette, E. Benítez, M. Villar-Martín, J.-A. de Diego, S. Haro-Corzo, and A. Humphrey. Large Scale Absorbers in the Environment of High-z Radio-Galaxies. In R. Guzmán, editor, *Revista Mexicana de Astronomia y Astrofisica Conference Series*, volume 29 of *Revista Mexicana de Astronomia y Astrofisica Conference Series*, pages 129–131, June 2007.

L. Bîrzan, D. A. Rafferty, B. R. McNamara, M. W. Wise, and P. E. J. Nulsen. A Systematic Study of Radio-induced X-Ray Cavities in Clusters, Groups, and Galaxies. *ApJ*, 607:800–809, June 2004. doi: 10.1086/383519.

R. D. Blandford and M. J. Rees. A 'twin-exhaust' model for double radio sources. *MNRAS*, 169:395–415, December 1974. doi: 10.1093/mnras/169.3.395.

T. Böker, R. P. van der Marel, L. Mazzuca, H.-W. Rix, G. Rudnick, L. C. Ho, and J. C. Shields. A Young Stellar Cluster in the Nucleus of NGC 4449. *AJ*, 121:1473–1481, March 2001. doi: 10.1086/319415.

T. Boller, W. N. Brandt, and H. Fink. Soft X-ray properties of narrow-line Seyfert 1 galaxies. *A&A*, 305:53, January 1996.

J. G. Bolton, G. J. Stanley, and O. B. Slee. Positions of Three Discrete Sources of Galactic Radio-Frequency Radiation. *Nature*, 164:101–102, July 1949. doi: 10.1038/164101b0.

C. M. Booth and J. Schaye. Cosmological simulations of the growth of supermassive black holes and feedback from active galactic nuclei: method and tests. *MNRAS*, 398:53–74, September 2009. doi: 10.1111/j.1365-2966.2009.15043.x.

E. Borisova, S. Cantalupo, S. J. Lilly, R. A. Marino, S. G. Gallego, R. Bacon, J. Blaizot, N. Bouché, J. Brinchmann, C. M. Carollo, J. Caruana, H. Finley, E. C. Herenz, J. Richard, J. Schaye, L. A. Straka, M. L. Turner, T. Urrutia, A. Verhamme, and L. Wisotzki. Ubiquitous Giant Lyα Nebulae around the Brightest Quasars at z $\backsim$ 3.5 Revealed with MUSE. *ApJ*, 831: 39, November 2016. doi: 10.3847/0004-637X/831/1/39.

T. A. Boroson. Black Hole Mass and Eddington Ratio as Drivers for the Observable Properties of Radio-loud and Radio-quiet QSOs. *ApJ*, 565:78–85, January 2002. doi: 10.1086/324486.

R. G. Bower, A. J. Benson, R. Malbon, J. C. Helly, C. S. Frenk, C. M. Baugh, S. Cole, and C. G. Lacey. Breaking the hierarchy of galaxy formation. *MNRAS*, 370:645–655, August 2006. doi: 10.1111/j.1365-2966.2006.10519.x.

W. N. Brandt and G. Hasinger. Deep Extragalactic X-Ray Surveys. *ARA&A*, 43:827–859, September 2005. doi: 10.1146/annurev.astro.43.051804.102213.

J. W. Broderick, C. De Breuck, R. W. Hunstead, and N. Seymour. An extreme rotation measure in the high-redshift radio galaxy PKS B0529-549. *MNRAS*, 375:1059–1069, March 2007. doi: 10.1111/j.1365-2966.2006.11375.x.

V. Bromm, R. P. Kudritzki, and A. Loeb. Generic Spectrum and Ionization Efficiency of a Heavy Initial Mass Function for the First Stars. *ApJ*, 552:464–472, May 2001. doi: 10.1086/320549.

M. Brusa, F. Civano, A. Comastri, T. Miyaji, M. Salvato, G. Zamorani, N. Cappelluti, F. Fiore, G. Hasinger, V. Mainieri, A. Merloni, A. Bongiorno, P. Capak, M. Elvis, R. Gilli, H. Hao, K. Jahnke, A. M. Koekemoer, O. Ilbert, E. Le Floc'h, E. Lusso, M. Mignoli, E. Schinnerer, J. D. Silverman, E. Treister, J. D. Trump, C. Vignali, M. Zamojski, T. Aldcroft, H. Aussel, S. Bardelli, M. Bolzonella, A. Cappi, K. Caputi, T. Contini, A. Finoguenov, A. Fruscione, B. Garilli, C. D. Impey, A. Iovino, K. Iwasawa, P. Kampczyk, J. Kartaltepe, J. P. Kneib, C. Knobel, K. Kovac, F. Lamareille, J.-F. Leborgne, V. Le Brun, O. Le Fevre, S. J. Lilly, C. Maier, H. J. McCracken, R. Pello, Y.-J. Peng, E. Perez-Montero, L. de Ravel, D. Sanders, M. Scodeggio, N. Z. Scoville, M. Tanaka, Y. Taniguchi, L. Tasca, S. de la Torre, L. Tresse, D. Vergani, and E. Zucca. The XMM-Newton Wide-field Survey in the Cosmos Field (XMM-COSMOS): Demography and Multiwavelength Properties of Obscured and Unobscured Luminous Active Galactic Nuclei. *ApJ*, 716:348–369, June 2010. doi: 10.1088/0004-637X/716/1/348.

Z. Cai, X. Fan, Y. Yang, F. Bian, J. X. Prochaska, A. Zabludoff, I. McGreer, Z.-Y. Zheng, R. Green, S. Cantalupo, B. Frye, E. Hamden, L. Jiang, N. Kashikawa, and R. Wang. Discovery of an Enormous Lyα Nebula in a Massive Galaxy Overdensity at z = 2.3. *ApJ*, 837:71, March 2017. doi: 10.3847/1538-4357/aa5d14.

S. Cantalupo. Gas Accretion and Giant Lyα Nebulae. In A. Fox and R. Davé, editors, *Gas Accretion onto Galaxies*, volume 430 of *Astrophysics and Space Science Library*, page 195, 2017.

S. Cantalupo, C. Porciani, S. J. Lilly, and F. Miniati. Fluorescent Lyα Emission from the High-Redshift Intergalactic Medium. *ApJ*, 628:61–75, July 2005.

S. Cantalupo, S. J. Lilly, and C. Porciani. Plausible Fluorescent Lyα Emitters around the z = 3.1 QSO 0420-388. *ApJ*, 657:135–144, March 2007. doi: 10.1086/510883.

S. Cantalupo, C. Porciani, and S. J. Lilly. Mapping Neutral Hydrogen during Reionization with the Lyα Emission from Quasar Ionization Fronts. *ApJ*, 672:48-58, January 2008. doi: 10.1086/523298.

S. Cantalupo, F. Arrigoni-Battaia, J. X. Prochaska, J. F. Hennawi, and P. Madau. A cosmic web filament revealed in Lyman-α emission around a luminous high-redshift quasar. *Nature*, 506:63–66, February 2014. doi: 10.1038/nature12898.

M. Cappi, F. Panessa, L. Bassani, M. Dadina, G. Di Cocco, A. Comastri, R. della Ceca, A. V. Filippenko, F. Gianotti, L. C. Ho, G. Malaguti, J. S. Mulchaey, G. G. C. Palumbo, E. Piconcelli, W. L. W. Sargent, J. Stephen, M. Trifoglio, and K. A. Weaver. X-ray spectral survey with XMM-Newton of a complete sample of nearby Seyfert galaxies. *A&A*, 446: 459–470, February 2006. doi: 10.1051/0004-6361:20053893.

J. A. Cardelli, G. C. Clayton, and J. S. Mathis. The relationship between infrared, optical, and ultraviolet extinction. *ApJ*, 345:245–256, October 1989. doi: 10.1086/167900.

C. L. Carilli, H. J. A. Röttgering, R. van Ojik, G. K. Miley, Breugel, and W. J. M. van. Radio Continuum Imaging of High-Redshift Radio Galaxies. *ApJS*, 109:1–44, 1997. doi: 10.1086/312973.

C. L. Carilli, D. E. Harris, L. Pentericci, H. J. A. Röttgering, G. K. Miley, J. D. Kurk, and W. van Breugel. The X-Ray-Radio Alignment in the z=2.2 Radio Galaxy PKS 1138-262. *ApJ*, 567:781–789, March 2002. doi: 10.1086/338669.

S. Carniani, A. Marconi, R. Maiolino, C. Feruglio, M. Brusa, G. Cresci, M. Cano-Díaz, C. Cicone, B. Balmaverde, F. Fiore, A. Ferrara, S. Gallerani, F. La Franca, V. Mainieri, F. Mannucci, H. Netzer, E. Piconcelli, E. Sani, R. Schneider, O. Shemmer, and L. Testi. AGN feedback on molecular gas reservoirs in quasars at z 2.4. *A&A*, 605:A105, September 2017. doi: 10.1051/0004-6361/201730672.

A. Cattaneo, J. Blaizot, D. H. Weinberg, D. Kereš, S. Colombi, R. Davé, J. Devriendt, B. Guiderdoni, and N. Katz. Accretion, feedback and galaxy bimodality: a comparison of the GalICS semi-analytic model and cosmological SPH simulations. *MNRAS*, 377:63–76, May 2007. doi: 10.1111/j.1365-2966.2007.11597.x.

R. Cen and Z. Zheng. The Nature of Lyα Blobs: Powered by Extreme Starbursts. *ApJ*, 775: 112, October 2013. doi: 10.1088/0004-637X/775/2/112.

W. Chamani, S. Dörschner, and D. R. G. Schleicher. Turbulent gas accretion between supermassive black-holes and star-forming rings in the circumnuclear disk. *A&A*, 602:A84, June 2017. doi: 10.1051/0004-6361/201730440.

K. C. Chambers, G. K. Miley, and W. van Breugel. Alignment of radio and optical orientations in high-redshift radio galaxies. *Nature*, 329:604–606, October 1987. doi: 10.1038/329604a0.

K. C. Chambers, G. K. Miley, W. J. M. van Breugel, M. A. R. Bremer, J.-S. Huang, and N. A. Trentham. Ultra–Steep-Spectrum Radio Sources. II. Radio, Infrared, Optical, and HST Imaging of High-Redshift 4C Objects. *ApJS*, 106:247, October 1996. doi: 10.1086/192338.

M. Chiaberge and A. Marconi. On the origin of radio loudness in active galactic nuclei and its relationship with the properties of the central supermassive black hole. *MNRAS*, 416: 917–926, September 2011. doi: 10.1111/j.1365-2966.2011.19079.x.

M. Chiaberge, A. Capetti, and F. D. Macchetto. The Hubble Space Telescope View of LINER Nuclei: Evidence for a Dual Population? *ApJ*, 625:716–726, June 2005. doi: 10.1086/429612.

C. Chiappini, D. Romano, and F. Matteucci. Oxygen, carbon and nitrogen evolution in galaxies. *MNRAS*, 339:63–81, February 2003. doi: 10.1046/j.1365-8711.2003.06154.x.

A. Cimatti and S. di Serego Alighieri. Is the UV Alignment Effect Present in Low Redshift Radio Galaxies? In R. D. Ekers, C. Fanti, and L. Padrielli, editors, *Extragalactic Radio Sources*, volume 175 of *IAU Symposium*, page 234, 1996.

A. Cimatti, S. di Serego Alighieri, J. Vernet, M. H. Cohen, and R. A. E. Fosbury. The UV Radiation from Z approximately 2.5 Radio Galaxies: Keck Spectropolarimetry of 4C 23.56 and 4C 00.54. *ApJ*, 499:L21–L25, May 1998. doi: 10.1086/311354.

N. E. Clark, D. J. Axon, C. N. Tadhunter, A. Robinson, and P. O'Brien. Jet-induced Shocks in 3C 171: An Intermediate-Redshift Analog of High-Redshift Radio Galaxies. *ApJ*, 494: 546–566, February 1998. doi: 10.1086/305225.

J. C. Clemens, J. A. Crain, and R. Anderson. The Goodman spectrograph. In A. F. M. Moorwood and M. Iye, editors, *Ground-based Instrumentation for Astronomy*, volume 5492 of *Proc. SPIE*, pages 331–340, September 2004.

J. W. Colbert, H. Teplitz, P. Francis, P. Palunas, G. M. Williger, and B. Woodgate. Ultraviolet-bright, High-Redshift Ultraluminous Infrared Galaxies. *ApJ*, 637:L89–L92, February 2006. doi: 10.1086/500647.

E. A. Cooke, N. A. Hatch, S. I. Muldrew, E. E. Rigby, and J. D. Kurk. A z = 2.5 protocluster associated with the radio galaxy MRC 2104-242: star formation and differing mass functions in dense environments. *MNRAS*, 440:3262–3274, June 2014. doi: 10.1093/mnras/stu522.

R. Coziol, H. Andernach, J. P. Torres-Papaqui, R. A. Ortega-Minakata, and F. Moreno del Rio. What sparks the radio-loud phase of nearby quasars? *MNRAS*, 466:921–944, April 2017. doi: 10.1093/mnras/stw3164.

V. Cracco, S. Ciroi, M. Berton, F. Di Mille, L. Foschini, G. La Mura, and P. Rafanelli. A spectroscopic analysis of a sample of narrow-line Seyfert 1 galaxies selected from the Sloan Digital Sky Survey. *MNRAS*, 462:1256–1280, October 2016. doi: 10.1093/mnras/stw1689.

D. M. Crenshaw, S. B. Kraemer, and J. R. Gabel. The Host Galaxies of Narrow-Line Seyfert 1 Galaxies: Evidence for Bar-Driven Fueling. *AJ*, 126:1690–1698, October 2003. doi: 10.1086/377625.

G. Cresci, A. Marconi, S. Zibetti, G. Risaliti, S. Carniani, F. Mannucci, A. Gallazzi, R. Maiolino, B. Balmaverde, M. Brusa, A. Capetti, C. Cicone, C. Feruglio, J. Bland-Hawthorn, T. Nagao, E. Oliva, M. Salvato, E. Sani, P. Tozzi, T. Urrutia, and G. Venturi. The MAGNUM survey: positive feedback in the nuclear region of NGC 5643 suggested by MUSE. *A&A*, 582:A63, October 2015. doi: 10.1051/0004-6361/201526581.

D. J. Croton, V. Springel, S. D. M. White, G. De Lucia, C. S. Frenk, L. Gao, A. Jenkins, G. Kauffmann, J. F. Navarro, and N. Yoshida. The many lives of active galactic nuclei: cooling flows, black holes and the luminosities and colours of galaxies. *MNRAS*, 365:11–28, January 2006a. doi: 10.1111/j.1365-2966.2005.09675.x.

D. J. Croton, V. Springel, S. D. M. White, G. De Lucia, C. S. Frenk, L. Gao, A. Jenkins, G. Kauffmann, J. F. Navarro, and N. Yoshida. Erratum: The many lives of active galactic nuclei: cooling flows, black holes and the luminosities and colours of galaxies. *MNRAS*, 367:864–864, April 2006b. doi: 10.1111/j.1365-2966.2006.09994.x.

R. A. Daly. Inverse Compton scattering and the alignments observed in high-redshift radio galaxies. *ApJ*, 386:L9–L12, February 1992. doi: 10.1086/186280.

R. I. Davies, L. Burtscher, D. Rosario, T. Storchi-Bergmann, A. Contursi, R. Genzel, J. Graciá-Carpio, E. Hicks, A. Janssen, M. Koss, M.-Y. Lin, D. Lutz, W. Maciejewski, F. Müller-Sánchez, G. Orban de Xivry, C. Ricci, R. Riffel, R. A. Riffel, M. Schartmann, A. Schnorr-Müller, A. Sternberg, E. Sturm, L. Tacconi, and S. Veilleux. Insights on the Dusty Torus and Neutral Torus from Optical and X-Ray Obscuration in a Complete Volume Limited Hard X-Ray AGN Sample. *ApJ*, 806:127, June 2015. doi: 10.1088/0004-637X/806/1/127.

C. De Breuck, H. Röttgering, G. Miley, W. van Breugel, and P. Best. A statistical study of emission lines from high redshift radio galaxies. *A&A*, 362:519–543, October 2000a.

C. De Breuck, W. van Breugel, H. J. A. Röttgering, and G. Miley. A sample of 669 ultra steep spectrum radio sources to find high redshift radio galaxies. *A&AS*, 143:303–333, April 2000b. doi: 10.1051/aas:2000181.

C. De Breuck, W. van Breugel, H. Röttgering, D. Stern, G. Miley, W. de Vries, S. A. Stanford, J. Kurk, and R. Overzier. Spectroscopy of Ultra-steep-Spectrum Radio Sources. *AJ*, 121: 1241–1265, March 2001. doi: 10.1086/319392.

C. De Breuck, N. Seymour, D. Stern, S. P. Willner, P. R. M. Eisenhardt, G. G. Fazio, A. Galametz, M. Lacy, A. Rettura, B. Rocca-Volmerange, and J. Vernet. The Spitzer High-redshift Radio Galaxy Survey. *ApJ*, 725:36–62, December 2010. doi: 10.1088/0004-637X/725/1/36.

D. S. De Young. Star formation in radio galaxies at large redshift. *ApJ*, 342:L59–L62, July 1989. doi: 10.1086/185484.

A. Dekel, Y. Birnboim, G. Engel, J. Freundlich, T. Goerdt, M. Mumcuoglu, E. Neistein, C. Pichon, R. Teyssier, and E. Zinger. Cold streams in early massive hot haloes as the main mode of galaxy formation. *Nature*, 457:451–454, January 2009. doi: 10.1038/nature07648.

A. Del Moro, D. M. Alexander, F. E. Bauer, E. Daddi, D. D. Kocevski, D. H. McIntosh, F. Stanley, W. N. Brandt, D. Elbaz, C. M. Harrison, B. Luo, J. R. Mullaney, and Y. Q. Xue. Mid-infrared luminous quasars in the GOODS-Herschel fields: a large population of heavily obscured, Compton-thick quasars at $z \approx 2$. *MNRAS*, 456:2105–2125, February 2016. doi: 10.1093/mnras/stv2748.

R. P. Deo, D. M. Crenshaw, and S. B. Kraemer. The Host Galaxies of Narrow-Line Seyfert 1 Galaxies: Nuclear Dust Morphology and Starburst Rings. *AJ*, 132:321–346, July 2006. doi: 10.1086/504894.

T. Di Matteo, V. Springel, and L. Hernquist. Energy input from quasars regulates the growth and activity of black holes and their host galaxies. *Nature*, 433:604–607, February 2005. doi: 10.1038/nature03335.

T. Di Matteo, J. Colberg, V. Springel, L. Hernquist, and D. Sijacki. Direct Cosmological Simulations of the Growth of Black Holes and Galaxies. *ApJ*, 676:33–53, March 2008. doi: 10.1086/524921.

S. di Serego Alighieri. Huge regions of ionized gas around radio galaxies. In H. C. Arp, editor, *New Ideas in Astronomy*, pages 111–113, 1988.

S. di Serego Alighieri, R. A. E. Fosbury, P. J. Quinn, and C. N. Tadhunter. Polarized light in high-redshift radio galaxies. *Nature*, 341:307–309, September 1989. doi: 10.1038/341307a0.

A. M. Diamond-Stanic and G. H. Rieke. The Relationship between Black Hole Growth and Star Formation in Seyfert Galaxies. *ApJ*, 746:168, February 2012. doi: 10.1088/0004-637X/746/2/168.

D. Dicken, C. Tadhunter, D. Axon, R. Morganti, A. Robinson, M. B. N. Kouwenhoven, H. Spoon, P. Kharb, K. J. Inskip, J. Holt, C. Ramos Almeida, and N. P. H. Nesvadba. Spitzer Mid-IR Spectroscopy of Powerful 2 Jy and 3CRR Radio Galaxies. I. Evidence against a Strong Starburst-AGN Connection in Radio-loud AGN. *ApJ*, 745:172, February 2012. doi: 10.1088/0004-637X/745/2/172.

M. Dietrich and F. Hamann. High Redshift Quasars and Star Formation History. In T. von Hippel, C. Simpson, and N. Manset, editors, *Astrophysical Ages and Times Scales*, volume 245 of *Astronomical Society of the Pacific Conference Series*, page 575, 2001.

M. Dietrich and U. Wilhelm-Erkens. Elemental abundances of high redshift quasars. *A&A*, 354:17–27, February 2000.

M. Dietrich, F. Hamann, J. C. Shields, A. Constantin, J. Heidt, K. Jäger, M. Vestergaard, and S. J. Wagner. Quasar Elemental Abundances at High Redshifts. *ApJ*, 589:722–732, June 2003. doi: 10.1086/374662.

M. Dijkstra. Lyα Emitting Galaxies as a Probe of Reionisation. *Publ. Astron. Soc. Australia*, 31:e040, October 2014. doi: 10.1017/pasa.2014.33.

M. Dijkstra. Saas-Fee Lecture Notes: Physics of Lyman Alpha Radiative Transfer. April 2017.

M. Dijkstra and R. Kramer. Line transfer through clumpy, large-scale outflows: Ly α absorption and haloes around star-forming galaxies. *MNRAS*, 424:1672–1693, August 2012. doi: 10.1111/j.1365-2966.2012.21131.x.

M. Dijkstra and A. Loeb. The polarization of scattered Lyα radiation around high-redshift galaxies. *MNRAS*, 386:492–504, May 2008. doi: 10.1111/j.1365-2966.2008.13066.x.

M. Dijkstra and A. Loeb. Lyα blobs as an observational signature of cold accretion streams into galaxies. *MNRAS*, 400:1109–1120, December 2009. doi: 10.1111/j.1365-2966.2009.15533.x.

M. Dijkstra, Z. Haiman, and M. Spaans. Lyα Radiation from Collapsing Protogalaxies. I. Characteristics of the Emergent Spectrum. *ApJ*, 649:14–36, September 2006a. doi: 10.1086/506243.

M. Dijkstra, Z. Haiman, and M. Spaans. Lyα Radiation from Collapsing Protogalaxies. II. Observational Evidence for Gas Infall. *ApJ*, 649:37–47, September 2006b. doi: 10.1086/506244.

A. Doi, H. Nagai, K. Asada, S. Kameno, K. Wajima, and M. Inoue. VLBI Observations of the Most Radio-Loud, Narrow-Line Quasar SDSS J094857.3+002225. *PASJ*, 58:829–834, October 2006. doi: 10.1093/pasj/58.5.829.

J. L. Donley, G. H. Rieke, J. R. Rigby, and P. G. Pérez-González. Unveiling a Population of AGNs Not Detected in X-Rays. *ApJ*, 634:169–182, November 2005. doi: 10.1086/491668.

J. L. Donley, A. M. Koekemoer, M. Brusa, P. Capak, C. N. Cardamone, F. Civano, O. Ilbert, C. D. Impey, J. S. Kartaltepe, T. Miyaji, M. Salvato, D. B. Sanders, J. R. Trump, and G. Zamorani. Identifying Luminous Active Galactic Nuclei in Deep Surveys: Revised IRAC Selection Criteria. *ApJ*, 748:142, April 2012. doi: 10.1088/0004-637X/748/2/142.

M. A. Dopita and R. S. Sutherland. Spectral Signatures of Fast Shocks. I. Low-Density Model Grid. *ApJS*, 102:161, January 1996. doi: 10.1086/192255.

G. Drouart, C. De Breuck, J. Vernet, N. Seymour, M. Lehnert, P. Barthel, F. E. Bauer, E. Ibar, A. Galametz, M. Haas, N. Hatch, J. R. Mullaney, N. Nesvadba, B. Rocca-Volmerange, H. J. A. Röttgering, D. Stern, and D. Wylezalek. Rapidly growing black holes and host galaxies in the distant Universe from the Herschel Radio Galaxy Evolution Project. *A&A*, 566:A53, June 2014. doi: 10.1051/0004-6361/201323310.

Y. Dubois, J. Devriendt, A. Slyz, and R. Teyssier. Jet-regulated cooling catastrophe. *MNRAS*, 409:985–1001, December 2010. doi: 10.1111/j.1365-2966.2010.17338.x.

J. S. Dunlop and J. A. Peacock. Luminosity Dependence of Optical Activity and Alignments Into Radio Galaxies. *MNRAS*, 263:936, August 1993. doi: 10.1093/mnras/263.4.936.

J. S. Dunlop, R. J. McLure, M. J. Kukula, S. A. Baum, C. P. O'Dea, and D. H. Hughes. Quasars, their host galaxies and their central black holes. *MNRAS*, 340:1095–1135, April 2003. doi: 10.1046/j.1365-8711.2003.06333.x.

R. J. H. Dunn, A. C. Fabian, and G. B. Taylor. Radio bubbles in clusters of galaxies. *MNRAS*, 364:1343–1353, December 2005. doi: 10.1111/j.1365-2966.2005.09673.x.

S. A. Eales. A new theory for the alignment effect. *ApJ*, 397:49–54, September 1992. doi: 10.1086/171765.

S. A. Eales, S. Rawlings, M. Dickinson, H. Spinrad, G. J. Hill, and M. Lacy. An optically luminous radio galaxy at Z = 3.22 and the K-z diagram at high redshift. *ApJ*, 409:578–583, June 1993. doi: 10.1086/172688.

D. O. Edge, J. R. Shakeshaft, W. B. McAdam, J. E. Baldwin, and S. Archer. A survey of radio sources at a frequency of 159 Mc/s. *Mem. RAS*, 68:37–60, 1959.

E. Egami, L. Armus, G. Neugebauer, T. W. Murphy, Jr., B. T. Soifer, K. Matthews, and A. S. Evans. Near-Infrared Observations of Powerful High-Redshift Radio Galaxies: 4C 40.36 and 4C 39.37. *AJ*, 125:1038–1052, March 2003. doi: 10.1086/367796.

P. R. M. Eisenhardt, J. Wu, C.-W. Tsai, R. Assef, D. Benford, A. Blain, C. Bridge, J. J. Condon, M. C. Cushing, R. Cutri, N. J. Evans, II, C. Gelino, R. L. Griffith, C. J. Grillmair, T. Jarrett, C. J. Lonsdale, F. J. Masci, B. S. Mason, S. Petty, J. Sayers, S. A. Stanford, D. Stern, E. L. Wright, and L. Yan. The First Hyper-luminous Infrared Galaxy Discovered by WISE. *ApJ*, 755:173, August 2012. doi: 10.1088/0004-637X/755/2/173.

M. Eisenreich, T. Naab, E. Choi, J. P. Ostriker, and E. Emsellem. Active galactic nuclei feedback, quiescence and circumgalactic medium metal enrichment in early-type galaxies. *MNRAS*, 468:751–768, June 2017. doi: 10.1093/mnras/stx473.

B. H. C. Emonts, R. Morganti, C. N. Tadhunter, T. A. Oosterloo, J. Holt, and J. M. van der Hulst. A jet-induced outflow of warm gas in 3C293. *MNRAS*, 362:931–944, September 2005. doi: 10.1111/j.1365-2966.2005.09354.x.

B. H. C. Emonts, R. Morganti, J. H. van Gorkom, T. A. Oosterloo, E. Brogt, and C. N. Tadhunter. From major merger to radio galaxy: low surface-brightness stellar counterpart to the giant

HI ring around B2 0648+27. *A&A*, 488:519–522, September 2008. doi: 10.1051/0004-6361:200810046.

B. H. C. Emonts, I. Feain, M. Y. Mao, R. P. Norris, G. Miley, R. D. Ekers, M. Villar-Martín, H. J. A. Röttgering, E. M. Sadler, G. Rees, R. Morganti, D. J. Saikia, T. A. Oosterloo, J. B. Stevens, and C. N. Tadhunter. Molecular CO(1-0) Gas in the z $\sim$ 2 Radio Galaxy MRC 0152-209. *ApJ*, 734:L25, June 2011a. doi: 10.1088/2041-8205/734/1/L25.

B. H. C. Emonts, R. P. Norris, I. Feain, G. Miley, E. M. Sadler, M. Villar-Martín, M. Y. Mao, T. A. Oosterloo, R. D. Ekers, J. B. Stevens, M. H. Wieringa, K. E. K. Coppin, and C. N. Tadhunter. CO observations of high-z radio galaxies MRC 2104-242 and MRC 0943-242: spectral-line performance of the Compact Array Broadband Backend. *MNRAS*, 415:655–664, July 2011b. doi: 10.1111/j.1365-2966.2011.18737.x.

B. H. C. Emonts, I. Feain, H. J. A. Röttgering, G. Miley, N. Seymour, R. P. Norris, C. L. Carilli, M. Villar-Martín, M. Y. Mao, E. M. Sadler, R. D. Ekers, G. A. van Moorsel, R. J. Ivison, L. Pentericci, C. N. Tadhunter, and D. J. Saikia. CO(1-0) detection of molecular gas in the massive Spiderweb Galaxy (z = 2). *MNRAS*, 430:3465–3471, April 2013. doi: 10.1093/mnras/stt147.

D. K. Erb, M. Bogosavljević, and C. C. Steidel. Filamentary Large-scale Structure Traced by Six Lyα Blobs at z = 2.3. *ApJ*, 740:L31, October 2011. doi: 10.1088/2041-8205/740/1/L31.

A. C. Fabian. The alignment of the optical continuum and radio axes of high-redshift radio galaxies - Electron scattering in intracluster gas? *MNRAS*, 238:41P–44P, June 1989. doi: 10.1093/mnras/238.1.41P.

A. C. Fabian, J. S. Sanders, G. B. Taylor, S. W. Allen, C. S. Crawford, R. M. Johnstone, and K. Iwasawa. A very deep Chandra observation of the Perseus cluster: shocks, ripples and conduction. *MNRAS*, 366:417–428, February 2006. doi: 10.1111/j.1365-2966.2005.09896.x.

X. Fan, C. L. Carilli, and B. Keating. Observational Constraints on Cosmic Reionization. *ARA&A*, 44:415–462, September 2006a. doi: 10.1146/annurev.astro.44.051905.092514.

X. Fan, M. A. Strauss, R. H. Becker, R. L. White, J. E. Gunn, G. R. Knapp, G. T. Richards, D. P. Schneider, J. Brinkmann, and M. Fukugita. Constraining the Evolution of the Ionizing Background and the Epoch of Reionization with z˜6 Quasars. II. A Sample of 19 Quasars. *AJ*, 132:117–136, July 2006b. doi: 10.1086/504836.

B. L. Fanaroff and J. M. Riley. The morphology of extragalactic radio sources of high and low luminosity. *MNRAS*, 167:31P–36P, May 1974. doi: 10.1093/mnras/167.1.31P.

N. Fanidakis, C. M. Baugh, A. J. Benson, R. G. Bower, S. Cole, C. Done, C. S. Frenk, R. C. Hickox, C. Lacey, and C. Del P. Lagos. The evolution of active galactic nuclei across cosmic time: what is downsizing? *MNRAS*, 419:2797–2820, February 2012. doi: 10.1111/j.1365-2966.2011.19931.x.

N. Fanidakis, A. Georgakakis, G. Mountrichas, M. Krumpe, C. M. Baugh, C. G. Lacey, C. S. Frenk, T. Miyaji, and A. J. Benson. Constraints on black hole fuelling modes from the clustering of X-ray AGN. *MNRAS*, 435:679–688, October 2013. doi: 10.1093/mnras/stt1327.

M. A. Fardal, N. Katz, J. P. Gardner, L. Hernquist, D. H. Weinberg, and R. Davé. Cooling Radiation and the Lyα Luminosity of Forming Galaxies. *ApJ*, 562:605–617, December 2001. doi: 10.1086/323519.

E. A. Fath. *The Spectra of Some Spiral Nebulae and Globular Star Clusters.* PhD thesis, UNIVERSITY OF CALIFORNIA, BERKELEY., 1909.

C.-A. Faucher-Giguère, D. Kereš, M. Dijkstra, L. Hernquist, and M. Zaldarriaga. Lyα Cooling Emission from Galaxy Formation. *ApJ*, 725:633–657, December 2010. doi: 10.1088/0004-637X/725/1/633.

G. J. Ferland, J. A. Baldwin, K. T. Korista, F. Hamann, R. F. Carswell, M. Phillips, B. Wilkes, and R. E. Williams. High Metal Enrichments in Luminous Quasars. *ApJ*, 461:683, April 1996. doi: 10.1086/177094.

L. Ferrarese and D. Merritt. A Fundamental Relation between Supermassive Black Holes and Their Host Galaxies. *ApJ*, 539:L9–L12, August 2000. doi: 10.1086/312838.

P. Ferruit, L. Binette, R. S. Sutherland, and E. Pecontal. Modeling extragalactic bowshocks. I. The model. *A&A*, 322:73–85, June 1997.

E. L. Fitzpatrick. Correcting for the Effects of Interstellar Extinction. *PASP*, 111:63–75, January 1999. doi: 10.1086/316293.

R. A. E. Fosbury, A. Boksenberg, M. A. J. Snijders, I. J. Danziger, M. J. Disney, W. M. Goss, M. V. Penston, W. Wamsteker, K. J. Wellington, and A. S. Wilson. Very extended ionized gas in radio galaxies. I - A radio, optical and ultraviolet study of PKS 2158-380. *MNRAS*, 201:991–1008, December 1982. doi: 10.1093/mnras/201.4.991.

L. Foschini, M. Berton, A. Caccianiga, S. Ciroi, V. Cracco, B. M. Peterson, E. Angelakis, V. Braito, L. Fuhrmann, L. Gallo, D. Grupe, E. Järvelä, S. Kaufmann, S. Komossa, Y. Y. Kovalev, A. Lähteenmäki, M. M. Lisakov, M. L. Lister, S. Mathur, J. L. Richards, P. Romano,

A. Sievers, G. Tagliaferri, J. Tammi, O. Tibolla, M. Tornikoski, S. Vercellone, G. La Mura, L. Maraschi, and P. Rafanelli. Properties of flat-spectrum radio-loud narrow-line Seyfert 1 galaxies. *A&A*, 575:A13, March 2015. doi: 10.1051/0004-6361/201424972.

P. C. Fragile, S. D. Murray, P. Anninos, and W. van Breugel. Radiative Shock-induced Collapse of Intergalactic Clouds. *ApJ*, 604:74–87, March 2004. doi: 10.1086/381726.

P. J. Francis, P. C. Hewett, C. B. Foltz, F. H. Chaffee, R. J. Weymann, and S. L. Morris. A high signal-to-noise ratio composite quasar spectrum. *ApJ*, 373:465–470, June 1991. doi: 10.1086/170066.

P. J. Francis, G. M. Williger, N. R. Collins, P. Palunas, E. M. Malumuth, B. E. Woodgate, H. I. Teplitz, A. Smette, R. S. Sutherland, A. C. Danks, R. S. Hill, D. Lindler, R. A. Kimble, S. R. Heap, and J. B. Hutchings. A Pair of Compact Red Galaxies at Redshift 2.38, Immersed in a 100 Kiloparsec Scale Lyα Nebula. *ApJ*, 554:1001–1011, June 2001. doi: 10.1086/321417.

S. R. Furlanetto, J. Schaye, V. Springel, and L. Hernquist. Lyα Emission from Structure Formation. *ApJ*, 622:7–27, March 2005. doi: 10.1086/426808.

V. Gaibler. Positive and negative feedback by AGN jets in high-redshift galaxies. *Astronomische Nachrichten*, 335:531, 2014. doi: 10.1002/asna.201412061.

J. E. Geach, Y. Matsuda, I. Smail, S. C. Chapman, T. Yamada, R. J. Ivison, T. Hayashino, K. Ohta, Y. Shioya, and Y. Taniguchi. A submillimetre survey of Lyman α haloes in the SA22 protocluster at z= 3.1. *MNRAS*, 363:1398–1408, November 2005. doi: 10.1111/j.1365-2966.2005.09538.x.

J. E. Geach, D. M. Alexander, B. D. Lehmer, I. Smail, Y. Matsuda, S. C. Chapman, C. A. Scharf, R. J. Ivison, M. Volonteri, T. Yamada, A. W. Blain, R. G. Bower, F. E. Bauer, and A. Basu-Zych. The Chandra Deep Protocluster Survey: Lyα Blobs are Powered by Heating, Not Cooling. *ApJ*, 700:1–9, July 2009. doi: 10.1088/0004-637X/700/1/1.

K. Gebhardt, R. Bender, G. Bower, A. Dressler, S. M. Faber, A. V. Filippenko, R. Green, C. Grillmair, L. C. Ho, J. Kormendy, T. R. Lauer, J. Magorrian, J. Pinkney, D. Richstone, and S. Tremaine. A Relationship between Nuclear Black Hole Mass and Galaxy Velocity Dispersion. *ApJ*, 539:L13–L16, August 2000. doi: 10.1086/312840.

R. Gilli, A. Comastri, and G. Hasinger. The synthesis of the cosmic X-ray background in the Chandra and XMM-Newton era. *A&A*, 463:79–96, February 2007. doi: 10.1051/0004-6361:20066334.

E. Glikman, T. Urrutia, M. Lacy, S. G. Djorgovski, A. Mahabal, A. D. Myers, N. P. Ross, P. Petitjean, J. Ge, D. P. Schneider, and D. G. York. FIRST-2MASS Red Quasars: Transitional Objects Emerging from the Dust. *ApJ*, 757:51, September 2012. doi: 10.1088/0004-637X/757/1/51.

T. Goerdt, A. Dekel, A. Sternberg, D. Ceverino, R. Teyssier, and J. R. Primack. Gravity-driven Lyα blobs from cold streams into galaxies. *MNRAS*, 407:613–631, September 2010. doi: 10.1111/j.1365-2966.2010.16941.x.

R. Gohil and D. R. Ballantyne. Modelling the vertical structure of nuclear starburst discs: a possible source of AGN obscuration at z $\sim$ 1. *MNRAS*, 468:4944–4955, July 2017. doi: 10.1093/mnras/stx776.

R. W. Goodrich. Spectropolarimetry of 'narrow-line' Seyfert 1 galaxies. *ApJ*, 342:224–234, July 1989. doi: 10.1086/167586.

Gopal-Krishna, A. Mangalam, and P. J. Wiita. Stellar Disruption by Supermassive Black Holes and the Quasar Radio Loudness Dichotomy. *ApJ*, 680:L13, June 2008. doi: 10.1086/589739.

A. Gould and D. H. Weinberg. Imaging the Forest of Lyman Limit Systems. *ApJ*, 468:462, September 1996. doi: 10.1086/177707.

A. W. Graham, P. Erwin, N. Caon, and I. Trujillo. A Correlation between Galaxy Light Concentration and Supermassive Black Hole Mass. *ApJ*, 563:L11–L14, December 2001. doi: 10.1086/338500.

G. L. Granato, L. Silva, P. Monaco, P. Panuzzo, P. Salucci, G. De Zotti, and L. Danese. Joint formation of QSOs and spheroids: QSOs as clocks of star formation in spheroids. *MNRAS*, 324:757–768, June 2001. doi: 10.1046/j.1365-8711.2001.04369.x.

G. L. Granato, L. Silva, G. de Zotti, A. Bressan, and L. Danese. A Physical Model for the Joint Evolution of QSOs and Spheroids. In M. Plionis, editor, *Astrophysics and Space Science Library*, volume 301 of *Astrophysics and Space Science Library*, page 129, 2004.

P. Grandi and G. G. C. Palumbo. Broad Line Radio Galaxies: Jet contribution to the nuclear X-γ-ray Continuum. In S. Ritz, P. Michelson, and C. A. Meegan, editors, *The First GLAST Symposium*, volume 921 of *American Institute of Physics Conference Series*, pages 335–336, July 2007. doi: 10.1063/1.2757339.

J. E. Greene, R. Alexandroff, M. A. Strauss, N. L. Zakamska, D. Lang, G. Liu, P. Pattarakijwanich, F. Hamann, N. P. Ross, A. D. Myers, W. N. Brandt, D. York, and D. P. Schneider.

Near-infrared Spectra and Intrinsic Luminosities of Candidate Type II Quasars at 2 < z < 3.4. *ApJ*, 788:91, June 2014. doi: 10.1088/0004-637X/788/1/91.

J. L. Greenstein and M. Schmidt. The Quasi-Stellar Radio Sources 3C 48 and 3C 273. *ApJ*, 140:1, July 1964. doi: 10.1086/147889.

D. Grupe. A Complete Sample of Soft X-Ray-selected AGNs. II. Statistical Analysis. *AJ*, 127: 1799–1810, April 2004. doi: 10.1086/382516.

B. Gullberg, C. De Breuck, M. D. Lehnert, J. Vernet, R. Bacon, G. Drouart, B. Emonts, A. Galametz, R. Ivison, N. P. H. Nesvadba, J. Richard, N. Seymour, D. Stern, and D. Wylezalek. The mysterious morphology of MRC0943-242 as revealed by ALMA and MUSE. *A&A*, 586:A124, February 2016. doi: 10.1051/0004-6361/201526858.

J. E. Gunn, W. A. Siegmund, E. J. Mannery, R. E. Owen, C. L. Hull, R. F. Leger, L. N. Carey, G. R. Knapp, D. G. York, W. N. Boroski, S. M. Kent, R. H. Lupton, C. M. Rockosi, M. L. Evans, P. Waddell, J. E. Anderson, J. Annis, J. C. Barentine, L. M. Bartoszek, S. Bastian, S. B. Bracker, H. J. Brewington, C. I. Briegel, J. Brinkmann, Y. J. Brown, M. A. Carr, P. C. Czarapata, C. C. Drennan, T. Dombeck, G. R. Federwitz, B. A. Gillespie, C. Gonzales, S. U. Hansen, M. Harvanek, J. Hayes, W. Jordan, E. Kinney, M. Klaene, S. J. Kleinman, R. G. Kron, J. Kresinski, G. Lee, S. Limmongkol, C. W. Lindenmeyer, D. C. Long, C. L. Loomis, P. M. McGehee, P. M. Mantsch, E. H. Neilsen, Jr., R. M. Neswold, P. R. Newman, A. Nitta, J. Peoples, Jr., J. R. Pier, P. S. Prieto, A. Prosapio, C. Rivetta, D. P. Schneider, S. Snedden, and S.-i. Wang. The 2.5 m Telescope of the Sloan Digital Sky Survey. *AJ*, 131:2332–2359, April 2006. doi: 10.1086/500975.

Z. Haiman and M. J. Rees. Extended Lyα Emission around Young Quasars: A Constraint on Galaxy Formation. *ApJ*, 556:87–92, July 2001. doi: 10.1086/321567.

Z. Haiman, M. Spaans, and E. Quataert. Lyα Cooling Radiation from High-Redshift Halos. *ApJ*, 537:L5–L8, July 2000a. doi: 10.1086/312754.

Z. Haiman, M. Spaans, and E. Quataert. Lyα Cooling Radiation from High-Redshift Halos. *ApJ*, 537:L5–L8, July 2000b. doi: 10.1086/312754.

K. N. Hainline, R. Hickox, J. E. Greene, A. D. Myers, and N. L. Zakamska. SALT Long-slit Spectroscopy of Luminous Obscured Quasars: An Upper Limit on the Size of the Narrow-line Region? *ApJ*, 774:145, September 2013. doi: 10.1088/0004-637X/774/2/145.

K. N. Hainline, R. C. Hickox, J. E. Greene, A. D. Myers, N. L. Zakamska, G. Liu, and X. Liu. Gemini Long-slit Observations of Luminous Obscured Quasars: Further Evidence for an Upper Limit on the Size of the Narrow-line Region. *ApJ*, 787:65, May 2014. doi: 10.1088/0004-637X/787/1/65.

F. Hamann and G. Ferland. The age and chemical evolution of high-redshift QSOs. *ApJ*, 391: L53–L57, June 1992. doi: 10.1086/186397.

F. Hamann and G. Ferland. The Chemical Evolution of QSOs and the Implications for Cosmology and Galaxy Formation. *ApJ*, 418:11, November 1993. doi: 10.1086/173366.

F. Hamann and G. Ferland. Elemental Abundances in Quasistellar Objects: Star Formation and Galactic Nuclear Evolution at High Redshifts. *ARA&A*, 37:487–531, 1999. doi: 10.1146/annurev.astro.37.1.487.

F. Hamann, K. T. Korista, G. J. Ferland, C. Warner, and J. Baldwin. Metallicities and Abundance Ratios from Quasar Broad Emission Lines. *ApJ*, 564:592–603, January 2002. doi: 10.1086/324289.

L. Hao, M. A. Strauss, C. A. Tremonti, D. J. Schlegel, T. M. Heckman, G. Kauffmann, M. R. Blanton, X. Fan, J. E. Gunn, P. B. Hall, Ž. Ivezić, G. R. Knapp, J. H. Krolik, R. H. Lupton, G. T. Richards, D. P. Schneider, I. V. Strateva, N. L. Zakamska, J. Brinkmann, R. J. Brunner, and G. P. Szokoly. Active Galactic Nuclei in the Sloan Digital Sky Survey. I. Sample Selection. *AJ*, 129:1783–1794, April 2005. doi: 10.1086/428485.

N. Häring and H.-W. Rix. On the Black Hole Mass-Bulge Mass Relation. *ApJ*, 604:L89–L92, April 2004. doi: 10.1086/383567.

G. Hasinger. Absorption properties and evolution of active galactic nuclei. *A&A*, 490:905–922, November 2008. doi: 10.1051/0004-6361:200809839.

N. A. Hatch, R. A. Overzier, H. J. A. Röttgering, J. D. Kurk, and G. K. Miley. Diffuse UV light associated with the Spiderweb Galaxy: evidence for in situ star formation outside galaxies. *MNRAS*, 383:931–942, January 2008. doi: 10.1111/j.1365-2966.2007.12626.x.

N. A. Hatch, R. A. Overzier, J. D. Kurk, G. K. Miley, H. J. A. Röttgering, and A. W. Zirm. The growth and assembly of a massive galaxy at z $\sim$ 2. *MNRAS*, 395:114–125, May 2009. doi: 10.1111/j.1365-2966.2009.14525.x.

N. A. Hatch, C. De Breuck, A. Galametz, G. K. Miley, R. A. Overzier, H. J. A. Röttgering, M. Doherty, T. Kodama, J. D. Kurk, N. Seymour, B. P. Venemans, J. Vernet, and A. W. Zirm. Galaxy protocluster candidates around z$\sim$ 2.4 radio galaxies. *MNRAS*, 410:1537–1549, January 2011. doi: 10.1111/j.1365-2966.2010.17538.x.

N. A. Hatch, H. J. A. Röttgering, G. K. Miley, E. Rigby, C. De Breuck, H. Ford, E. Kuiper, J. D. Kurk, R. A. Overzier, and L. Pentericci. The host galaxy of the z = 2.4 radio-loud AGN MRC 0406-244 as seen by HST. *MNRAS*, 436:2244–2253, December 2013. doi: 10.1093/mnras/stt1734.

N. A. Hatch, D. Wylezalek, J. D. Kurk, D. Stern, C. De Breuck, M. J. Jarvis, A. Galametz, A. H. Gonzalez, W. G. Hartley, A. Mortlock, N. Seymour, and J. A. Stevens. Why z > 1 radio-loud galaxies are commonly located in protoclusters. *MNRAS*, 445:280–289, November 2014. doi: 10.1093/mnras/stu1725.

M. Hayes. Lyman Alpha Emitting Galaxies in the Nearby Universe. *Publ. Astron. Soc. Australia*, 32:e027, July 2015. doi: 10.1017/pasa.2015.25.

M. Hayes, C. Scarlata, and B. Siana. Central powering of the largest Lyman-α nebula is revealed by polarized radiation. *Nature*, 476:304–307, August 2011. doi: 10.1038/nature10320.

T. M. Heckman, G. K. Miley, W. J. M. van Breugel, and H. R. Butcher. Emission-line profiles and kinematics of the narrow-line region in Seyfert and radio galaxies. *ApJ*, 247:403–418, July 1981. doi: 10.1086/159050.

T. M. Heckman, G. K. Miley, B. Balick, W. J. M. van Breugel, and H. R. Butcher. An optical and radio investigation of the radio galaxy 3C 305. *ApJ*, 262:529–553, November 1982. doi: 10.1086/160445.

S. Heinz and M. C. Begelman. Jet Acceleration by Tangled Magnetic Fields. *ApJ*, 535:104–117, May 2000. doi: 10.1086/308820.

J. F. Hennawi and J. X. Prochaska. Quasars Probing Quasars. IV. Joint Constraints on the Circumgalactic Medium from Absorption and Emission. *ApJ*, 766:58, March 2013. doi: 10.1088/0004-637X/766/1/58.

J. F. Hennawi, J. X. Prochaska, S. Cantalupo, and F. Arrigoni-Battaia. Quasar quartet embedded in giant nebula reveals rare massive structure in distant universe. *Science*, 348:779–783, May 2015. doi: 10.1126/science.aaa5397.

B. M. B. Henriques, S. D. M. White, P. A. Thomas, R. Angulo, Q. Guo, G. Lemson, V. Springel, and R. Overzier. Galaxy formation in the Planck cosmology - I. Matching the observed evolution of star formation rates, colours and stellar masses. *MNRAS*, 451:2663–2680, August 2015. doi: 10.1093/mnras/stv705.

R. B. C. Henry, M. G. Edmunds, and J. Köppen. On the Cosmic Origins of Carbon and Nitrogen. *ApJ*, 541:660–674, October 2000. doi: 10.1086/309471.

R. C. Hickox and D. M. Alexander. Obscured Active Galactic Nuclei. *ARA&A*, 56:625–671, September 2018. doi: 10.1146/annurev-astro-081817-051803.

G. J. Hill and S. J. Lilly. A change in the cluster environments of radio galaxies with cosmic epoch. *ApJ*, 367:1–18, January 1991. doi: 10.1086/169597.

G. Hinshaw, D. Larson, E. Komatsu, D. N. Spergel, C. L. Bennett, J. Dunkley, M. R. Nolta, M. Halpern, R. S. Hill, N. Odegard, L. Page, K. M. Smith, J. L. Weiland, B. Gold, N. Jarosik, A. Kogut, M. Limon, S. S. Meyer, G. S. Tucker, E. Wollack, and E. L. Wright. Nine-year Wilkinson Microwave Anisotropy Probe (WMAP) Observations: Cosmological Parameter Results. *ApJS*, 208:19, October 2013. doi: 10.1088/0067-0049/208/2/19.

L. C. Ho, A. V. Filippenko, and W. L. Sargent. A search for 'dwarf' Seyfert nuclei. 2: an optical spectral atlas of the nuclei of nearby galaxies. *ApJS*, 98:477–593, June 1995. doi: 10.1086/192170.

J. Holt, C. N. Tadhunter, and R. Morganti. Fast outflows in compact radio sources: evidence for AGN-induced feedback in the early stages of radio source evolution. *MNRAS*, 387:639–659, June 2008. doi: 10.1111/j.1365-2966.2008.13089.x.

P. F. Hopkins and M. Elvis. Quasar feedback: more bang for your buck. *MNRAS*, 401:7–14, January 2010. doi: 10.1111/j.1365-2966.2009.15643.x.

P. F. Hopkins, L. Hernquist, T. J. Cox, and D. Kereš. A Cosmological Framework for the Co-Evolution of Quasars, Supermassive Black Holes, and Elliptical Galaxies. I. Galaxy Mergers and Quasar Activity. *ApJS*, 175:356–389, April 2008. doi: 10.1086/524362.

P. F. Hopkins, P. Torrey, C.-A. Faucher-Giguère, E. Quataert, and N. Murray. Stellar and quasar feedback in concert: effects on AGN accretion, obscuration, and outflows. *MNRAS*, 458: 816–831, May 2016. doi: 10.1093/mnras/stw289.

E. P. Hubble. Extragalactic nebulae. *ApJ*, 64, December 1926. doi: 10.1086/143018.

A. Humphrey, M. Villar-Martín, R. Fosbury, J. Vernet, and S. di Serego Alighieri. Jet-gas interactions in $z \backsim 2.5$ radio galaxies: evolution of the ultraviolet line and continuum emission with radio morphology. *MNRAS*, 369:1103–1114, July 2006. doi: 10.1111/j.1365-2966.2006.10224.x.

A. Humphrey, M. Villar-Martín, R. Fosbury, L. Binette, J. Vernet, C. De Breuck, and S. di Serego Alighieri. Giant Lyα nebulae around z > 2 radio galaxies: evidence for infall. *MNRAS*, 375:705–714, February 2007. doi: 10.1111/j.1365-2966.2006.11344.x.

A. Humphrey, M. Villar-Martín, S. F. Sánchez, S. di Serego Alighieri, C. De Breuck, L. Binette, C. Tadhunter, J. Vernet, R. Fosbury, and J. Stasielak. Spatially extended absorption around the z = 2.63 radio galaxy MRC 2025-218: outflow or infall? *MNRAS*, 390:1505–1516, November 2008a. doi: 10.1111/j.1365-2966.2008.13826.x.

A. Humphrey, M. Villar-Martín, J. Vernet, R. Fosbury, S. di Serego Alighieri, and L. Binette. Deep spectroscopy of the FUV-optical emission lines from a sample of radio galaxies at z $\backsim$ 2.5: metallicity and ionization. *MNRAS*, 383:11–40, January 2008b. doi: 10.1111/j.1365-2966.2007.12506.x.

A. Humphrey, F. Iwamuro, M. Villar-Martín, L. Binette, and E. C. Sung. The extended ionized gas around the z = 2.44 radio galaxy MRC 0406-244: the nature of the superbubbles and the optical line brightness asymmetries. *MNRAS*, 399:L34–L38, October 2009. doi: 10.1111/j.1745-3933.2009.00719.x.

A. Humphrey, M. Villar-Martín, S. F. Sánchez, A. Martínez-Sansigre, R. G. Delgado, E. Pérez, C. Tadhunter, and M. A. Pérez-Torres. Integral-field spectroscopy of type II QSOs at z = 0.3-0.4. *MNRAS*, 408:L1–L5, October 2010. doi: 10.1111/j.1745-3933.2010.00906.x.

A. Humphrey, M. Zeballos, I. Aretxaga, D. H. Hughes, M. S. Yun, R. Cybulski, G. W. Wilson, J. Austermann, H. Ezawa, R. Kawabe, K. Kohno, T. Perera, K. Scott, D. Sánchez-Arguelles, and R. Gutermuth. AzTEC 1.1-mm images of 16 radio galaxies at 0.5 < z < 5.2 and a quasar at z= 6.3. *MNRAS*, 418:74–89, November 2011. doi: 10.1111/j.1365-2966.2011.19437.x.

A. Humphrey, L. Binette, M. Villar-Martín, I. Aretxaga, and P. Papaderos. A massive bubble of extremely metal-poor gas around a collapsing Lyα blob at z = 2.54. *MNRAS*, 428:563–572, January 2013a. doi: 10.1093/mnras/sts055.

A. Humphrey, J. Vernet, M. Villar-Martín, S. di Serego Alighieri, R. A. E. Fosbury, and A. Cimatti. Polarized Extended Lyα Emission from a z = 2.3 Radio Galaxy. *ApJ*, 768:L3, May 2013b. doi: 10.1088/2041-8205/768/1/L3.

A. Humphrey, M. Villar-Martín, C. Ramos Almeida, C. N. Tadhunter, S. Arribas, P. S. Bessiere, and A. Cabrera-Lavers. VLT FORS2 optical imaging and spectroscopy of nine luminous type 2 AGN at 0.3 < z < 0.6 - I. Ionized gas nebulae. *MNRAS*, 454:4452–4466, December 2015. doi: 10.1093/mnras/stv2177.

A. Humphrey, M. Villar-Martín, and P. Lagos. GTC optical imaging of extremely red 5C radio galaxies at high redshift. *A&A*, 585:A32, January 2016. doi: 10.1051/0004-6361/201526411.

A. Humphrey, M. Villar-Martín, L. Binette, and R. Raj. Photoionization models for extreme Lyα λ1216 and HeII λ1640 line ratios in quasar halos, and PopIII vs. AGN diagnostics. *A&A*, 621:A10, January 2019. doi: 10.1051/0004-6361/201732007.

K. J. Inskip, P. N. Best, S. Rawlings, M. S. Longair, G. Cotter, H. J. A. Röttgering, and S. Eales. Deep spectroscopy of z ~ 1 6C radio galaxies - I. The effects of radio power and size on the properties of the emission-line gas. *MNRAS*, 337:1381–1406, December 2002. doi: 10.1046/j.1365-8711.2002.06012.x.

F. Iwamuro, K. Motohara, T. Maihara, M. Kimura, S. Eto, T. Shima, D. Mochida, S. Wada, S. Imai, and K. Aoki. Infrared Spectroscopy of 15 Radio Galaxies at 2v< z < 2.6. *ApJ*, 598: 178–189, November 2003. doi: 10.1086/378845.

M. J. Jarvis, R. J. Wilman, H. J. A. Röttgering, and L. Binette. Probing the absorbing haloes around two high-redshift radio galaxies with VLT-UVES*. *MNRAS*, 338:263–272, January 2003. doi: 10.1046/j.1365-8711.2003.06053.x.

L. Jiang, X. Fan, M. Vestergaard, J. D. Kurk, F. Walter, B. C. Kelly, and M. A. Strauss. Gemini Near-Infrared Spectroscopy of Luminous z ~ 6 Quasars: Chemical Abundances, Black Hole Masses, and Mg II Absorption. *AJ*, 134:1150, September 2007. doi: 10.1086/520811.

Y. Juarez, R. Maiolino, R. Mujica, M. Pedani, S. Marinoni, T. Nagao, A. Marconi, and E. Oliva. The metallicity of the most distant quasars. *A&A*, 494:L25–L28, February 2009. doi: 10.1051/0004-6361:200811415.

G. Kauffmann, T. M. Heckman, C. Tremonti, J. Brinchmann, S. Charlot, S. D. M. White, S. E. Ridgway, J. Brinkmann, M. Fukugita, P. B. Hall, Ž. Ivezić, G. T. Richards, and D. P. Schneider. The host galaxies of active galactic nuclei. *MNRAS*, 346:1055–1077, December 2003. doi: 10.1111/j.1365-2966.2003.07154.x.

D. Kereš, N. Katz, D. H. Weinberg, and R. Davé. How do galaxies get their gas? *MNRAS*, 363: 2–28, October 2005. doi: 10.1111/j.1365-2966.2005.09451.x.

A. King. Black Holes, Galaxy Formation, and the M_{BH}-σ Relation. *ApJ*, 596:L27–L29, October 2003. doi: 10.1086/379143.

G. P. Knopp and K. C. Chambers. Deep Imaging of the Field of the High-Redshift Radio Source 4C 23.56. *ApJS*, 109:367–396, April 1997. doi: 10.1086/312981.

A. M. Koekemoer and G. V. Bicknell. Dynamics and Excitation of Radio Galaxy Emission-Line Regions. I. PKS 2356-61. *ApJ*, 497:662–680, April 1998. doi: 10.1086/305490.

J. A. Kollmeier, Z. Zheng, R. Davé, A. Gould, N. Katz, J. Miralda-Escudé, and D. H. Weinberg. Lyα Emission from Cosmic Structure. I. Fluorescence. *ApJ*, 708:1048–1075, January 2010. doi: 10.1088/0004-637X/708/2/1048.

S. Komossa, W. Voges, D. Xu, S. Mathur, H.-M. Adorf, G. Lemson, W. J. Duschl, and D. Grupe. Radio-loud Narrow-Line Type 1 Quasars. *AJ*, 132:531–545, August 2006. doi: 10.1086/505043.

J. Kormendy and K. Gebhardt. Supermassive black holes in galactic nuclei. In J. C. Wheeler and H. Martel, editors, *20th Texas Symposium on relativistic astrophysics*, volume 586 of *American Institute of Physics Conference Series*, pages 363–381, October 2001. doi: 10.1063/1.1419581.

J. Kormendy and L. C. Ho. Coevolution (Or Not) of Supermassive Black Holes and Host Galaxies. *ARA&A*, 51:511–653, August 2013. doi: 10.1146/annurev-astro-082708-101811.

J. Kormendy and D. Richstone. Inward Bound—The Search For Supermassive Black Holes In Galactic Nuclei. *ARA&A*, 33:581, 1995. doi: 10.1146/annurev.aa.33.090195.003053.

E. Kuiper, N. A. Hatch, G. K. Miley, N. P. H. Nesvadba, H. J. A. Röttgering, J. D. Kurk, M. D. Lehnert, R. A. Overzier, L. Pentericci, J. Schaye, and B. P. Venemans. A SINFONI view of flies in the Spiderweb: a galaxy cluster in the making. *MNRAS*, 415:2245–2256, August 2011. doi: 10.1111/j.1365-2966.2011.18852.x.

Z. Kuncic and G. V. Bicknell. Dynamics and Energetics of Turbulent, Magnetized Disk Accretion around Black Holes: A First-Principles Approach to Disk-Corona-Outflow Coupling. *ApJ*, 616:669–687, December 2004. doi: 10.1086/425032.

J. Kurk, B. Venemans, H. Röttgering, G. Miley, and L. Pentericci. Proto-clusters Associated with Radio Galaxies from z=2 to z=4. In M. Plionis, editor, *Astrophysics and Space Science Library*, volume 301 of *Astrophysics and Space Science Library*, page 141, 2004a.

J. D. Kurk. *The cluster environments and gaseous halos of distant radio galaxies*. PhD thesis, Leiden University, P.O. Box 9504, 2300 RA Leiden, The Netherlands, May 2003.

J. D. Kurk, H. J. A. Röttgering, L. Pentericci, G. K. Miley, W. van Breugel, C. L. Carilli, H. Ford, T. Heckman, P. McCarthy, and A. Moorwood. A Search for clusters at high redshift. I. Candidate Lyalpha emitters near 1138-262 at z=2.2. *A&A*, 358:L1–L4, June 2000.

J. D. Kurk, L. Pentericci, H. J. A. Röttgering, and G. K. Miley. Observations of Radio Galaxy MRC 1138-262: Merging Galaxies Embedded in a Giant Ly alpha Halo. In W. J. Henney, W. Steffen, L. Binette, and A. Raga, editors, *Revista Mexicana de Astronomia y Astrofisica Conference Series*, volume 13 of *Revista Mexicana de Astronomia y Astrofisica Conference Series*, pages 191–195, June 2002.

J. D. Kurk, L. Pentericci, R. A. Overzier, H. J. A. Röttgering, and G. K. Miley. A search for clusters at high redshift. IV. Spectroscopy of Hα emitters in a proto-cluster at z = 2.16. *A&A*, 428:817–821, December 2004b. doi: 10.1051/0004-6361:20041819.

M. Lacy, L. J. Storrie-Lombardi, A. Sajina, P. N. Appleton, L. Armus, S. C. Chapman, P. I. Choi, D. Fadda, F. Fang, D. T. Frayer, I. Heinrichsen, G. Helou, M. Im, F. R. Marleau, F. Masci, D. L. Shupe, B. T. Soifer, J. Surace, H. I. Teplitz, G. Wilson, and L. Yan. Obscured and Unobscured Active Galactic Nuclei in the Spitzer Space Telescope First Look Survey. *ApJS*, 154:166–169, September 2004. doi: 10.1086/422816.

M. Lacy, A. Sajina, A. O. Petric, N. Seymour, G. Canalizo, S. E. Ridgway, L. Armus, and L. J. Storrie-Lombardi. Large Amounts of Optically Obscured Star Formation in the Host Galaxies of Some Type 2 Quasars. *ApJ*, 669:L61–L64, November 2007. doi: 10.1086/523851.

M. Lacy, S. E. Ridgway, E. L. Gates, D. M. Nielsen, A. O. Petric, A. Sajina, T. Urrutia, S. Cox Drews, C. Harrison, N. Seymour, and L. J. Storrie-Lombardi. The Spitzer Mid-infrared Active Galactic Nucleus Survey. I. Optical and Near-infrared Spectroscopy of Obscured Candidates and Normal Active Galactic Nuclei Selected in the Mid-infrared. *ApJS*, 208:24, October 2013. doi: 10.1088/0067-0049/208/2/24.

M. Lacy, S. E. Ridgway, A. Sajina, A. O. Petric, E. L. Gates, T. Urrutia, and L. J. Storrie-Lombardi. The Spitzer Mid-infrared AGN Survey. II. The Demographics and Cosmic Evolution of the AGN Population. *ApJ*, 802:102, April 2015. doi: 10.1088/0004-637X/802/2/102.

C. D. P. Lagos, S. A. Cora, and N. D. Padilla. Effects of AGN feedback on ΛCDM galaxies. *MNRAS*, 388:587–602, August 2008. doi: 10.1111/j.1365-2966.2008.13456.x.

M. I. Large, B. Y. Mills, A. G. Little, D. F. Crawford, and J. M. Sutton. The Molonglo Reference Catalogue of Radio Sources. *MNRAS*, 194:693, February 1981. doi: 10.1093/mnras/194.3.693.

J. E. Larkin, I. S. McLean, J. R. Graham, E. E. Becklin, D. F. Figer, A. M. Gilbert, N. A. Levenson, H. I. Teplitz, M. K. Wilcox, and T. M. Glassman. Discovery of an Obscured

Broad-Line Region in the High-Redshift Radio Galaxy MRC 2025-218. *ApJ*, 533:L61–L64, April 2000. doi: 10.1086/312598.

P. Laursen and J. Sommer-Larsen. Lyα Resonant Scattering in Young Galaxies: Predictions from Cosmological Simulations. *ApJ*, 657:L69–L72, March 2007. doi: 10.1086/513191.

P. Laursen, A. O. Razoumov, and J. Sommer-Larsen. Lyα Radiative Transfer in Cosmological Simulations Using Adaptive Mesh Refinement. *ApJ*, 696:853–869, May 2009. doi: 10.1088/0004-637X/696/1/853.

P. Laursen, J. Sommer-Larsen, and A. O. Razoumov. Intergalactic Transmission and Its Impact on the Lyα Line. *ApJ*, 728:52, February 2011. doi: 10.1088/0004-637X/728/1/52.

M. J. Ledlow and F. N. Owen. Optical Properties of FRI Radio Galaxies. In R. D. Ekers, C. Fanti, and L. Padrielli, editors, *Extragalactic Radio Sources*, volume 175 of *IAU Symposium*, page 238, 1996.

M. J. Ledlow, F. N. Owen, M. S. Yun, and J. M. Hill. A Large-Scale Jet and FR I Radio Source in a Spiral Galaxy: The Host Properties and External Environment. *ApJ*, 552:120–132, May 2001. doi: 10.1086/320458.

M. D. Lehnert, W. J. M. van Breugel, T. M. Heckman, and G. K. Miley. HUBBLE SPACE TELESCOPE Imaging of the Host Galaxies of High-RedshiftRadio-loud Quasars. *ApJS*, 124:11–31, September 1999. doi: 10.1086/313252.

K. M. Leighly. A Comprehensive Spectral and Variability Study of Narrow-Line Seyfert 1 Galaxies Observed by ASCA. II. Spectral Analysis and Correlations. *ApJS*, 125:317–348, December 1999a. doi: 10.1086/313287.

K. M. Leighly. A Comprehensive Spectral and Variability Study of Narrow-Line Seyfert 1 Galaxies Observed by ASCA. I. Observations and Time Series Analysis. *ApJS*, 125:297–316, December 1999b. doi: 10.1086/313277.

D. Lena, A. Robinson, T. Storchi-Bergman, A. Schnorr-Müller, T. Seelig, R. A. Riffel, N. M. Nagar, G. S. Couto, and L. Shadler. The Complex Gas Kinematics in the Nucleus of the Seyfert 2 Galaxy NGC 1386: Rotation, Outflows, and Inflows. *ApJ*, 806:84, June 2015. doi: 10.1088/0004-637X/806/1/84.

J. León-Tavares, V. Chavushyan, V. Patiño-Álvarez, E. Valtaoja, T. G. Arshakian, L. Č. Popović, M. Tornikoski, A. Lobanov, A. Carramiñana, L. Carrasco, and A. Lähteenmäki. Flare-like

Variability of the Mg II λ2800 Emission Line in the Γ-Ray Blazar 3C 454.3. *ApJ*, 763:L36, February 2013. doi: 10.1088/2041-8205/763/2/L36.

G. Liu, N. L. Zakamska, J. E. Greene, N. P. H. Nesvadba, and X. Liu. Observations of feedback from radio-quiet quasars - I. Extents and morphologies of ionized gas nebulae. *MNRAS*, 430: 2327–2345, April 2013. doi: 10.1093/mnras/stt051.

I. Lonoce, M. Longhetti, C. Maraston, D. Thomas, C. Mancini, A. Cimatti, F. Ciocca, A. Citro, E. Daddi, S. di Serego Alighieri, A. Gargiulo, R. Maiolino, F. Mannucci, M. Moresco, L. Pozzetti, S. Quai, and P. Saracco. Old age and supersolar metallicity in a massive z $\sim$ 1.4 early-type galaxy from VLT/X-Shooter spectroscopy. *MNRAS*, 454:3912–3919, December 2015. doi: 10.1093/mnras/stv2150.

T. Lyman. The Spectrum of Hydrogen in the Region of Extremely Short Wave-Lengths. *ApJ*, 23:181, April 1906. doi: 10.1086/141330.

Theodore Lyman. An extension of the spectrum in the extreme ultra-violet. *Nature*, 93:241–241, 01 1914. doi: 10.1038/093241a0.

H. L. Marshall, J. M. Gelbord, D. M. Worrall, M. Birkinshaw, D. A. Schwartz, D. L. Jauncey, G. Griffiths, D. W. Murphy, J. E. J. Lovell, E. S. Perlman, and L. Godfrey. An X-Ray Imaging Survey of Quasar Jets: The Complete Survey. *ApJ*, 856:66, March 2018. doi: 10.3847/1538-4357/aaaf66.

C. L. Martin. Mapping Large-Scale Gaseous Outflows in Ultraluminous Galaxies with Keck II ESI Spectra: Variations in Outflow Velocity with Galactic Mass. *ApJ*, 621:227–245, March 2005. doi: 10.1086/427277.

D. C. Martin, M. Matuszewski, P. Morrissey, J. D. Neill, A. Moore, S. Cantalupo, J. X. Prochaska, and D. Chang. A giant protogalactic disk linked to the cosmic web. *Nature*, 524: 192–195, August 2015. doi: 10.1038/nature14616.

A. Martínez-Sansigre, S. Rawlings, M. Lacy, D. Fadda, F. R. Marleau, C. Simpson, C. J. Willott, and M. J. Jarvis. The obscuration by dust of most of the growth of supermassive black holes. *Nature*, 436:666–669, August 2005. doi: 10.1038/nature03829.

A. Martínez-Sansigre, S. Rawlings, M. Lacy, D. Fadda, M. J. Jarvis, F. R. Marleau, C. Simpson, and C. J. Willott. A population of high-redshift type 2 quasars - I. Selection criteria and optical spectra. *MNRAS*, 370:1479–1498, August 2006. doi: 10.1111/j.1365-2966.2006.10563.x.

S. Mateos, A. Alonso-Herrero, F. J. Carrera, A. Blain, M. G. Watson, X. Barcons, V. Braito, P. Severgnini, J. L. Donley, and D. Stern. Using the Bright Ultrahard XMM-Newton survey to define an IR selection of luminous AGN based on WISE colours. *MNRAS*, 426:3271–3281, November 2012. doi: 10.1111/j.1365-2966.2012.21843.x.

S. Mateos, F. J. Carrera, A. Alonso-Herrero, A. Hernán-Caballero, X. Barcons, A. Asensio Ramos, M. G. Watson, A. Blain, A. Caccianiga, L. Ballo, V. Braito, and C. Ramos Almeida. X-Ray Absorption, Nuclear Infrared Emission, and Dust Covering Factors of AGNs: Testing Unification Schemes. *ApJ*, 819:166, March 2016. doi: 10.3847/0004-637X/819/2/166.

S. Mateos, F. J. Carrera, X. Barcons, A. Alonso-Herrero, A. Hernán-Caballero, M. Page, C. Ramos Almeida, A. Caccianiga, T. Miyaji, and A. Blain. Survival of the Obscuring Torus in the Most Powerful Active Galactic Nuclei. *ApJ*, 841:L18, June 2017. doi: 10.3847/2041-8213/aa7268.

K. Matsuoka, T. Nagao, R. Maiolino, A. Marconi, and Y. Taniguchi. Chemical evolution of high-redshift radio galaxies. *A&A*, 503:721–730, September 2009. doi: 10.1051/0004-6361/200811478.

F. Matteucci. Chemical Evolution at Low and High Redshift. In C. Leitherer, U. Fritze-von-Alvensleben, and J. Huchra, editors, *From Stars to Galaxies: the Impact of Stellar Physics on Galaxy Evolution*, volume 98 of *Astronomical Society of the Pacific Conference Series*, page 529, 1996.

F. Matteucci and P. Padovani. Chemical Evolution of Galaxies and Quasar Metallicities. *ApJ*, 419:485, December 1993. doi: 10.1086/173502.

T. A. Matthews, W. W. Morgan, and M. Schmidt. A Discussion of Galaxies Indentified with Radio Sources. *ApJ*, 140:35, July 1964. doi: 10.1086/147890.

P. J. McCarthy. High redshift radio galaxies. *ARA&A*, 31:639–688, 1993. doi: 10.1146/annurev.aa.31.090193.003231.

P. J. McCarthy, W. van Breugel, H. Spinrad, and S. Djorgovski. A correlation between the radio and optical morphologies of distant 3Cr radio galaxies. *ApJ*, 321:L29–L33, October 1987. doi: 10.1086/185000.

P. J. McCarthy, V. K. Kapahi, W. van Breugel, and C. R. Subrahmanya. High-redshift radio galaxies from the Molonglo Catalogue. *AJ*, 100:1014–1027, October 1990a. doi: 10.1086/115575.

P. J. McCarthy, H. Spinrad, M. Dickinson, W. van Breugel, J. Liebert, S. Djorgovski, and P. Eisenhardt. Extended Ly-alpha emission associated with 3C 294. *ApJ*, 365:487–501, December 1990b. doi: 10.1086/169503.

P. J. McCarthy, S. E. Persson, and S. C. West. Infrared imaging of Z greater than 2 radio galaxies. *ApJ*, 386:52–58, February 1992. doi: 10.1086/170991.

P. J. McCarthy, H. Spinrad, and W. van Breugel. Emission-Line Imaging of 3CR Radio Galaxies. I. Imaging Data. *ApJS*, 99:27, July 1995. doi: 10.1086/192178.

R. J. McLure and M. J. Jarvis. The relationship between radio luminosity and black hole mass in optically selected quasars. *MNRAS*, 353:L45–L49, October 2004. doi: 10.1111/j.1365-2966.2004.08305.x.

G. Mellema, J. Kurk, and H. Röttgering. The fate of clouds in radio lobes. *New Astron. Rev.*, 47:243–247, September 2003. doi: 10.1016/S1387-6473(03)00033-2.

G. Miley and C. De Breuck. Distant radio galaxies and their environments. *A&ARv*, 15:67–144, February 2008. doi: 10.1007/s00159-007-0008-z.

G. K. Miley, R. A. Overzier, A. W. Zirm, H. C. Ford, J. Kurk, L. Pentericci, J. P. Blakeslee, M. Franx, G. D. Illingworth, M. Postman, P. Rosati, H. J. A. Röttgering, B. P. Venemans, and E. Helder. The Spiderweb Galaxy: A Forming Massive Cluster Galaxy at $z \sim 2$. *ApJ*, 650:L29–L32, October 2006. doi: 10.1086/508534.

J. S. Miller and R. W. Goodrich. Spectropolarimetry of high-polarization Seyfert 2 galaxies and unified Seyfert theories. *ApJ*, 355:456–467, June 1990. doi: 10.1086/168780.

S. G. Morais, A. Humphrey, M. Villar-Martín, P. Lagos, M. Moyano, R. Overzier, S. di Serego Alighieri, J. Vernet, and C. A. C. Fernandes. Ionization and feedback in Lyα haloes around two radio galaxies at $z \sim 2.5$. *MNRAS*, 465:2698–2713, March 2017. doi: 10.1093/mnras/stw2926.

D. J. Mortlock, S. J. Warren, B. P. Venemans, M. Patel, P. C. Hewett, R. G. McMahon, C. Simpson, T. Theuns, E. A. Gonzáles-Solares, A. Adamson, S. Dye, N. C. Hambly, P. Hirst, M. J. Irwin, E. Kuiper, A. Lawrence, and H. J. A. Röttgering. A luminous quasar at a redshift of $z = 7.085$. *Nature*, 474:616–619, June 2011. doi: 10.1038/nature10159.

M. M. Moyano, A. J. Humphrey, and D. C. Merlo. A project to constrain emission from giant gaseous shells around high redshift radio galaxies. *Boletin de la Asociacion Argentina de Astronomia La Plata Argentina*, 57:12–13, August 2015.

J. R. Mullaney, E. Daddi, M. Béthermin, D. Elbaz, S. Juneau, M. Pannella, M. T. Sargent, D. M. Alexander, and R. C. Hickox. The Hidden "AGN Main Sequence": Evidence for a Universal Black Hole Accretion to Star Formation Rate Ratio since z ˜ 2 Producing an M $_{BH}$-M $_*$ Relation. *ApJ*, 753:L30, July 2012a. doi: 10.1088/2041-8205/753/2/L30.

J. R. Mullaney, M. Pannella, E. Daddi, D. M. Alexander, D. Elbaz, R. C. Hickox, F. Bournaud, B. Altieri, H. Aussel, D. Coia, H. Dannerbauer, K. Dasyra, M. Dickinson, H. S. Hwang, J. Kartaltepe, R. Leiton, G. Magdis, B. Magnelli, P. Popesso, I. Valtchanov, F. E. Bauer, W. N. Brandt, A. Del Moro, D. J. Hanish, R. J. Ivison, S. Juneau, B. Luo, D. Lutz, M. T. Sargent, D. Scott, and Y. Q. Xue. GOODS-Herschel: the far-infrared view of star formation in active galactic nucleus host galaxies since z $\approx$ 3. *MNRAS*, 419:95–115, January 2012b. doi: 10.1111/j.1365-2966.2011.19675.x.

J. R. Mullaney, D. M. Alexander, S. Fine, A. D. Goulding, C. M. Harrison, and R. C. Hickox. Narrow-line region gas kinematics of 24 264 optically selected AGN: the radio connection. *MNRAS*, 433:622–638, July 2013. doi: 10.1093/mnras/stt751.

K. Nagamine, J.-H. Choi, and H. Yajima. Effects of Ultraviolet Background and Local Stellar Radiation on the H I Column Density Distribution. *ApJ*, 725:L219–L222, December 2010. doi: 10.1088/2041-8205/725/2/L219.

T. Nagao, K. S. Kawabata, T. Murayama, Y. Ohyama, Y. Taniguchi, R. Sumiya, and S. S. Sasaki. Detection of the Polarized Broad Emission Line in the Seyfert 2 Galaxy Markarian 573. *AJ*, 128:109–114, July 2004. doi: 10.1086/421740.

T. Nagao, R. Maiolino, and A. Marconi. Gas metallicity in the narrow-line regions of high-redshift active galactic nuclei. *A&A*, 447:863–876, March 2006a. doi: 10.1051/0004-6361:20054127.

T. Nagao, A. Marconi, and R. Maiolino. The evolution of the broad-line region among SDSS quasars. *A&A*, 447:157–172, February 2006b. doi: 10.1051/0004-6361:20054024.

C. H. Nelson and M. Whittle. Stellar and Gaseous Kinematics of Seyfert Galaxies. I. Spectroscopic Data. *ApJS*, 99:67, July 1995. doi: 10.1086/192179.

N. P. H. Nesvadba, M. D. Lehnert, F. Eisenhauer, A. Gilbert, M. Tecza, and R. Abuter. Extreme Gas Kinematics in the z=2.2 Powerful Radio Galaxy MRC 1138-262: Evidence for Efficient Active Galactic Nucleus Feedback in the Early Universe? *ApJ*, 650:693–705, October 2006. doi: 10.1086/507266.

N. P. H. Nesvadba, M. D. Lehnert, C. De Breuck, A. Gilbert, and W. van Breugel. Compact radio sources and jet-driven AGN feedback in the early universe: constraints from integral-field spectroscopy. *A&A*, 475:145–153, November 2007. doi: 10.1051/0004-6361:20078175.

N. P. H. Nesvadba, M. D. Lehnert, R. I. Davies, A. Verma, and F. Eisenhauer. Integral-field spectroscopy of a Lyman-break galaxy at z = 3.2: evidence for merging. *A&A*, 479:67–73, February 2008a. doi: 10.1051/0004-6361:20078555.

N. P. H. Nesvadba, M. D. Lehnert, C. De Breuck, A. M. Gilbert, and W. van Breugel. Evidence for powerful AGN winds at high redshift: dynamics of galactic outflows in radio galaxies during the "Quasar Era". *A&A*, 491:407–424, November 2008b. doi: 10.1051/0004-6361:200810346.

N. P. H. Nesvadba, F. Boulanger, P. Salomé, P. Guillard, M. D. Lehnert, P. Ogle, P. Appleton, E. Falgarone, and G. Pineau Des Forets. Energetics of the molecular gas in the H_2 luminous radio galaxy 3C 326: Evidence for negative AGN feedback. *A&A*, 521:A65, October 2010. doi: 10.1051/0004-6361/200913333.

N. P. H. Nesvadba, C. De Breuck, M. D. Lehnert, P. N. Best, L. Binette, and D. Proga. The black holes of radio galaxies during the "Quasar Era": masses, accretion rates, and evolutionary stage. *A&A*, 525:A43, January 2011. doi: 10.1051/0004-6361/201014960.

N. P. H. Nesvadba, C. De Breuck, M. D. Lehnert, P. N. Best, and C. Collet. The SINFONI survey of powerful radio galaxies at z 2: Jet-driven AGN feedback during the Quasar Era. *A&A*, 599:A123, March 2017a. doi: 10.1051/0004-6361/201528040.

N. P. H. Nesvadba, G. Drouart, C. De Breuck, P. Best, N. Seymour, and J. Vernet. Gas kinematics in powerful radio galaxies at z $\sim$ 2: Energy supply from star formation, AGN, and radio jets. *A&A*, 600:A121, April 2017b. doi: 10.1051/0004-6361/201629357.

H. Netzer. Revisiting the Unified Model of Active Galactic Nuclei. *ARA&A*, 53:365–408, August 2015. doi: 10.1146/annurev-astro-082214-122302.

Matthew Newville, Till Stensitzki, Daniel B. Allen, and Antonino Ingargiola. LMFIT: Non-Linear Least-Square Minimization and Curve-Fitting for Python, September 2014.

D. C. Nicholls, R. S. Sutherland, M. A. Dopita, L. J. Kewley, and B. A. Groves. Abundance scaling in stars, nebulae and galaxies. *MNRAS*, 466:4403–4422, April 2017. doi: 10.1093/mnras/stw3235.

C. Norman, G. Hasinger, R. Giacconi, R. Gilli, L. Kewley, M. Nonino, P. Rosati, G. Szokoly, P. Tozzi, J. Wang, W. Zheng, A. Zirm, J. Bergeron, R. Gilmozzi, N. Grogin, A. Koekemoer, and E. Schreier. A Classic Type 2 QSO. *ApJ*, 571:218–225, May 2002. doi: 10.1086/339855.

P. Ogle, J. E. Davies, P. N. Appleton, B. Bertincourt, N. Seymour, and G. Helou. Ultraluminous Star-forming Galaxies and Extremely Luminous Warm Molecular Hydrogen Emission at z = 2.16 in the PKS 1138-26 Radio Galaxy Protocluster. *ApJ*, 751:13, May 2012. doi: 10.1088/0004-637X/751/1/13.

J. B. Oke. Absolute Energy Distribution in the Optical Spectrum of 3C 273. *Nature*, 197: 1040–1041, March 1963. doi: 10.1038/1971040b0.

A. Olguín-Iglesias, J. León-Tavares, J. K. Kotilainen, V. Chavushyan, M. Tornikoski, E. Valtaoja, C. Añorve, J. Valdés, and L. Carrasco. The host galaxies of active galactic nuclei with powerful relativistic jets. *MNRAS*, 460:3202–3220, August 2016. doi: 10.1093/mnras/stw1208.

Á. A. Orsi, N. Fanidakis, C. G. Lacey, and C. M. Baugh. The environments of high-redshift radio galaxies and quasars: probes of protoclusters. *MNRAS*, 456:3827–3839, March 2016. doi: 10.1093/mnras/stv2919.

D. E. Osterbrock. The Escape of Resonance-Line Radiation from an Optically Thick Nebula. *ApJ*, 135:195, January 1962. doi: 10.1086/147258.

D. E. Osterbrock. Markarian 376: a Seyfert Galaxy with Strong fe II Emission. *ApJ*, 203: 329–334, January 1976. doi: 10.1086/154083.

D. E. Osterbrock. Spectrophotometry of Seyfert 1 galaxies. *ApJ*, 215:733–745, August 1977. doi: 10.1086/155407.

D. E. Osterbrock. Seyfert galaxies with weak broad H alpha emission lines. *ApJ*, 249:462–470, October 1981. doi: 10.1086/159306.

D. E. Osterbrock. *Astrophysics of gaseous nebulae and active galactic nuclei*. University Science Books, 1989.

D. E. Osterbrock and R. W. Pogge. The spectra of narrow-line Seyfert 1 galaxies. *ApJ*, 297: 166–176, October 1985. doi: 10.1086/163513.

R. A. Overzier, H. J. A. Röttgering, J. D. Kurk, and C. De Breuck. Deep VLT spectroscopy of the z= 2.49 radio galaxy MRC 2104-242. Evidence for a metallicity gradient in its extended emission line region. *A&A*, 367:L5–L8, February 2001. doi: 10.1051/0004-6361:20010041.

R. A. Overzier, N. P. H. Nesvadba, M. Dijkstra, N. A. Hatch, M. D. Lehnert, M. Villar-Martín, R. J. Wilman, and A. W. Zirm. Resolving the Optical Emission Lines of Lyα Blob "B1" at z = 2.38: Another Hidden Quasar. *ApJ*, 771:89, July 2013. doi: 10.1088/0004-637X/771/2/89.

F. N. Owen and M. J. Ledlow. The FRI/Il Break and the Bivariate Luminosity Function in Abell Clusters of Galaxies. In G. V. Bicknell, M. A. Dopita, and P. J. Quinn, editors, *The Physics of Active Galaxies*, volume 54 of *Astronomical Society of the Pacific Conference Series*, page 319, 1994.

P. Padovani. High energy emission from AGN and unified schemes. In F. Giovannelli and G. Mannocchi, editors, *Vulcano Workshop 1998: Frontier Objects in Astrophysics and Particle Physics*, volume 65, page 159, 1999.

P. Padovani, D. M. Alexander, R. J. Assef, B. De Marco, P. Giommi, R. C. Hickox, G. T. Richards, V. Smolčić, E. Hatziminaoglou, V. Mainieri, and M. Salvato. Active galactic nuclei: what's in a name? *A&ARv*, 25:2, August 2017. doi: 10.1007/s00159-017-0102-9.

V. S. Paliya, C. S. Stalin, A. Shukla, and S. Sahayanathan. The Nature of γ-Ray Loud Narrow-line Seyfert I Galaxies PKS 1502+036 and PKS 2004-447. *ApJ*, 768:52, May 2013. doi: 10.1088/0004-637X/768/1/52.

V. S. Paliya, M. Ajello, S. Rakshit, A. K. Mandal, C. S. Stalin, A. Kaur, and D. Hartmann. Gamma-Ray-emitting Narrow-line Seyfert 1 Galaxies in the Sloan Digital Sky Survey. *ApJ*, 853:L2, January 2018. doi: 10.3847/2041-8213/aaa5ab.

R. B. Partridge and P. J. E. Peebles. Are Young Galaxies Visible? *ApJ*, 147:868, March 1967. doi: 10.1086/149079.

S. M. Pascarelle, R. A. Windhorst, S. P. Driver, E. J. Ostrander, and W. C. Keel. The Serendipitous Discovery of a Group or Cluster of Young Galaxies at z2.40 in Deep Hubble Space Telescope WFPC2 Images. *ApJ*, 456:L21, January 1996. doi: 10.1086/309852.

L. Pentericci, H. J. A. Roettgering, G. K. Miley, C. L. Carilli, and P. McCarthy. The radio galaxy 1138-262 at z=2.2: a giant elliptical galaxy at the center of a proto-cluster? *A&A*, 326:580–596, October 1997.

L. Pentericci, H. J. A. Röttgering, G. K. Miley, H. Spinrad, P. J. McCarthy, W. J. M. van Breugel, and F. Macchetto. HST Images of the Extremely Clumpy Radio Galaxy 1138-262 at z = 2.2. *ApJ*, 504:139–146, September 1998. doi: 10.1086/306087.

L. Pentericci, H. J. A. Röttgering, G. K. Miley, P. McCarthy, H. Spinrad, W. J. M. van Breugel, and F. Macchetto. HST images and properties of the most distant radio galaxies. *A&A*, 341: 329–347, January 1999.

L. Pentericci, P. J. McCarthy, H. J. A. Röttgering, G. K. Miley, W. J. M. van Breugel, and R. Fosbury. NICMOS Observations of High-Redshift Radio Galaxies: Witnessing the Formation of Bright Elliptical Galaxies? *ApJS*, 135:63–85, July 2001. doi: 10.1086/321781.

R. W. Pogge. Narrow-line Seyfert 1s: 15 years later. *New Astron. Rev.*, 44:381–385, September 2000. doi: 10.1016/S1387-6473(00)00065-8.

K. A. Pounds, C. Done, and J. P. Osborne. RE 1034+39: a high-state Seyfert galaxy? *MNRAS*, 277:L5–L10, November 1995. doi: 10.1093/mnras/277.1.L5.

M. K. M. Prescott, A. Dey, and B. T. Jannuzi. The Discovery of a Large Lyα+He II Nebula at z $\approx$ 1.67: A Candidate Low Metallicity Region? *ApJ*, 702:554–566, September 2009. doi: 10.1088/0004-637X/702/1/554.

J. X. Prochaska, B. Weiner, H.-W. Chen, J. Mulchaey, and K. Cooksey. Probing the Intergalactic Medium/Galaxy Connection. V. On the Origin of Lyα and O VI Absorption at z < 0.2. *ApJ*, 740:91, October 2011. doi: 10.1088/0004-637X/740/2/91.

S. Rakshit and C. S. Stalin. Optical Variability of Narrow-line and Broad-line Seyfert 1 Galaxies. *ApJ*, 842:96, June 2017. doi: 10.3847/1538-4357/aa72f4.

S. Rakshit, C. S. Stalin, H. Chand, and X.-G. Zhang. A Catalog of Narrow Line Seyfert 1 Galaxies from the Sloan Digital Sky Survey Data Release 12. *ApJS*, 229:39, April 2017. doi: 10.3847/1538-4365/aa6971.

M. Rauch, M. Haehnelt, A. Bunker, G. Becker, F. Marleau, J. Graham, S. Cristiani, M. Jarvis, C. Lacey, S. Morris, C. Peroux, H. Roettgering, and T. Theuns. Faint Lyα Emitters, Star-forming Galaxies, and Damped Lyα Systems. In T. Kodama, T. Yamada, and K. Aoki, editors, *Panoramic Views of Galaxy Formation and Evolution*, volume 399 of *Astronomical Society of the Pacific Conference Series*, page 59, October 2008a.

M. Rauch, M. Haehnelt, A. Bunker, G. Becker, F. Marleau, J. Graham, S. Cristiani, M. Jarvis, C. Lacey, S. Morris, C. Peroux, H. Röttgering, and T. Theuns. A Population of Faint Extended Line Emitters and the Host Galaxies of Optically Thick QSO Absorption Systems. *ApJ*, 681: 856–880, July 2008b. doi: 10.1086/525846.

J. I. Rawlings, N. Seymour, M. J. Page, C. De Breuck, D. Stern, M. Symeonidis, P. N. Appleton, A. Dey, M. Dickinson, M. Huynh, E. Le Floc'h, M. Lehnert, J. R. Mullaney, N. Nesvadba, P. Ogle, A. Sajina, J. Vernet, and A. Zirm. Polycyclic aromatic hydrocarbon emission in powerful high-redshift radio galaxies. *MNRAS*, 429:744–756, February 2013. doi: 10.1093/mnras/sts368.

M. J. Rees. The radio/optical alignment of high-z radio galaxies - Triggering of star formation in radio lobes. *MNRAS*, 239:1P–4P, July 1989. doi: 10.1093/mnras/239.1.1P.

M. Reuland, W. van Breugel, H. Röttgering, W. de Vries, S. A. Stanford, A. Dey, M. Lacy, J. Bland-Hawthorn, M. Dopita, and G. Miley. Giant Lyα Nebulae Associated with High-Redshift Radio Galaxies. *ApJ*, 592:755–766, August 2003. doi: 10.1086/375619.

R. Reyes, N. L. Zakamska, M. A. Strauss, J. Green, J. H. Krolik, Y. Shen, G. T. Richards, S. F. Anderson, and D. P. Schneider. Space Density of Optically Selected Type 2 Quasars. *AJ*, 136:2373–2390, December 2008. doi: 10.1088/0004-6256/136/6/2373.

D. Richstone, E. A. Ajhar, R. Bender, G. Bower, A. Dressler, S. M. Faber, A. V. Filippenko, K. Gebhardt, R. Green, L. C. Ho, J. Kormendy, T. R. Lauer, J. Magorrian, and S. Tremaine. Supermassive black holes and the evolution of galaxies. *Nature*, 395:A14, October 1998.

S. E. Ridgway and A. Stockton. Deep WFPC2 and Ground-Based Imaging of a Complete Sample of 3C Quasars and Galaxies. *AJ*, 114:511–543, August 1997. doi: 10.1086/118490.

B. Rocca-Volmerange, G. Drouart, C. De Breuck, J. Vernet, N. Seymour, D. Wylezalek, M. Lehnert, N. Nesvadba, and M. Fioc. Starburst and old stellar populations in the z $\sim$ 3.8 radio galaxies 4C 41.17 and TN J2007-1316. *MNRAS*, 429:2780–2790, March 2013. doi: 10.1093/mnras/sts413.

N. Roche, A. Humphrey, and L. Binette. Spectroscopy of 7 radio-loud QSOs at $2 < z < 6$: giant Lyman α emission nebulae accreting on to host galaxies. *MNRAS*, 443:3795–3808, October 2014. doi: 10.1093/mnras/stu1430.

J. Rosdahl and J. Blaizot. Extended Lyα emission from cold accretion streams. *MNRAS*, 423: 344–366, June 2012. doi: 10.1111/j.1365-2966.2012.20883.x.

N. P. Ross, F. Hamann, N. L. Zakamska, G. T. Richards, C. Villforth, M. A. Strauss, J. E. Greene, R. Alexandroff, W. N. Brandt, G. Liu, A. D. Myers, I. Pâris, and D. P. Schneider. Extremely red quasars from SDSS, BOSS and WISE: classification of optical spectra. *MNRAS*, 453: 3932–3952, November 2015. doi: 10.1093/mnras/stv1710.

H. J. A. Röttgering, M. Lacy, G. K. Miley, K. C. Chambers, and R. Saunders. Samples of ultra-steep spectrum radio sources. *A&AS*, 108, November 1994.

H. J. A. Röttgering, R. W. Hunstead, G. K. Miley, R. van Ojik, and M. H. Wieringa. Spatially Resolved Lyman-Alpha Absorption in the Z=2.9 Radio Galaxy 0943-242. *MNRAS*, 277:389, November 1995a. doi: 10.1093/mnras/277.2.389.

H. J. A. Röttgering, G. K. Miley, K. C. Chambers, and F. Macchetto. CCD imaging of ultra-steep-spectrum radio sources. *A&AS*, 114:51, November 1995b.

H. J. A. Röttgering, R. van Ojik, G. K. Miley, K. C. Chambers, W. J. M. van Breugel, and S. de Koff. Spectroscopy of ultra-steep spectrum radio sources: a sample of z>2 radio galaxies. *A&A*, 326:505–527, October 1997.

J. C. Runnoe, M. S. Brotherton, and Z. Shang. Updating quasar bolometric luminosity corrections. *MNRAS*, 422:478–493, May 2012. doi: 10.1111/j.1365-2966.2012.20620.x.

B. Rush, P. J. McCarthy, R. M. Athreya, and S. E. Persson. The High-Redshift Radio Galaxy MRC 0406-244. *ApJ*, 484:163–179, July 1997. doi: 10.1086/304307.

S. F. Sánchez and A. Humphrey. Integral field spectroscopy of two radio galaxies at z $\sim$ 2.3. *A&A*, 495:471–478, February 2009. doi: 10.1051/0004-6361:200811231.

R. Scarpa, C. M. Urry, P. Padovani, D. Calzetti, and M. O'Dowd. The Hubble Space Telescope Survey of BL Lacertae Objects. IV. Infrared Imaging of Host Galaxies. *ApJ*, 544:258–268, November 2000. doi: 10.1086/317199.

P. A. G. Scheuer. Models of extragalactic radio sources with a continuous energy supply from a central object. *MNRAS*, 166:513–528, March 1974. doi: 10.1093/mnras/166.3.513.

M. Schmidt. 3C 273 : A Star-Like Object with Large Red-Shift. *Nature*, 197:1040, March 1963. doi: 10.1038/1971040a0.

N. J. Schurch, R. S. Warwick, R. E. Griffiths, and S. M. Kahn. The complex soft X-ray spectrum of NGC 4151. *MNRAS*, 350:1–9, May 2004. doi: 10.1111/j.1365-2966.2004.07632.x.

C. K. Seyfert. Nuclear Emission in Spiral Nebulae. *ApJ*, 97:28, January 1943. doi: 10.1086/144488.

N. Seymour, D. Stern, C. De Breuck, J. Vernet, A. Rettura, M. Dickinson, A. Dey, P. Eisenhardt, R. Fosbury, M. Lacy, P. McCarthy, G. Miley, B. Rocca-Volmerange, H. Röttgering, S. A.

Stanford, H. Teplitz, W. van Breugel, and A. Zirm. The Massive Hosts of Radio Galaxies across Cosmic Time. *ApJS*, 171:353–375, August 2007. doi: 10.1086/517887.

N. Seymour, B. Altieri, C. De Breuck, P. Barthel, D. Coia, L. Conversi, H. Dannerbauer, A. Dey, M. Dickinson, G. Drouart, A. Galametz, T. R. Greve, M. Haas, N. Hatch, E. Ibar, R. Ivison, M. Jarvis, A. Kovács, J. Kurk, M. Lehnert, G. Miley, N. Nesvadba, J. I. Rawlings, A. Rettura, H. Röttgering, B. Rocca-Volmerange, M. Sánchez-Portal, J. S. Santos, D. Stern, J. Stevens, I. Valtchanov, J. Vernet, and D. Wylezalek. Rapid Coeval Black Hole and Host Galaxy Growth in MRC 1138-262: The Hungry Spider. *ApJ*, 755:146, August 2012. doi: 10.1088/0004-637X/755/2/146.

S. S. Shabala, A. Deller, S. Kaviraj, E. Middelberg, R. J. Turner, Y. S. Ting, J. R. Allison, and T. A. Davis. Delayed triggering of radio active galactic nuclei in gas-rich minor mergers in the local Universe. *MNRAS*, 464:4706–4720, February 2017. doi: 10.1093/mnras/stw2536.

D. Sijacki, V. Springel, T. Di Matteo, and L. Hernquist. A unified model for AGN feedback in cosmological simulations of structure formation. *MNRAS*, 380:877–900, September 2007. doi: 10.1111/j.1365-2966.2007.12153.x.

J. Silk. Unleashing Positive Feedback: Linking the Rates of Star Formation, Supermassive Black Hole Accretion, and Outflows in Distant Galaxies. *ApJ*, 772:112, August 2013. doi: 10.1088/0004-637X/772/2/112.

J. Silk and M. J. Rees. Quasars and galaxy formation. *A&A*, 331:L1–L4, March 1998.

M. Silva, A. Humphrey, P. Lagos, R. Guimarães, T. Scott, P. Papaderos, and S. G. Morais. Detection of large-scale Ly α absorbers at large angles to the radio axis of high-redshift radio galaxies using SOAR. *MNRAS*, 481:1401–1415, November 2018a. doi: 10.1093/mnras/sty2351.

M. Silva, A. Humphrey, P. Lagos, M. Villar-Martín, S. G. Morais, S. di Serego Alighieri, A. Cimatti, R. Fosbury, R. A. Overzier, J. Vernet, and L. Binette. The MUSE 3D view of feedback in a high-metallicity radio galaxy at z = 2.9. *MNRAS*, 474:3649–3672, March 2018b. doi: 10.1093/mnras/stx3019.

L. E. Simon and F. Hamann. Metallicity and far-infrared luminosity of high-redshift quasars. *MNRAS*, 407:1826–1834, September 2010. doi: 10.1111/j.1365-2966.2010.17022.x.

C. Simpson, A. Martínez-Sansigre, S. Rawlings, R. Ivison, M. Akiyama, K. Sekiguchi, T. Takata, Y. Ueda, and M. Watson. Radio imaging of the Subaru/XMM-Newton Deep Field

- I. The 100-μJy catalogue, optical identifications, and the nature of the faint radio source population. *MNRAS*, 372:741–757, October 2006. doi: 10.1111/j.1365-2966.2006.10907.x.

V. M. Slipher. The spectrum and velocity of the nebula N.G.C. 1068 (M 77). *Lowell Observatory Bulletin*, 3:59–62, 1917.

D. A. Smith and C. Done. Unified theories of active galactic nuclei: a hard X-ray sample of Seyfert 2 galaxies. *MNRAS*, 280:355–377, May 1996. doi: 10.1093/mnras/280.2.355.

A. Soltan. Masses of quasars. *MNRAS*, 200:115–122, July 1982. doi: 10.1093/mnras/200.1.115.

R. S. Somerville, P. F. Hopkins, T. J. Cox, B. E. Robertson, and L. Hernquist. A semi-analytic model for the co-evolution of galaxies, black holes and active galactic nuclei. *MNRAS*, 391: 481–506, December 2008. doi: 10.1111/j.1365-2966.2008.13805.x.

V. Springel. The cosmological simulation code GADGET-2. *MNRAS*, 364:1105–1134, December 2005. doi: 10.1111/j.1365-2966.2005.09655.x.

C. C. Steidel, K. L. Adelberger, A. E. Shapley, M. Pettini, M. Dickinson, and M. Giavalisco. Lyα Imaging of a Proto-Cluster Region at <z>=3.09. *ApJ*, 532:170–182, March 2000. doi: 10.1086/308568.

C. C. Steidel, M. Bogosavljević, A. E. Shapley, J. A. Kollmeier, N. A. Reddy, D. K. Erb, and M. Pettini. Diffuse Lyα Emitting Halos: A Generic Property of High-redshift Star-forming Galaxies. *ApJ*, 736:160, August 2011. doi: 10.1088/0004-637X/736/2/160.

D. Stern, P. Tozzi, S. A. Stanford, P. Rosati, B. Holden, P. Eisenhardt, R. Elston, K. L. Wu, A. Connolly, H. Spinrad, S. Dawson, A. Dey, and F. H. Chaffee. SPICES II: Optical and Near-Infrared Identifications of Faint X-Ray Sources from Deep Chandra Observations of Lynx. *AJ*, 123:2223–2245, May 2002. doi: 10.1086/339967.

D. Stern, P. Eisenhardt, V. Gorjian, C. S. Kochanek, N. Caldwell, D. Eisenstein, M. Brodwin, M. J. I. Brown, R. Cool, A. Dey, P. Green, B. T. Jannuzi, S. S. Murray, M. A. Pahre, and S. P. Willner. Mid-Infrared Selection of Active Galaxies. *ApJ*, 631:163–168, September 2005. doi: 10.1086/432523.

D. Stern, R. J. Assef, D. J. Benford, A. Blain, R. Cutri, A. Dey, P. Eisenhardt, R. L. Griffith, T. H. Jarrett, S. Lake, F. Masci, S. Petty, S. A. Stanford, C.-W. Tsai, E. L. Wright, L. Yan, F. Harrison, and K. Madsen. Mid-infrared Selection of Active Galactic Nuclei with the Wide-Field Infrared Survey Explorer. I. Characterizing WISE-selected Active Galactic Nuclei in COSMOS. *ApJ*, 753:30, July 2012. doi: 10.1088/0004-637X/753/1/30.

D. Stern, G. B. Lansbury, R. J. Assef, W. N. Brandt, D. M. Alexander, D. R. Ballantyne, M. Baloković, F. E. Bauer, D. Benford, A. Blain, S. E. Boggs, C. Bridge, M. Brightman, F. E. Christensen, A. Comastri, W. W. Craig, A. Del Moro, P. R. M. Eisenhardt, P. Gandhi, R. L. Griffith, C. J. Hailey, F. A. Harrison, R. C. Hickox, T. H. Jarrett, M. Koss, S. Lake, S. M. LaMassa, B. Luo, C.-W. Tsai, C. M. Urry, D. J. Walton, E. L. Wright, J. Wu, L. Yan, and W. W. Zhang. NuSTAR and XMM-Newton Observations of Luminous, Heavily Obscured, WISE-selected Quasars at z ˜ 2. *ApJ*, 794:102, October 2014. doi: 10.1088/0004-637X/794/2/102.

R. S. Sutherland, G. V. Bicknell, and M. A. Dopita. Shock excitation of the emission-line filaments in Centaurus A. *ApJ*, 414:510–526, September 1993. doi: 10.1086/173099.

A. M. Swinbank, J. D. R. Vernet, I. Smail, C. De Breuck, R. Bacon, T. Contini, J. Richard, H. J. A. Röttgering, T. Urrutia, and B. Venemans. Mapping the dynamics of a giant Ly α halo at z = 4.1 with MUSE: the energetics of a large-scale AGN-driven outflow around a massive, high-redshift galaxy. *MNRAS*, 449:1298–1308, May 2015. doi: 10.1093/mnras/stv366.

C. Tadhunter. Radio AGN in the local universe: unification, triggering and evolution. *A&ARv*, 24:10, June 2016. doi: 10.1007/s00159-016-0094-x.

C. N. Tadhunter, A. Robinson, and R. Morganti. The OIII Temperature Problem for Extended Nebulosities. In E. J. A. Meurs and R. A. E. Fosbury, editors, *European Southern Observatory Conference and Workshop Proceedings*, volume 32 of *European Southern Observatory Conference and Workshop Proceedings*, page 293, July 1989.

C. N. Tadhunter, S. M. Scarrott, P. Draper, and C. Rolph. The optical polarizations of high- and intermediate-redshift radio galaxies. *MNRAS*, 256:53P–58P, June 1992. doi: 10.1093/mnras/256.1.53P.

Y. Taniguchi, Y. Ohyama, T. Murayama, M. Yoshida, N. Kashikawa, M. Iye, K. Aoki, T. Sasaki, G. Kosugi, T. Takata, Y. Saito, K. S. Kawabata, K. Sekiguchi, K. Okita, Y. Shimizu, M. Inata, N. Ebizuka, T. Ozawa, Y. Yadomaru, H. Taguchi, Y. Shioya, S. Nishiura, H. Sudou, T. Nagao, S. Noda, Y. Koyama, Y. Kakazu, M. Ajiki, S. S. Fujita, and R. R. Kobayashi. A Shock-induced Pair of Superbubbles in the High-Redshift Powerful Radio Galaxy MRC 0406-244. *ApJ*, 559: L9–L12, September 2001. doi: 10.1086/323652.

G. Tenorio-Tagle, S. A. Silich, D. Kunth, E. Terlevich, and R. Terlevich. The evolution of superbubbles and the detection of Lyα in star-forming galaxies. *MNRAS*, 309:332–342, October 1999. doi: 10.1046/j.1365-8711.1999.02809.x.

R. F. Trainor and C. C. Steidel. The Halo Masses and Galaxy Environments of Hyperluminous QSOs at z ≅ 2.7 in the Keck Baryonic Structure Survey. *ApJ*, 752:39, June 2012. doi: 10.1088/0004-637X/752/1/39.

H. D. Tran, M. H. Cohen, and M. Villar-Martin. Keck Observations of the Hidden Quasar IRAS P09104+4109. *AJ*, 120:562–574, August 2000. doi: 10.1086/301470.

J. Tumlinson, C. Thom, J. K. Werk, J. X. Prochaska, T. M. Tripp, D. H. Weinberg, M. S. Peeples, J. M. O'Meara, B. D. Oppenheimer, J. D. Meiring, N. S. Katz, R. Davé, A. B. Ford, and K. R. Sembach. The Large, Oxygen-Rich Halos of Star-Forming Galaxies Are a Major Reservoir of Galactic Metals. *Science*, 334:948, November 2011. doi: 10.1126/science.1209840.

T. J. Turner, I. M. George, K. Nandra, and R. F. Mushotzky. ASCA Observations of Type 2 Seyfert Galaxies. II. The Importance of X-Ray Scattering and Reflection. *ApJ*, 488:164–173, October 1997. doi: 10.1086/304701.

C. M. Urry and P. Padovani. Unified Schemes for Radio-Loud Active Galactic Nuclei. *PASP*, 107:803, September 1995. doi: 10.1086/133630.

M. Urry. The AGN Paradigm for Radio-Loud Objects. In S. Collin, F. Combes, and I. Shlosman, editors, *Active Galactic Nuclei: From Central Engine to Host Galaxy*, volume 290 of *Astronomical Society of the Pacific Conference Series*, page 3, 2003.

I. van Bemmel and P. Barthel. Broad-line radio galaxies: Old and feeble? *A&A*, 379:L21–L24, November 2001. doi: 10.1051/0004-6361:20011348.

W. van Breugel, T. Heckman, H. Butcher, and G. Miley. Extended optical line emission from 3C 293 - Radio jets propagating through a rotating gaseous disk. *ApJ*, 277:82–91, February 1984. doi: 10.1086/161673.

W. J. M. van Breugel, S. A. Stanford, H. Spinrad, D. Stern, and J. R. Graham. Morphological Evolution in High-Redshift Radio Galaxies and the Formation of Giant Elliptical Galaxies. *ApJ*, 502:614–629, August 1998. doi: 10.1086/305925.

R. van Ojik, H. J. A. Rottgering, G. K. Miley, M. N. Bremer, F. Macchetto, and K. C. Chambers. TX0211-122: A starburst radio galaxy at Z = 2.34? *A&A*, 289:54–60, September 1994.

R. van Ojik, H. J. A. Röttgering, C. L. Carilli, G. K. Miley, M. N. Bremer, and F. Macchetto. A powerful radio galaxy at z=3.6 in a giant rotating Lyman α halo. *A&A*, 313:25–44, September 1996.

R. van Ojik, H. J. A. Röttgering, G. K. Miley, and R. W. Hunstead. The gaseous environments of radio galaxies in the early Universe: kinematics of the Lyman α emission and spatially resolved H I absorption. *AAP*, 317:358–384, January 1997.

B. P. Venemans, H. J. A. Röttgering, R. A. Overzier, G. K. Miley, C. De Breuck, J. D. Kurk, W. van Breugel, C. L. Carilli, H. Ford, T. Heckman, P. McCarthy, and L. Pentericci. Discovery of six Lyα emitters near a radio galaxy at z ~ 5.2. *A&A*, 424:L17–L20, September 2004. doi: 10.1051/0004-6361:200400041.

B. P. Venemans, H. J. A. Röttgering, G. K. Miley, W. J. M. van Breugel, C. de Breuck, J. D. Kurk, L. Pentericci, S. A. Stanford, R. A. Overzier, S. Croft, and H. Ford. Protoclusters associated with z > 2 radio galaxies . I. Characteristics of high redshift protoclusters. *A&A*, 461:823–845, January 2007. doi: 10.1051/0004-6361:20053941.

A. Verhamme, D. Schaerer, and A. Maselli. 3D Lyα radiation transfer. I. Understanding Lyα line profile morphologies. *A&A*, 460:397–413, December 2006. doi: 10.1051/0004-6361:20065554.

A. Verhamme, Y. Dubois, J. Blaizot, T. Garel, R. Bacon, J. Devriendt, B. Guiderdoni, and A. Slyz. Lyman-α emission properties of simulated galaxies: interstellar medium structure and inclination effects. *AAP*, 546:A111, October 2012. doi: 10.1051/0004-6361/201218783.

R. C. Vermeulen and M. H. Cohen. Superluminal motion statistics and cosmology. *ApJ*, 430: 467–494, August 1994. doi: 10.1086/174424.

J. Vernet, R. A. E. Fosbury, M. Villar-Martín, M. H. Cohen, A. Cimatti, S. di Serego Alighieri, and R. W. Goodrich. Radio galaxies at z ~ 2.5: Results from Keck spectropolarimetry. *A&A*, 366:7–25, January 2001. doi: 10.1051/0004-6361:20000076.

J. Vernet, H. Dekker, S. D'Odorico, L. Kaper, P. Kjaergaard, F. Hammer, S. Randich, F. Zerbi, P. J. Groot, J. Hjorth, I. Guinouard, R. Navarro, T. Adolfse, P. W. Albers, J.-P. Amans, J. J. Andersen, M. I. Andersen, P. Binetruy, P. Bristow, R. Castillo, F. Chemla, L. Christensen, P. Conconi, R. Conzelmann, J. Dam, V. de Caprio, A. de Ugarte Postigo, B. Delabre, P. di Marcantonio, M. Downing, E. Elswijk, G. Finger, G. Fischer, H. Flores, P. François, P. Goldoni, L. Guglielmi, R. Haigron, H. Hanenburg, I. Hendriks, M. Horrobin, D. Horville, N. C. Jessen, F. Kerber, L. Kern, M. Kiekebusch, P. Kleszcz, J. Klougart, J. Kragt, H. H. Larsen, J.-L. Lizon, C. Lucuix, V. Mainieri, R. Manuputy, C. Martayan, E. Mason, R. Mazzoleni, N. Michaelsen, A. Modigliani, S. Moehler, P. Møller, A. Norup Sørensen, P. Nørregaard, C. Péroux, F. Patat, E. Pena, J. Pragt, C. Reinero, F. Rigal, M. Riva, R. Roelfsema, F. Royer,

G. Sacco, P. Santin, T. Schoenmaker, P. Spano, E. Sweers, R. Ter Horst, M. Tintori, N. Tromp, P. van Dael, H. van der Vliet, L. Venema, M. Vidali, J. Vinther, P. Vola, R. Winters, D. Wistisen, G. Wulterkens, and A. Zacchei. X-shooter, the new wide band intermediate resolution spectrograph at the ESO Very Large Telescope. *A&A*, 536:A105, December 2011. doi: 10.1051/0004-6361/201117752.

J. Vernet, M. D. Lehnert, C. De Breuck, M. Villar-Martín, D. Wylezalek, T. Falkendal, G. Drouart, S. Kolwa, A. Humphrey, B. P. Venemans, and F. Boulanger. Are we seeing accretion flows in a 250 kpc Lyα halo at z = 3? *A&A*, 602:L6, June 2017. doi: 10.1051/0004-6361/201730865.

M.-P. Véron-Cetty, P. Véron, and A. C. Gonçalves. A spectrophotometric atlas of Narrow-Line Seyfert 1 galaxies. *A&A*, 372:730–754, June 2001. doi: 10.1051/0004-6361:20010489.

M. Villar-Martín, C. Tadhunter, and N. Clark. The ionization mechanism of the extended gas in high redshift radio galaxies: shocks or AGN photoionization? *A&A*, 323:21–30, July 1997.

M. Villar-Martín, L. Binette, and R. A. E. Fosbury. The nature of the extreme kinematics in the extended gas of high redshift radio galaxies. *A&A*, 346:7–12, June 1999a.

M. Villar-Martín, R. A. E. Fosbury, L. Binette, C. N. Tadhunter, and B. Rocca-Volmerange. UV rest frame spectroscopy of four high redshift (z>2) active galaxies. *A&A*, 351:47–58, November 1999b.

M. Villar-Martín, C. Tadhunter, R. Morganti, D. Axon, and A. Koekemoer. PKS 2250-41 and the role of jet-cloud interactions in powerful radio galaxies. *MNRAS*, 307:24–40, July 1999c. doi: 10.1046/j.1365-8711.1999.02603.x.

M. Villar-Martín, A. Alonso-Herrero, S. di Serego Alighieri, and J. Vernet. Interpreting the kinematics of the extended gas in distant radiogalaxies from 8-10 m telescope spectra. *A&AS*, 147:291–297, December 2000. doi: 10.1051/aas:2000303.

M. Villar-Martín, D. De Young, A. Alonso-Herrero, M. Allen, and L. Binette. Shocks and dust survival in nearby active galaxies: implications for the alignment effect. *MNRAS*, 328: 848–854, December 2001. doi: 10.1046/j.1365-8711.2001.04916.x.

M. Villar-Martín, J. Vernet, S. di Serego Alighieri, R. Fosbury, L. Pentericci, M. Cohen, R. Goodrich, and A. Humphrey. Giant low surface brightness haloes in distant radio galaxies: USS0828+193. *MNRAS*, 336:436–444, October 2002. doi: 10.1046/j.1365-8711.2002.05751.x.

M. Villar-Martín, J. Vernet, S. di Serego Alighieri, R. Fosbury, A. Humphrey, and L. Pentericci. Kinematically quiet haloes around z ∽ 2.5 radio galaxies. Keck spectroscopy. *MNRAS*, 346: 273–294, November 2003. doi: 10.1046/j.1365-2966.2003.07090.x.

M. Villar-Martín, S. F. Sánchez, C. De Breuck, R. Peletier, J. Vernet, A. Rettura, N. Seymour, A. Humphrey, D. Stern, S. di Serego Alighieri, and R. Fosbury. VIMOS-VLT and Spitzer observations of a radio galaxy at z= 2.5*. *MNRAS*, 366:L1–L5, February 2006. doi: 10.1111/j.1745-3933.2005.00118.x.

M. Villar-Martín, A. Humphrey, C. De Breuck, R. Fosbury, L. Binette, and J. Vernet. Lyα excess in high-redshift radio galaxies: a signature of star formation. *MNRAS*, 375:1299–1310, March 2007a. doi: 10.1111/j.1365-2966.2006.11371.x.

M. Villar-Martín, S. F. Sánchez, A. Humphrey, M. Dijkstra, S. di Serego Alighieri, C. De Breuck, and R. González Delgado. VIMOS-VLT spectroscopy of the giant Lyα nebulae associated with three z ∽ 2.5 radio galaxies. *MNRAS*, 378:416–428, June 2007b. doi: 10.1111/j.1365-2966.2007.11811.x.

M. Villar-Martín, S. Arribas, B. Emonts, A. Humphrey, C. Tadhunter, P. Bessiere, A. Cabrera Lavers, and C. Ramos Almeida. Ionized outflows in luminous type 2 AGNs at z < 0.6: no evidence for significant impact on the host galaxies. *MNRAS*, 460:130–162, July 2016. doi: 10.1093/mnras/stw901.

T. Wang, W. Brinkmann, and J. Bergeron. X-ray properties of active galactic nuclei with optical FeII emission. *A&A*, 309:81–96, May 1996.

T. M. A. Webb, T. Yamada, J.-S. Huang, M. L. N. Ashby, Y. Matsuda, E. Egami, M. Gonzalez, and T. Hayashimo. Spitzer Observations of Extended Lyman-α Clouds in the SSA22 Field. *ApJ*, 692:1561–1570, February 2009. doi: 10.1088/0004-637X/692/2/1561.

D. W. Weedman. Seyfert galaxies. *ARA&A*, 15:69–95, 1977. doi: 10.1146/annurev.aa.15.090177.000441.

M. Weidinger, P. Møller, J. P. U. Fynbo, and B. Thomsen. The extended Lyman-α emission surrounding the z = 3.04 radio-quiet QSO1205-30: Primordial infalling gas illuminated by the quasar? *A&A*, 436:825–835, June 2005. doi: 10.1051/0004-6361:20042304.

R. J. Wilman, M. J. Jarvis, H. J. A. Röttgering, and L. Binette. HI in the protocluster environment at z > 2: absorbing haloes and the Lyα forest. *MNRAS*, 351:1109–1119, July 2004. doi: 10.1111/j.1365-2966.2004.07857.x.

X.-B. Wu, F. Wang, X. Fan, W. Yi, W. Zuo, F. Bian, L. Jiang, I. D. McGreer, R. Wang, J. Yang, Q. Yang, D. Thompson, and Y. Beletsky. An ultraluminous quasar with a twelve-billion-solar-mass black hole at redshift 6.30. *Nature*, 518:512–515, February 2015. doi: 10.1038/nature14241.

D. Wylezalek, N. L. Zakamska, G. Liu, and G. Obied. Towards a comprehensive picture of powerful quasars, their host galaxies and quasar winds at z $\sim$ 0.5. *MNRAS*, 457:745–763, March 2016. doi: 10.1093/mnras/stv3022.

D. Xu, S. Komossa, H. Zhou, H. Lu, C. Li, D. Grupe, J. Wang, and W. Yuan. Correlation Analysis of a Large Sample of Narrow-line Seyfert 1 Galaxies: Linking Central Engine and Host Properties. *AJ*, 143:83, April 2012. doi: 10.1088/0004-6256/143/4/83.

F. Xu, F. Bian, Y. Shen, W. Zuo, X. Fan, and Z. Zhu. The Evolution of Chemical Abundance in Quasar Broad Line Region. *MNRAS*, July 2018. doi: 10.1093/mnras/sty1763.

Y. Yang, A. I. Zabludoff, R. Davé, D. J. Eisenstein, P. A. Pinto, N. Katz, D. H. Weinberg, and E. J. Barton. Probing Galaxy Formation with He II Cooling Lines. *ApJ*, 640:539–552, April 2006. doi: 10.1086/497898.

Y. Yang, A. Zabludoff, K. Jahnke, and R. Davé. The Properties of Lyα Nebulae: Gas Kinematics from Nonresonant Lines. *ApJ*, 793:114, October 2014. doi: 10.1088/0004-637X/793/2/114.

S. Young, J. H. Hough, D. J. Axon, A. C. Fabian, and M. J. Ward. The obscured BLR in the radio galaxy 3C 234. *MNRAS*, 294:478, March 1998. doi: 10.1046/j.1365-8711.1998.01243.x.

W. Yuan, H. Y. Zhou, S. Komossa, X. B. Dong, T. G. Wang, H. L. Lu, and J. M. Bai. A Population of Radio-Loud Narrow-Line Seyfert 1 Galaxies with Blazar-Like Properties? *ApJ*, 685:801–827, October 2008. doi: 10.1086/591046.

N. L. Zakamska, M. A. Strauss, J. H. Krolik, M. J. Collinge, P. B. Hall, L. Hao, T. M. Heckman, Ž. Ivezić, G. T. Richards, D. J. Schlegel, D. P. Schneider, I. Strateva, D. E. Vanden Berk, S. F. Anderson, and J. Brinkmann. Candidate Type II Quasars from the Sloan Digital Sky Survey. I. Selection and Optical Properties of a Sample at 0.3<Z<0.83. *AJ*, 126:2125–2144, November 2003. doi: 10.1086/378610.

N. L. Zakamska, G. D. Schmidt, P. S. Smith, M. A. Strauss, J. H. Krolik, P. B. Hall, G. T. Richards, D. P. Schneider, J. Brinkmann, and G. P. Szokoly. Candidate Type II Quasars from the Sloan Digital Sky Survey. III. Spectropolarimetry Reveals Hidden Type I Nuclei. *AJ*, 129:1212–1224, March 2005. doi: 10.1086/427543.

S. Zhang, H. Zhou, X. Shi, X. Pan, T. Ji, and P. Jiang. Ultra-dense Broad-line Region Scale Outflow in Highly Reddened Quasar SDSS J145057.28+530007.6. *AJ*, 156:4, July 2018. doi: 10.3847/1538-3881/aac433.

Z. Zheng, R. Cen, H. Trac, and J. Miralda-Escudé. Radiative Transfer Modeling of Lyα Emitters. I. Statistics of Spectra and Luminosity. *ApJ*, 716:574–598, June 2010. doi: 10.1088/0004-637X/716/1/574.

Z. Zheng, R. Cen, D. Weinberg, H. Trac, and J. Miralda-Escudé. Extended Lyα Emission around Star-forming Galaxies. *ApJ*, 739:62, October 2011. doi: 10.1088/0004-637X/739/2/62.

P.-C. Zinn, E. Middelberg, R. P. Norris, and R.-J. Dettmar. Active Galactic Nucleus Feedback Works Both Ways. *ApJ*, 774:66, September 2013. doi: 10.1088/0004-637X/774/1/66.

K. Zubovas, S. Nayakshin, S. Sazonov, and R. Sunyaev. Outflows of stars due to quasar feedback. *MNRAS*, 431:793–798, May 2013. doi: 10.1093/mnras/stt214.